Ph.D Thesis

8th December 2017

A search for top-antitop resonances in all hadronic mode using proton-proton collisions at a center-of-mass energy of 13 TeV with the ATLAS detector

Suzuki, Shota[a]

[a]*Department of Particle and Nuclear Physics, School of High Energy Accelerator Science, The Graduate University for Advanced Studies*

Contents

Abstract

This thesis describes the search for heavy resonances decaying into top quark pairs in fully hadronic decay modes. The search uses proton-proton collidiing events recorded with the ATLAS detector at the Large Hadron Collider (LHC) running at a center-of-mass energy of 13 TeV. The data corresponds to an integrated luminosity of 36.1 fb^{-1}.

A lot of new physics models beyond the Standard Model predicts heavy new particles decaying into top quark pairs. This search is a model independent search of new particles, and many kinds of new models can be tested at the same time.
The fully-hadronic final state has the highest branching ratio in the decay of top quark pairs. The resolution of reconstructed top mass and top paire mass are better than the other final-states because all the final-state particles can be reconstructed. The target mass region of new particle is in a TeV scale where yields of multijets background is relatively low. In addition, both of top quarks decaying from heavy new particle are highly boosted in the region.
The boosted top quark is reconstructed using the anti-k_T jet algorithm with a radius parameter of 1.0, refered to as large-R jets.

Top-quark jets are identified with mass of the large-R jet and τ_{32}^{wta}, which shows whether the substructure of large-R jet is three-prong like or not. The top quark jet is also required to include an associated b-tagged track jet reconstructed with the radius parameter of 0.2. multijets background is estimated using a data-driven method.

The sensitivity of this search is expected as the same as a search in the semi-leptonic final state. If no new particles are found, expected exclusion limits can reach to a mass of 3.1 TeV for the Leptophobic Z'_{TC2} at the 95% confidential level and a mass of 3.5 TeV for the Kaluza–Klein gluon.

1. Introduction

Resonance search is to look for a evidence of new particles which make a statistical difference between the expected distribution and the experimental data. The expected distribution is estimated from the Standard Model (SM). If a new particle decays into two top quarks, a mass peak can be observed around the mass of new particle in the invariant mass of the $t\bar{t}$ system. This analysis looks for a significant difference in $m_{t\bar{t}}$ distribution. The search does not depend on a certain physics model, because the approach of resonance search is to simply evaluate any enhancement in the $m_{t\bar{t}}$ distributions observed in data. This feature is a strong point of this analysis, because several physics models can be judged through this analysis.

This thesis focuses on the top-antitop ($t\bar{t}$) mass spectrum. The top quark is the heaviest particle in the SM and has a very large coupling to the Higgs boson. New physics models propose an alternative Electroweak Symmetry Breaking mechanism, which predicts new particles with a larger coupling to the top quark, than to the lighter quarks.

The search reconstructs hadronically decaing $t\bar{t}$ events, where each of W bosons from top and anti-top quarks decays to two quarks. This decay topology is called as a all-hadronic channel. The chanel has a large statistics, which is suitable for the search. However the large contamination of the multijet events makes the reconstruction of the events challenging. The reconstruction of top quarks is performed large size jets, namely anti-k_T jets with the radius parameter R=1.0. In the high mass region of the $t\bar{t}$ system, top and anti-top quarks are highly boosted and their decay products are expected to be collimated. As a results, a top quark can be reconstructed as a large-R jet. This allow to access high p_T top quarks with a reasonable resolution.

Previous searches performed by the ATLAS, CMS, CDF and DØ collaborations [1–4] have set limits on this resonance. In case of the Z' search, the most stringent mass limit has been set as $m_{Z'} > 2.1$ TeV [1, 3, 5–14].

In this thesis, the search is performed using the proton-proton colliding events recorded with the ATLAS detector at the Large Hadron Collider (LHC) running at a center-of-mass energy of 13 TeV. The data corresponds to an integrated luminosity of 36.1 fb^{-1}.

The outline of this thesis is as follows.

Chapter 2 states the strategy of the resonance search and theoretical background of this analysis.
Chapter 3 shows a belief summary of the LHC and the ATLAS detector.
Monte-Carlo simulation samples are summarized in Chapter 4.
Chapter 5 provides the definition of objects which are used in the event selection of this analysis.
From Chapter 6 to 9, the details for main part of this analysis are described.
How to optimize the signal event selections is written in Chapter 6
In Chapter 7, the result of checking the contributions of every possible background is shown, and the details of multi-jet estimation with data driven method is provided.
Chapter 8 summarizes the systematic uncertainties in this analysis.
Expected cross section limits for several signal models are provided as a result in Chapter 9.
Chapter 10 gives the conclusions of this thesis.

In this thesis, a resonance search is performed using a $t\bar{t}$ invariant mass spectrum.

2. Theoretical background

The Standard Model (SM) of particle physics can explain the most of the fundamental physics phenomena. However the SM still gives remained some problems. In order to solve those problems, the new physics beyond the SM (BSM) are needed, and many kinds of the BSM models have been proposed.

In this chapter, the SM is introduced, and those problems of the SM are summarized. Some theories of the BSM which can be searched in this analysis are also introduced.

2.1. The Standard Model

On 2012, the Higgs boson which was the last piece of the SM was discovered, and all elementary particles predicted in the SM are found [15]. There are two types of elementary particles. One of them is called fermions which obeys the Fermi-Dirac statistics, while the other is called bosons obeying the Bose-Einstein statistics. Fermions and bosons are summarized in Table 1 and 2, respectively.

Table 1: Fermions in the SM. The quantum numbers Q, I, I^3, Y are electrical charge, weak isospin, third components of weak isospin, and weak hyper charge, respectively. L and R denote left- and right-handed chiral states, respectively.

	Generation			Quantum Number			
	1st	2nd	3rd	Q	I	I^3	Y
Quarks	$\begin{pmatrix} u \\ d \end{pmatrix}_L$	$\begin{pmatrix} c \\ s \end{pmatrix}_L$	$\begin{pmatrix} t \\ b \end{pmatrix}_L$	$\begin{pmatrix} 2/3 \\ -1/3 \end{pmatrix}$	1/2	$\begin{pmatrix} 1/2 \\ -1/2 \end{pmatrix}$	1/3
	u_R	c_R	t_R	$2/3$	0	0	$4/3$
	d_R	s_R	b_R	$-1/3$	0	0	$-2/3$
Leptons	$\begin{pmatrix} \nu_e \\ e^- \end{pmatrix}_L$	$\begin{pmatrix} \nu_\mu \\ \mu^- \end{pmatrix}_L$	$\begin{pmatrix} \nu_\tau \\ \tau^- \end{pmatrix}_L$	$\begin{pmatrix} 0 \\ -1 \end{pmatrix}$	1/2	$\begin{pmatrix} 1/2 \\ -1/2 \end{pmatrix}$	-1
	e^-_R	μ^-_R	τ^-_R	-1	0	0	-2

Table 2: Bosons in the SM. The quantum numbers S^p, Q, I, I^3, Y are spin-parity,electrical charge, weak isospin, third components of weak isospin, and weak hyper charge, respectively. The values of mass are taken from [16].

		mass[GeV/c^2]	S^p	Q	I	I^3	Y	Interaction
Photon	γ	0	1^-	0	0	0	0	electromagnetic
Weak bosons	$W^\pm$	80.385	1^-	± 1	1	± 1	0	weak
	Z	91.1876	1^-	0	0	0	0	
Gluon	g	0	1^-	0	0	0	0	strong
Higgs	h	125.7	0^+	0	1/2	-1/2	1	

The SM provides unified description of fundamental interaction in the nature. The fermions are quarks and leptons, and form a matter. Quarks have up-type and down-type, and then both quarks and leptons are separated by the three categories called generation (1st, 2nd and 3rd). In addition, there are anti-fermions which has the same mass for fermions but has the opposite values for the other properties. The bosons are consist of four gauge bosons and the Higgs boson. Photon, weak bosons and gluon mediate electromagnetic interaction, weak interaction (See Sec. 2.1.3) and strong interaction (See Sec. 2.1.2), respectively. The Higgs boson interacts to all particles by the Yukawa interaction and the particles obtain

own masses by this interaction through the Brout-Englert-Higgs mechanism (BEH mechanism) [17] (See Sec. 2.1.4).

2.1.1. Quantum electrodynamics (QED)

In 1865, electricity and magnetism were unified into a single theory as the electromagnetic theory by Clerk Maxwell. Later, the electromagnetic theory was quantized by Dirac, and the quantum-electromagnetic dynamics (QED) was completed by Tomonaga, Schwinger and Feynman [18–21].

The Lagrangian of an electron in a field-free space can be written as

$$\mathcal{L}_{\text{Dirac}} = \bar{\Psi}\,(i\gamma^{\mu}\partial_{\mu} - m)\Psi, \tag{1}$$

where Ψ denotes the electromagnetic fields, γ^{μ} (μ =0,1,2,3) satisfy

$$\gamma^{0} = \begin{bmatrix} 1 & -0 \\ 0 & -1 \end{bmatrix},\ \gamma^{i} = \begin{bmatrix} 0 & \sigma_i \\ -\sigma_i & 0 \end{bmatrix}, \tag{2}$$

where σ_i (i =1,2,3) denote Pauli matrix. If local phase transformation ($U(1)$ transformation)

$$\Psi \to e^{-ie\theta}\Psi$$

is performed, the $\mathcal{L}_{\text{Dirac}}$ has local gauge invariance with the following covariant derivative :

$$D_{\mu} = \partial_{\mu} + ieA_{\mu}, \tag{3}$$

where A_{μ} denote a vector field (photon field). The $\mathcal{L}_{\text{Dirac}}$ is changed as

$$\begin{aligned} \mathcal{L}_{\text{Dirac}} &= \bar{\Psi}\,(i\gamma^{\mu}D_{\mu} - m)\Psi - \frac{1}{4}F_{\mu\nu}F^{\mu\nu} \\ &= \bar{\Psi}\,(i\gamma^{\mu}\partial_{\mu} - m)\Psi - \frac{1}{4}F_{\mu\nu}F^{\mu\nu} - e(\bar{\Psi}\gamma^{\mu}\Psi)A_{\mu}, \end{aligned} \tag{4}$$

where $F_{\mu\nu}$ is field-strength and satisfy

$$F_{\mu\nu} = \partial_{\mu}A_{\nu} - \partial_{\nu}A_{\mu}. \tag{5}$$

The first term of Eq.4 shows the electron kinetic term and the electron mass term. The second term is the photon kinetic term, and the third term denotes an interaction between electromagnetic current and photon field (electromagnetic interaction). It is important to obtain the interaction term through the local gauge transformation, and it means that the form of an interaction is decided by introducing a gauge field.

If the $U(1)$ transform is generalized by Lie-group, the transformation can be denoted as

$$G(\epsilon) = e^{i\epsilon^{a}T^{a}}, \tag{6}$$

where ϵ denotes a parameter, and T is a generator of the Lie-group. T satisfy

$$[T^{a}, T^{b}] = if^{abc}T^{c}, \tag{7}$$

where f denotes a structure constant of the Lie-group. When the gauge transformation can be written as

$$\Psi_i(x) \to [G(g\epsilon(x))]_{ij}\Psi_j(x) = [e^{ig\epsilon^a(x)T^a}]_{ij}\Psi_j(x), \tag{8}$$

Eq. (5) can be written as

$$F^a_{\mu\nu} = \partial_\mu A^a_\nu - \partial_\nu A^a_\mu + g f^{abc} A^b_\mu A^c_\nu. \tag{9}$$

g denotes the gauge coupling constant.

2.1.2. Quantum chromodynamics (QCD)

The color quantum number of quark is known as 3 by the observation of π_0 decay and the measurement of cross-section ratio σ ($e^+e^- \to$ hadrons)/σ ($e^+e^- \to \mu^+\mu^-$) [22]. Quark dynamics can be understood using a non-abelian gauge theory with the symmetry group of the $SU(3)$. The Lagrangian of QCD can be written as

$$\begin{aligned}\mathcal{L}_{\rm QCD} &= \bar{q}(i\gamma^\mu D_\mu)q - \frac{1}{2}TrG_{\mu\nu}G^{\mu\nu} \\ &= \bar{q}(i\gamma^\mu\partial_\mu)q - g_{\rm s}(\bar{q}\gamma^\mu T_a q)G^a_\mu - \frac{1}{2}TrG_{\mu\nu}G^{\mu\nu},\end{aligned} \tag{10}$$

where q denotes the color-triplet quark fields, G denotes gluon fields and D_μ is chosen as

$$D_\mu = \partial_\mu + ig_s G_\mu. \tag{11}$$

G_μ satisfies the followings

$$G_\mu = T_a G^a_\mu \tag{12}$$

$$G_{\mu\nu}G^{\mu\nu} = \partial_\mu G_\nu - \partial_\nu G_\mu + ig_s[G_\mu, G_\nu]. \tag{13}$$

$g_{\rm s}$ is the strong coupling constant. The coupling constant can be written as

$$\alpha_s = \frac{g_s^2}{4\pi}, \tag{14}$$

where scale dependence of α_s can be described by

$$\alpha_s(Q) = \frac{4\pi\alpha_s(\mu_R)}{4\pi + \beta_0\alpha_s(\mu_R \ln(Q^2/\Lambda^2_{\rm QCD}))}, \tag{15}$$

where μ_R denotes the renormalization scale, $\Lambda_{\rm QCD}$ is the cut-off scale and β_0 denotes a constant computed from a beta function for QCD [23–27], it can be negative, therefore the strong interaction decreases logarithmically as a function of Q. As a result, a behavior of the strong interaction is quite local (the behavior is well known as asymptotic freedom). Quarks and gluons can not be isolated because of the color confinement. At high energy interactions, a generated quark interacts with other quarks and antiquarks generated in the vacuum, and then they form a lot of hadrons. The hadrons are observed in the direction of the motion of the original quark, and resulting in a collimated spray of hadronds. It is

called as jet, and the phenomena is called as hadronaization. The time scale of hadronization is equal to $1/\Lambda_{\rm QCD} \sim 10^{-24}$ s. The life time of quarks except for top quarks are longer than the hadronization time-scale, while the life time of top quark is about 10^{-25} s. Therefore, top quarks are not hadronized, and it can not form mesons.

2.1.3. Electroweak theory

The electroweak theory achieved to combine QED and electroweak interaction [28–30]. Each fermion has weak isospin (I, I^3) and weak hyper charge Y as seen in Table 1. From an analogy to QED, weak interaction is occurred by exchanging the charge via weak fields. There are four fields and four massless bosons for each charge (Q, I, I^3 and Y). A gauge symmetry $SU(2)_L \times U(1)_Y$ is introduced. The iso-triplet ($SU(2)$) has three bosons $\mathbf{W}_\mu = (W^1_\mu, W^2_\mu, W^3_\mu)$, and the iso-singlet ($U(1)_Y$) has B_μ.

The Lagrangian of the electroweak interaction can be written as

$$\mathcal{L}_{\rm EW} = \bar{\psi}(i\gamma^\mu D_\mu - m)\psi - \frac{1}{4}\mathbf{W}_{\mu\nu}\mathbf{W}^{\mu\nu} - \frac{1}{4}B_{\mu\nu}B^{\mu\nu}, \tag{16}$$

where $\mathbf{W}_{\mu\nu}$ is defined as

$$\mathbf{W}_{\mu\nu} = \partial_\mu \mathbf{W}_\nu - \partial_\nu \mathbf{W}_\mu - g\mathbf{W}_\mu \times \mathbf{W}_\nu, \tag{17}$$

$B_{\mu\nu}$ is also defined as

$$B_{\mu\nu} = \partial_\mu B_\nu - \partial_\nu B_\mu. \tag{18}$$

D_μ is set as

$$D_\mu = \partial_\mu + ig\sum_{a=1}^{3}\mathbf{W}^a_\mu \tau_a + ig'\frac{Y}{2}B_\mu, \tag{19}$$

where g and g' denote the coupling constant of $SU(2)_L$ and $U(1)_Y$, respectively, and τ is given by

$$\tau = \frac{1}{2}(\sigma_1, \sigma_2, \sigma_3). \tag{20}$$

Using the covariant derivative Eq. (19), the Lagrangian of electroweak(Eq. 16) can be written as

$$\mathcal{L}_{\rm EW} = i\bar{\psi}\gamma^\mu\partial_\mu\psi - g'\bar{\psi}\gamma^\mu\frac{Y}{2}B_\mu\psi - \frac{1}{4}\mathbf{W}_{\mu\nu}\mathbf{W}^{\mu\nu} - \frac{1}{4}B_{\mu\nu}B^{\mu\nu} - \frac{g}{2}\bar{\psi}_L\gamma^\mu\begin{bmatrix} W^3_\mu & (W^1_\mu - iW^2_\mu) \\ (W^1_\mu + iW^2_\mu) & -W^3_\mu \end{bmatrix}\psi_L. \tag{21}$$

2.1.4. Spontaneous symmetry braking and the Brout-Englert-Higgs mechanism

As seen in Eq. (21), the Lagrangian do not have a mass term. It means that the bosons and all fermions do not have mass. However we know fermions are massive and massive bosons have been discovered. Therefore, a mechanism which naturally gives mass to those fundamental particles is needed, and the Brout-Englert-Higgs mechanism (the BEH mechanism) has achieved success to solve this problem. In

the BEH mechanism, scalar fields $\phi = (\phi^+, \phi^0)$ and $SU(2)$ doublet are introduced. ϕ^+ has weak isospin +1/2 and weak hyper charge +1/2, and ϕ^0 has weak isospin -1/2 and weak hyper charge +1/2.

The Lagrangian of the higgs field can be written as

$$\mathcal{L}_{\text{higgs}} = (D_\mu \phi)^\dagger (D^\mu \phi) - V(\phi), \tag{22}$$

where $V(\phi)$ denotes the higgs potential and satisfies

$$\begin{aligned} V(\phi) &= \mu^2 |\phi|^2 + \lambda |\phi|^4 \\ &= \lambda (|\phi|^2 - \frac{v^2}{2})^2 (if \mu^2 < 0). \end{aligned} \tag{23}$$

The potential is always minimum at $\phi = (0, 0)$, if $\mu^2 > 0$. However the potential is minimum at $|\phi|^2 = -\mu^2/2\lambda$, if μ^2 has a negative value. Hence the vacuum has an expected value, which it is called the vacuum expectation value and denoted by v. This means that the phase transition of vacuum can be occurred for μ^2, and the vacuum obtains a freedom on the $\phi^+ - \phi^0$ plane associated with $\phi = (0, v)$. The phase transition of vacuum is called spontaneous symmetry braking, and the vacuum can be redefined as

$$\phi = \begin{pmatrix} 0 \\ v + h(x) \end{pmatrix}. \tag{24}$$

$\partial_\mu \to D_\mu$ is applied in Eq. (19), the mass terms of gauge bosons are generated. As a result, W and Z bosons obtain mass as

$$m_W = \frac{gv}{2}, \tag{25}$$

$$m_Z = \frac{v\sqrt{g^2 + g'^2}}{2}. \tag{26}$$

The higgs mass is

$$m_{higgs} = \sqrt{-2\mu^2}. \tag{27}$$

Fermions also obtains mass, and this interaction is known as Yukawa interaction. The Lagrangian of Yukawa interaction can be written as

$$\mathcal{L}_{\text{Yukawa}} = -\bar{\psi}_{i,L} y^a_{ij} \phi \psi_{j,R} - \bar{\psi}_{i,R} y^a_{ij} \phi^\dagger \psi_{j,L}. \tag{28}$$

2.2. Problem of the Standard Model

The SM achieves to unify the electromagnetic theory and the weak theory, and the QCD theory in the SM can explain the strong interaction. However the gravitational interaction is not included in the SM,

and some problems have remained. One of the problems is the fine-tuning problem, and another is the existence of Dark Matter.

2.2.1. The fine-tuning problem

The physical Higgs mass is defined by

$$m_{\mathrm{h}}^2 = 2\, m_{\mathrm{h,bare}}^2 + \delta m_{\mathrm{h}}^2 \tag{29}$$

where $m_{\mathrm{h,bare}}$ denotes the bare Higgs mass and δm_{h}^2 is the quadratically divergent radiative correction given by

$$\delta m_{\mathrm{h}}^2 = \frac{3|\lambda|^2}{8\pi^2}\Lambda^2 + O(\log\Lambda) \tag{30}$$

where Λ denotes the cut off scale which is the effective limit of the SM and λ denote the Yukawa coupling constant. If the effective limit of the SM is at the Plank scale ($O(10^{19}$ GeV)), the radiative correction can be $O(10^{38}$ GeV). The physical Higgs mass is observed as 125 GeV. Therefore, $m_{\mathrm{h,bare}}$ and δm_{h}^2 should be canceled with a precision of $O(10^{-17})$. This unnatural treatment is called the fine-tuning problem.

2.2.2. Dark Matter

The existence of Dark Matter (DM) is predicted from the observation of the rotation of a galaxy by Rubin and Ford [31, 32] for the first time by Rubin and Ford [31, 32]. Later, the spatial distribution of DM is estimated, and a 3-dimensional map of DM in the universe is created by measuring the effect of the gravitational lens [33]. However there is no candidate of DM in the SM. Therefore the existence of a new particle is needed.

2.3. Candidates of a new particle detectable in the $t\bar{t}$ resonance search

Candidates of a new particle which can be found in the $t\bar{t}$ resonance search are introduced in this section.

2.3.1. Leptophobic top-color Z'

The first candidate is a spin-1 color-singlet vector boson, denoted Z'_{TC2}, predicted in the topcolour-assisted technicolor model based on the extended technicolor model [34–36]. This model assumes the existence of additional strong dynamics and a new gauge boson at TeV scale.

This boson couples strongly to first and third generation quarks, and does not decay to leptons. The tendency is referred to as Model IV in [35]. In this model, Z'_{TC2} is produced by quark-antiquark annihilation.

2.3.2. Bulk Randall–Sundrum Kaluza–Klein Graviton

The second candidate is a spin-2 bulk Randall–Sundrum Kaluza–Klein graviton, denoted RS-G_{KK}, predicted in the Randall–Sundrum models [37]. The model assumes the existence of an extra dimension. Our dimension is defined as a weak brane and an additional brane is defined as gravity brane. In this model, the vacuum expectation value V_{eff} is given by

$$V_{\mathrm{eff}} = e^{-kL} V \tag{31}$$

where $k = \sqrt{\frac{-\Lambda}{12M^3}}$, and it is related to an oscillating warp factor. L denotes the distance between the two branes. Even if the bare Higgs mass is at the order of the Plank scale, the physical Higgs mass on the weak brane could be wrapped down to the weak scale without the fine tuning.

2.3.3. Kaluza–Klein gluon

The third candidate is a spin-1 Kaluza–Klein(KK) gluon predicted by the Kaluza Klein theories [38, 39]. Those theories assume the existence of warped extra-dimensions. In particular, the Randall-Sundrum (RS) model [40] of KK theories assumes the existence one extra dimension, and predicts the existence of gluon excitations with strong coupling with quarks $g_f \approx 0.2 g_s$, and stronger coupling with a top quark. The RS-model predicts chiral coupling with the top quark: $g_R^{(t)} \approx 4 g_s$ and $g_L^{(t)} \approx 1 g_s$ [41]. The KK-gluon is produced in $p-p$ collisions mostly from a $q\bar{q}$ initial state. The tree-level gluon-gluon-KKgluon interaction is calculated to be exactly zero in the Randall-Sundrum model [42], and 1-loop (anomalous) production ('a la Higgs) is forbidden at the first order by Yang's theorm where spin-1 particles do not decay into two massless vectors. At a higher order, the gluon-initiated cross section is calculated to be 10^{-3} to 10^{-4} of the quark-initiated cross section [42].

Those lightest KK particles can be the candidate of the DM.

3. LHC and the ATLAS experiment

3.1. Large Hadron Collider

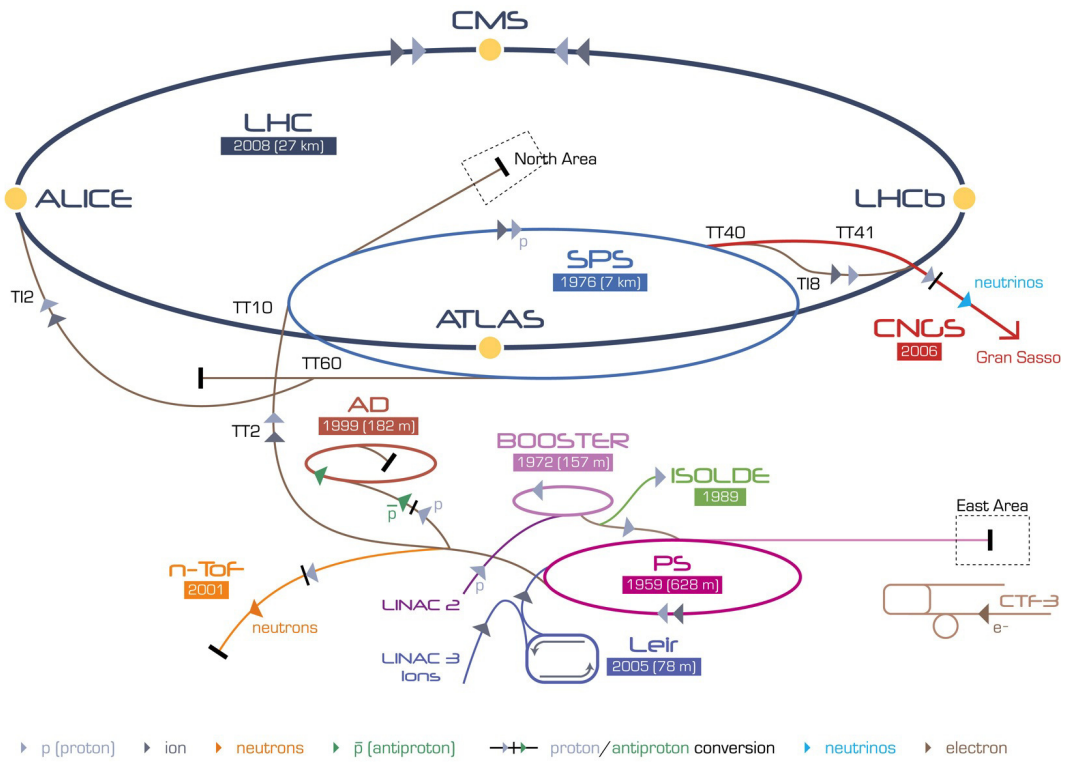

Figure 1: The LHC and the other facilities [43]

The Large Hadron Collider (LHC) is the largest proton-proton circular collider (length: 26.7 km) at CERN. The accelerator complex at CERN for accelerating proton beam is schematically illustrated in Fig. 1. The proton beams are produced at the positive ion source and accelerated at the Linac 2. The beam energy reaches 50 MeV. The beams are further accelerated to 1.4 GeVat the Proton Synchrotron Booster (PSB), and to 2.5 GeVin the Proton Synchrotron (PS). The beam are then injected to the Super Proton Synchrotron (SPS), and accelerated upto 450 GeV, to be instead to the LHC. Here, beams circulated opposite directions are injected . Finally the beams are accelerated to 6.5 TeVin the LHC.

3.2. ATLAS

ATLAS (A Toroidal LHC Apparatus) detector [44] is placed at CERN. It covers nearly the entire solid angle around a collision point. It consists of an inner tracking detector surrounded by a thin superconducting solenoid, electromagnetic and hadronic calorimeters,and a muon spectrometer incorporating three large superconducting toroid magnets (Fig. 2).

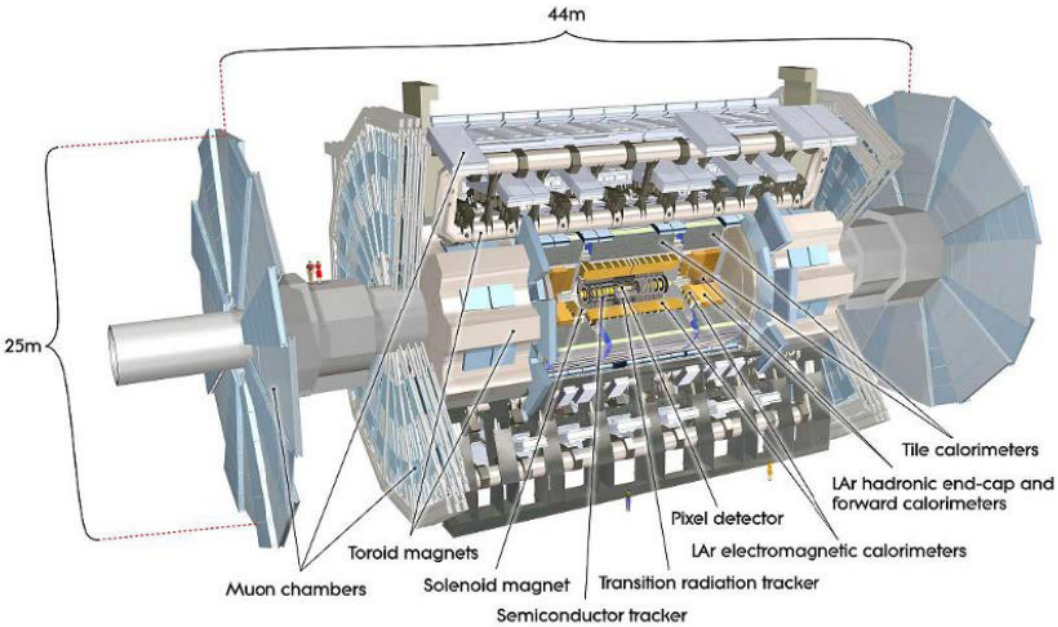

Figure 2: The ATLAS detector overview [45]. The height, length and weight are 25 m,44 m and 7000 t, respectively

3.2.1. Coordinate system in the ATLAS experiment

The ATLAS coordination system uses a right-handed coordinate system with its origin at the nominal interaction point (IP) in the centre of the ATLAS detector and the z-axis along the beam pipe. The x-axis points from the IP to the centre of the LHC ring, and the y-axis points upwards. Cylindrical coordinates (r, ϕ) are used in the transverse plane, ϕ being the azimuthal angle around the z-axis. The pseudo-rapidity is defined in terms of the polar angle θ as written in the Eq. (32).

$$\eta = -\ln\tan(\theta/2), \tag{32}$$

Covered regions are separated to three regions as Barrel,End-cap and Fore-ward by the pseudo-rapidity, respectively $|\eta| < 1.05$,$1.05 < |\eta| < 2.4$,$2.4 < |\eta|$.

Angular distance is measured in units of ΔR defined as the Eq. (33).

$$\Delta R \equiv \sqrt{(\Delta\eta)^2 + (\Delta\phi)^2} \tag{33}$$

3.2.2. Inner Detector

The inner-detector system (ID) is immersed in a 2 T axial magnetic field and provides charged particle tracking in the range $|\eta| < 2.5$. The system overview is showed in Fig. 3.

The high-granularity silicon pixel detector covers the vertex region and typically provides three measurements per track, the first hit being normally in the innermost layer. The total number of channels are about

80 million, and the detector resolutions are 12 μm for the direction of r and ϕ, 70 μm for the direction of z axis.

It is followed by the silicon micro-strip tracker which usually provides four two-dimensional measurement points per track. These silicon detectors are complemented by the transition radiation tracker (TRT), which enables radially extended track reconstruction up to $|\eta| = 2.0$. The transition radiation tracker also provides electron identification information based on the fraction of hits (typically 30 in total) above a higher energy deposit threshold corresponding to transition radiation. The total number of channels are about 300000, and the detector resolutions are 170 μm.

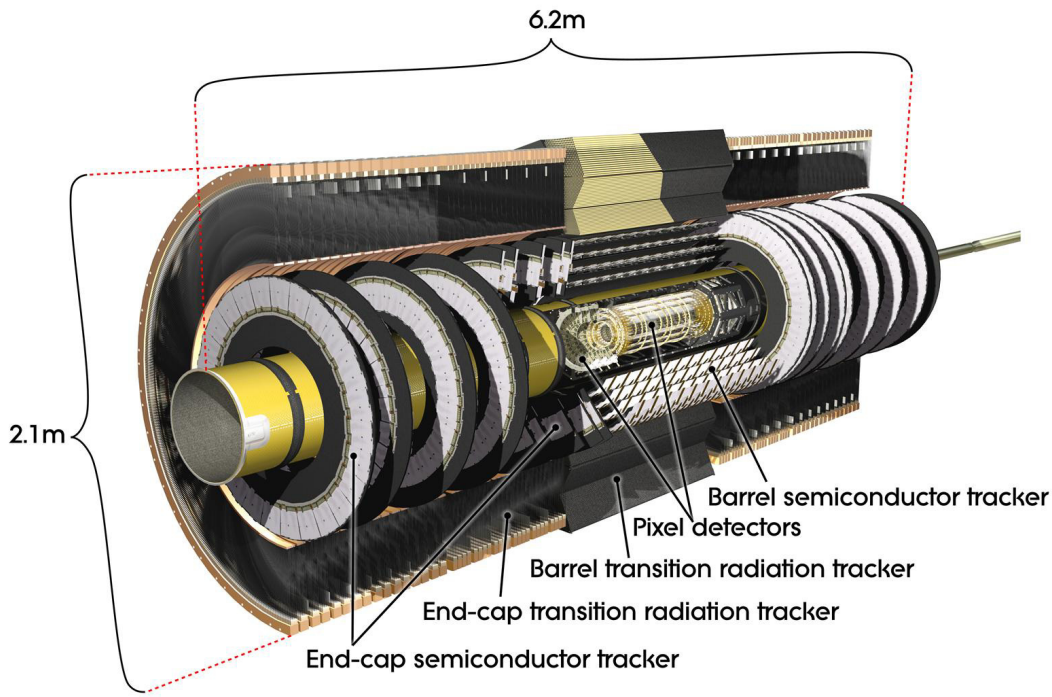

Figure 3: Inner Detector overview [46]

The detector system is the most important for the bottom quark identification.

3.2.3. Calorimeter

The calorimeter system covers the pseudo-rapidity range $|\eta| < 4.9$. The overview is in Fig. 4. Within the region $|\eta| < 3.2$, electromagnetic calorimetry is provided by barrel and end-cap high-granularity lead/liquid-argon (LAr) electromagnetic calorimeters, with an additional thin LAr pre-sampler covering $|\eta| < 1.8$, to correct for energy loss in material upstream of the calorimeters. The electromagnetic calorimeter is mainly used by detection and separation of electron and photon. The resolution of energy is given in the Eq. (34).

$$\sigma = \frac{10\%}{\sqrt{E_\gamma[\text{ GeV}]}} \tag{34}$$

$\sqrt{E_\gamma}$ denote the energy of photon. The resolutions are $9/\sqrt{E_\gamma}mm$ for the direction of ϕ and $3mm$ for the direction of the η.

Hadronic calorimetry is provided by the steel/scintillating-tile calorimeter, segmented into three barrel structures within $|\eta| < 1.7$, and two copper/LAr hadronic end-cap calorimeters. The solid angle coverage is completed with forward copper/LAr and tungsten/LAr calorimeter modules optimized for electromagnetic and hadronic measurements respectively. Boosted top quark is tagged as large-R jet, the large-R jet object

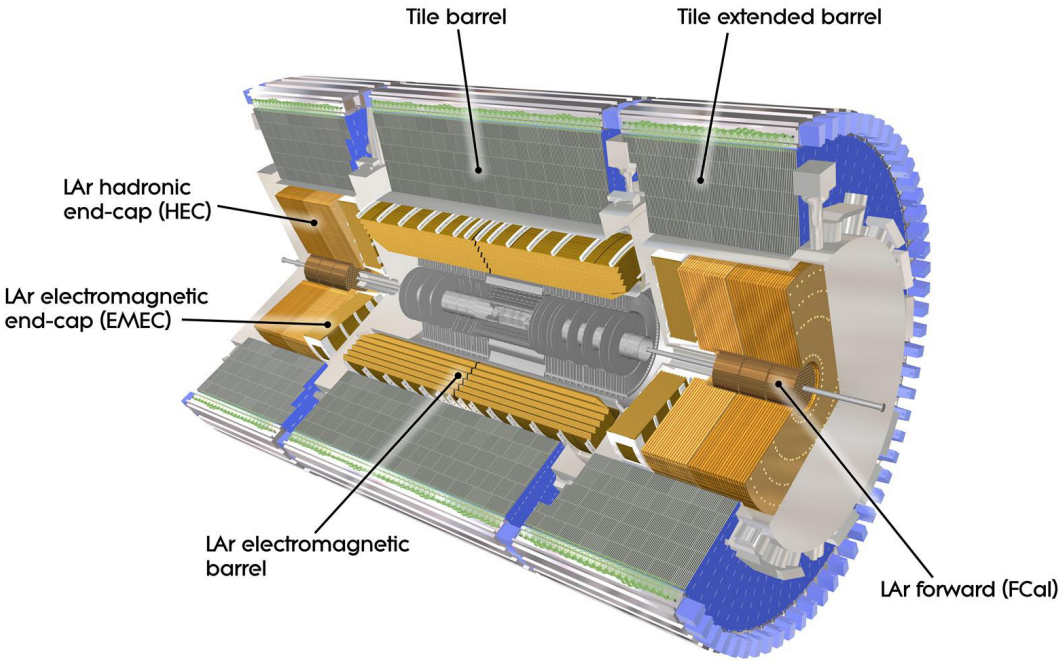

Figure 4: Calorimeter overview [46]

is reconstructed and calibrated with the information measured in the calorimeter system.

3.2.4. Muon Spectrometer

The muon spectrometer (MS) comprises separate trigger and high-precision tracking chambers measuring the deflection of muons in a magnetic field generated by superconducting air-core toroids. The precision chamber system covers the region $|\eta| < 2.7$ with three layers of monitored drift tubes, complemented by cathode strip chambers in the forward region, where the background is highest. The muon trigger system covers the range $|\eta| < 2.4$ with resistive plate chambers in the barrel, and thin gap chambers in the end-cap regions.

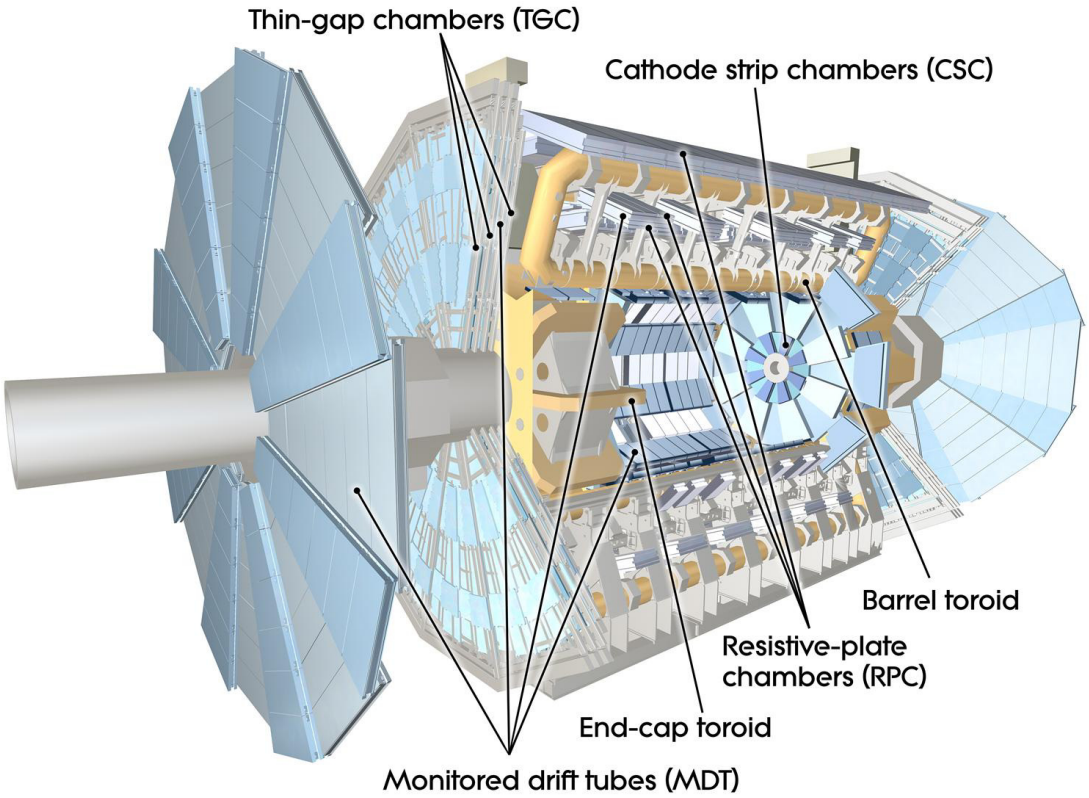

Figure 5: Muon Spectrometer overview [46]

3.2.5. Magnetic System

The ATLAS magnetic system is made of three large air-core toroid superconducting magnets with eight coils each as the Fig. 6. Its bending power is in the range from 2.0 to 7.5 T m.

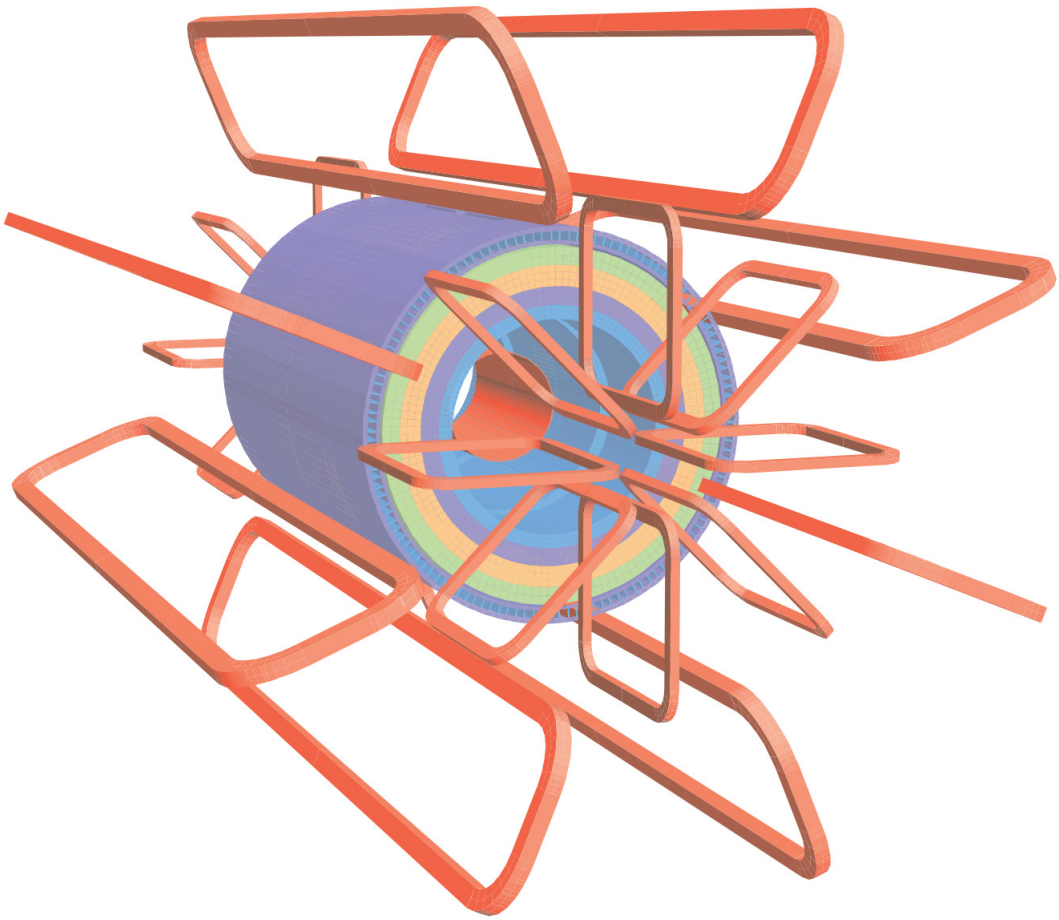

Figure 6: Sketch of the magnet system of ATLAS [46]. The eight barrel toroid and the solenoid magnet are shown, and the tile calorimeter is also shown.

3.2.6. Trigger System

A trigger system is used to select interesting physics events [47].

The Level-1 trigger is implemented in hardware and uses a subset of detector information to reduce the event rate to a design value of at most 100 kHz. This is followed by a software-based High Level Trigger (HLT) which reduce the event rate to about 1 kHz. Several trigger conditions are prepared in order to manage a wide variety of analyses.

4. Monte-Carlo simulation

The signal and background simulation samples were produced with Monte Calro (MC) generators. The main backgrounds for this analysis are the Standard Model $t\bar{t}$ production and QCD multi-jet production.

The EvtGen v1.2.0 program [48] is used in all simulated samples to model the properties of heavy-flavor hadron decays. All simulated samples include the effects of multiple pp interactions in the same and neighbouring bunch crossings (pile-up) and are processed through the ATLAS detector simulation [49] based on Geant4 [50]. Pile-up effects are emulated by overlaying simulated minimum-bias events from Pythia 8.186 [51], generated with the MSTW2008LO PDF set [52] and the A2 tune [53] for the underlying event. The number of overlaid minimum-bias events is adjusted to match the luminosity profile of the recorded data. All the simulated samples are reconstructed with the same software as that used for collision data.

4.1. Signal samples

Although the analysis is done in a very generic way, the benchmark signal models are used to get the final results and consequently to set limits on their production rates. The bentch mark signal models are prepared with respect to each spin.

4.1.1. $Z'_{TC2} \rightarrow t\bar{t}$ signal

The spin-1 color-singlet vector Z'_{TC2} bosons decaying to $t\bar{t}$ are generated with Pythia v8.165 with the leading-order (LO) NNPDF2.3 [54] PDF set and the A14 set of tuned parameters [55]. To account for higher-order contributions, the LO calculation of the cross section is multiplied by a factor 1.3 obtained at next-to-leading order (NLO) in QCD [56] using the PDF4LHC2015 PDF set [54].

Parameters of the model (Sec. 2.3.1) are tuned such that the resonance has a width of 1.2% of its mass. The next-to-leading-order calculation is taken into account by multiplying its cross section by 1.3, based on the calculations performed in [57, 58]. The cross-sections of Z'_{TC2} production at $\sqrt{s}$ = 13TeV calculated at leading-order (LO) are presented in the Table 3. Following [36] and the previous searches for $t\bar{t}$ resonances, a multiplicative K-factor of 1.3 is used to bring them at next-to-leading order (NLO). The benchmark model has a width of 1.2% or 3% of the mass.

Table 3: Leading-order theoretical cross-sections for the Z'_{TC2} signal extracted from LO MCs, on top of which a K-factor of 1.3 is applied.

Z' mass	LO cross-section [pb]
400 GeV	70.3
500 GeV	40.1
750 GeV	10.7
1 TeV	3.70
1.25 TeV	1.51
1.5 TeV	0.684
1.75 TeV	0.334
2. TeV	0.172
2.25 TeV	0.0924
2.5 TeV	0.0511
2.75 TeV	0.0289
3 TeV	0.0167
4 TeV	0.00213
5 TeV	0.000331

Figure 7 shows the truth $m_{t\bar{t}}$ distributions in MC for each Z'_{TC2} mass.

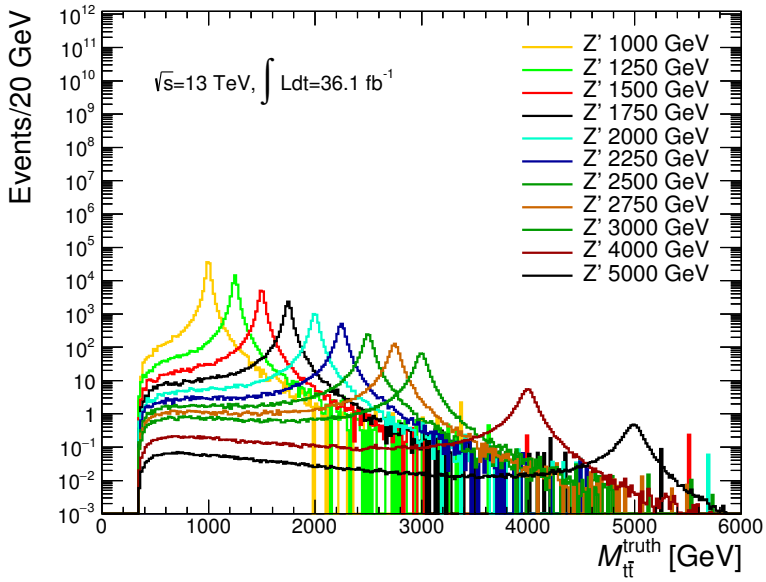

Figure 7: Distributing of $m_{t\bar{t}}$ for the generated Z'_{TC2} signals. Those distributions are scaled to 36.1 fb^{-1} of data

4.1.2. $G_{KK} \to t\bar{t}$ signal

The production of a spin-2 Bulk RS graviton with a curvature $C = k/\bar{M}_P = 1$ is performed using `MadGraph5_aMC@NLO` [59] with the LO NNPDF2.3 [60] PDF set, interfaced with Pythia v8.165 with the A14 set of tuned parameters for parton shower and hadronization.

Table 4: Leading order cross-section times branching ratio, $\sigma_{G_{KK}} \times BR(G_{KK} \to t\bar{t})$, for RS graviton.

G_{KK} mass	$\sigma_{G_{KK}} \times BR(G_{KK} \to t\bar{t})$ [pb]
400	7.19
500	5.84
750	1.18
1000	2.89E-01
2000	4.98E-03
3000	2.48E-04

This spin-2 benchmark model also assumes a narrow resonance (width varied between 3 and 6% of the mass).

The cross-section times branching ratio$\sigma_{G_{KK}} \times BR(G_{KK} \to t\bar{t})$ predicted by MADGRAPH 5, are shown in Table 4 and are much smaller than those of the Z'_{TC2} production.

Figure 8 shows the truth $m_{t\bar{t}}$ distributions for each RS-graviton signal in the generated samples.

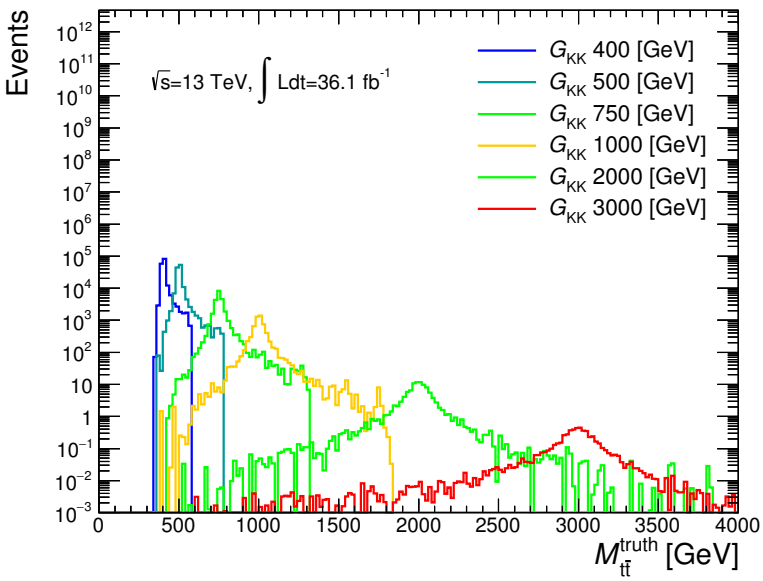

Figure 8: Distributing of $m_{t\bar{t}}$ for the truth-level RS-graviton signals. Those distributions are scaled to 36.1 fb^{-1} of data

4.1.3. $g_{KK} \to t\bar{t}$ signal

Simulated samples of spin-1 color-octet KK gluon g_{KK} with a width of 15% are generated with PYTHIA v8.165 with the same PDF and tuned parameters as those used for the Z' samples. Samples of g_{KK} with 30% width are derived from reweighting the corresponding samples with 15% width and adjusting their normalization according to the prediction for the g_{KK} with 30% width.

Table 5: Leading order cross-section times branching ratio, $\sigma_{g_{KK}} \times BR(g_{KK} \to t\bar{t})$, for KK gluon.

g_{KK} mass	$\sigma_{g_{KK}} \times BR(g_{KK} \to t\bar{t})$ [pb]
500	240.86
1000	20.176
1500	3.79
2000	1.052
2500	0.37339
3000	0.15607
3500	0.074283
4000	0.039494
4500	0.022862
5000	0.014241

The cross-section times branching ratio $\sigma_{g_{KK}} \times BR(g_{KK} \to t\bar{t})$ predicted by Pythia v8.165, are shown in Table 5.

Figure 9 shows the truth $m_{t\bar{t}}$ distributions for each KK gluon signal sample.

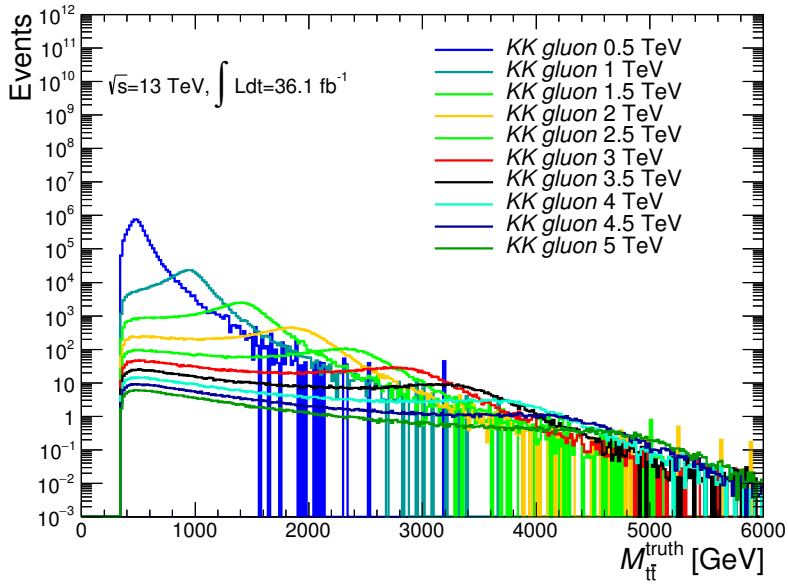

Figure 9: Distributing of $m_{t\bar{t}}$ for the truth-level KK gluon signals. Those distributions are scaled to 36.1 fb^{-1} of data

4.2. Standard Model $t\bar{t}$

The $t\bar{t}$ contribution and the modeling uncertainties are evaluated using MC simulated events.

For the generation of SM $t\bar{t}$ events, the Powheg-Box v2 [61–63] is used with the CT10 [64, 65] parton distribution function (PDF) set in the matrix element calculations. The $t\bar{t}$ production cross section in pp collisions at $\sqrt{s}$ = 13 TeV is $\sigma_{t\bar{t}} = 832^{+46}_{-52}$ pb for a top-quark mass of 172.5 GeV. It has been

calculated at next-to-next-to leading order (NNLO) in QCD including resummation of next-to-next-to-leading logarithmic soft gluon terms with Top++2.0 [66–72]. Parton showering, hadronization and the underlying event are simulated using PYTHIA v6.428 [73] with the CTEQ6L1 [74] PDF set and the corresponding Perugia 2012 set of tuned parameters [75]. The h_{damp} parameter, which controls the transverse momentum of the first additional emission beyond the Born configuration, is set equal to the top-quark mass. The main effect of this parameter is to regulate the high-p_{T} emission against which the $t\bar{t}$ system recoils.

Figure 10 shows the truth-level $m_{t\bar{t}}$ distribution obtained in the generated $t\bar{t}$ samples. The samples are properly added according to their cross sections. Each $t\bar{t}$ samples correspond to samples with different $m_{t\bar{t}}$ thresholds.

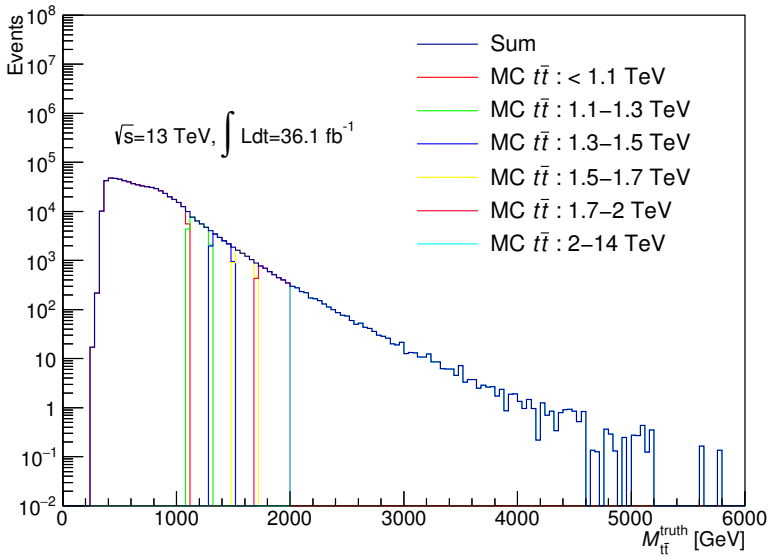

Figure 10: Distributions of the $t\bar{t}$ background (truth-level).

4.3. QCD multijets

Although the amount of QCD multi-jet background is estimated by a data driven method (Sec. 7). MC simulation samples are used for cross-checking.

As the QCD multi-jet samples, di-jet events are generated with PYTHIA 8.186, using the A14 set of tuned parameters for the underlying event and the LO NNPDF2.3 PDF set. Those samples are generated with a filtering on p_T of the truth leading jet, where jets are clustered using the anti-k_T algorithm with R=0.6 as can be seen in Fig. 11.

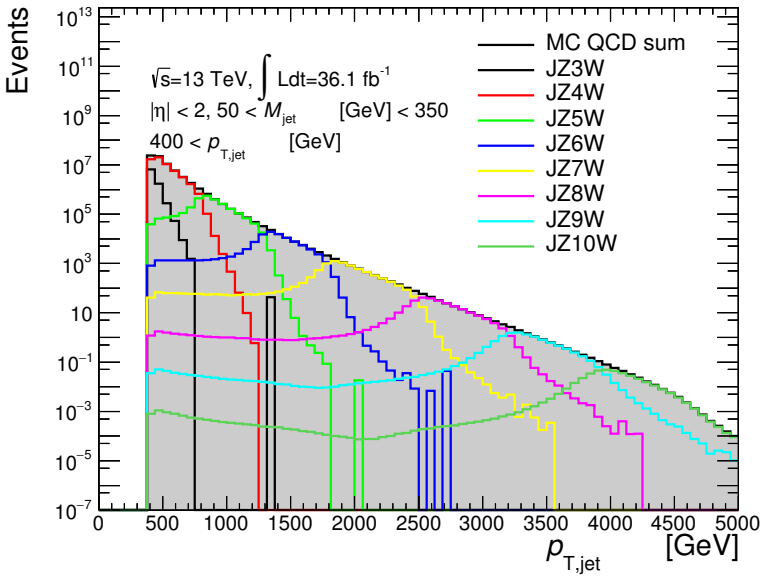

Figure 11: Distribution of reconstructed large-R jet p_T for the QCD multi-jet background in Monte Carlo simulation after selection of $|\eta| < 2$, 50 GeV $< m_{\text{jet}} <$ 350 GeV and $p_{T,jet} >$ 400 GeV. The distribution is scaled to 36.1 fb^{-1} of data

5. Object definitions and reconstruction

A top quark decays into a W boson (decaying to two quarks) and a bottom quark. The analysis focuses on the high $m_{t\bar{t}}$ region and is performed in the boosted regime, in which hadronic decay products of a highly Lorentz-boosted top quarks are detected as a single large-R jet. A bottom quark can be tagged using a track jet within the large-R jet.

The analysis selects the events using refined and calibrated objects. These objects are described in the following section.

5.1. Small-R jets

Small-R jets are built from three-dimensional topological clusters of energy deposits in the calorimeter [76] at the electromagnetic energy scale using the anti-k_t algorithm [77] with a radius parameter $R = 0.4$. These jets are calibrated to the hadronic energy scale by applying p_{T}- and η-dependent corrections derived from MC simulations and in situ measurements obtained from Z/γ+jets and multijet events at $\sqrt{s}$ = 13 TeV [78]. Jets from pile-up interactions are suppressed by applying the jet vertex tagger (JVT) [79], which uses information about tracks associated with the hard-scatter and pile-up vertices, to jets with $p_{\mathrm{T}} < 60$ GeV and $|\eta| < 2.4$. Events containing jets from calorimeter noise or non-collision backgrounds are removed by discarding events containing at least one jet failing the loose quality criteria defined in Ref. [80].

5.2. Large-R jets

Large-R jets are jets reconstructed from three-dimensional topological clusters of energy deposits in the calorimeter calibrated with the local cluster weighting (LCW) procedure [76] with the anti-k_T algorithm [77] with radius parameter R=1.0. The non-compensating response of the calorimeter and the energy loss in dead material and by out-of-cluster leakage for charged and neutral particles are corrected in the LCW procedure before reconstructing jets. The reconstructed jets are "trimmed" [81] to mitigate contributions from pile-up and soft radiation. In the trimming procedure, the jet constituents are reclustered into subjets using the k_t algorithm [82–84] with a radius parameter $R = 0.2$ and subjets with p_{T} less than 5% of the p_{T} of the parent jet are removed [85]. Finally, the large-R jets are formed from the four-vectors of the remaining subjets and selected by requiring $p_{\mathrm{T}} > 200$ GeV and $|\eta| < 2.0$ for later use. For highly boosted top quarks, the mass calculation of a large-R jet containing the top-quark decay products deteriorates with increasing top p_{T} due to the limited angular resolution of the calorimeter. To overcome this effect the mass of the large-R jet, m_J, is calculated by combining the calorimeter energy measurement and the angular information from the ID, as described in Ref. [86]. The two leading large-R jets in the event are required to have $50 < m_{J1,2} < 350$ GeV.

5.3. Track jets

Track jets are built from charged particle tracks using the anti-k_t algorithm with a radius parameter $R = 0.2$. Tracks used in the reconstruction are selected by requiring that they are associated with the primary vertex, and have $p_{\mathrm{T}} > 400$ MeV and $|\eta| < 2.5$. Track jets composed of at least two constituent

tracks, with $p_T > 10$ GeV and $|\eta| < 2.5$, are used to identify jets containing b-hadrons in the boosted analysis. In the dense environment chracteristic of the boosted topology, the b-tagging is more efficient if performed on track jets than on the calorimeter jets [87]. The same b-tagging algorithm as small-R jets with 77% (tight) and 85% (loose) efficiency working points to b-quark-induced jets is employed. The training of multi-variate analysis used in the algorithm and the evaluation of systematic uncertainties associated with the track-jet b-tagging efficiency are performed separately from small-R calorimeter jets. The corresponding misidentification rates at the tight (loose) working point are 1.7% (5.3%) and 23.8% (40.5%) for light-flavor quarks and c-quarks, respectively.

5.4. Electrons

Electrons are reconstructed from clusters of EM calorimeter energy deposits matched to an ID track within $|\eta| < 2.47$, excluding the barrel and endcap transition region of $1.37 < |\eta| < 1.52$. The electron candidates are required to have $E_T > 25$ GeV and to satisfy the "tight" identification criteria defined in Ref. [88]. To suppress backgrounds from multijet production, the electron candidates are further required to be isolated from other hadronic activity in an event. This is achieved by requiring the sum of track p_T within a cone around the electron direction, excluding the track associated with the electron, to be less than 6% of the electron transverse momentum p_T^e. The cone radius is given by either $R = 10\,\text{GeV}/p_T^e$ or $R = 0.2$, whichever is smaller.

5.5. Muons

Muons are reconstructed by combining tracks reconstructed in both the ID and to muon spectrometer. The muon candidates are required to have $p_T > 25$ GeV and $|\eta| < 2.5$, and satisfy the "medium" quality requirements defined in Ref. [89]. The muons are also required to be isolated by using the same track-based isolation conditions as for electron, except that the choice of $R = 0.2$ is replaced with $R = 0.3$.

Both electron and muon candidate tracks are required to be associated with the primary vertex by criteria on the longitudinal and transverse impact parameters. To avoid the misidentification of jets as electrons, the closest small-R jet within $\Delta R_y = \sqrt{(\Delta y)^2 + (\Delta\phi)^2} < 0.2$ around a reconstructed electron is removed.[1] If an electron is then found within $\Delta R_y < 0.4$ around a jet, the electron is removed. If a muon is found within $\Delta R_y < 0.04 + 10\,\text{GeV}/p_T^\mu$ (where p_T^μ is the muon transverse momentum) around a jet, the muon is removed if the jet contains at least three tracks, otherwise the jet is removed.

[1] The rapidity is defined as $y = \frac{1}{2}\ln\frac{E+p_z}{E-p_z}$ where E is the energy and p_z is the longitudinal component of the momentum along the beam pipe.

6. Event Selections

6.1. Pre-selection

The ATLAS detector recorded the data at a center-of-mass energy of 13 TeV in 2015 and 2016. The total integrated luminosity is 36.07 fb^{-1}, and the uncertainty in the luminosity measurement is 2.1%. Events were collected under stable conditions for the beams and the detecter, and all events used in this analysis were selected by a single large-R jet trigger which nominal p_T. Thresholds were 360 GeV and 420 GeV in 2015 and 2016, respectively.

The selected events are required to have at least one primary vertex (PV) that has at least two associated ID tracks, each with the transverse momenta $p_{T,track} > 0.4$ GeV, and be consistent with the beam spot of the pp colicions. For events with more than one PV candidate, that with the largest $\Sigma p^2_{T,track}$ is chosen as PV of the hard-scattering.

In order to reduce its size, the sample was skimmed before studying the analysis detail. The selections applied are as follows.

- At least one large-R jet ($p_T > 300$ GeV and $|\eta| < 2.2$) and at least one small-R jet ($p_T > 300$ GeV and $|\eta| < 2.7$)
- Both small-R and large-R jets are passed ΔR between large-R jet and small-R jet < 1.0 (At least one pair is required)
- Soft lepton veto : If an event has at least one lepton (electron or muon) with $p_T > 30$ GeV and $|\eta| < 2.4$, the event is vetoed

The other pre-selection are :

- A good condition flag of the calorimeteres is required.
- Events are rejected if there are leptons with $p_T > 25$ GeV to ensure that both top quarks decay hadronically.
- The transverse momentum of the leading large-R jet has to be greater than 500 GeV (to ensure 100% trigger efficiency (see Fig. 12),) and that for the sub-leading large-R jet has to be greater than 400 GeV to ensure that we deal with mostly contained top quarks and have better mass resolution (see Fig. 13).
- Events containing jets which fail the quality criteria are rejected (Sec. 5)

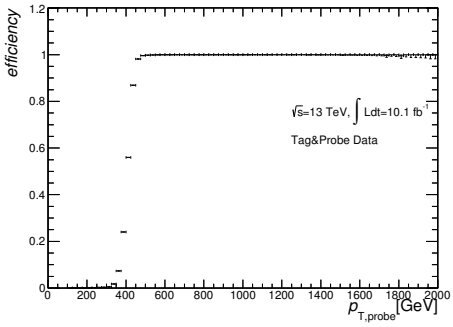

Figure 12: Trigger efficiency measured for the HLT_j420_a10r_L1J100 trigger, which requires a large-R jet (anti-k_T, R=1.0) with $p_T > 420GeV$. To measure this efficiency, offline jet object is matched with an HLT jet object within a cone of $\Delta R < 0.04$. The tag-and-probe method is used to avoid possible trigger bias. Two offline jets are required in an event, and the one is required to be matched with the trigger object (tag), and then the other is examined if it is matched with the trigger object (probe).

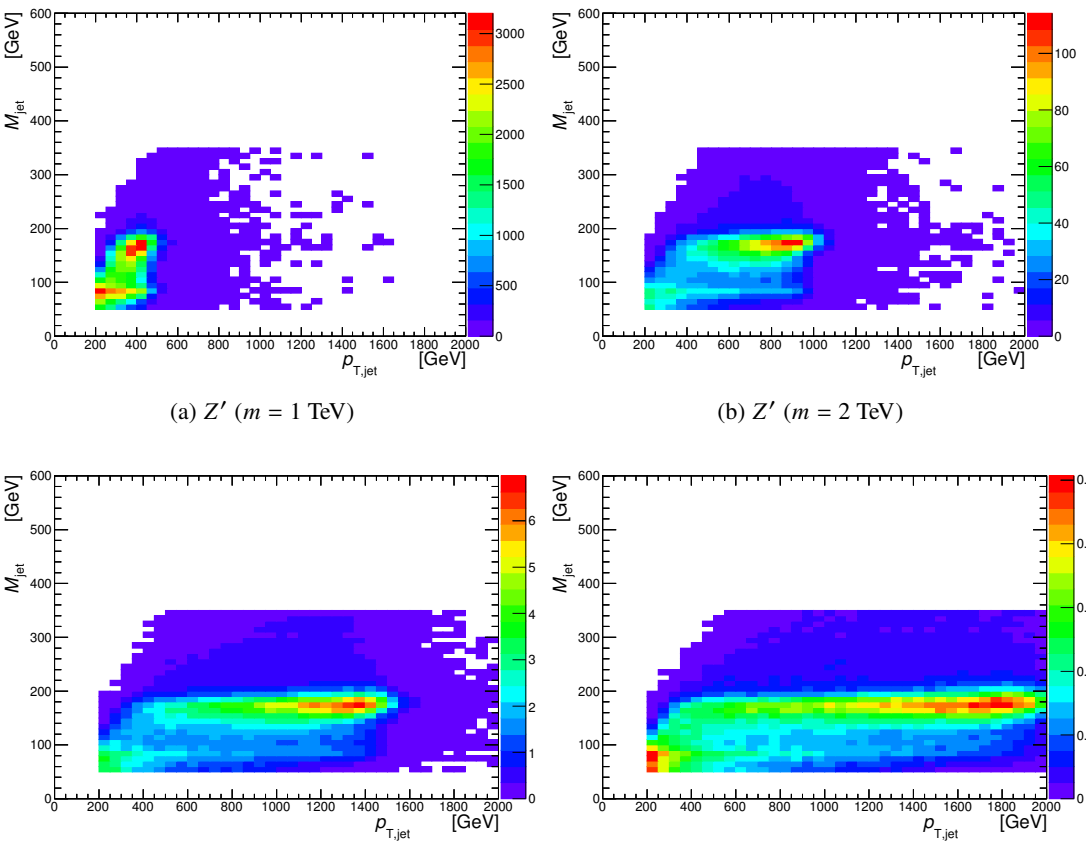

(a) Z' (m = 1 TeV)

(b) Z' (m = 2 TeV)

(c) Z' (m = 3 TeV)

(d) Z' (m = 4 TeV)

Figure 13: Two dimensional distributions of the reconstructed large-R jet p_T and jet mass before pre-selection.

- Each of the two highest-p_T large-R jets has to include at least 1 track jet with loose b-tag quality (85% working point) within ΔR (large-R jet, track jet) < 1.0. (Fig. 14 shows the distribution of the minimum angle difference in R between a large-R jet matched to a top quark and track jet matched to a bottom quark in the standard model $t\bar{t}$ Monte Carlo. It shows that a requiement of ΔR (large-R jet, track jet) is good enough to correctly match a top quark jet and a bottom quark jet.) The requairements of loose b-tagging is to largely reduce the number of the multijet events which contain no top decay. The b-tagging efficiency as a function of p_T is estimated using the MC simulation, and is shown in Fig. 15. The b-tagging fake rate, b-tagging efficiency for non-b track jet, is shown in Fig. 16. This is a fraction of track jets which are not matched with a truth bottom quark but b-tagged in the $t\bar{t}$ MC. The fake rate in $t\bar{t}$ events can be higher than those for other samples Non-b jets can be charm quark jets from W boson in top decays and c-jets have higher fake rate. Table 6 shows the efficiency of b-tag and rejection rates of c-flavor jets and light-flavor jets.

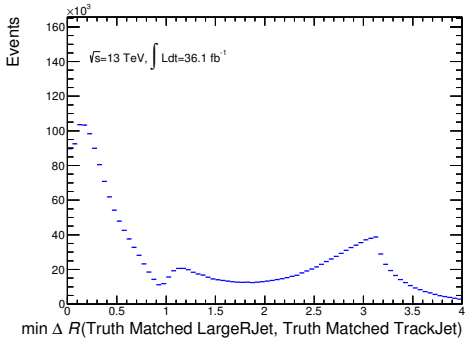

Figure 14: Distribution of the minimum angle difference in R between a large-R jet and a track jet, matched to a top quark and to a bottom quark respectively, in the standard model $t\bar{t}$ Monte Carlo. Reconstructed objects (jets) are required to match with corresponding truth-level objects (quarks). The large-R jet is required to be matched with the truth top quark with a cone $\Delta R < 0.1$. The track jet is required to be matched with the closest truth bottom quark with a cone $\Delta R < 1.0$.

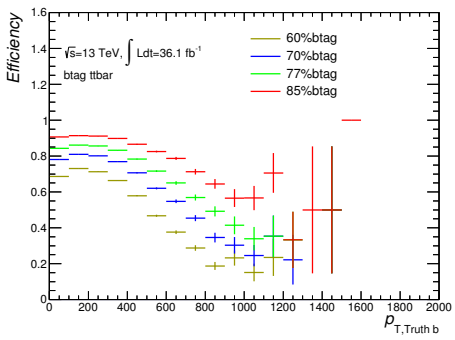

Figure 15: B-tagging efficiency for track jets as a function of truth-level b-quark p_T. The b-tagging efficiency is determined per track jet matched with the closest truth b quark with a cone $\Delta R < 0.1$ using the standard model $t\bar{t}$ Monte Carlo simulation. Track jets are required to be within the detector coverage, $|\eta| < 2.5$, and $p_T > 10$ GeV.

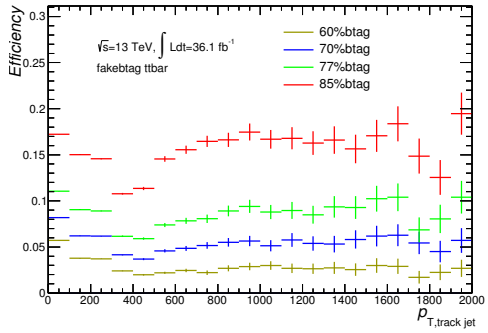

Figure 16: B-tagging fake rate for track jets as a function of reconstructed track jet p_T. The b-tagging fake rate is the fraction of track jets which are not coming from a b-quark but are tagged as a b quark. The efficiency is determined per track jet not matched with the closest truth b quark with a cone $\Delta R < 0.1$ using the standard model $t\bar{t}$ Monte Carlo simulation. Track jets are required to be within the detector coverage, $|\eta| < 2.5$, and $p_T > 10$ GeV.

b-jet efficiency[%]	c-jet Rejection	Light-jet Rejection	τ Rejection
85%	2.47(40.5%)	18.97(5.3%)	3.75
77%	4.21(23.8%)	57.9(1.7%)	8.09
70%	7.09(14.1%)	119.69(0.85%)	17.25
60%	16.16(6.2%)	276.16(0.36%)	53.47

Table 6: Efficiency of b-tag and rejection rates **??**. The number in the bracket next to the rejection rate is the fake efficiency (inverse of the rejection).

6.2. Event selection

6.2.1. Angular difference selection

The decays of a new particle products two top quarks back-to-back. The angular difference in azimuthal angle (ϕ) between the leading and sub-leading large-R jets has to be larger than 1.6. Figure 17 shows the distribution of angular difference of the two large-R jets, $\Delta\phi_{\text{di-large-Rjet}}$, in the signal and background MC samples.

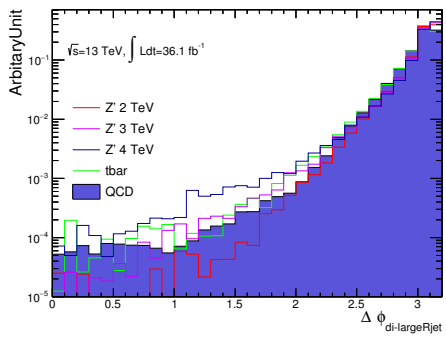

Figure 17: Distribution of the angle difference in ϕ between the leading and sub-leading large-R jets in the signal and background Monte Carlo samples after pre-selection.

6.2.2. Large-R jet τ_{32}^{wta}-likelihood ratio

τ_{32}^{wta} is a jet substructure variable defined using the N-subjettiness τ_N [90, 91]. The N-subjettiness is based on the reconstruction of exactly N sub-jets with the k_T jet algorithm [82–84] from the constituents of a jet. The τ_N is defined as

$$\tau_N = \frac{1}{d_0}\Sigma_k p_{T,k} \times min(\delta R_{1,k}, \delta R_{2,k}, ..., \delta\ R_{N,k}), \tag{35}$$

where $d_0 = \Sigma_k p_{T,k} \times R$, R is the radius parameter of the jet, $p_{T,k}$ is the transverse momentum of the constituent k, and $\delta R_{i,k}$ is the distance between the sub-jets i and the constituent k. The τ_{32} is then defined as

$$\tau_{32} = \frac{\tau_3}{\tau_2} \tag{36}$$

In order to obtain an observable independent of the recoil of soft radiation inside the jet, the sub-jets are reconstructed with a winner-take-all (WTA) recombination scheme [92]. The N-subjettiness variable τ_N expresses how well a jet can be described as containing N or fewer sub-jets. If τ_N ~0, the jet has N (or fewer) sub-jets, while jets with $\tau_N >> 0$ have more sub-jets. The τ_{32}^{wta} allows discrimination between jets with a three-prong structure and those with a two-prong structure. Since top quarks decay into three particles, a large-R jet of a top quark candidate is expected to have a three-prong structure, and τ_{32}^{wta} is useful for the top quark identification.

Probability density functions are defined based on the τ_{32} distributions and a likelihood ratio is calculated for each events. Events are seleceted and categorized using the likelihood ratios (Sec. 6.3.3 for the categorization).

Two large-R jets (the leading and sub-leading large-R jets) are selected as top candidates. As the τ_{32}^{wta} variable is defined per large-R jet, a combination of two τ_{32}^{wta} variables has to be dealt with in each event. To minimize the complexity of dealing with the two τ_{32}^{wta} values, a probability density function for an event $P(\tau_{32,i}^{wta}, \tau_{32,j}^{wta})$ is defined as

$$P(\tau_{32,i}^{wta}, \tau_{32,j}^{wta}) = P(\tau_{32,i}^{wta}) \times P(\tau_{32,j}^{wta}), \tag{37}$$

where $P(\tau_{32,i}^{wta})$ denotes a probability density function for a single jet i. It is produced by templates of the τ_{32}^{wta} distributions obtained from Z' MC for the signal and QCD multijet MC for the background. A τ_{32}^{wta}-likelihood ratio is then produced using the signal and background probability density functions as

$$\begin{aligned} & L(P(\tau_{32,i}^{wta}, \tau_{32,j}^{wta})|\tau_{32,i}^{wta}, \tau_{32,j}^{wta}) \\ \equiv & \frac{P_{\text{signal}}(\tau_{32,i}^{wta}, \tau_{32,j}^{wta})}{P_{\text{signal}}(\tau_{32,i}^{wta}, \tau_{32,j}^{wta}) + P_{\text{background}}(\tau_{32,i}^{wta}, \tau_{32,j}^{wta})}, \end{aligned} \tag{38}$$

where $L(P(\tau_{32,i}^{wta}, \tau_{32,j}^{wta})|\tau_{32,i}^{wta}, \tau_{32,j}^{wta})$ is the τ_{32}^{wta} - likelihood ratio. The τ_{32}^{wta} - likelihood ratio is calculated per event.

Figure 18 shows the two-dimensional distribution of the τ_{32}^{wta} for the leading and sub-leading jets. No correlation between the two jets is seen.

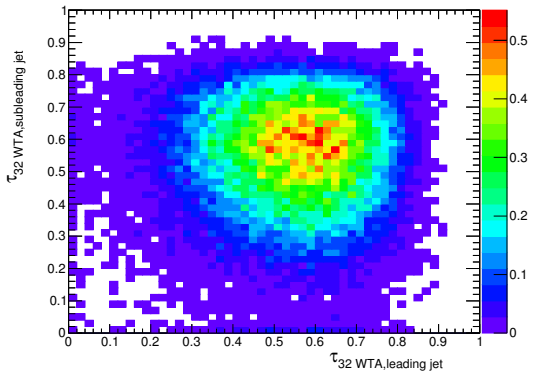

Figure 18: Two-dimensional τ_{32}^{wta} distribution of the leading large-R jet and the sub-leading large-R jet for Z' 3 TeV.

Figure 19 shows the τ_{32}^{wta} distribution of each Z'Monte Carlo sample after pre-selection up to Sec. 6.1. The Monte Carlo samples of Z' with a mass larger than 2.5 TeV show the similar shape of τ_{32}^{wta}.

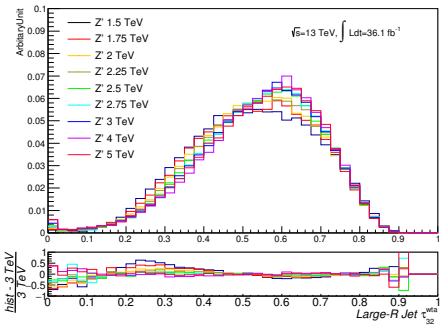

Figure 19: Distribution of τ_{32}^{wta} after pre-selection up to Sec. 6.1 in the signal Monte Carlo samples shown for reconstructed jets. The top panel shows the distribution and the bottom panel shows the relative difference with respect to the Z' 3 TeVsample

The signal template is made using the several Z' Monte Carlo samples with Z' mass larger than 2.5 TeV in order to obtain statistics.

Figure 20 shows the distributions of τ_{32}^{wta} for Monte Carlo QCD multijet events and data after the subtraction of the SM $t\bar{t}$ events estimated from the MC sample. Both are shown for events after the pre-selection up to Sec. 6.1. Distributions of the Monte Carlo QCD multijet events are in good agreement with data after the $t\bar{t}$ subtraction.

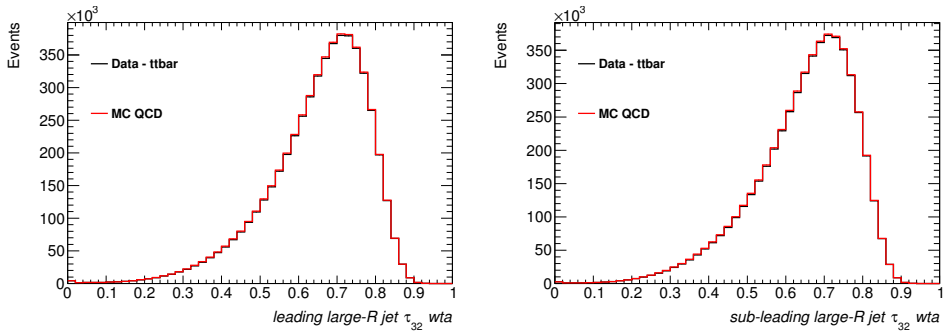

(a) Leading large-R jet τ_{32}^{wta} (b) Sub-leading large-R jet τ_{32}^{wta}

Figure 20: Distribution of τ_{32}^{wta} for Monte Carlo QCD multijet events and data after subtraction of the SM $t\bar{t}$ events estimated from the Monte Carlo sample. The pre-selections described in the Sec. 6.1 are applied on the both samples. The distributions are shown separately for the leading large-R jets and the sub-leading large-R jets

Figure 21 shows the resulting distribution of the τ_{32}^{wta}-likelihood ratio for the Z' MC and multijet MC samples.

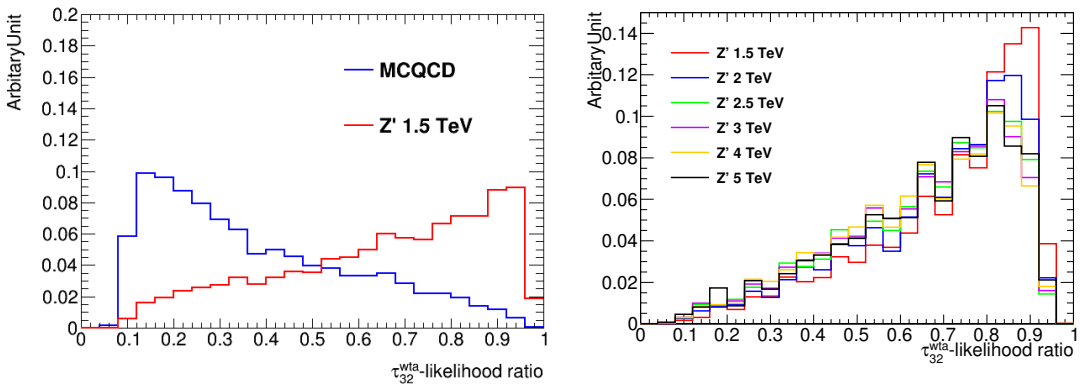

(a) MC QCD v.s. Z' 3 TeV (b) Several Z' samples

Figure 21: Distribution of the likelihood ratio formed from two τ_{32}^{wta} histograms. (a) Discribations of the likelihood ratios of the Z' MC sample the multijet MC sample. (b) Distributions of the likelihood ratios of the Z' MC samples with different Z' mass values.

Correlations between the τ_{32}^{wta}-likelihood ratio and other kinematics variables are checked in Fig. 22 and Fig. 23. The variables checked are jet p_T, η and $m_{t\bar{t}}$. No significant correlation between the τ_{32}^{wta}-likelihood ratio and the other kinematic variables is found. There is only small correlation between the large-R jet η and the τ_{32}^{wta}-likelihood ratio.

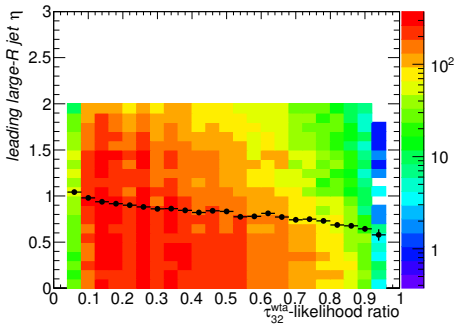

(a) τ_{32}^{wta}-likelihood ratio v.s. leading large-R jet η

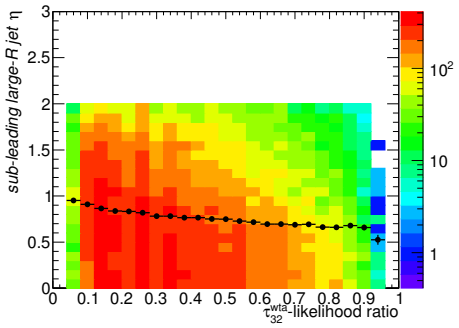

(b) τ_{32}^{wta}-likelihood ratio v.s. sub-leading large-R jet η

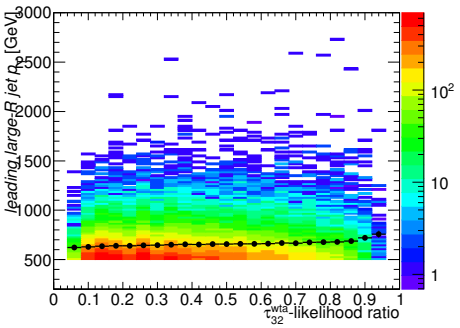

(c) τ_{32}^{wta}-likelihood ratio v.s. leading large-R jet p_T

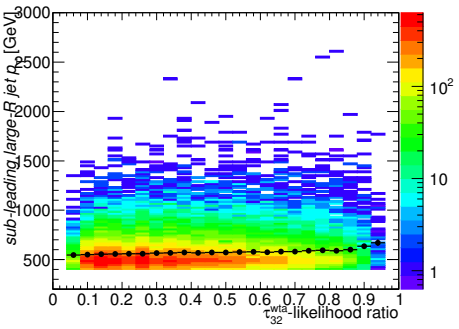

(d) τ_{32}^{wta}-likelihood ratio v.s. sub-leading large-R jet p_T

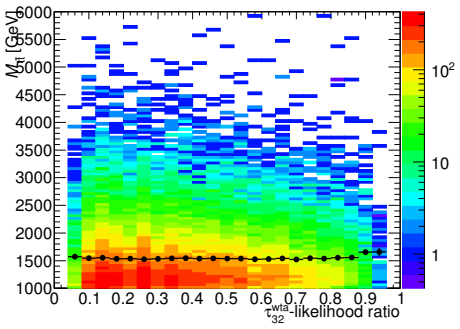

(e) τ_{32}^{wta}-likelihood ratio v.s. $m_{t\bar{t}}$

Figure 22: Correlation between τ_{32}^{wta}-likelihood ratio and other kinematic variables, for data after the subtraction of $t\bar{t}$ contribution estimated using MC simulation in a region which is enhanced multijet events with no tight b-tagging requirement and large-R jet mass cut ($50GeV < m_{\text{large-Rjet}} < 140GeV \parallel 190GeV < m_{\text{large-Rjet}} < 350GeV$). (a) leading large-$R$ jet η. (b) sub-leading large-R jet η. (c) leading large-R jet τ_{32}^{wta}. (d) sub-leading large-R jet τ_{32}^{wta}. (e) reconstructed $t\bar{t}$ mass. Markers show the mean values of the kinematic variable in each bin of the likelihood ratio.

We found a small bias in η and $m_{t\bar{t}}$ for τ_{32}^{wta}-likelihood ratio below 0.35 as can be seen in Figs 23. Therefore, only events with τ_{32}^{wta}-likelihood ratio above 0.35 are selected. The selected events are categorised in Loose, Medium and Tight based on the values of the likelihood ratio (See Sec. 6.3).

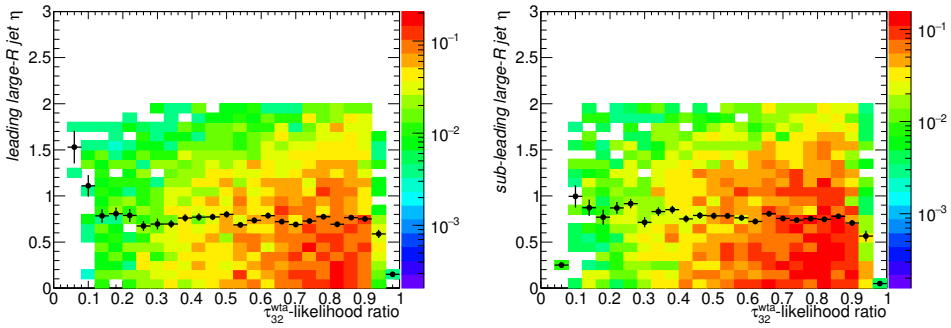

(a) τ_{32}^{wta}-likelihood ratio v.s. leading large-R jet η (b) τ_{32}^{wta}-likelihood ratio v.s. sub-leading large-R jet η

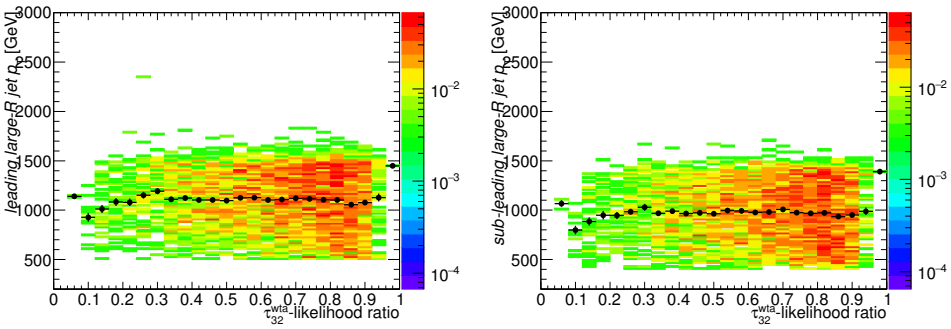

(c) τ_{32}^{wta}-likelihood ratio v.s. leading large-R jet p_T (d) τ_{32}^{wta}-likelihood ratio v.s. sub-leading large-R jet p_T

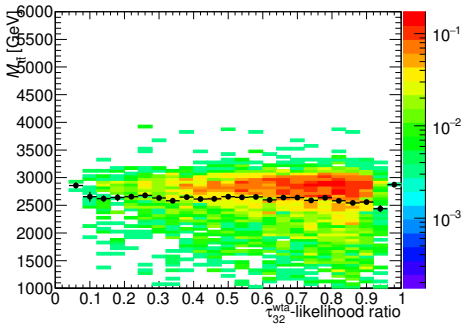

(e) τ_{32}^{wta}-likelihood ratio v.s. $m_{t\bar{t}}$

Figure 23: Correlation between τ_{32}^{wta}-likelihood ratio and other kinematics for Z' 3 TeV in a region after selection of two tight b-tagging requirement and large-R jet mass cut ($140GeV < m_{\text{large-Rjet}} < 190GeV$. (a) leading large-$R$ jet η. (b) sub-leading large-R jet η. (c) leading large-R jet τ_{32}^{wta}. (d) sub-leading large-R jet τ_{32}^{wta}. (e) reconstructed $t\bar{t}$ mass. Markers show the mean values of the kinematic variable in each bin of the likelihood ratio.

6.2.3. Large-R jet mass selection

The leading and sub-leading large-R jets are required to have their reconstructed mass, m_{jet}, in the range [140:190] GeV, consistent with the expected top quark mass. The criteria for the m_{jet} is optimized by scanning the Z' signal sensitivity by varying the range boundaries. The sensitivity is defined as Eq. (39).

$$Sensitivity = \frac{S}{\sqrt{S + B + (B \times \Delta)^2}}, \tag{39}$$

where S denotes the number of signal events, B denotes the number of background events, and Δ denotes the systematic uncertainty, where we use Δ=20% during the scans.

The stability of the criteria is checked in Fig. 24 and Fig. 25 for lower and upper boundaries respectively, using the Z' MC samples with $m_{Z'}$ = 2.5, 3 and 4 TeV. The value of the coordinate on the vertical axis in Fig. 24 and Fig. 25 is the sensitivity, and the value of the coordinate on the longitudinal axis is the range boundaries. From those figures, sensistivity is stable and higher than other boundary around 140 GeV and 190 GeV.

The optimized values are found to be 140 GeV for lower mass cut, and 190 GeV for higher mass cut. This study uses events with the τ_{32}^{wta}-likelihood ratio greater than 0.8 (after the pre-selection described in 6.1).

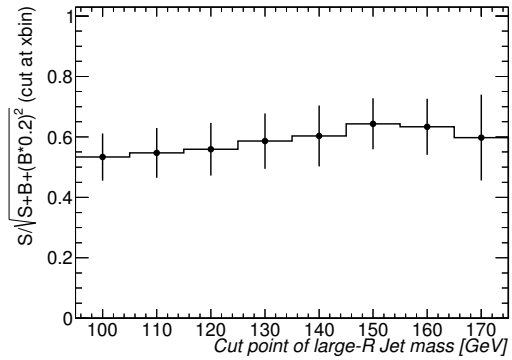

(a) One tight b-tag. Z' 2.5 TeV sample

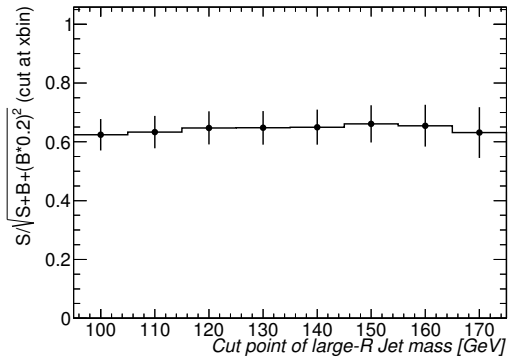

(b) Two tight b-tag. Z' 2.5 TeV sample

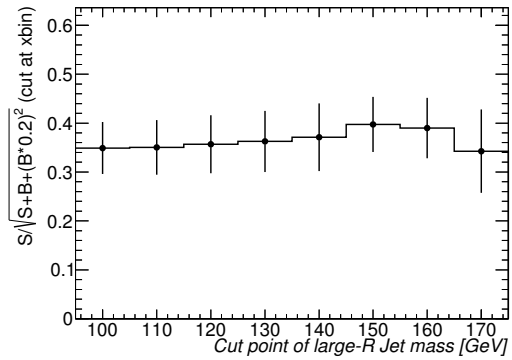

(c) One tight b-tag. Z' 3 TeV sample

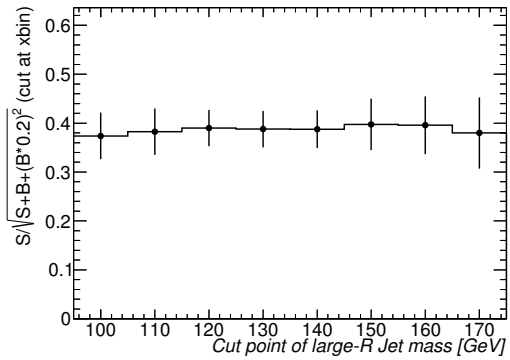

(d) Two tight b-tag. Z' 3 TeV sample

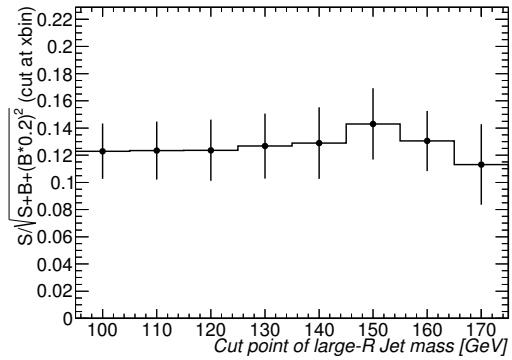

(e) One tight b-tag. Z' 4 TeV sample

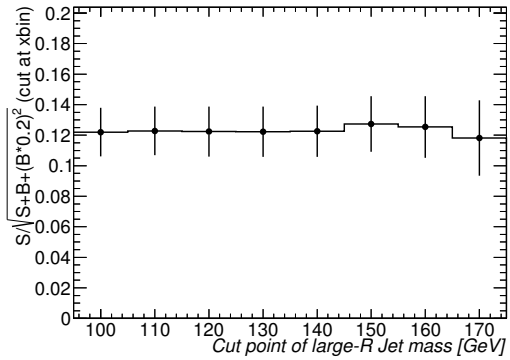

(f) Two tight b-tag. Z' 4 TeV sample

Figure 24: Sensitivities as a function of the lower boundary of the m_{jet} requirement. The upper boundary of $m_{\text{jet}} < 190$ GeV and τ_{32}^{wta}-likelihood> 0.8 are applied. They are shown separately for events containing one b-tag jet and those with two b-tag jets and for the Z' MC samples with $m_{Z'}$ =2.5, 3 and 4 TeV (The pre-selection described in 6.1).

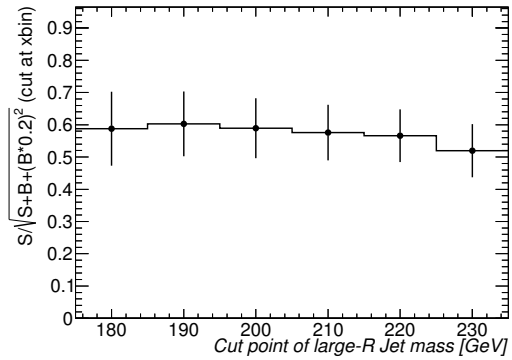

(a) One tight b-tag. Z' 2.5 TeV sample

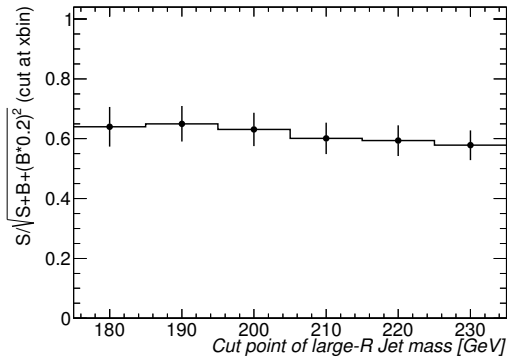

(b) Two tight b-tag. Z' 2.5 TeV sample

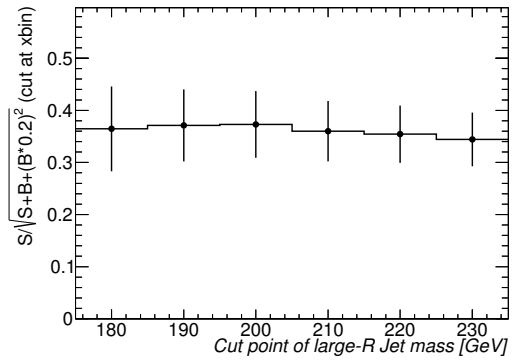

(c) One tight b-tag. Z' 3 TeV sample

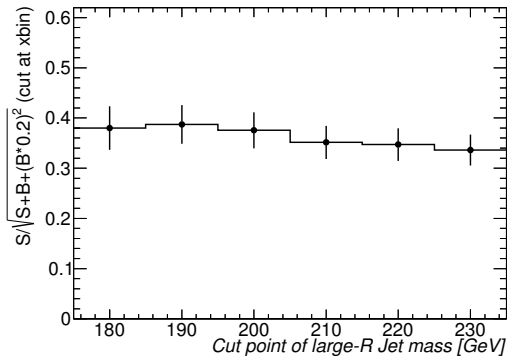

(d) Two tight b-tag. Z' 3 TeV sample

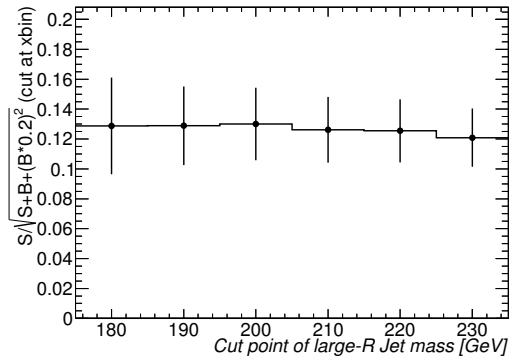

(e) One tight b-tag. Z' 4 TeV sample

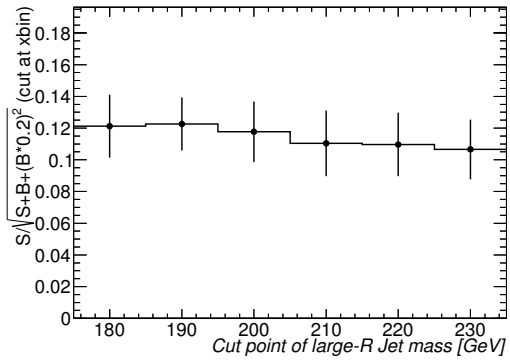

(f) Two tight b-tag. Z' 4 TeV sample

Figure 25: Sensitivities as a function of the lower boundary of the m_{jet} requirement. The upper boundary of 140 GeV $< m_{\text{jet}}$ and τ_{32}^{wta}-likelihood$>$ 0.8 are applied. They are shown separately for events containing one b-tag jet and those with two b-tag jets and for the Z' MC samples with $m_{Z'}$ =2.5, 3 and 4 TeV (The pre-selection described in 6.1).

6.2.4. Selection efficiencies

If a large-R jet satisfies $140 < m_{\text{jet}} < 190$ GeV and the event satisfies τ_{32}^{wta}-likelihood ratio > 0.65, the jet is considered as a top-quark. Figure 26 shows the efficiency of the large-R jet mass selection and τ_{32}^{wta}-likelihood ratio selection. Figure 27 shows the efficiency of each selection.

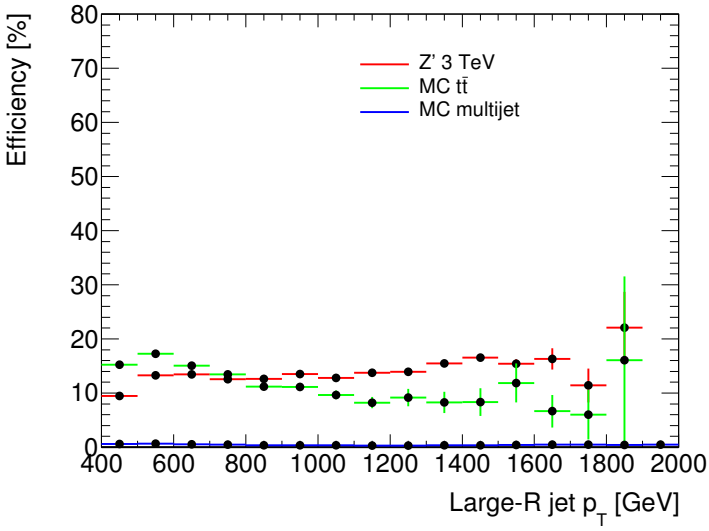

Figure 26: Top quark tagging efficiency. The pre-selection is applied and at least 2 large-R jets are for the denominator. For the numerator, 140 GeV $< m_j <$ 190 GeV and τ_{32}^{wta}-likelihood > 0.65 are additionaly for numerator.

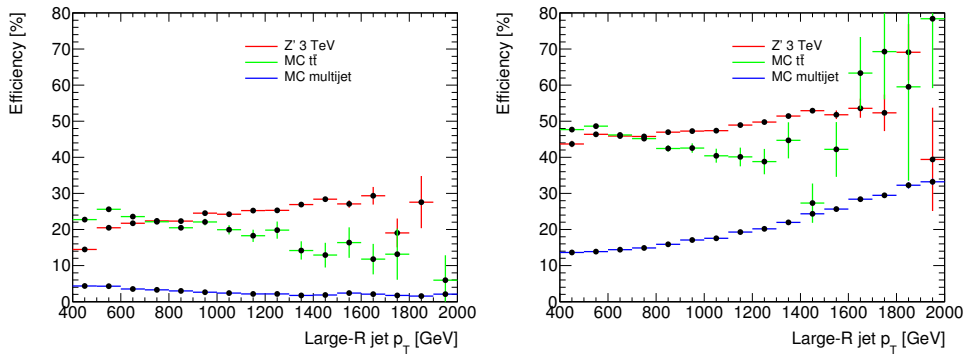

(a) Selection efficiency of large-R jet mass selection(b) Selection efficiency of τ_{32}^{wta}-likelihood ratio selection(> 0.65)

Figure 27: Selection efficiency of large-R jet mass and τ_{32}^{wta}-likelihood ratio selection for MC $t\bar{t}$ and Z' 3 TeV as a function of large-R jet p_T. Denominator is the events passing pre-selection. Numerator is the events passing pre-selection and each selection.

There is a difference between SM $t\bar{t}$ and Z' 3 TeV MC samples. It is caused by the difference of loose b-tagging efficiency as a function of the large-R jet η distribution between $t\bar{t}$ and Z' 3 TeV samples. The high p_T events of Z' 3 TeV are mainly at the central region, and the low p_T events of Z' 3 TeV are mainly at forward region as seen in Fig 28.

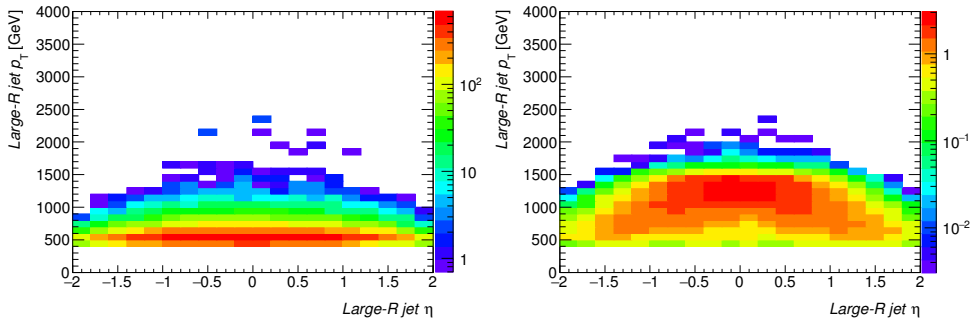

(a) MC $t\bar{t}$ (b) Z' 3 TeV

Figure 28: 2D distribution for large-R jet p_T V.S. large-R jet η for MC $t\bar{t}$ and Z' 3 TeV

The distribution of SM $t\bar{t}$ events is uniform compared to the Z' sample. The selection efficiency of loose b-tag as a function of large-R jet p_T is also checked in Fig. 29. From the figure, the loose b-tag selection cause the difference of efficiency for SM $t\bar{t}$ and the Z' sample because of the difference of the large-R jet η distribution.

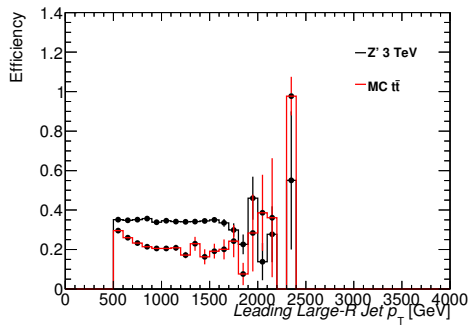

Figure 29: Selection efficiency of the loose b-tag selection for MC $t\bar{t}$ and Z' 3 TeV as a function of large-R jet p_T.

Figure 30, 31 show the acceptance and the efficiency of the event selection. Acceptance is defined as "Truth events after truth the selections" over "Truth events with pre-selection". The truth selections are $|\eta_t| < 2.0$, $p_{T,\text{leading}t} > 500$ GeV, $p_{\text{sub-leading}t} > 400$ GeV, 140 GeV $< m_t < 190$ GeV, $|\eta_b| < 2.5$, $p_{T,b} > 10$ GeV, $\Delta\phi(\text{top}, \text{anti}-\text{top}) < 1.6$, $\Delta R(t, b) < 1.0$ and $m_{t\bar{t}} > 1$ TeV (t denote truth top quark object and b denote truth bottom quark object). The truth selection also include. Derivation cut is included in following cut.

- At least one large-R jet ($p_T > 300$ GeV and $|\eta| < 2.2$) and at least one small-R jet ($p_T > 300$ GeV and $|\eta| < 2.7$)
- At least one large-R jet or small-R jet (passing a cut ΔR between large-R jet and small-R jet< 1.0)
- Soft lepton veto : If a event has at least one electron ($p_T > 30$ GeV and $|\eta| < 2.4$) or at least one muon ($p_T > 30$ GeV and $|\eta| < 2.4$)

The acceptance at the low $m_{t\bar{t}}$ region is low because of the kinematic boundary of the analysis, i.e. the jet p_T is required to be greater than 500 GeV for the leading jet and 400 GeV for the sub-leading jet, and also the existence of a b-jet in the large-R jet is required.

Efficiency is defined as "Truth events after reco and truth selections" over "Truth events after truth selection".

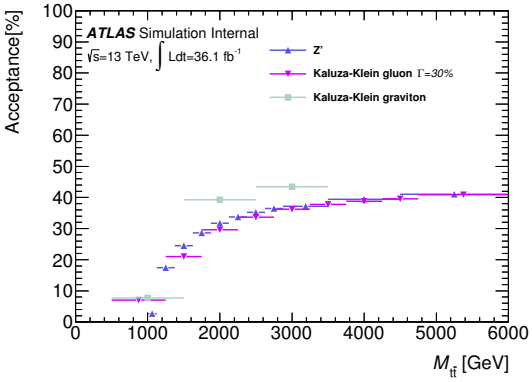

Figure 30: Acceptance show for Z',KK gluon and KK graviton. Both truth top quarks are required 140 GeV$< m_{\mathrm{j}} <$ 190 GeV, $p_{T,\mathrm{top}} > 400$, $p_{T,\mathrm{leadingtop}} > 500$, $|\eta_{\mathrm{top}}| < 2.0$, $\Delta R(\mathrm{top}, \mathrm{bottom}) < 1.0$, $\Delta\phi_{t\bar{t}}$, $p_{T,\mathrm{bottom}} > 10$ GeV, $|\eta_{\mathrm{bottom}}| <$ 2.5, $\Delta R(t, b) < 1.0$ and $m_{t\bar{t}} > 1$ TeV for the numerator. Only deriviation cut is applied for the denominator.

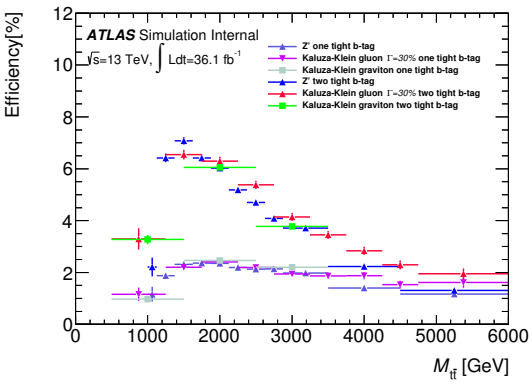

Figure 31: Efficiency as a function of truth $m_{t\bar{t}}$. In addition to the event selection described in the text, exactly one or two tight b-tagging, large-R jet mass [140 GeV:190 GeV] and $0.65 < \tau_{32}$-likelihood ratio are required for the numerator. is required for the numerator. Both truth top quarks are required 140 GeV$< m_j <$ 190 GeV, $p_{T,\mathrm{top}} > 400$, $p_{T,\mathrm{leadingtop}} > 500$, $|\eta_{\mathrm{top}}| < 2.0$, $\Delta R(\mathrm{top}, \mathrm{bottom}) < 1.0$, $\Delta\phi_{t\bar{t}}$, $p_{T,\mathrm{bottom}} > 10$ GeVand $|\eta_{\mathrm{bottom}}| < 2.5$ for the denominator.

Results of efficiency (two tight b-tag) times acceptance for each signal model and each mass point are summarized in Table 7.

$m_{t\bar{t}}$ point [GeV]	1000	2000	3000	4000	5000
Z' 3 TeV	2.2%	6.1%	3.8%	2.3%	1.8%
RS-Graviton 3 TeV	3.3%	6.1%	3.9%	–	–
KK-gluon 3 TeV	3.2%	6.3%	4.2%	2.9%	2.0%

Table 7: Efficiency × acceptance for each signal model. Two tight b-tag is applied.

6.3. Event categories

Event selections are optimized with respect to the signal sensitivity as mentioned earlier. Our events are categorized by types of b-tag conditions, τ_{32}^{wta}-likelihood ratio selections and m_{jet} selections to define the signal region and to estimate the amoun of multijet background from data.

The b-tag categories are defined as:

- No tight b-tag : both large-R jets have associated loose b-tagged track jets, but have no associated tight b-tagged track jets. Multijet background contributions are dominant in this category, therefore this category is used to obtain the template shape of the shape multijet background.
- One tight b-tag : only one of the two large-R jets has an associated tight b-tagged track jet. Having a lot of signal events, a part of this category is included in the signal region.
- Two tight b-tag : both large-R jets have associated tight b-tagged track jets. This category is the most sensitive to the signal among the b-tag categories, and is included in signal region.

where 'tight' b-tagging is defined as the 77% b-tag efficiency track jet working point.

Three categories are defined based on τ_{32}^{wta}-likelihood ratio requirements as mentioned before (see Section 6.3.2): And the categories based on the m_{jet} selection are mentioned in the Sec. 6.3.1).

6.3.1. m_{jet} categories

We define m_{jet}-categories based on the m_{jet} values of the leading and sub-leading large-R jets. The definition is illustrated in Fig. 32. The region R0 has the largest amount of the signal events, and the region R3 also has reasonable sensitivity. Therefore, the regions R0 and R3 are to be used as the signal region. Details are summarized in the later section (Table 8 in Sec. 6.3.3).

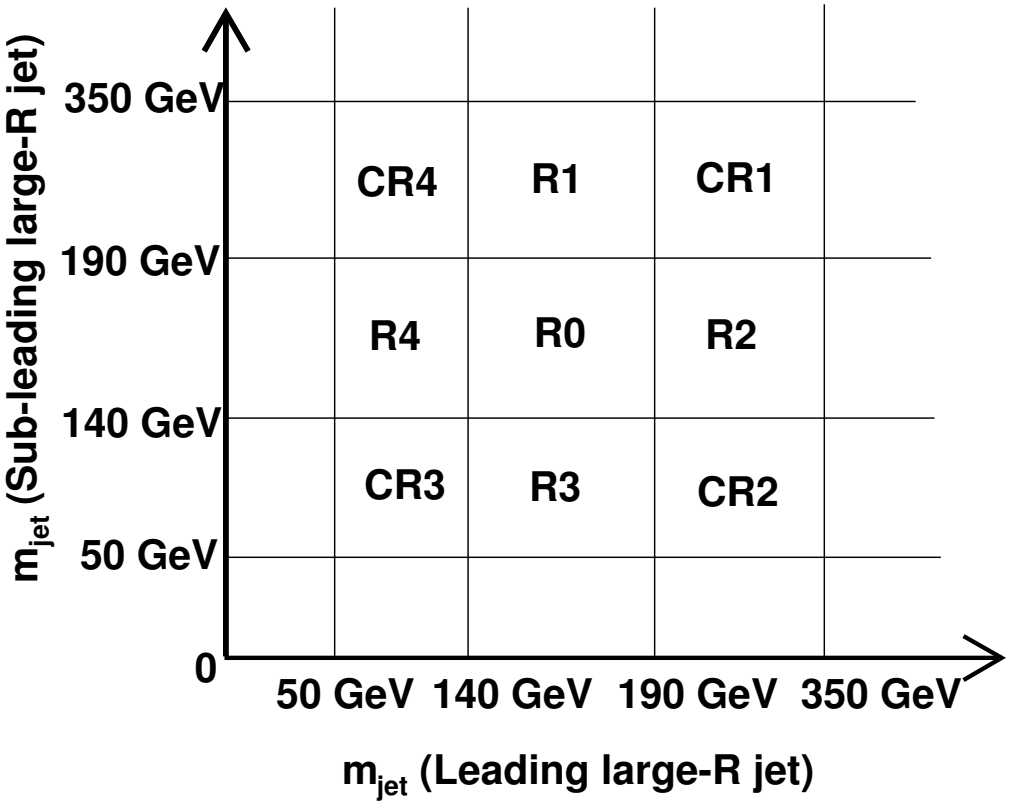

Figure 32: Event categories based on the m_{jet}.

6.3.2. τ_{32}^{wta}-likelihood ratio categories

As already mentioned in Sec. 6.2.2, events are split into further categories based on the τ_{32}^{wta}-likelihood ratio values.

- Loose : 0.35 < τ_{32}^{wta}-likelihood ratio < 0.65
- Medium : 0.65 < τ_{32}^{wta}-likelihood ratio < 0.8
- Tight : 0.8 < τ_{32}^{wta}-likelihood ratio < 1.0

Figure 33 shows the amount of contributions from the Z' signal and the SM $t\bar{t}$ events as a function of the upper threshold on the τ_{32}^{wta}-likelihood ratio values. The lower threshold is set at 0.35. As seen in the figure, events in the R0 region with two tight b-tagged jets have the largest contributions from Z' and SM $t\bar{t}$, e.g. the contribution from Z' 1.5 TeV signal is about 10% and those of other Z' signals are below 5% at the likelihood ratio around 0.5-0.6. This is the maximum amount of the signal contamination in the lower region with low values of the τ_{32}^{wta}-likelihood ratio, which is defined as the Loose category as the validation region.

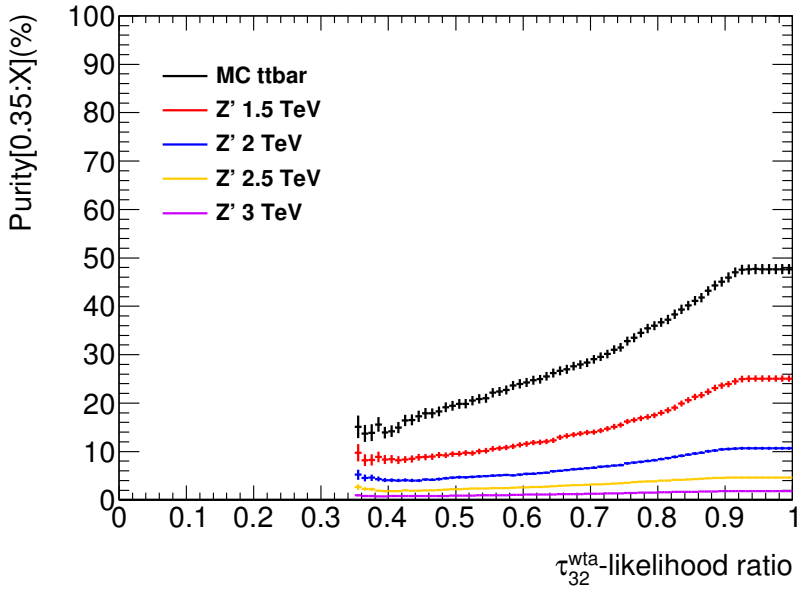

Figure 33: Scans of signal contamination (= each signal events/total background events) as a function of the upper threshold value of the τ_{32}^{wta}-likelihood ratio. The event satisfies the two tight b-tag and the mass selection of R0. The lower threshold is fixed as 0.35.

In order to define the signal region, we scan the signal sensitivity using the Z' 3 TeV signal sample by varying the lower threshold value of the τ_{32}^{wta}-likelihood ratio from 0.35 to 1.0. The upper threshold value is fixed as 1.0. The definition of the signal sensitivity used in the scan is the same as used in the earlier section, Eq. 39. The results are shown in Fig. 34. In the R0 region with two tight b-tagged jets, where the contribution of Z' events is expected to be largest, the best sensitivity is found at the value 0.8. We define the Tight category to be τ_{32}^{wta}-likelihood ratio from 0.8 to 1.0.

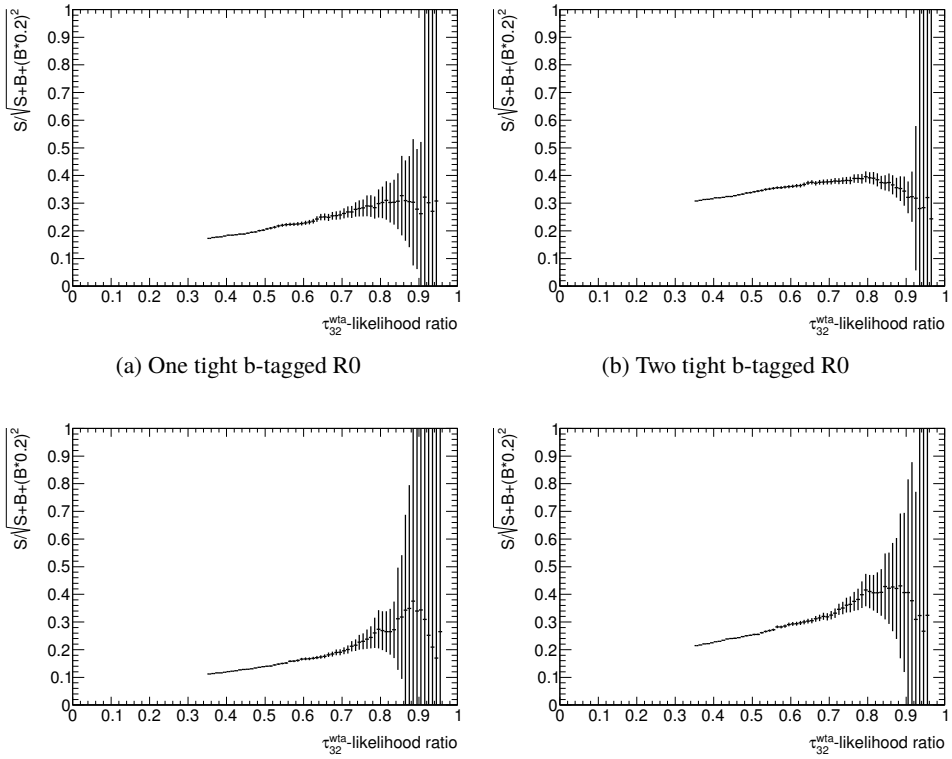

(a) One tight b-tagged R0

(b) Two tight b-tagged R0

(c) One tight b-tagged R3

(d) Two tight b-tagged R3

Figure 34: The signal sensitivity scans as a function of the lower threshold value of the τ_{32}^{wta}-likelihood ratio using 3 TeV Z' signal sample. The upper threshold is fixed at 1.0. Events within 2σ of $|m_{t\bar{t}} - m_{Z'}|$ are considered. They are shown for the different four regions : (a) the R0 region with one tight b-tagged jet. (b) the R0 region with two tight b-tagged jets. (c) the R3 region with one tight b-tagged jet. (d) the R3 region with two tight b-tagged jets.

The scan is repeated to define the region with the highest-sensitivity (Medium). We scan the sensitivity by changing the lower threshold value of the τ_{32}^{wta}-likelihood ratio from 0.35 to 0.8 of the τ_{32}^{wta}-likelihood ratio. The upper threshold is set at 0.8. The results are shown in Fig. 35. The best sensitivity is found at the value 0.65 in the R0 region with two tight b-tagged jets. The events with the τ_{32}^{wta}-likelihood ratio between 0.65 and 0.8 are categorized as the Medium category.

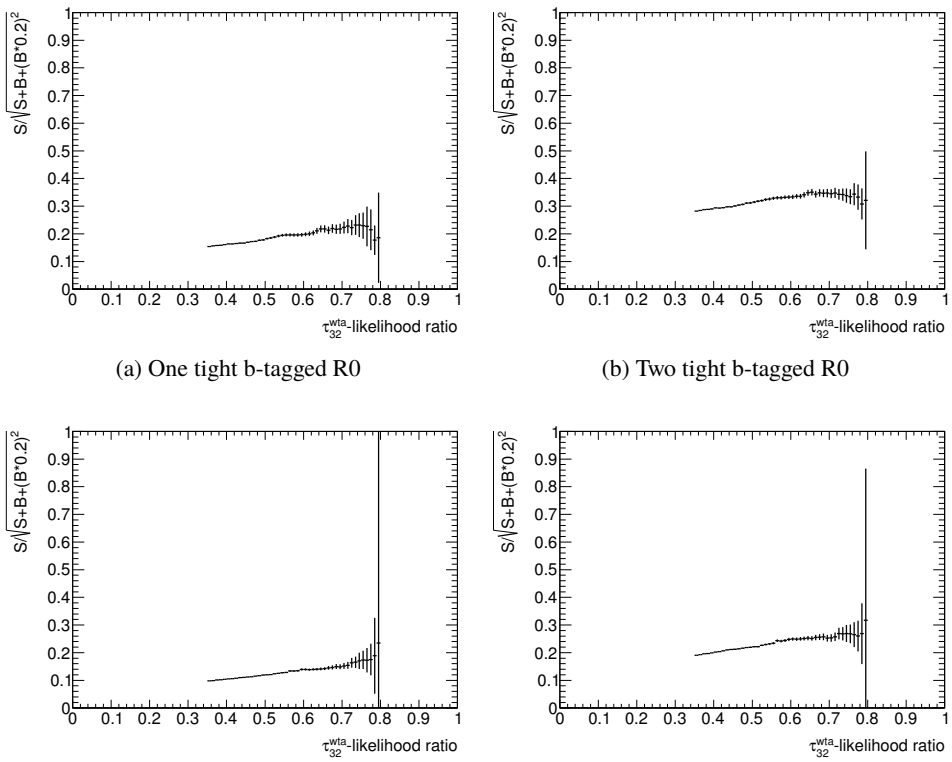

(a) One tight b-tagged R0

(b) Two tight b-tagged R0

(c) One tight b-tagged R3

(d) Two tight b-tagged R3

Figure 35: The signal sensitivity scans as a function of the lower threshold value of the τ_{32}^{wta}-likelihood ratio using 3 TeV Z' signal sample. The upper threshold is fixed at 0.8. Events within 2σ of $|m_{t\bar{t}} - m_{Z'}|$ are considered. They are shown for the different four regions : (a) the R0 region with one tight b-tagged jet. (b) the R0 region with two tight b-tagged jets. (c) the R3 region with one tight b-tagged jet. (d) the R3 region with two tight b-tagged jets.

We define the Loose category to have τ_{32}^{wta}-likelihood ratio from 0.35 to 0.65.

In summary, we define the Loose, Medium and Tight categoies based on the values of τ_{32}^{wta}-likelihood ratio as [0.35:0.65], [0.65:0.8] and [0.8:1.0], respectively. Loose category is used to validate the background modeling and the limit extraction procedure, and Medium and Tight categories are used to extract the final cross section limits.

6.3.3. Yields and sensitivity in the event categories

Figure 36 shows the two-dimensional distributions of the leading large-R jet mass and sub-leading large-R jet mass for zero, one, and two tight b-tagged jets event categories, respectively. Figure 36 (a), (c), (e) show that most of the $t\bar{t}$ events are within the optimized large-R jet mass selection[140 GeV: 190 GeV], and small amount of events in which a top quark is partially reconstrucred is seen in the lower sub-leading m_{jet} region.

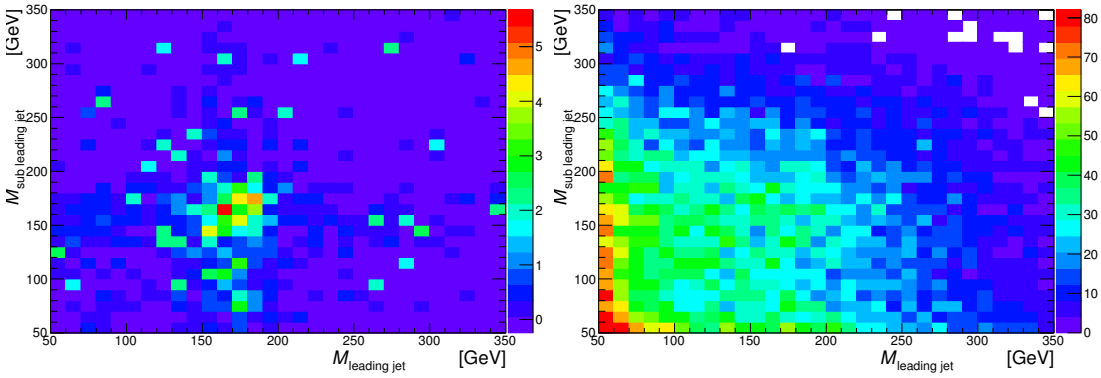

(a) No tight b-tag, $t\bar{t}$ MC

(b) No tight b-tag, Data

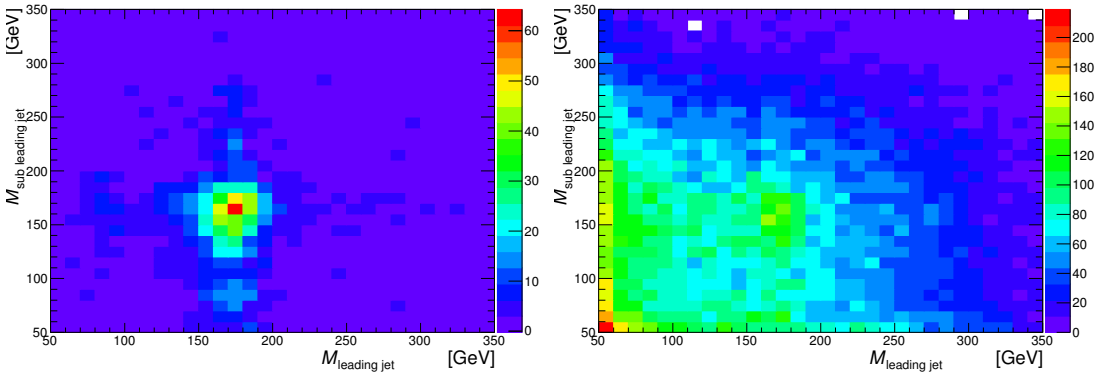

(c) One tight b-tag, $t\bar{t}$ MC

(d) One tight b-tag, Data

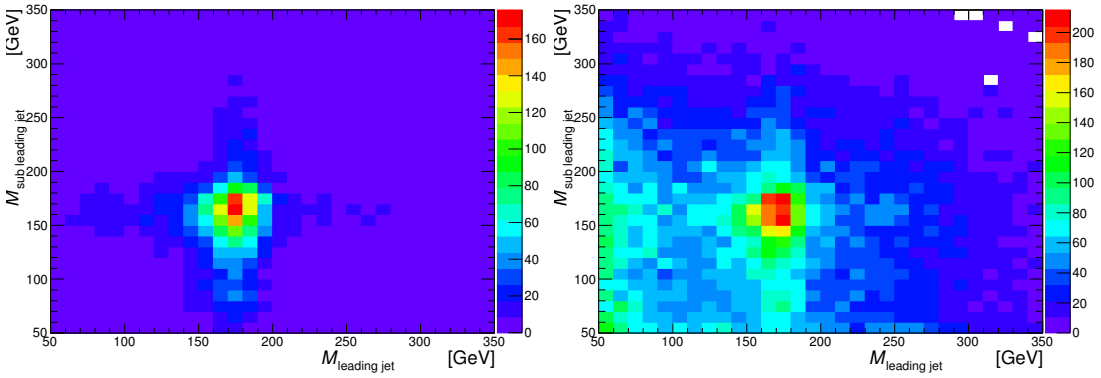

(e) Two tight b-tag, $t\bar{t}$ MC

(f) Two tight b-tag, Data

Figure 36: Two-dimensional distributions of the leading large-R jet m_{jet} and the subleading large-R jet m_{jet}, Shown separately for each b-tag categories. (a), (c), (e) are for the SM $t\bar{t}$ sample and (b), (d), (f) are for data. The m_{jet} categorisation and τ_{32}^{wta} categorisation not applied.

The definition of the categories (regions) are summarized in Fig. 37. The m_{jet} sideband region is defined as the control region (CR), where the multi-jet events are dominant while the contribution from the SM $t\bar{t}$ events is relatively small. This region is used to normalize the QCD multijet background while the shape is extracted from 0 b-tagged events in each region.

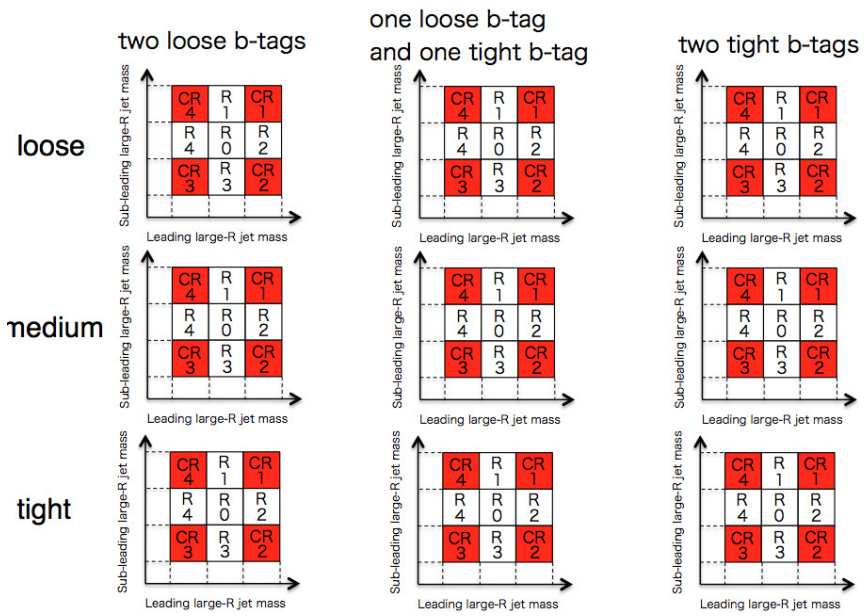

Figure 37: Difinition of regions

Signal and background yields around signal mass points (Z' 1.5 TeV and Z' 3 TeV) in each region are checked and the sensitivity in each region is estimated. They are summarised in Table. 8, 9. Each sensitivity is also shown. As seen in the tables, the Loose region has lower sensitivity. The R0 and R3 regions have higher sensitivities compared to other regions, In the region R0, the selected two jets are both consistent with the top quark mass. In the region R1, the selected leading jet is consistent with the top quark mass while the sub-leading jet is not but still contains major amount of decay objects from the top quark.

Regions	$t\bar{t}$	Data Driven QCD	Total BG	Z' 1.5 TeV	$\frac{S}{\sqrt{S+B}}$	S/B
One tight b-tagged R0 Loose	227.5	2805.8	3033.4	92.2	1.7	0.03
One tight b-tagged R0 Medium	197.3	837.0	1034.3	94.0	2.8	0.09
One tight b-tagged R0 Tight	286.4	323.8	610.2	146.1	5.3	0.2
Two tight b-tagged R0 Loose	594.8	1745.3	2340.1	242.1	4.8	0.1
Two tight b-tagged R0 Medium	610.5	523.7	1134.2	269.3	7.2	0.2
Two tight b-tagged R0 Tight	903.8	204.5	1108.3	445.7	11.3	0.4
One tight b-tagged R1 Loose	98.1	3073.4	3171.5	26.7	0.5	0.01
One tight b-tagged R1 Medium	102.9	1074.4	1177.2	29.5	0.9	0.03
One tight b-tagged R1 Tight	85.0	471.0	556.0	30.9	1.3	0.06
Two tight b-tagged R1 Loose	240.5	1896.2	2136.7	78.0	1.7	0.04
Two tight b-tagged R1 Medium	240.9	664.7	905.6	85.3	2.7	0.09
Two tight b-tagged R1 Tight	246.7	295.7	542.4	105.4	4.1	0.2
One tight b-tagged R2 Loose	108.5	3259.7	3368.2	28.0	0.5	0.008
One tight b-tagged R2 Medium	78.9	1209.6	1288.5	30.5	0.8	0.02
One tight b-tagged R2 Tight	79.7	517.7	596.7	31.6	1.3	0.05
Two tight b-tagged R2 Loose	216.4	2016.5	2232.9	70.7	1.5	0.03
Two tight b-tagged R2 Medium	207.3	748.5	955.8	78.7	2.5	0.08
Two tight b-tagged R2 Tight	248.8	325.6	574.3	103.5	4.0	0.2
One tight b-tagged R3 Loose	286.8	7324.8	7611.6	116.1	1.3	0.02
One tight b-tagged R3 Medium	161.7	1741.3	1903.0	77.4	1.7	0.04
One tight b-tagged R3 Tight	116.3	460.7	577.0	61.8	2.4	0.1
Two tight b-tagged R3 Loose	719.4	4554.6	5273.9	302.5	4.1	0.06
Two tight b-tagged R3 Medium	421.7	1082.0	1503.7	197.1	4.8	0.1
Two tight b-tagged R3 Tight	306.4	290.4	596.8	179.7	6.5	0.3
One tight b-tagged R4 Loose	201.6	8951.7	9153.3	58.7	0.6	0.01
One tight b-tagged R4 Medium	86.2	2247.2	2333.4	36.6	0.8	0.02
One tight b-tagged R4 Tight	59.0	688.3	747.2	30.4	1.1	0.04
Two tight b-tagged R4 Loose	423.3	5566.8	5990.1	149.2	1.9	0.03
Two tight b-tagged R4 Medium	235.8	1398.5	1634.2	87.0	2.1	0.05
Two tight b-tagged R4 Tight	167.0	431.0	598.0	70.9	2.7	0.1

Table 8: Event yields and the sensitivity to the Z' 1.5 TeV sample in each region. Events within 2σ from $m_{Z'}$ =1.5 TeV are considered as the signal.

Regions	$t\bar{t}$	Data Driven QCD	Total BG	Z' 3 TeV	$\frac{S}{\sqrt{S+B}}$	S/B
One tight b-tagged R0 Loose	84.1	1062.8	1146.9	4.9	0.1	0.0
One tight b-tagged R0 Medium	61.2	317.0	378.2	4.2	0.2	0.01
One tight b-tagged R0 Tight	62.7	122.7	185.3	3.5	0.3	0.02
Two tight b-tagged R0 Loose	162.7	637.8	800.5	8.6	0.3	0.01
Two tight b-tagged R0 Medium	148.9	191.4	340.3	7.5	0.4	0.02
Two tight b-tagged R0 Tight	161.9	74.7	236.7	7.0	0.5	0.03
One tight b-tagged R1 Loose	37.4	1642.7	1680.2	2.6	0.06	0.002
One tight b-tagged R1 Medium	30.9	574.3	605.1	1.9	0.08	0.003
One tight b-tagged R1 Tight	23.3	251.8	275.0	1.4	0.09	0.005
Two tight b-tagged R1 Loose	70.0	963.7	1033.8	4.5	0.1	0.004
Two tight b-tagged R1 Medium	62.2	337.8	400.0	3.3	0.2	0.008
Two tight b-tagged R1 Tight	61.3	150.3	211.5	2.6	0.2	0.01
One tight b-tagged R2 Loose	45.1	1697.7	1742.9	2.3	0.06	0.001
One tight b-tagged R2 Medium	28.7	630.0	658.6	1.8	0.07	0.003
One tight b-tagged R2 Tight	18.6	269.6	288.2	1.2	0.07	0.004
Two tight b-tagged R2 Loose	81.5	1004.7	1086.1	4.0	0.1	0.004
Two tight b-tagged R2 Medium	68.4	372.9	441.3	3.1	0.2	0.007
Two tight b-tagged R2 Tight	55.5	162.2	217.7	2.3	0.2	0.01
One tight b-tagged R3 Loose	81.3	2641.0	2722.3	4.7	0.1	0.002
One tight b-tagged R3 Medium	41.9	627.8	669.7	3.4	0.1	0.005
One tight b-tagged R3 Tight	22.3	166.1	188.4	2.6	0.2	0.01
Two tight b-tagged R3 Loose	147.5	1568.5	1716.0	8.2	0.2	0.005
Two tight b-tagged R3 Medium	87.0	372.6	459.6	5.1	0.2	0.01
Two tight b-tagged R3 Tight	54.4	100.0	154.5	4.3	0.3	0.03
One tight b-tagged R4 Loose	62.1	3242.0	3304.1	2.0	0.04	0.00
One tight b-tagged R4 Medium	26.5	813.8	840.3	1.1	0.04	0.001
One tight b-tagged R4 Tight	14.7	249.3	263.9	0.9	0.06	0.004
Two tight b-tagged R4 Loose	93.1	1933.0	2026.1	3.0	0.07	0.002
Two tight b-tagged R4 Medium	47.3	485.6	533.0	1.8	0.08	0.004
Two tight b-tagged R4 Tight	25.9	149.7	175.5	1.4	0.10	0.008

Table 9: Event yields and the sensitivity to the Z' 3 TeV sample in each region. Events within 2σ from $m_{Z'}$ =3 TeV are considered as the signal.

Signal region, template control region and validation region are defined as described in Fig. 38.

The template region (TR) is defined to obtain multi-jet background templates. Details of multi-jet background estimation is written in Sec. 7.2.

As already mentioned, R0 and R3 have high sensitivity to the signal. In order to simplify the analysis, only R0 and R3 are used to obtain the final cross section limits. Table 10 and Fig. 39 show the comparisons of the expected limits between the results using the R0+R3 Medium and Tight region and those using R0+1+2+3+4 Medium and Tight. The reduction of sensitivity using the R0-4 regions is about 4.8% for the $t\bar{t}$ mass point of 3 TeV.

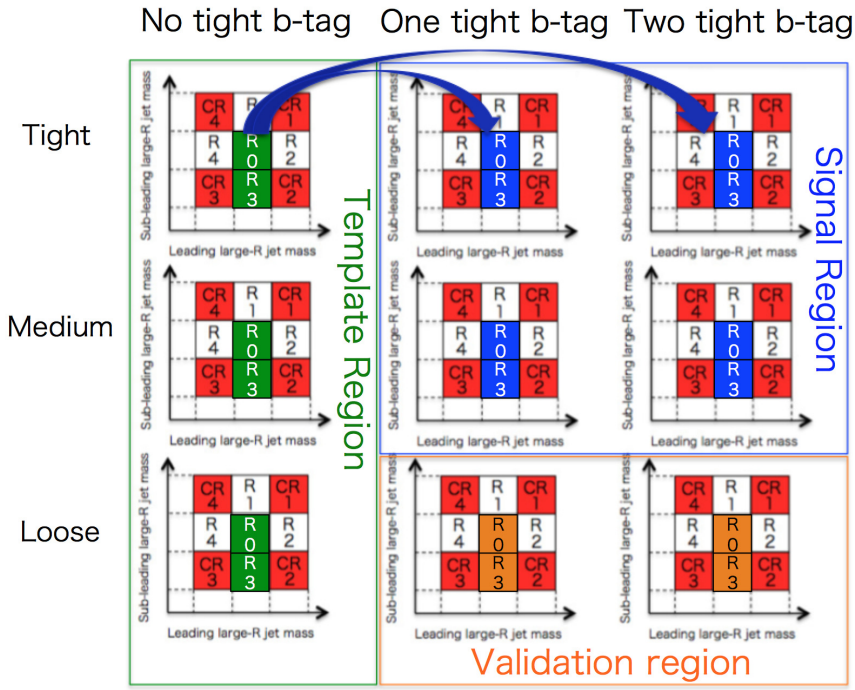

Figure 38: Definition of template region, control region and validation region.

Mass Points (TeV)	1	1.25	1.5	1.75	2	2.25	2.5	2.75	3	4	5
R0	3.9	0.27	0.128	0.10	0.061	0.044	0.037	0.031	0.026	0.015	0.016
R3	12.0	0.63	0.36	0.23	0.15	0.11	0.086	0.072	0.060	0.042	0.040
R0+R3	4.58	0.25	0.13	0.094	0.054	0.039	0.031	0.027	0.021	0.013	0.014
R0+1+2+3+4	2.6	0.21	0.11	0.084	0.052	0.037	0.031	0.027	0.022	0.013	0.012
Residual (%)	-43.2	-16.0	-15.4	-10.6	-3.7	5.1	0	0	4.8	0	-14.3

Table 10: Expected cross-section limits for each Z' mass point using different regions. Residual means ((R0+1+2+3+4)- (R0+R3))/ (R0+R3).

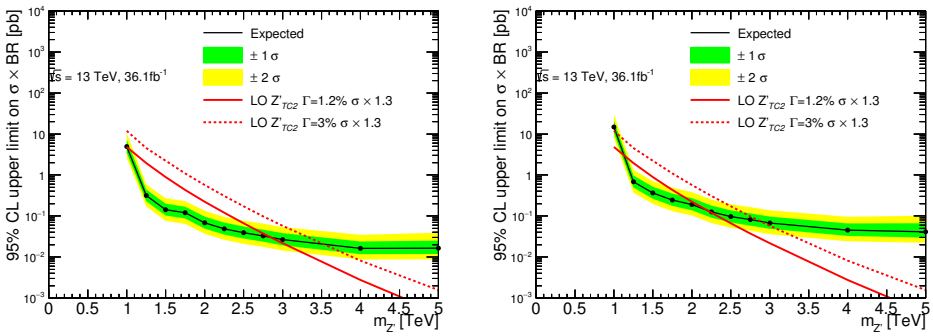

(a) Expected limits with R0

(b) Expected limits with R3

(c) Expected limits with R0 and R3

(d) Expected limits with R0-4

Figure 39: Expected limits R0 and R3, and of all R0-4 regions. All systematic uncertainties are considered in the estimation. Black line shows expected 95% confidence level (CL) upper limit on cross section times branching ratio (pb). Green (Yellow) band shows $\pm 1\sigma$ ($\pm 2\sigma$) band for the expected limit. Red solid (dash) line shows theoretical expectation of Z' with 1.2% (3%) width of $m_{t\bar{t}}$. Details of using calculation is described in Sec. 9

7. Background Estimation

QCD multijet events and the Standard Model $t\bar{t}$ events are considered as backgrounds in this analysis. Other contributions (Single top Wt channel, W+Jets, Z+Jets and top pair production associated with W are also checked and found to be negligible as can be seen in Table 11.

Table 11: Background yields and ratio

Region	DataDrivenQCD	$t\bar{t}$	SingleTop Wtch	WJets	ZJets	ttW
CR1 no tight b-tag merge	4540.98(98.44%)	22.02(0.48%)	3.38(0.07%)	40.68(0.88%)	5.51(0.12%)	0.49(0.01%)
CR2 no tight b-tag merge	8491.12(98.80%)	39.88(0.46%)	4.13(0.05%)	29.40(0.34%)	29.47(0.34%)	0.38(0.00%)
CR3 no tight b-tag merge	18660.90(98.74%)	55.10(0.29%)	10.86(0.06%)	118.58(0.63%)	53.33(0.28%)	0.26(0.00%)
CR4 no tight b-tag merge	9854.72(98.86%)	36.28(0.36%)	5.84(0.06%)	55.49(0.56%)	15.35(0.15%)	0.53(0.01%)
R1 no tight b-tag merge	3139.04(98.47%)	37.96(1.19%)	1.58(0.05%)	8.84(0.28%)	0.00(0.00%)	0.46(0.01%)
R2 no tight b-tag merge	3387.09(98.02%)	38.91(1.13%)	2.63(0.08%)	21.48(0.62%)	5.08(0.15%)	0.47(0.01%)
R3 no tight b-tag merge	6300.54(98.14%)	78.46(1.22%)	7.53(0.12%)	22.62(0.35%)	10.00(0.16%)	0.44(0.01%)
R4 no tight b-tag merge	7773.24(98.51%)	52.76(0.67%)	8.56(0.11%)	38.26(0.48%)	17.66(0.22%)	0.36(0.00%)
R0 no tight b-tag merge	2558.88(96.02%)	94.12(3.53%)	2.22(0.08%)	7.36(0.28%)	1.81(0.07%)	0.49(0.02%)
CR1-4 no tight b-tag merge	41547.73(98.75%)	153.27(0.36%)	24.21(0.06%)	244.13(0.58%)	103.66(0.25%)	1.66(0.00%)
CR1 one tight b-tag merge	10595.40(96.76%)	244.99(2.24%)	19.29(0.18%)	51.68(0.47%)	35.37(0.32%)	3.35(0.03%)
CR2 one tight b-tag merge	20306.36(97.26%)	345.33(1.65%)	42.94(0.21%)	141.62(0.68%)	37.73(0.18%)	3.09(0.01%)
CR3 one tight b-tag merge	45119.93(98.25%)	367.19(0.80%)	77.06(0.17%)	242.02(0.53%)	112.50(0.24%)	2.20(0.00%)
CR4 one tight b-tag merge	23351.05(97.30%)	367.40(1.53%)	52.41(0.22%)	146.42(0.61%)	77.15(0.32%)	3.15(0.01%)
R1 one tight b-tag merge	7463.96(94.11%)	410.15(5.17%)	16.98(0.21%)	21.69(0.27%)	13.74(0.17%)	4.20(0.05%)
R2 one tight b-tag merge	8103.68(94.56%)	395.95(4.62%)	15.42(0.18%)	32.33(0.38%)	18.22(0.21%)	3.80(0.04%)
R3 one tight b-tag merge	15290.96(93.48%)	865.51(5.29%)	55.02(0.34%)	96.06(0.59%)	45.47(0.28%)	4.12(0.03%)
R4 one tight b-tag merge	18877.41(95.94%)	545.62(2.77%)	76.19(0.39%)	120.99(0.61%)	51.26(0.26%)	3.51(0.02%)
R0 one tight b-tag merge	6238.10(84.59%)	1070.24(14.51%)	18.25(0.25%)	24.47(0.33%)	18.13(0.25%)	5.35(0.07%)
CR1-4 one tight b-tag merge	99372.70(97.67%)	1324.91(1.30%)	191.69(0.19%)	581.75(0.57%)	262.75(0.26%)	11.79(0.01%)
CR1 two tight b-tag merge	6371.11(92.45%)	424.30(6.16%)	27.52(0.40%)	14.54(0.21%)	48.73(0.71%)	5.25(0.08%)
CR2 two tight b-tag merge	12454.77(93.21%)	750.00(5.61%)	60.94(0.46%)	45.76(0.34%)	41.77(0.31%)	5.92(0.04%)
CR3 two tight b-tag merge	27913.19(96.27%)	743.24(2.56%)	85.48(0.29%)	127.39(0.44%)	118.25(0.41%)	3.33(0.01%)
CR4 two tight b-tag merge	14218.74(94.78%)	534.00(3.56%)	70.26(0.47%)	94.23(0.63%)	78.58(0.52%)	4.63(0.03%)
R1 two tight b-tag merge	4556.70(80.79%)	1002.97(17.78%)	35.90(0.64%)	9.61(0.17%)	26.28(0.47%)	8.93(0.16%)
R2 two tight b-tag merge	4971.58(81.90%)	969.90(15.98%)	43.79(0.72%)	47.66(0.79%)	29.40(0.48%)	7.32(0.12%)
R3 two tight b-tag merge	9485.83(80.26%)	2185.44(18.49%)	68.16(0.58%)	49.58(0.42%)	21.50(0.18%)	8.44(0.07%)
R4 two tight b-tag merge	11715.98(89.14%)	1210.65(9.21%)	90.62(0.69%)	71.17(0.54%)	48.48(0.37%)	5.72(0.04%)
R0 two tight b-tag merge	3882.64(55.47%)	3033.03(43.34%)	39.89(0.57%)	14.87(0.21%)	15.33(0.22%)	12.88(0.18%)
CR1-4 two tight b-tag merge	60957.80(94.88%)	2451.54(3.82%)	244.20(0.38%)	281.93(0.44%)	287.33(0.45%)	19.14(0.03%)

7.1. Standard Model $t\bar{t}$ background

The background due to the Standard Model production of $t\bar{t}$ events is estimated directly from Monte Carlo simulation, generated with the Powheg generator and Pythia for the parton shower. For a more precise estimate of this background at very high mass region, $m_{t\bar{t}}$-sliced samples are being used in this analysis.

Comparing the $m_{t\bar{t}}$ distributions for the three τ_{32}^{wta}-likelihood categories (Loose, Medium and Tight), as can be seen in Fig. 40, shows that they are all consistent with each other. Therefore,the three are all merged to have more statistics for a better determination of the $m_{t\bar{t}}$ distribution for the SM $t\bar{t}$ background. We also checked difference of $m_{t\bar{t}}$ distributions between the two different b-tagging categories, as can be seen in Fig. 41, it is found that their distributions are different because of the difference of b-tagging efficiency drop at high p_T, therefore we don't merge the distributions of one tight b-tagged events and two tight b-tagged events, and they are to be dealt with separately for the estimation of the Standard Model$t\bar{t}$ background.

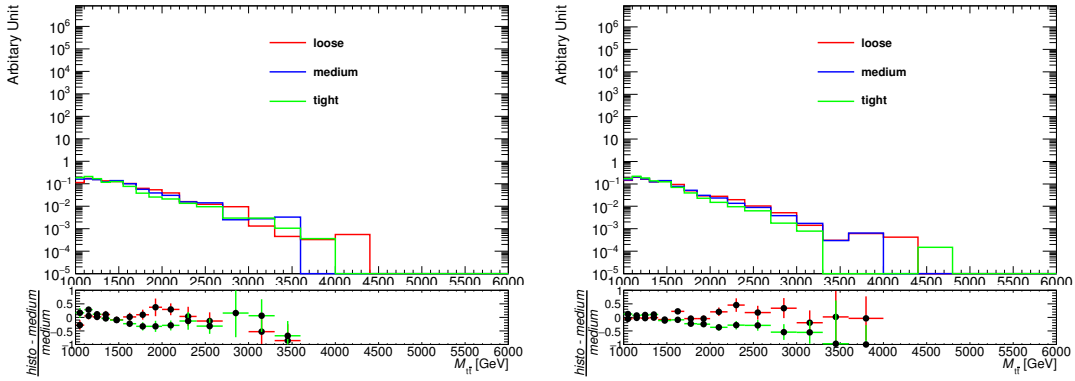

(a) One tight b-tag

(b) Two tight b-tag

Figure 40: Distributions of the $m_{t\bar{t}}$ in the signal region with the three τ_{32}^{wta}-likelihood categories in SM $t\bar{t}$ Monte Carlo sample.

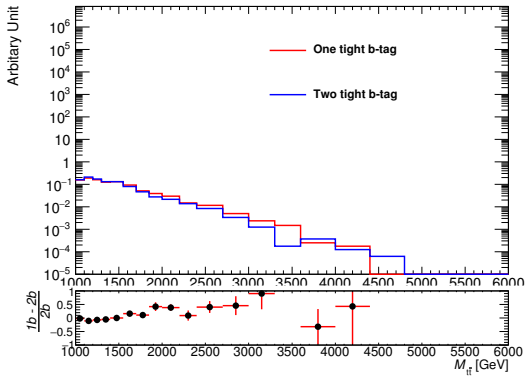

Figure 41: Distributions of the $m_{t\bar{t}}$ in the signal region with the two b-tagging categories in SM $t\bar{t}$ Monte Carlo sample. The three τ_{32}^{wta}-likelihood categories are merged.

7.2. QCD multijet background

The QCD multijet background is estimated from data with the help of Monte Carlo samples.

The shape of the $m_{t\bar{t}}$ distribution of the QCD multijet background is determined from events where no tight b-tagged track jets are found while other selections are passed. This region is defined as the 'template region' or 'TR' in Sec. 6.3.3. The template yields and $t\bar{t}$ purity in each template region are summarized in the Table 12. $t\bar{t}$ purity is sufficiently low, and the TRs can be used to obtain the shape of multijet from data suppressed the contributions of the MC $t\bar{t}$.

Table 12: Template yields and $t\bar{t}$ purity in each multijet template region (no tight b-tag). Templates are obtained by data subtracted MC $t\bar{t}$

Region	Loose R0	Loose R1	Loose R2	Loose R3	Loose R4
Yields	1823.08 ± 43.23	2100.75 ± 46.06	2225.62 ± 47.47	4859.19 ± 70.12	5869.97 ± 76.88
$t\bar{t}$ purity(%)	1.67 ± 0.21	0.63 ± 0.132	0.64 ± 0.165	0.83 ± 0.08	0.48 ± 0.062
Region	Medium R0	Medium R1	Medium R2	Medium R3	Medium R4
Yields	532.55 ± 23.87	724.39 ± 27.29	816.81 ± 28.86	1143.07 ± 34.26	1456.62 ± 38.45
$t\bar{t}$ purity(%)	4.90 ± 0.60	1.58 ± 0.41	1.35 ± 0.27	1.80 ± 0.27	0.98 ± 0.18
Region	Tight R0	Tight R1	Tight R2	Tight R3	Tight R4
Yields	203.25 ± 15.90	313.89 ± 18.36	344.66 ± 19.14	298.28 ± 17.94	446.65 ± 21.51
$t\bar{t}$ purity(%)	14.96 ± 1.836	4.01 ± 0.99	3.73 ± 0.839	5.31 ± 0.89	2.26 ± 0.53

In order to reduce the statistical uncertainty of the shape extraction, τ_{32}^{wta}-likelihood categories (Loose, Medium, Tight) are merged, after checking shape consistency of $m_{t\bar{t}}$ distributions, as can be found in Fig. 42.

The normalization of the QCD multijet background is estimated from the number of events in the template region multiplied by the ratio between events with no tight b-tagged jets and events with two tight b-tagged jets (or one tight b-tagged jets) in control regions (as defined below). This ratio is called the 'normalization factor'.

The contamination from Standard Model $t\bar{t}$ events in the QCD control regions is also checked and summarized in Table 13. This contamination from the Standard Model $t\bar{t}$ events is subtracted using Monte Carlo simulation in the QCD multijet background estimation.

The normalization factor n_{category} is estimated from a simple average of the four control regions (Eq. (40)),

$$n_{\text{category}} = \frac{n_{\text{CR1,category}} + n_{\text{CR2,category}} + n_{\text{CR3,category}} + n_{\text{CR4,category}}}{4} \tag{40}$$

after checking their consistency. The resulting normalization factors are summarized in Fig. 43 and Table 14.

Distributions of the $m_{t\bar{t}}$ for tight b-tagged events and no tight b-tagged events are compared in the control region, and small difference is found as can be seen in Fig. 44. This difference is corrected by using a correction function ($p_0/x + p_1 \times x + p_2$) as a function of scalar sum of jet p_T's ($p_{T(jet1)} + p_{T(jet2)}$) estimated from QCD multijet Monte Carlo simulation, as shown in ratio between two tight b-tagged events and zero tight b-tagged events in Fig. 45. In order to reduce the statistical uncertainty of the extraction of the correction function, τ_{32}^{wta}-likelihood categories (Loose, Medium, Tight) are merged for this extraction, after checking shape consistency for various distributions (See Appendix E).

The correction function for data is also checked, and it is found to be consistent. Figure 47 shows the distribution of the $m_{t\bar{t}}$ in the control region for no b-tagged region after the correction and b-tagged region. The corrected no b-tagged distributions agree well with that for tight b-tagged events. Figure 46 shows the ratio of the $m_{t\bar{t}}$ between one or two tight b-tagged events and no tight b-tagged events before and after the shape correction. Those ratios become flat after the shape correction.

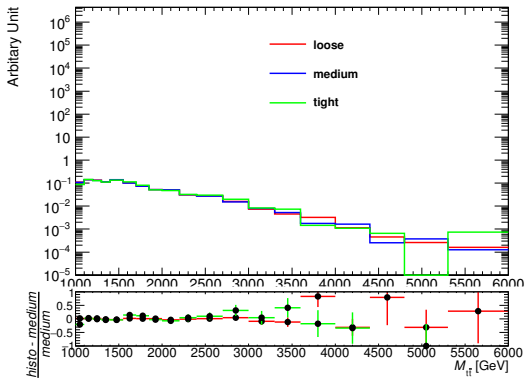

(a) No tight b-tag

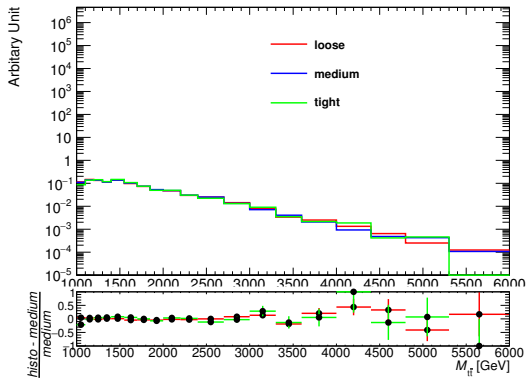

(b) One tight b-tag

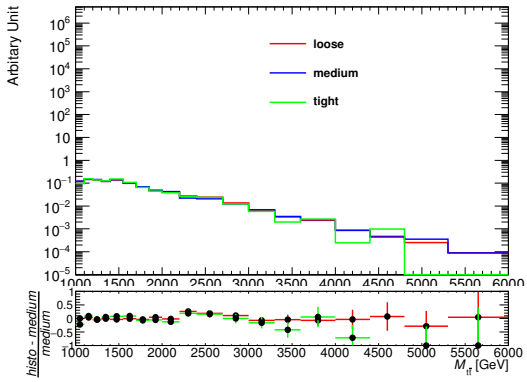

(c) Two tight b-tag

Figure 42: Distributions of the $m_{t\bar{t}}$ for the QCD multijet background (Data subtracted $t\bar{t}$ contributions with MC $t\bar{t}$) with several τ_{32}^{wta}-likelihood categories in control region (CR1+CR2+CR3+CR4).

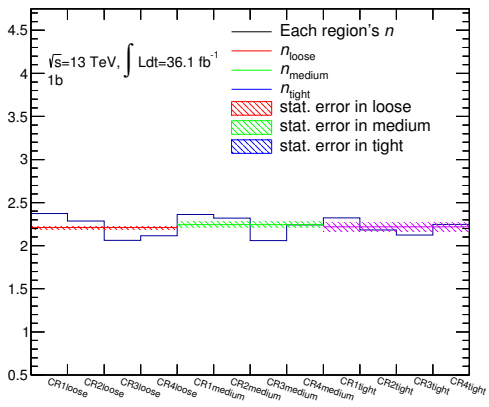

(a) One tight b-tag

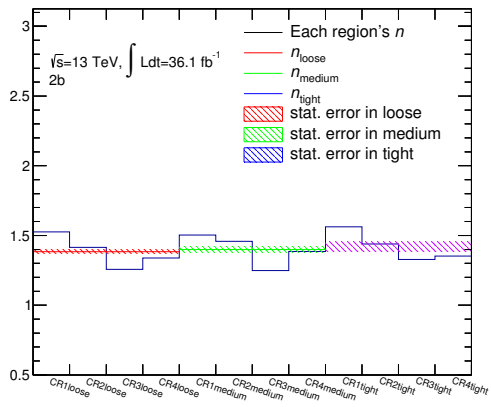

(b) Two tight b-tag

Figure 43: Normalization factors in each control region, and the averaged values.

Table 13: Contamination from the Standard Model $t\bar{t}$ events in the QCD control regions.

control region	$t\bar{t}$ contrib. in no tight b-tag	$t\bar{t}$ contrib. in 1 tight b-tag	$t\bar{t}$ contrib. in 2 tight b-tag
CR1-Loose	(0.27 ± 0.088)%	(1.51 ± 0.142)%	(3.68 ± 0.283)%
CR2-Loose	(0.43 ± 0.083)%	(1.27 ± 0.078)%	(4.28 ± 0.177)%
CR3-Loose	(0.23 ± 0.032)%	(0.70 ± 0.032)%	(2.34 ± 0.071)%
CR4-Loose	(0.32 ± 0.060)%	(1.43 ± 0.092)%	(2.88 ± 0.154)%
CR1-Medium	(0.80 ± 0.241)%	(2.68 ± 0.307)%	(8.00 ± 0.634)%
CR2-Medium	(0.58 ± 0.148)%	(2.39 ± 0.197)%	(7.37 ± 0.445)%
CR3-Medium	(0.42 ± 0.093)%	(1.28 ± 0.102)%	(3.98 ± 0.193)%
CR4-Medium	(0.42 ± 0.137)%	(1.81 ± 0.171)%	(5.13 ± 0.383)%
CR1-Tight	(0.89 ± 0.369)%	(4.12 ± 0.508)%	(10.51 ± 0.932)%
CR2-Tight	(0.55 ± 0.164)%	(3.03 ± 0.344)%	(12.05 ± 0.832)%
CR3-Tight	(1.05 ± 0.316)%	(2.24 ± 0.234)%	(7.93 ± 0.526)%
CR4-Tight	(0.66 ± 0.266)%	(2.39 ± 0.309)%	(7.31 ± 0.688)%
Total CR-Loose	(0.29 ± 0.028)%	(1.06 ± 0.033)%	(3.01 ± 0.067)%
Total CR-Medium	(0.51 ± 0.069)%	(1.88 ± 0.086)%	(5.70 ± 0.186)%
Total CR-Tight	(0.80 ± 0.145)%	(2.88 ± 0.174)%	(9.37 ± 0.373)%

Table 14: Normalization factors in each control region.

Category	Normalization factor	Stat. error (%)	Max deviation (%)
1 tight b-tag, Loose	2.370	±0.85	+7.4, -6.6
1 tight b-tag, Medium	2.395	±1.5	+10.2, -9.1
1 tight b-tag, Tight	2.404	±2.4	+4.7, -4.3
2 tight b-tag, Loose	1.384	±0.92	+10.2, -9.1
2 tight b-tag, Medium	1.399	±1.6	+7.5, -10.8
2 tight b-tag, Tight	1.421	±2.6	+10.0, -6.5

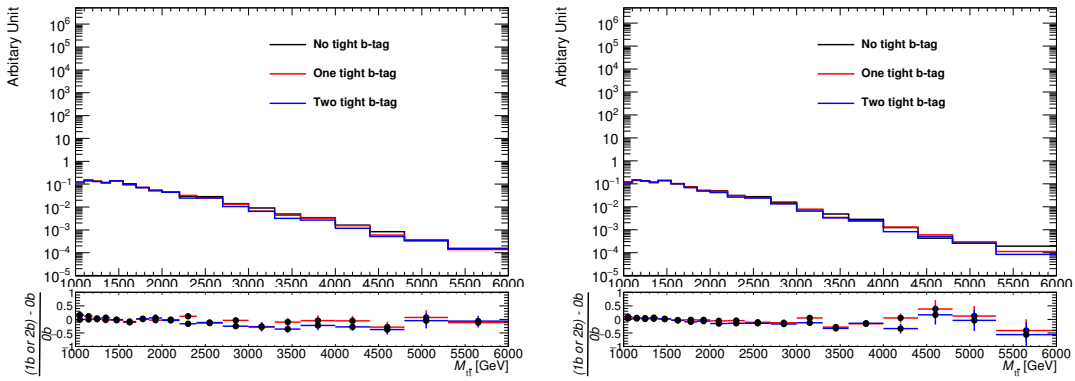

(a) MC QCD

(b) Data - MC $t\bar{t}$

Figure 44: Distribution of the $m_{t\bar{t}}$ for tight b-tagged events and no tight b-tagged events in the control region. Tiny difference is seen between tight b-tagged events and no tight b-tagged events.

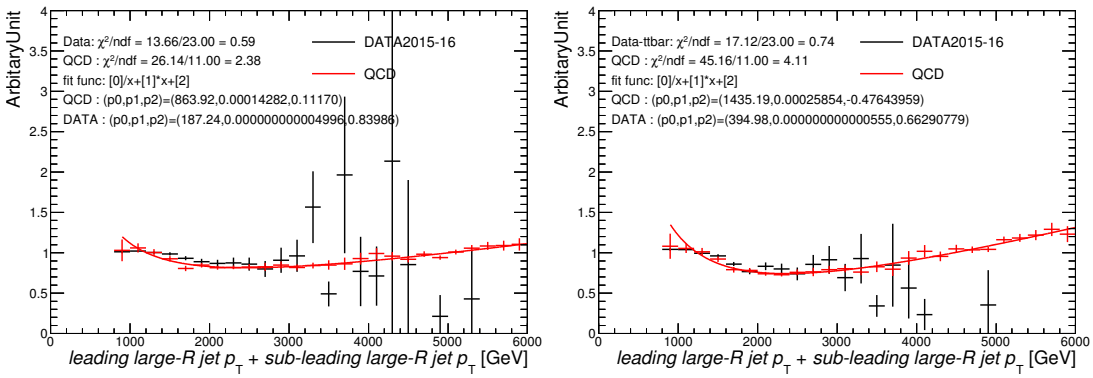

(a) One tight b-tag

(b) Two tight b-tag

Figure 45: Ratio of large-R jet p_T sum distributions between one or two tight b-tagged events and no tight b-tagged events in control region.

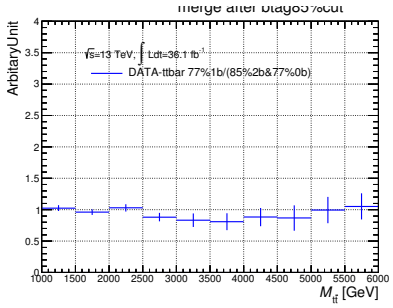

(a) One tight b-tag, QCD MC, before corr.

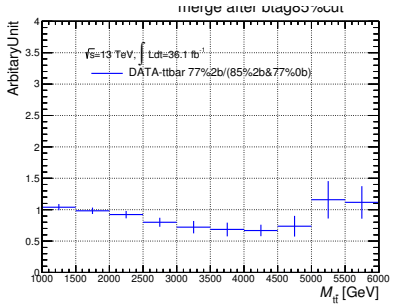

(b) Two tight b-tag, QCD MC, before corr.

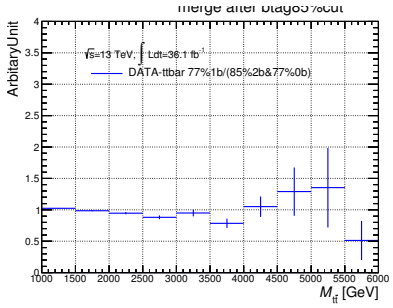

(c) One tight b-tag, Data, before corr.

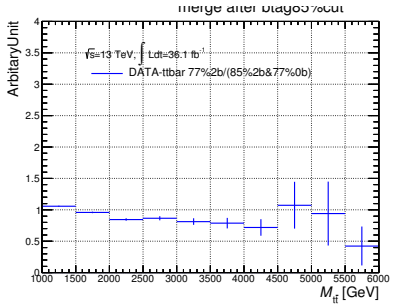

(d) Two tight b-tag, Data, before corr.

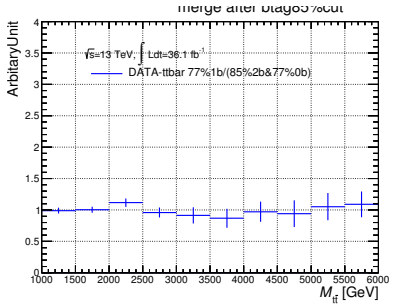

(e) One tight b-tag, QCD MC, after corr.

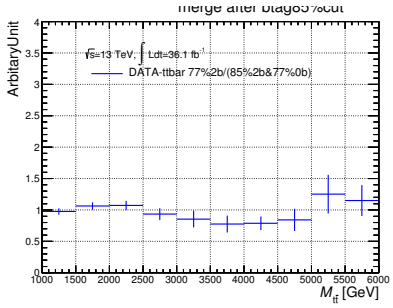

(f) Two tight b-tag, QCD MC, after corr.

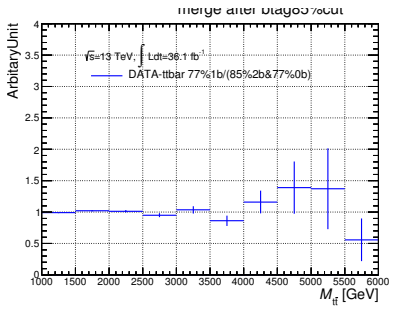

(g) One tight b-tag, Data, after corr.

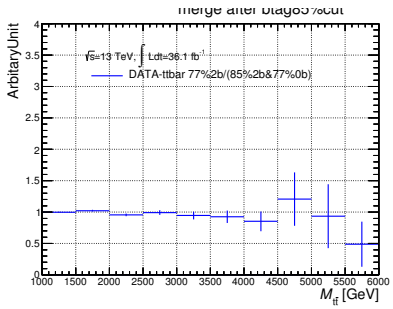

(h) Two tight b-tag, Data, after corr.

Figure 46: Ratio of $m_{t\bar{t}}$ distributions between one or two tight b-tagged events and no tight b-tagged events before and after the shape correction.

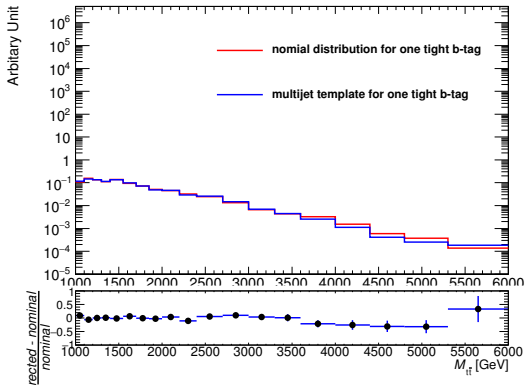

(a) MC QCD, One tight b-tag

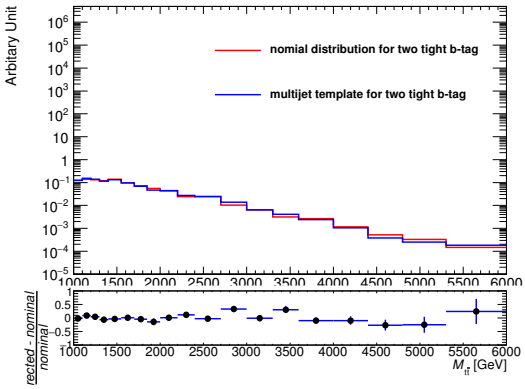

(b) MC QCD, Two tight b-tag

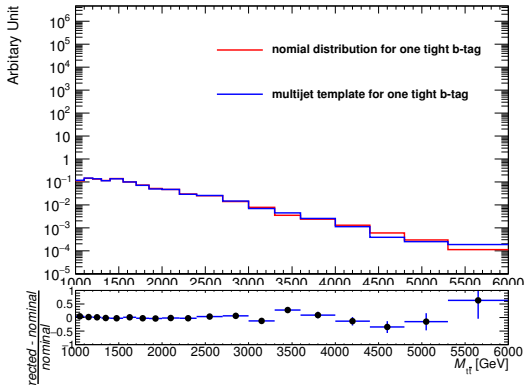

(c) Data - MC $t\bar{t}$, One tight b-tag

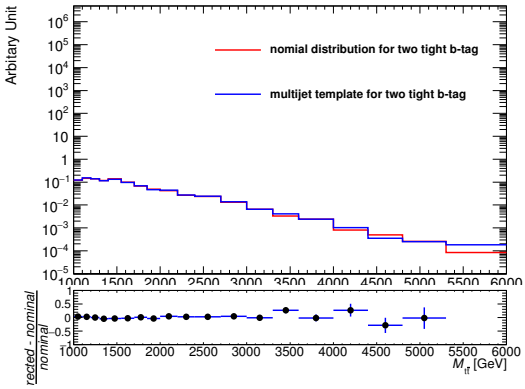

(d) Data - MC $t\bar{t}$, Two tight b-tag

Figure 47: Distribution of $m_{t\bar{t}}$ for tight b-tagged events and no tight b-tagged events with corrections for background estimation in the control region.

7.3. Extrapolation to the high $m_{t\bar{t}}$ region

Given the limited size of the samples being used by this analysis, the background estimation at very high mass region, $m_{t\bar{t}} > 2.5$ TeV, is not that accurate as can be seen in Fig. 48. We perform a fitting of the $m_{t\bar{t}}$ distribution using an exponential function ($exp(p0 + p1 \times x)$) to estimate the $m_{t\bar{t}}$ distribution in high mass region.

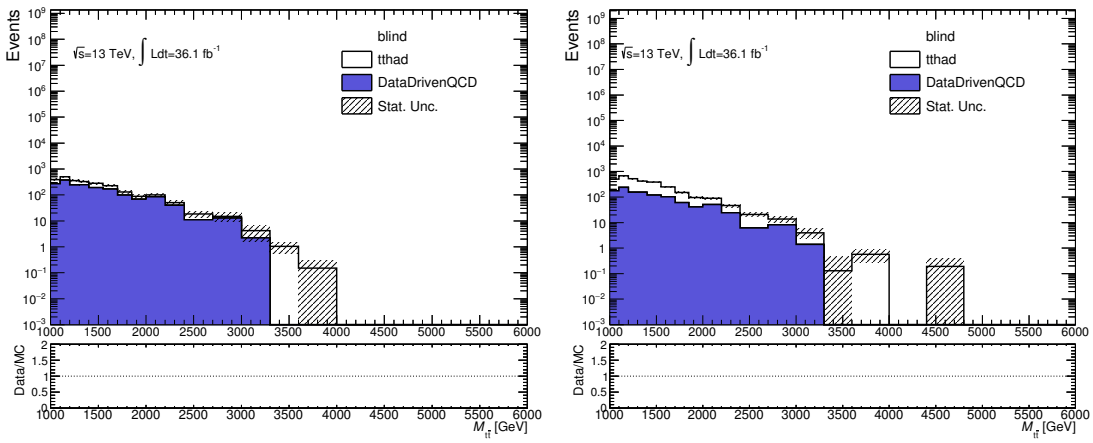

(a) One tight b-tag

(b) Two tight b-tag

Figure 48: Distributions of the $m_{t\bar{t}}$ in the signal region (data blinded). τ_{32}^{wta}-likelihood categories are merged.

The fit range is determined by checking the slope parameter of the fit varying the fit range from certain lower $m_{t\bar{t}}$ point to $m_{t\bar{t}} = 4$ TeV. Figure 49 shows the scan result of the parameter p_0, varying the fit starting point for the QCD multijet template in R0,R3,VR0 and VR3. From this result, any lower edges from 1.2 TeV to 2 TeV can be used for the multijet sample, where the slope parameter is stable and the size of the uncertainty is reasonably small. We do not this exponential extrapolation from the lowest edge of the histogram 1 TeV, because there is a strong bias from turn-on of the $m_{t\bar{t}}$ distribution due to kinematical selections. We choose 1.2 TeV as the lower edge of the exponential fit, and use 1.5 TeV as the start point of the exponential extrapolation for the multijet background. We use the original histograms before 1.5 TeV, because the region less than 1.5 TeV has sufficient statistics and it is better that the raw histogram shape is kept in this region. Figure 50 shows the scan result of the parameter p_1, varying the fit starting point for the QCD multijet template in R0,R3,VR0 and VR3. The parameter 1 is not widely moved in comparison of parameter 0.

Figure 51 and 52 show similar results for the Standard Model $t\bar{t}$ all-hadronic events. For $t\bar{t}$ background, the extrapolation is performed to inclusive distribution. Inclusive means that all-hadronic channel and semi-leptonic channel are combined. The size of this background is very small, a few % level compared to the all-hadronic $t\bar{t}$ events in the signal region. From this result, any lower edges from 1.2 TeV to 2 TeV can be used for the SM $t\bar{t}$ background. We choose 1.2 TeV as the lower edge of the exponential fit, and use 1.5 TeV as the start point of the exponential extrapolation for the SM $t\bar{t}$ background.

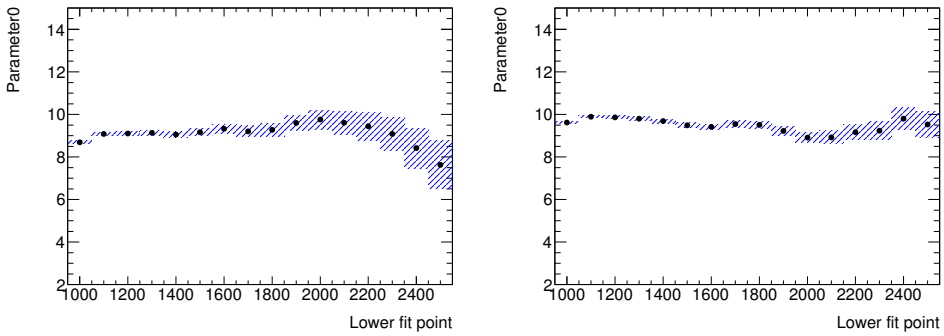

(a) Parameter 0 for R0

(b) Parameter 0 for SR3

Figure 49: Slope parameter of the exponential $m_{t\bar{t}}$ fit, varying fitting lower edge for QCD multijet background for two tight b-tagged category, and one tight b-tagged category is also similar because of using a common template shape.

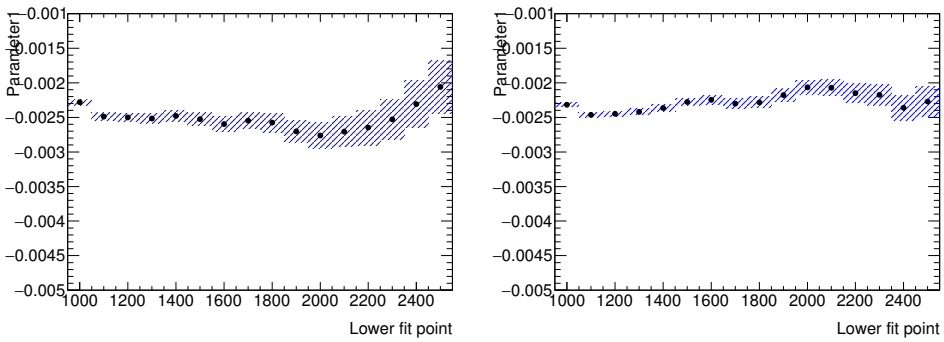

(a) Parameter 1 for SR0

(b) Parameter 1 for SR3

Figure 50: Constat parameter of the exponential $m_{t\bar{t}}$ fit, varying fitting lower edge for QCD multijet background for two tight b-tagged category, and one tight b-tagged category is also similar because of using a common template shape.

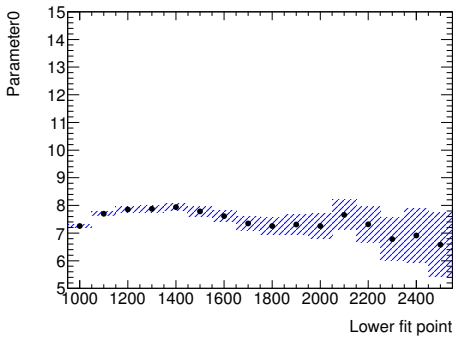

(a) Parameter 0 for 1b SR0

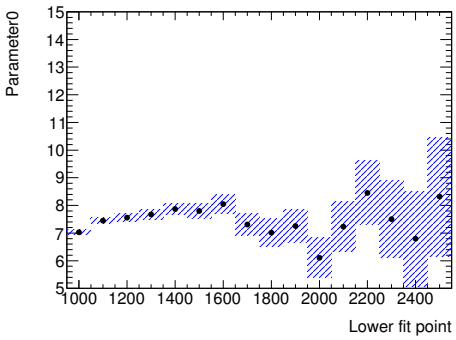

(b) Parameter 0 for 1b SR3

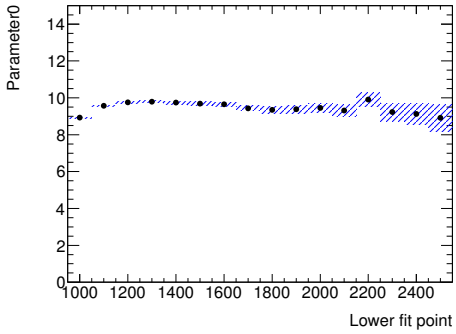

(c) Parameter 0 for 2b SR0

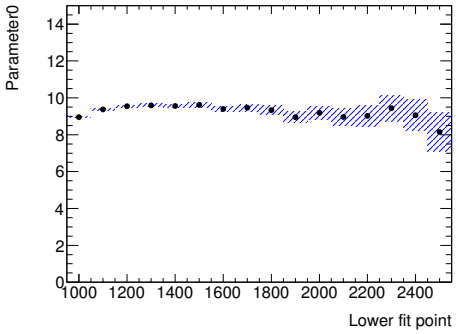

(d) Parameter 0 for 2b SR3

Figure 51: Slope parameter of the exponential $m_{t\bar{t}}$ fit, varying fitting lower edge for the Standard Model $t\bar{t}$ background.

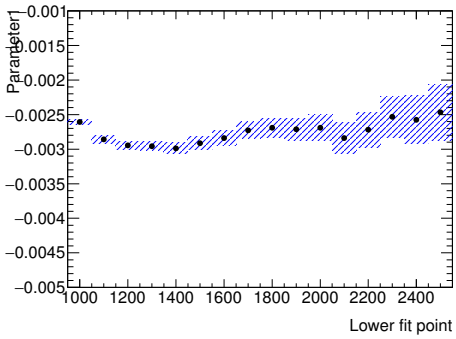

(a) Parameter 1 for 1b SR0

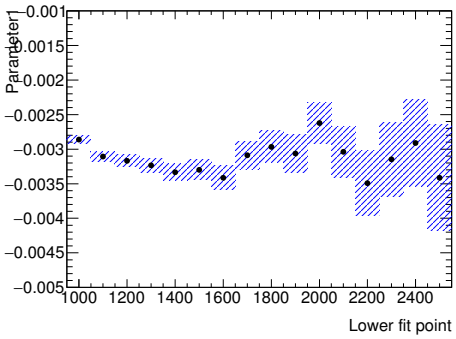

(b) Parameter 1 for 1b SR3

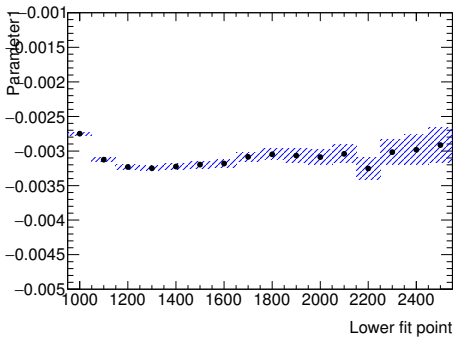

(c) Parameter 1 for 2b SR0

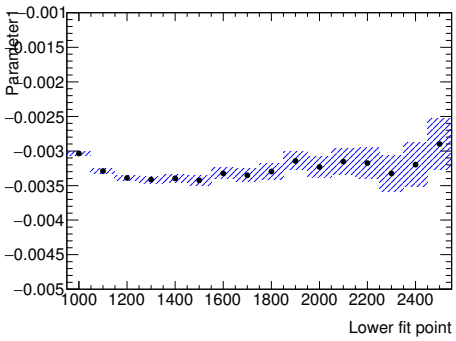

(d) Parameter 1 for 2b SR3

Figure 52: Constat parameter of the exponential $m_{t\bar{t}}$ fit, varying fitting lower edge for the Standard Model $t\bar{t}$ background.

Systematic uncertainty on this extrapolation method includes statistical uncertainty of the fit, and stability of the fit range choice. Stability of the fit range choice is evaluated by taking the maximum deviation from the nominal slope parameter when changing the lower edge of the fit range, until the statistical fluctuation becomes large, as can be seen from Fig. 49 for the QCD multijet background, and Fig. 51 for the SM $t\bar{t}$ background.

We take the difference of the exponential fit results between when we use 1.2 TeV as the lower edge of the fit and when we use 1.7 TeV as the lower edge of the fit, as a systematic uncertainty. The statistical uncertainty in the lower $m_{t\bar{t}}$ region is low, therefore lower fit point decide the precision of fit. In addition, region of $m_{t\bar{t}}$ which has sufficient events is limited from 1.2 TeV to 4 TeV. Hence, we keep higher fit point 4 TeV, and only check the variation of the lower fit point. Exactly, there is the way of using alternative function to estimate systematics, but it is hard to check if fit is successful or not, because we have many regions. Therefore current method is the simplest and can be easily treated.

An alternative function, di-jet mass function ($p_0 \times (1 - \frac{x}{\sqrt{s}})^{p_1} \times (\frac{x}{\sqrt{s}})^{p_2}$), is also tried, and it is observed that the extrapolated shapes are consistent with the nominal function (exponential) within the statistical uncertainty.

8. Systematic Uncertainties

We describe the details of all systematic uncertainties considered in this analysis. In the Loose, Medium, and Tight region, all systematic uncertainties of $t\bar{t}$ and multi-jet background are estimated from merged distributions (Loose+Medium+Tight). Systematic uncertainties are consistent between each τ_{32}^{WTA}-likelihood category, therefore only systematic plots in the Tight region are shown here.

Systematic uncertainties for the SM $t\bar{t}$ are estimated by fitting the difference between the systematic sample and nominal sample with a linear function in order to reduce the statistical jumps due to the limited sample statistics, and the systematic uncertainty for the shape correction for the multi-jet background is also estimated by the same way. We checked alternative method, using original ratio distributions with merged bins instead of using the linear fit, and found reasonable results and it does not change the final results as can be found Appendix A

8.1. Systematic uncertainty on integrated luminosity

The combined luminosity error for 2015 and 2016 is 2.1%, assuming fully uncorrelated uncertainties in 2015 and 2016. It is applied as a constant shift to signal and SM $t\bar{t}$ backgrounds.

8.2. Systematic uncertainty on b-tagging of the track-jets

The prescription for implementing the b-tagging uncertainty recommended by the performance group has been followed. The eigenvector breakdown approach has been tested to avoid over-profiling. There are 4 (4 and 11) eigenvectors for the b-flavor (c- and light-flavor) quarks, and 2 eigenvectors specifically for the extrapolation of the scale factor in high p_{T} regimes, which are correlated across the flavors.

Nominal $m_{t\bar{t}}$ distribution and systematic varied distributions are shown in Fig. 53 for the SM $t\bar{t}$ background, Fig. 54 for Z'. Bottom distributions are the differences between nominal and systematic varied distributions in those plots.

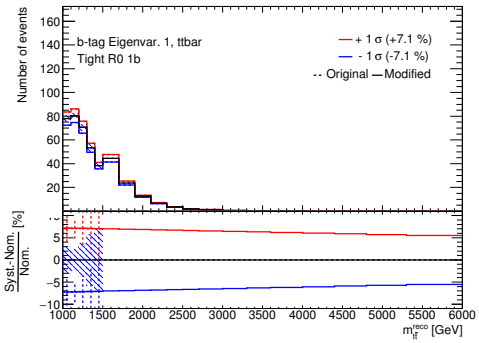

(a) 1 tight b-tag Tight R0

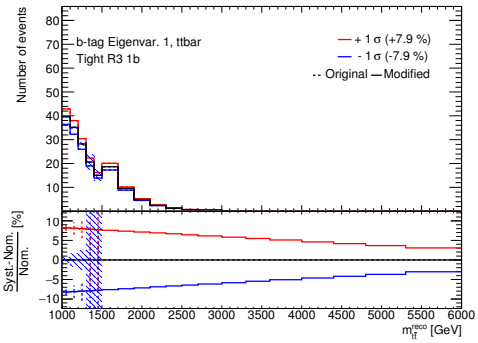

(b) 1 tight b-tag Tight R3

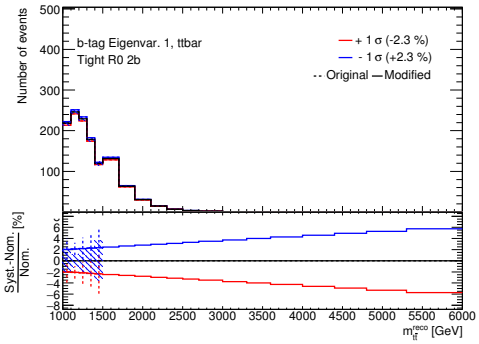

(c) 2 tight b-tag Tight R0

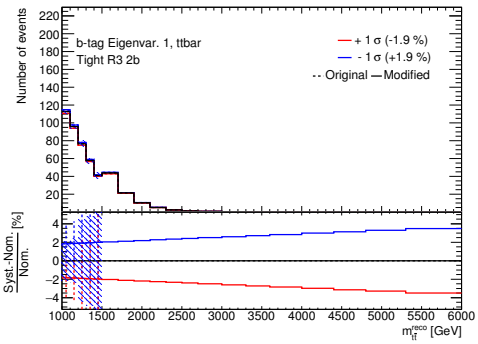

(d) 2 tight b-tag Tight R3

Figure 53: Systematics of b-tagging EV1 of the b-flavor for the SM $t\bar{t}$ background

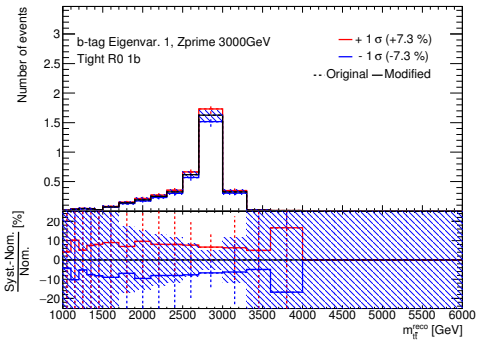

(a) 1 tight b-tag Tight R0

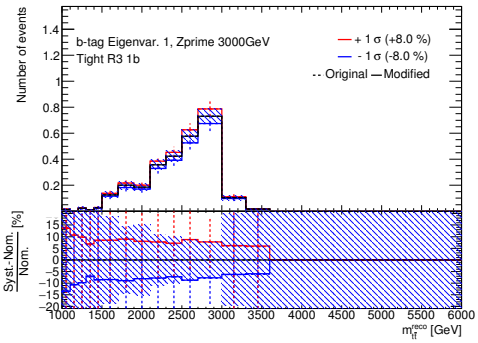

(b) 1 tight b-tag Tight R3

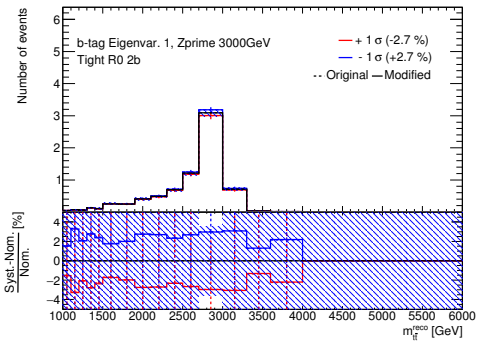

(c) 2 tight b-tag Tight R0

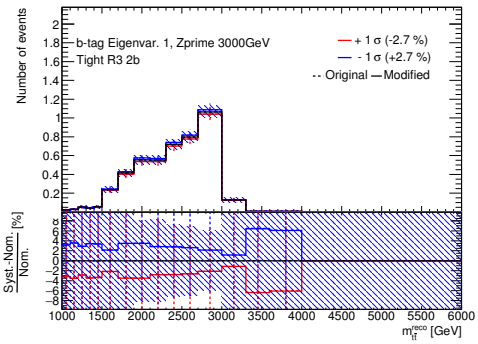

(d) 2 tight b-tag Tight R3

Figure 54: Systematics of b-tagging EV1 of the b-flavor for Z' 3 TeV

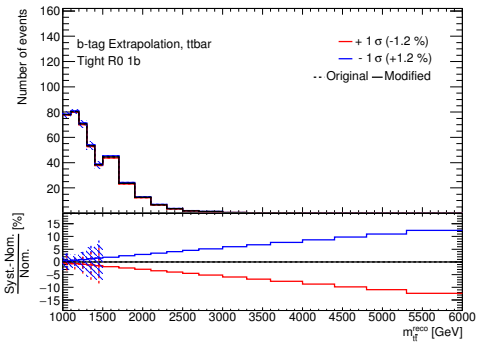

(a) 1 tight b-tag Tight R0

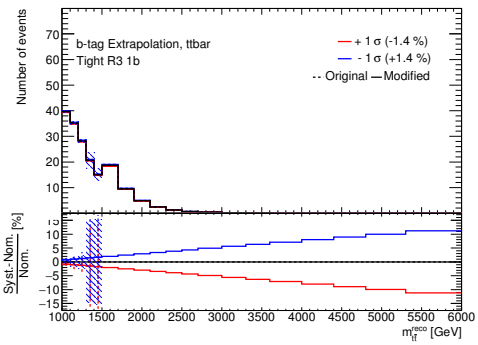

(b) 1 tight b-tag Tight R3

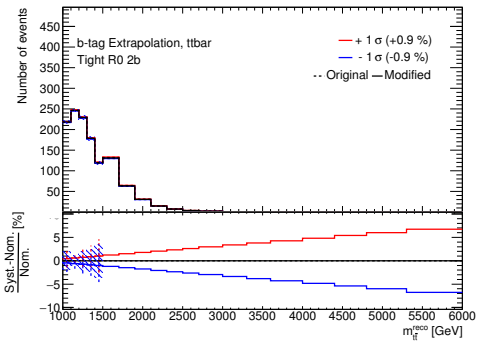

(c) 2 tight b-tag Tight R0

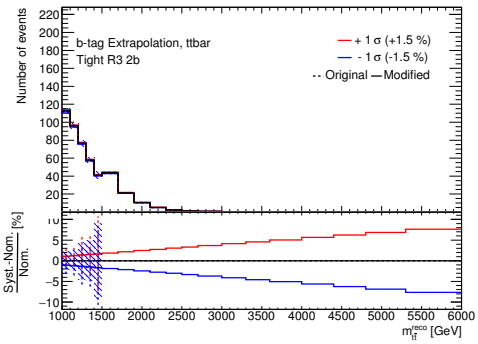

(d) 2 tight b-tag Tight R3

Figure 55: Systematics of b-tagging extrapolation from RUN2 for the SM $t\bar{t}$ background

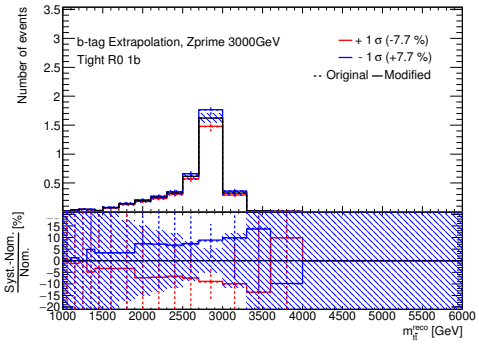

(a) 1 tight b-tag Tight R0

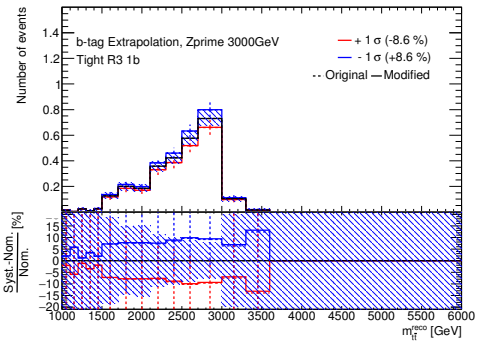

(b) 1 tight b-tag Tight R3

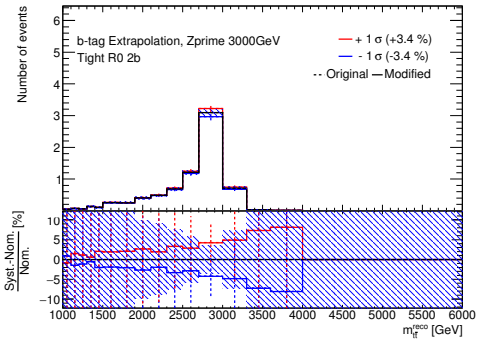

(c) 2 tight b-tag Tight R0

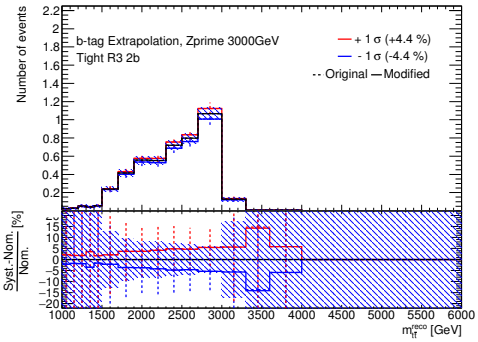

(d) 2 tight b-tag Tight R3

Figure 56: Systematics of b-tagging extrapolation from RUN2 for Z' 3 TeV

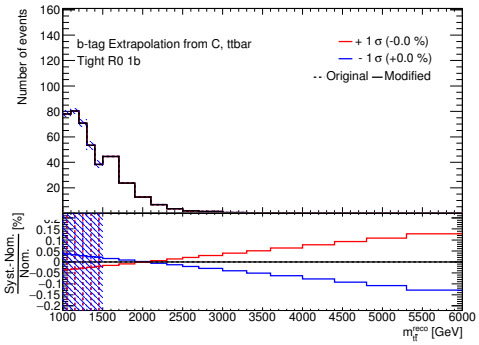

(a) 1 tight b-tag Tight R0

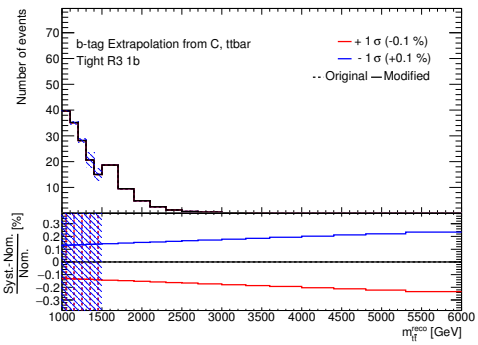

(b) 1 tight b-tag Tight R3

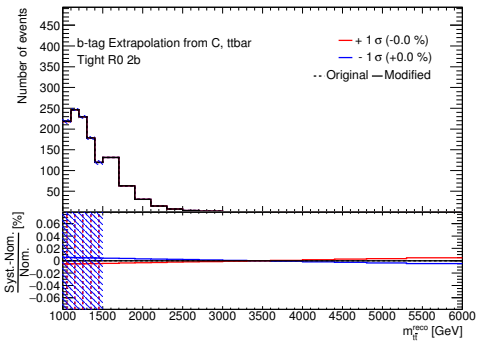

(c) 2 tight b-tag Tight R0

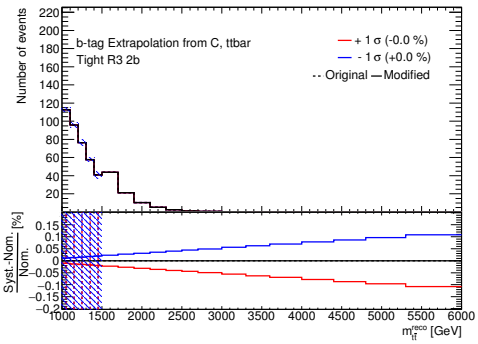

(d) 2 tight b-tag Tight R3

Figure 57: Systematics of b-tagging extrapolation from c-flavor for the SM $t\bar{t}$ background

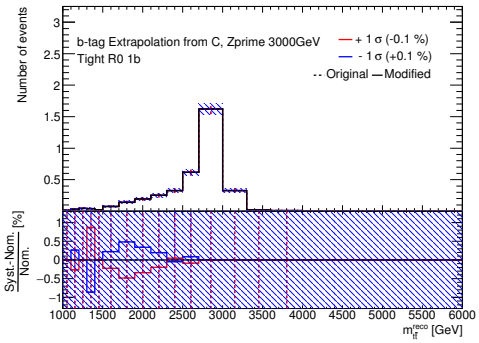

(a) 1 tight b-tag Tight R0

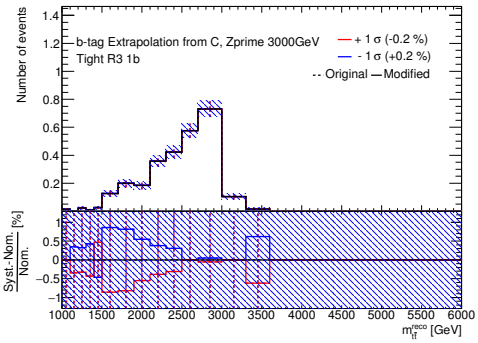

(b) 1 tight b-tag Tight R3

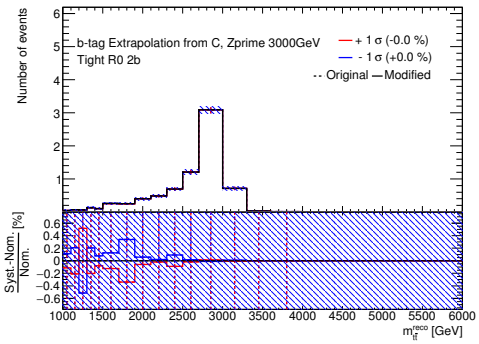

(c) 2 tight b-tag Tight R0

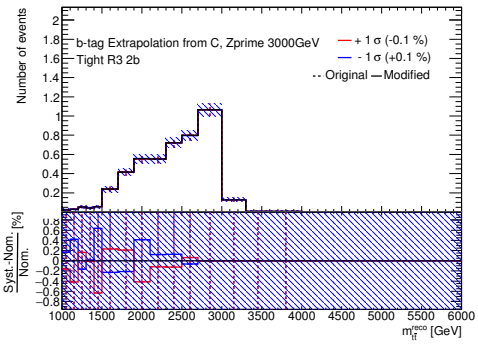

(d) 2 tight b-tag Tight R3

Figure 58: Systematics of b-tagging extrapolation from c-flavor for Z' 3 TeV

8.3. Systematic uncertainty on large-R jet

The scale uncertainties on the large-R jets (which is propagated to the top-tagging performance) are estimated using the r_{trk} method. The method assumes that the tracking device-related uncertainties are uncorrelated with the calorimeter cluster-related uncertainties. The procedure works by estimating the ratio r_{trk} between an observable (which can be the transverse momentum, mass or a substructure quantity) calorimeter-jet and a track-jet, which have been matched to be in the same detector region. Such ratio is estimated in both data and in simulation and the deviation of the average double ratio $< R_{trk} >= \frac{<r_{trk}^{\text{data}}>}{<r_{trk}^{\text{MC}}>}$ from 1 is used as a figure of merit to quantify the uncertainty. In addition, a track measurement uncertainty is estimated and added in quadrature.

The large-R jet uncertainty is broken down into 4 components: "baseline", which refers to the difference between data and the Pythia 8 simulation; "modelling", which refers to the difference between data and the Herwig simulation; "tracking", which refers to the uncertainty on the tracks used as a reference; and the statistical uncertainty. Different configurations of uncertainties are available, depending on whether one assumes the p_T, mass and τ_{32}^{wta} observables to be correlated or not. This analysis uses the "strong" configuration, on which all observables are assumed to be correlated, since the signal region is rather pure in the $t\bar{t}$ background.

Nominal $m_{t\bar{t}}$ distribution and systematic varied distributions for large-R jet baseline uncertainty are shown in Fig. 59 for the SM $t\bar{t}$ background, Fig. 60 for Z'. Bottom distributions are the differences between nominal and systematic varied distributions in those plots.

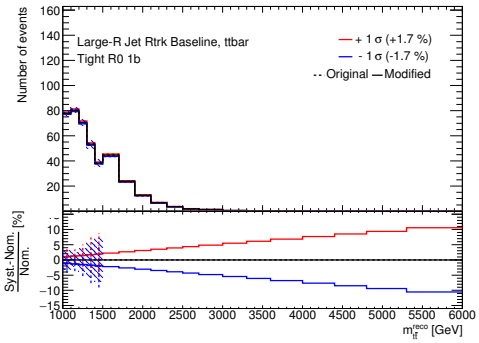

(a) 1 tight b-tag Tight R0

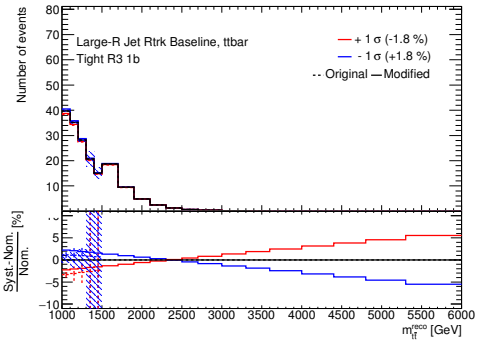

(b) 1 tight b-tag Tight R3

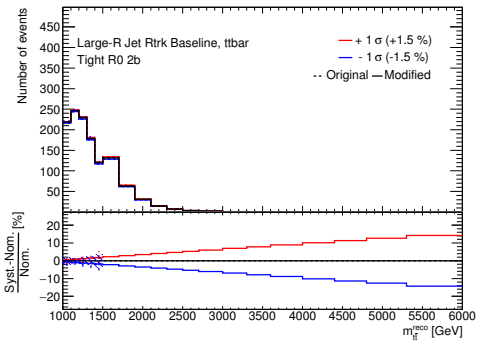

(c) 2 tight b-tag Tight R0

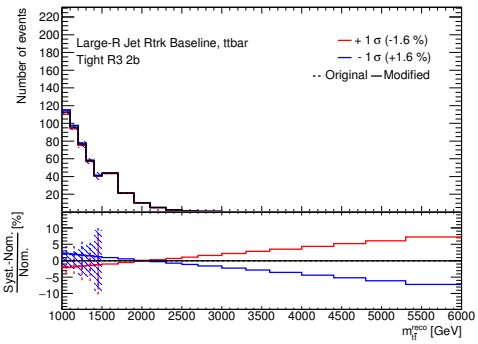

(d) 2 tight b-tag Tight R3

Figure 59: Systematics of “baseline” for the SM $t\bar{t}$ background

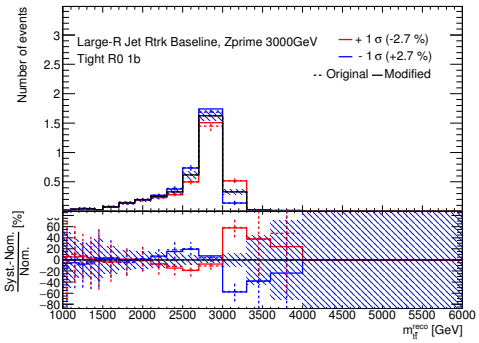

(a) 1 tight b-tag Tight R0

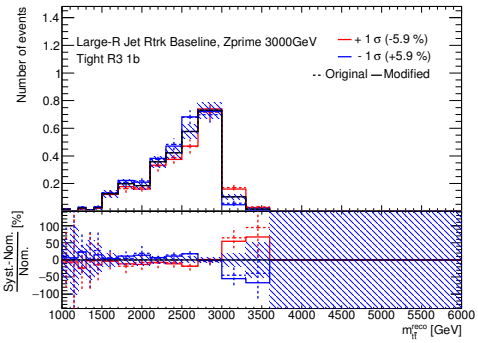

(b) 1 tight b-tag Tight R3

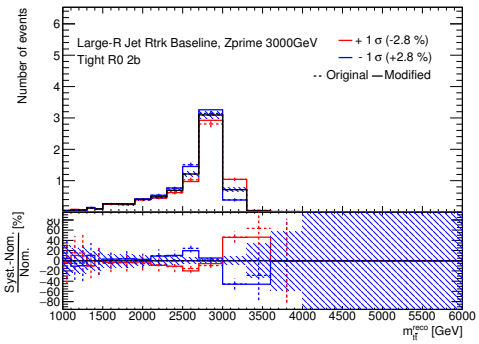

(c) 2 tight b-tag Tight R0

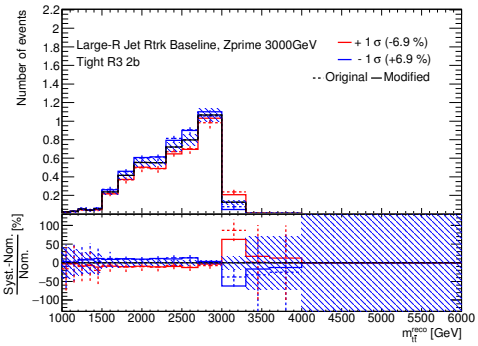

(d) 2 tight b-tag Tight R3

Figure 60: Systematics of “baseline” for Z' 3 TeV

Nominal $m_{t\bar{t}}$ distribution and systematic varied distributions for large-R jet model uncertainty are shown in Fig. 61 for the SM $t\bar{t}$ background, Fig. 62 for Z'. Bottom distributions are the differences between nominal and systematic varied distributions in those plots.

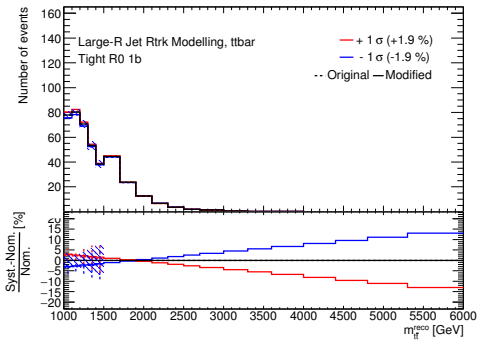

(a) 1 tight b-tag Tight R0

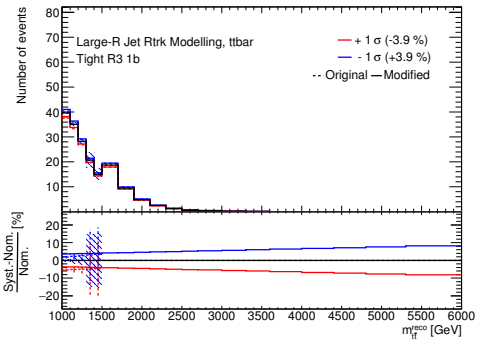

(b) 1 tight b-tag Tight R3

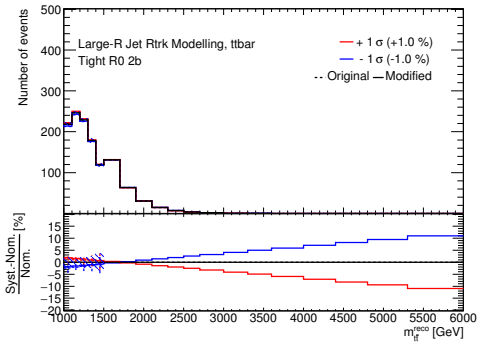

(c) 2 tight b-tag Tight R0

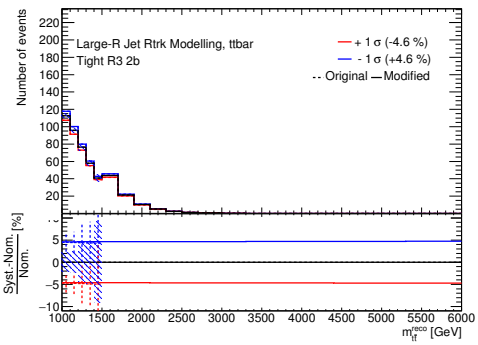

(d) 2 tight b-tag Tight R3

Figure 61: Systematics of "modelling" for the SM $t\bar{t}$ background

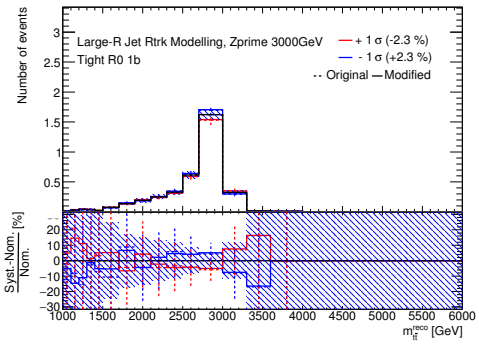

(a) 1 tight b-tag Tight R0

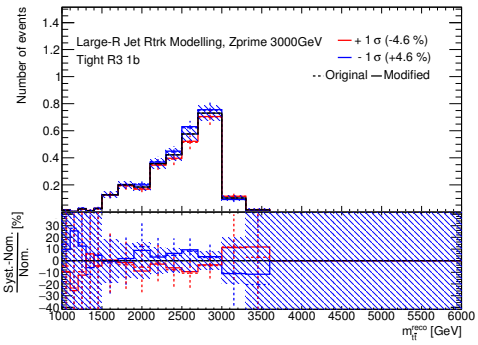

(b) 1 tight b-tag Tight R3

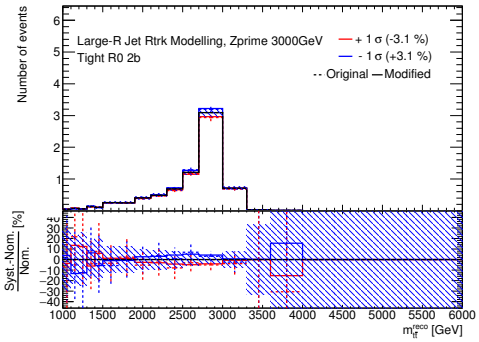

(c) 2 tight b-tag Tight R0

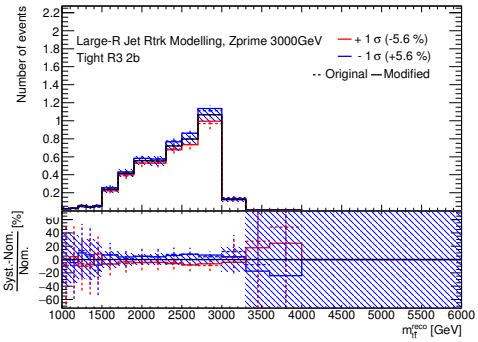

(d) 2 tight b-tag Tight R3

Figure 62: Systematics of "modelling" for Z' 3 TeV

Nominal $m_{t\bar{t}}$ distribution and systematic varied distributions for large-R jet track uncertainty are shown in Fig. 63 for the SM $t\bar{t}$ background, Fig. 64 for Z'. Bottom distributions are the differences between nominal and systematic varied distributions in those plots.

Nominal $m_{t\bar{t}}$ distribution and systematic varied distributions for large-R jet statistics uncertainty are shown in Fig. 65 for the SM $t\bar{t}$ background, Fig. 66 for Z'. Bottom distributions are the differences between nominal and systematic varied distributions in those plots.

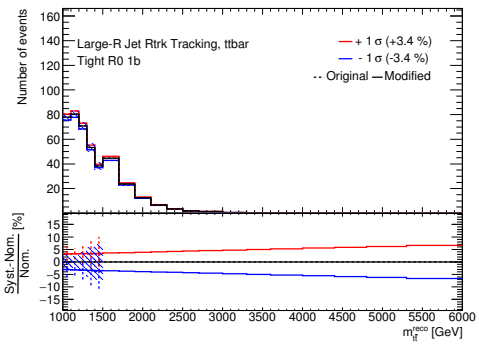

(a) 1 tight b-tag Tight R0

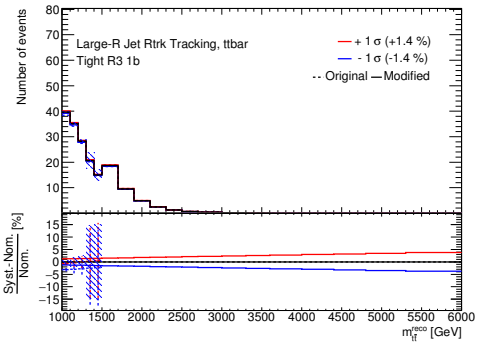

(b) 1 tight b-tag Tight R3

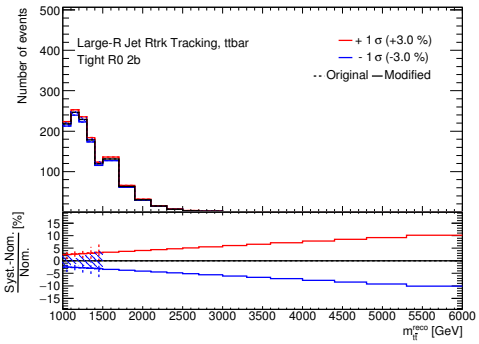

(c) 2 tight b-tag Tight R0

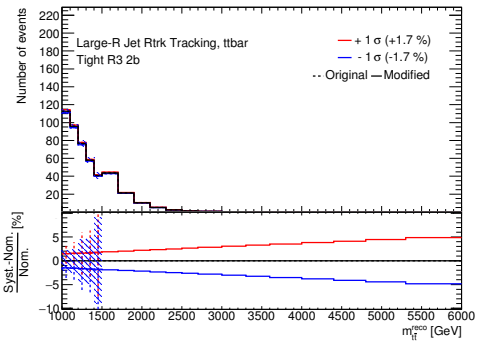

(d) 2 tight b-tag Tight R3

Figure 63: Systematics of “tracking” for the SM $t\bar{t}$ background

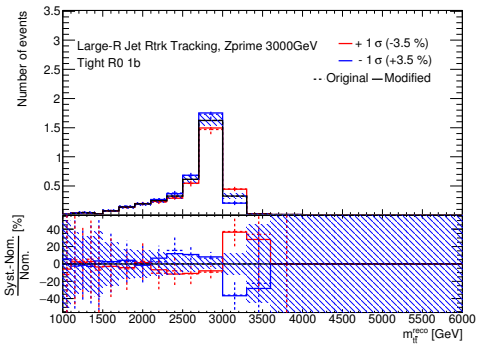

(a) 1 tight b-tag Tight R0

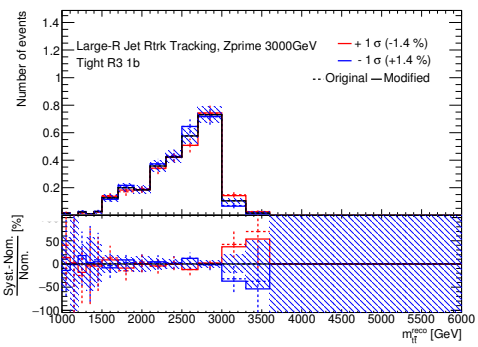

(b) 1 tight b-tag Tight R3

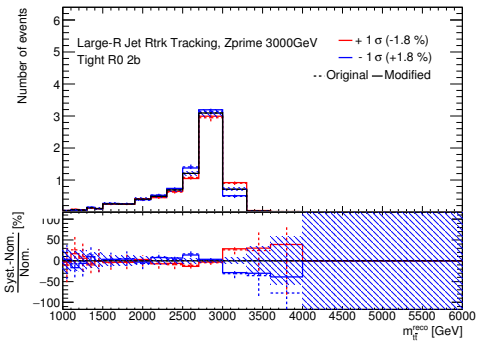

(c) 2 tight b-tag Tight R0

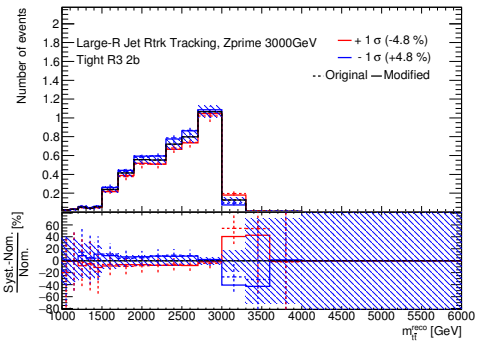

(d) 2 tight b-tag Tight R3

Figure 64: Systematics of “tracking” for Z' 3 TeV

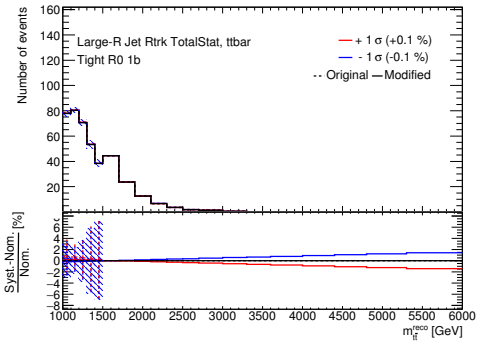

(a) 1 tight b-tag Tight R0

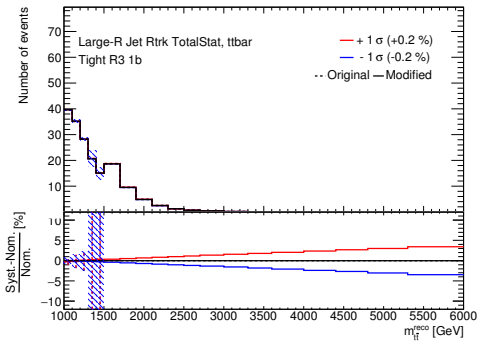

(b) 1 tight b-tag Tight R3

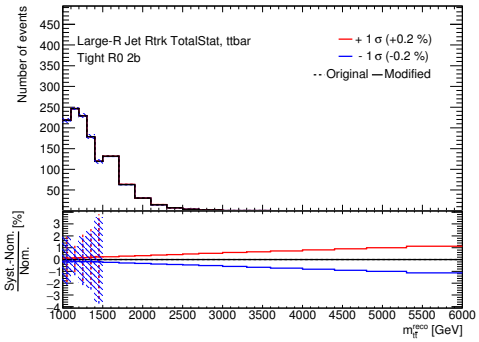

(c) 2 tight b-tag Tight R0

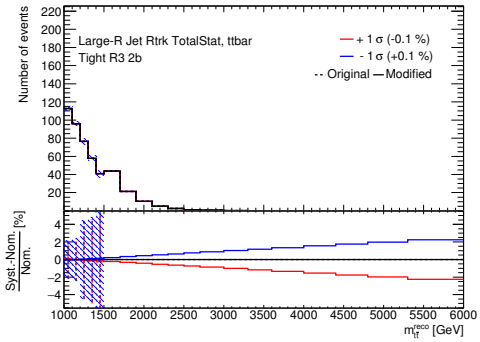

(d) 2 tight b-tag Tight R3

Figure 65: Systematics of "Statistical" for the SM $t\bar{t}$ background

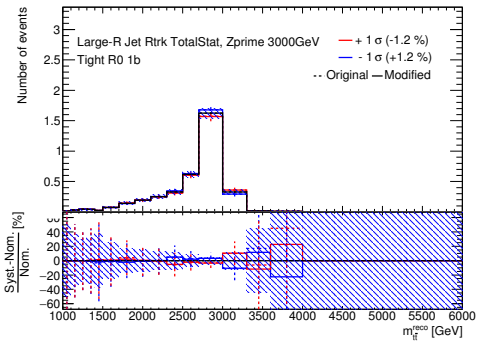

(a) 1 tight b-tag Tight R0

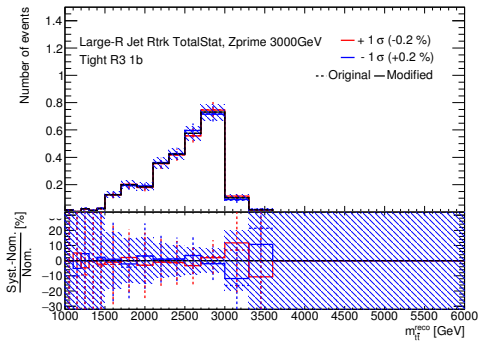

(b) 1 tight b-tag Tight R3

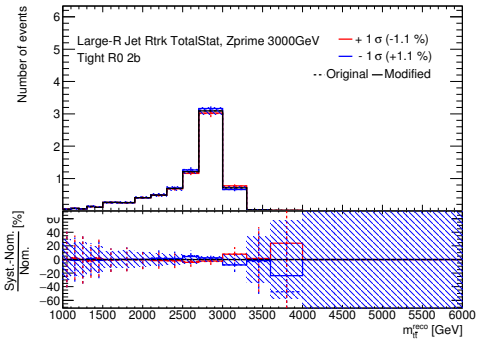

(c) 2 tight b-tag Tight R0

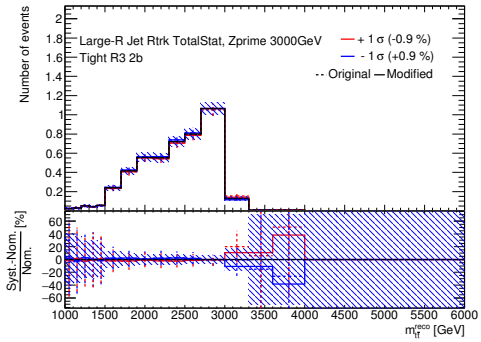

(d) 2 tight b-tag Tight R3

Figure 66: Systematics of "Statistical" for Z' 3 TeV

In addition, some differences for resolution of large-R jet can be seen between data and MC. The differences are estimated for large-R jet p_T (2%), mass (20%) and τ_{32}^{wta} (15%).

The value for large-R jet p_T is absolute value. The values for large-R jet mass and τ_{32}^{wta} are relative value to each resolution simulated by MC, $\sigma_{nominal}$. If σ_{NEW} is defined as a resolution after smearing by a Gaussian with recommended value, σ_{NEW} is related to $\sigma_{nominal}$ as a Eq. (41).

$$\sigma_{\text{NEW}}^2 = \sigma_{\text{nominal}}^2 + (x \cdot \sigma_{\text{nominal}})^2 \tag{41}$$

$x \cdot \sigma_{nominal}$ is used to smearing for mass and τ_{32}^{wta}. For example, σ_{NEW} is equal to $1.2\sigma_{nominal}$ for mass, therefore x can be calculated. Each uncertainty is estimated by smearing p_T by a Gaussian with a width of 2%, smearing mass by a Gaussian with a width of $0.66\sigma_{nominal}$ and smearing τ_{32}^{wta} by a Gaussian a width of $0.57\sigma_{nominal}$, respectively. Each $\sigma_{nominal}$ is estimated by inter quantile range (IQR) as Fig. 67. p_T dependency is small, and η dependency also small in Fig. 68.

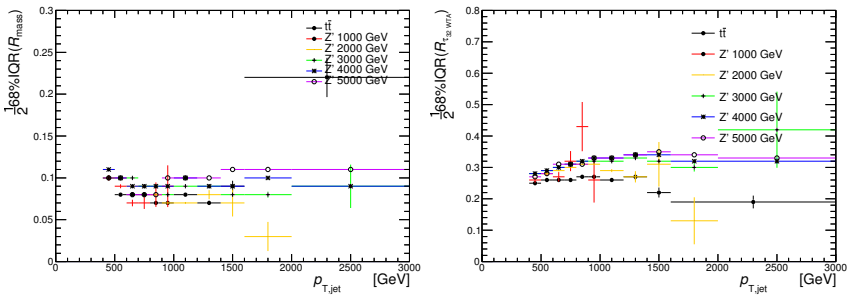

(a) Large-R jet mass response

(b) Large-R jet τ_{32}^{wta} response

Figure 67: Response of large-R jet kinematics

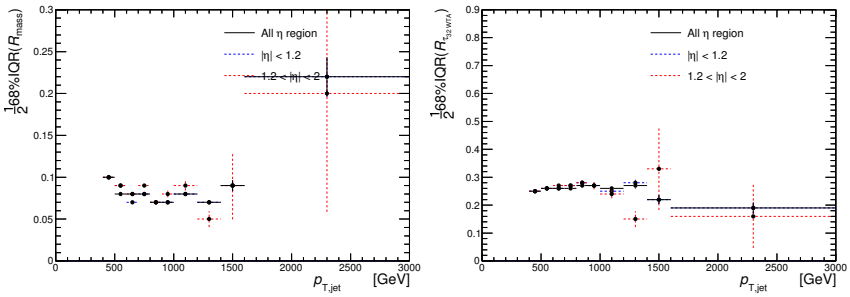

(a) Large-R jet mass response for the SM $t\bar{t}$ background

(b) Large-R jet τ_{32}^{wta} response for the SM $t\bar{t}$ background

Figure 68: Check η dependency for response of large-R jet kinematics

Each smeared distribution is showed in Fig. 69.

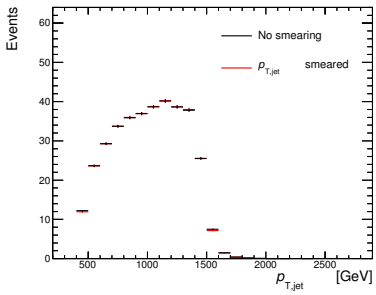

(a) Large-R jet p_T

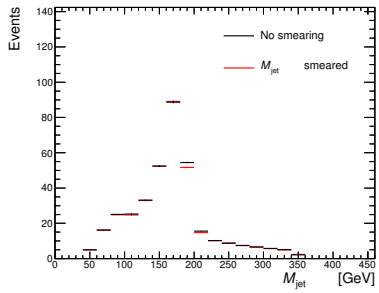

(b) Large-R jet mass

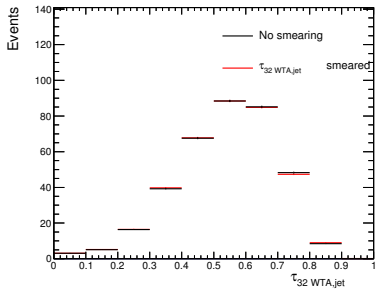

(c) Large-R jet τ_{32}^{wta}

Figure 69: Smeared distribution for Z' 3 TeV

Each systematic uncertainty is estimated by using same event selection with smeared value. The results are showed in $m_{t\bar{t}}$ distribution(Figure 70, 71 and 72 and Figure 73, 74 and 75).

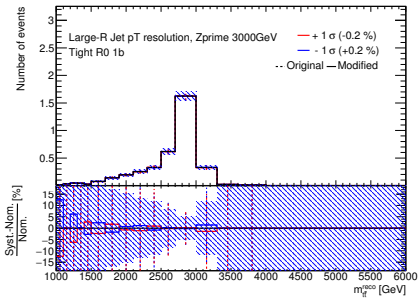

(a) 1 tight b-tag Tight R0

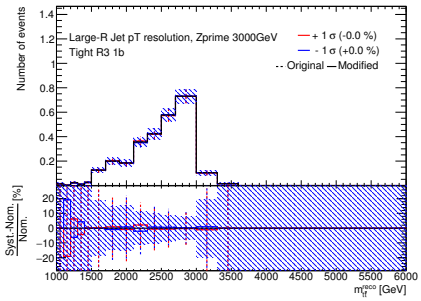

(b) 1 tight b-tag Tight R3

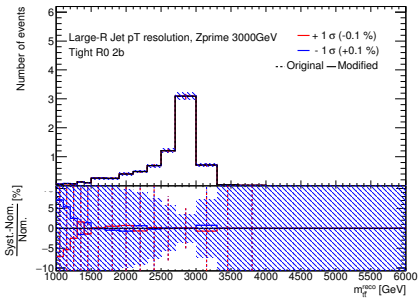

(c) 2 tight b-tag Tight R0

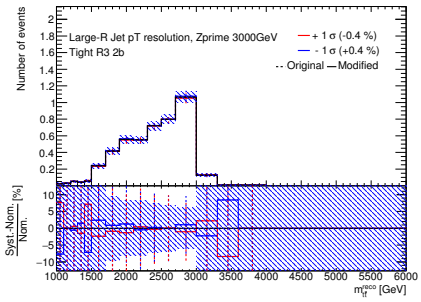

(d) 2 tight b-tag Tight R3

Figure 70: Systematic uncertainty associated with large-R jet p_T resolution distribution for Z' 3 TeV

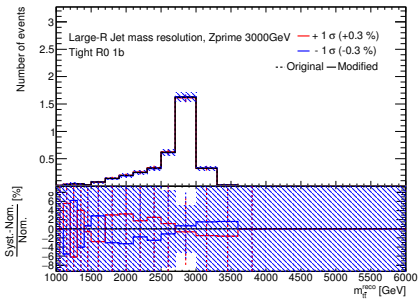

(a) 1 tight b-tag Tight R0

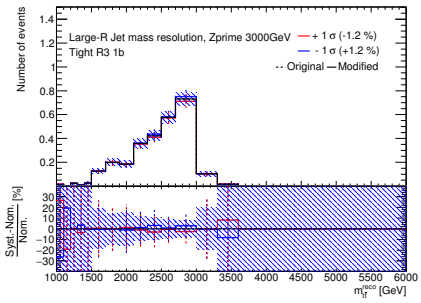

(b) 1 tight b-tag Tight R3

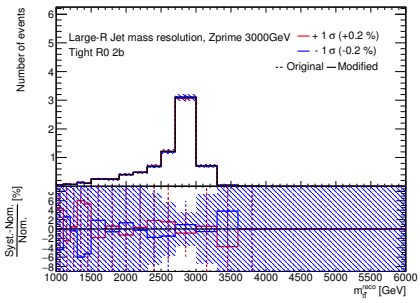

(c) 2 tight b-tag Tight R0

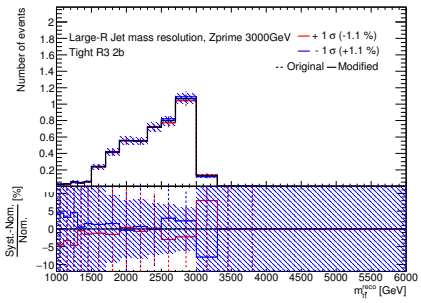

(d) 2 tight b-tag Tight R3

Figure 71: Systematic uncertainty associated with large-R jet mass resolution distribution for Z' 3 TeV

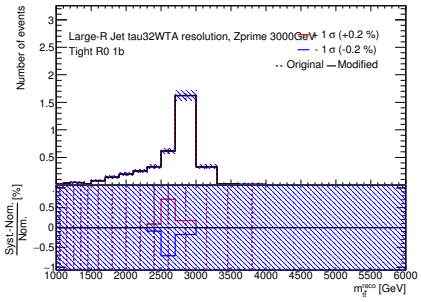

(a) 1 tight b-tag Tight R0

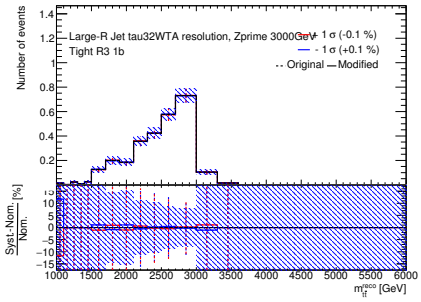

(b) 1 tight b-tag Tight R3

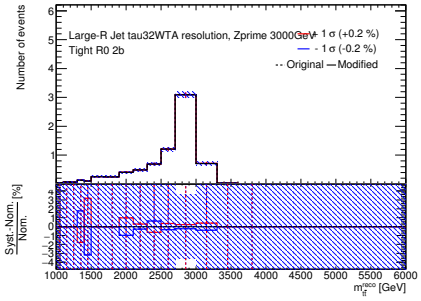

(c) 2 tight b-tag Tight R0

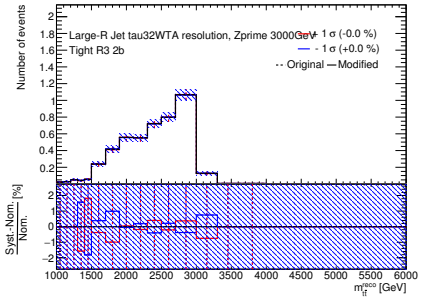

(d) 2 tight b-tag Tight R3

Figure 72: Systematic uncertainty associated with large-R jet τ_{32}^{wta} resolution distribution for Z' 3 TeV

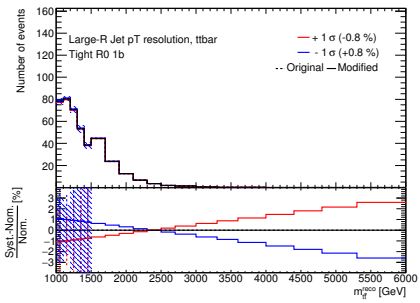

(a) 1 tight b-tag Tight R0

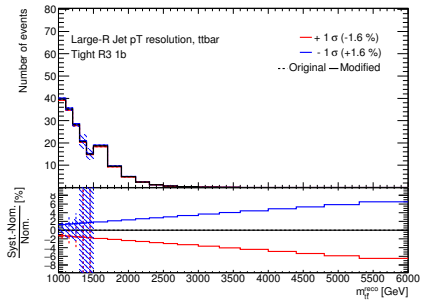

(b) 1 tight b-tag Tight R3

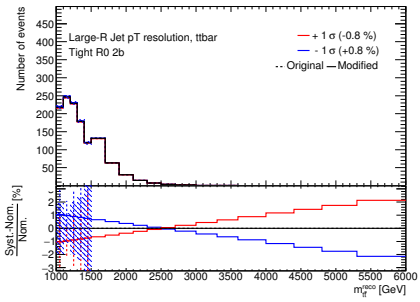

(c) 2 tight b-tag Tight R0

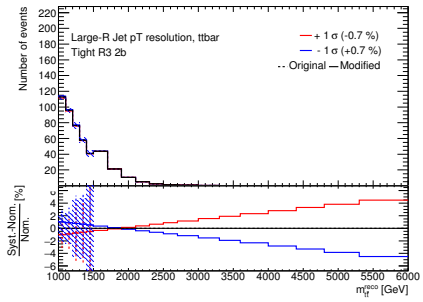

(d) 2 tight b-tag Tight R3

Figure 73: Systematic uncertainty associated with large-R jet p_T resolution distribution for Z' 3 TeV

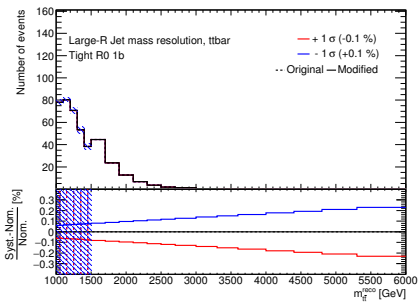

(a) 1 tight b-tag Tight R0

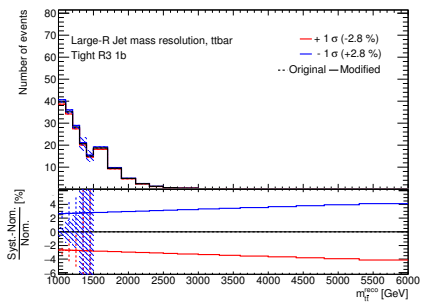

(b) 1 tight b-tag Tight R3

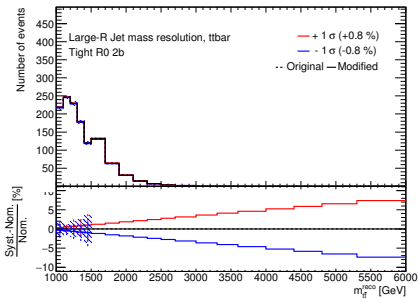

(c) 2 tight b-tag Tight R0

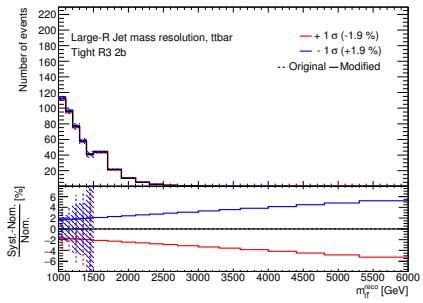

(d) 2 tight b-tag Tight R3

Figure 74: Systematic uncertainty associated with large-R jet mass resolution distribution for Z' 3 TeV

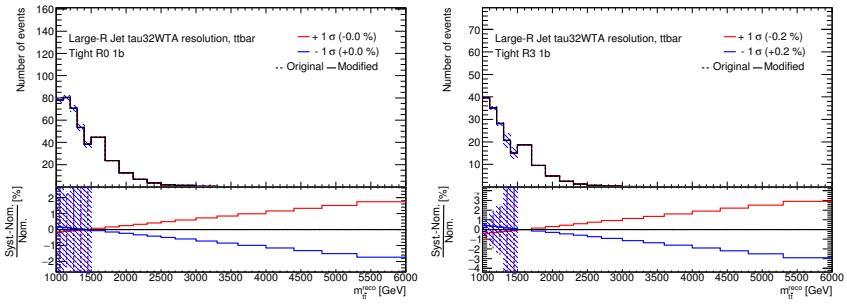

(a) 1 tight b-tag Tight R0

(b) 1 tight b-tag Tight R3

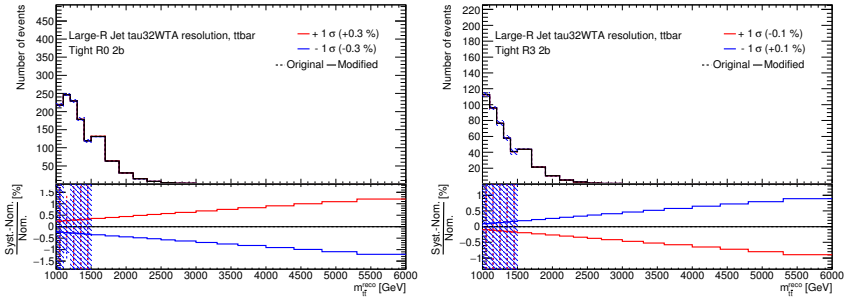

(c) 2 tight b-tag Tight R0

(d) 2 tight b-tag Tight R3

Figure 75: Systematic uncertainty associated with large-R jet τ_{32}^{wta} resolution distribution for Z' 3 TeV

8.4. Systematic uncertainty on $t\bar{t}$ modeling

The $t\bar{t}$ production cross section in pp collisions at $\sqrt{s} = 13$ TeV is $\sigma_{t\bar{t}} = 832^{+46}_{-52}$ pb for a top-quark mass of 172.5 GeV. It has been calculated at next-to-next-to leading order (NNLO) in QCD including resummation of next-to-next-to-leading logarithmic soft gluon terms with Top++2.0 [66–72].

The top-quark kinematics in $t\bar{t}$ events are corrected to account for electroweak higher-order effects [93]. This correction is applied to the generated events applyied as a function of the flavor and center-of-mass energy of the initial partons and on the decay angle of the top quarks in the center-of-mass frame of the initial partons. The value of the correction factor decreases with increasing $m_{t\bar{t}}$ from 0.98 at $m_{t\bar{t}} = 0.4$ TeV to 0.87 at $m_{t\bar{t}} = 3.5$ TeV. The impact of electroweak correction is estimated in Fig. 76.

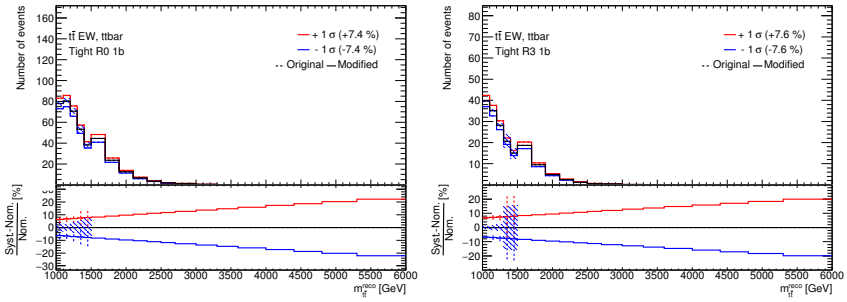

(a) 1 tight b-tag Tight R0

(b) 1 tight b-tag Tight R3

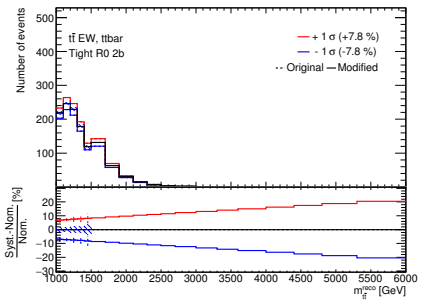

(c) 2 tight b-tag Tight R0

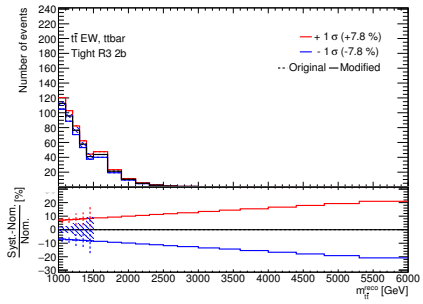

(d) 2 tight b-tag Tight R3

Figure 76: Impact of electroweak correction, i.e. $m_{t\bar{t}}$ before and after application of the EW weights.

The modeling uncertainties also come from what generator, parton shower model and other parameters are chosen. Powheg + Pythia 6 is used as nominal sample for the SM $t\bar{t}$ background. The modeling uncertainties associated generator difference is estimated by comparing Powheg + Herwig ++ with aMC@NLO + Herwig ++ (See Fig. 77). The modeling uncertainties associated parton shower model difference is estimated by comparing Powheg + Pythia 6 with Powheg + Herwig ++ (See Fig. 78). Above two uncertainties are estimated with Eq. (42) and Eq. (43).

$$\Delta_{\text{generator}}\ (\%) = \frac{n_{\text{aMC@NLO + Herwig ++}} - n_{\text{Powheg + Herwig ++}}}{n_{\text{Powheg + Herwig ++}}} \times 100 \tag{42}$$

$$\Delta_{\text{parton shower}}\ (\%) = \frac{n_{\text{Powheg + Herwig ++}} - n_{\text{Powheg + Pythia 6}}}{n_{\text{Powheg + Pythia 6}}} \times 100 \tag{43}$$

The modeling uncertainties associated ISR/FSR effect is estimated by comparing higher ISR/FSR conditions with lower ISR/FSR conditions in Powheg + Pythia (See Fig. 79). This uncertainty is estimated with Eq. (44).

$$\Delta_{\text{ISRFSR}}\ (\%) = \frac{n_{\text{Powheg + Pythia 6 high}} - n_{\text{Powheg + Pythia 6 low}}}{2 \times n_{\text{Powheg + Pythia 6 low}}} \times 100 \tag{44}$$

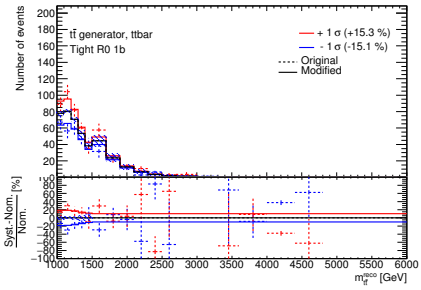

(a) 1 tight b-tag Tight R0

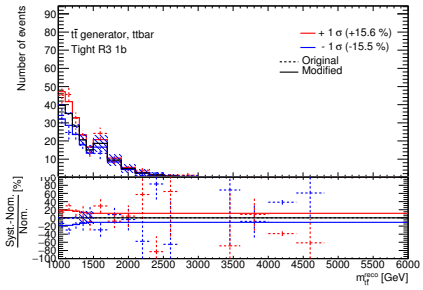

(b) 1 tight b-tag Tight R3

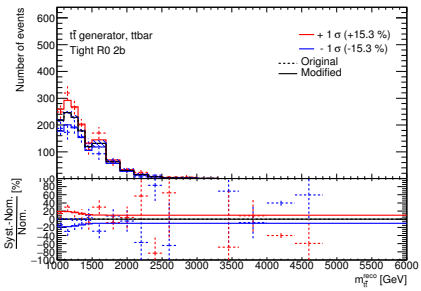

(c) 2 tight b-tag Tight R0

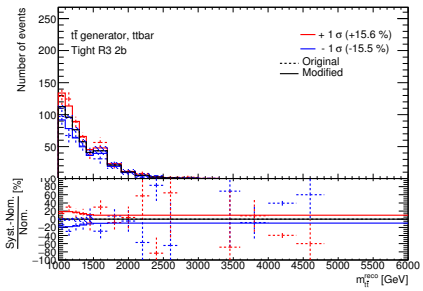

(d) 2 tight b-tag Tight R3

Figure 77: Systematics of different $t\bar{t}$ Monte Carlo generators.

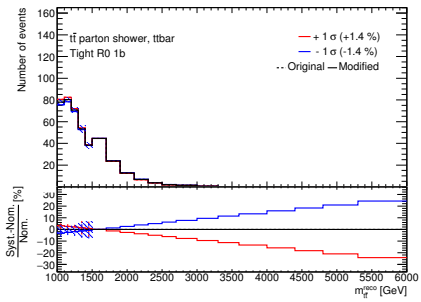

(a) 1 tight b-tag Tight R0

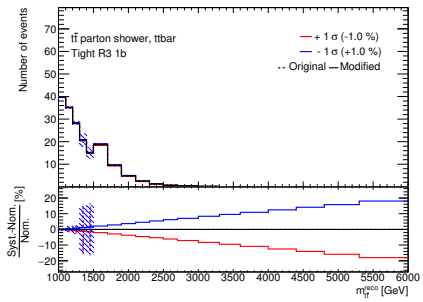

(b) 1 tight b-tag Tight R3

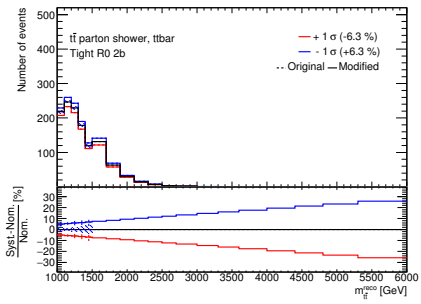

(c) 2 tight b-tag Tight R0

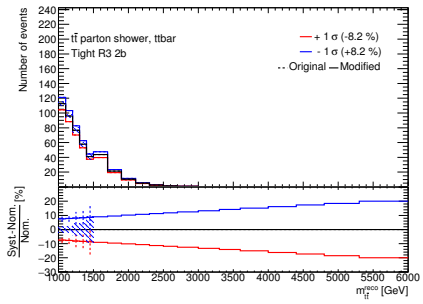

(d) 2 tight b-tag Tight R3

Figure 78: Systematics of different $t\bar{t}$ Monte Carlo parton showers models.

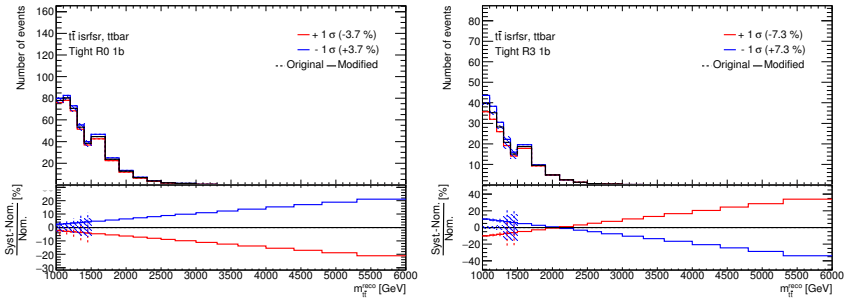

(a) 1 tight b-tag Tight R0

(b) 1 tight b-tag Tight R3

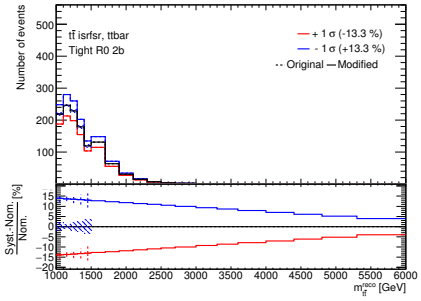

(c) 2 tight b-tag Tight R0

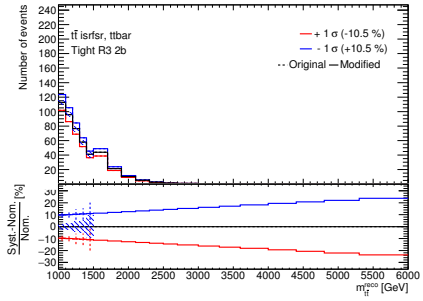

(d) 2 tight b-tag Tight R3

Figure 79: Systematics of different $t\bar{t}$ Monte Carlo ISR/FSR models

8.5. Systematic uncertainty on PDF

30 eigensets of the `PDF4LHC_nlo_30` are used and the relative effect is taken as a systematic uncertainty in the Powheg +Pythia 6 sample for the SM $t\bar{t}$ background. Parts of the nominal $m_{t\bar{t}}$ distribution and systematic varied distribution for PDF uncertainty are shown in Fig. 80 for PDF CT10 v.s. PDF4LHC15, Fig. 81 for PDF eigenvalue 1. Bottom distributions are the differences between nominal and systematic varied distribution in those plots. This PDF CT10 v.s. PDF4LHC15 uncertainty does not depend on b-tag condition, therefore 1b and 2b distribtuions are merged to estimate this uncertainty in order to obtain statistics.

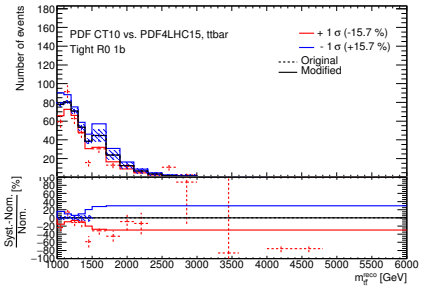

(a) 1 tight b-tag Tight R0

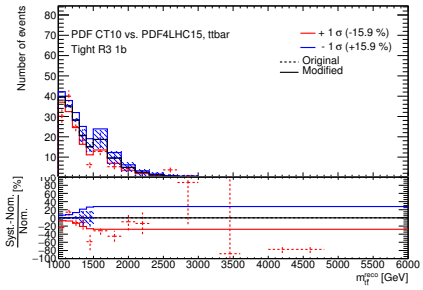

(b) 1 tight b-tag Tight R3

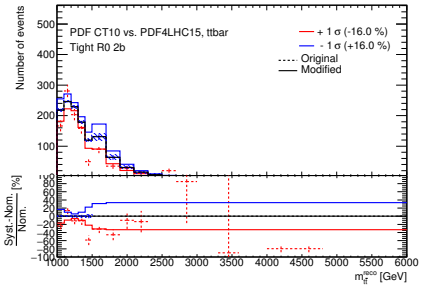

(c) 2 tight b-tag Tight R0

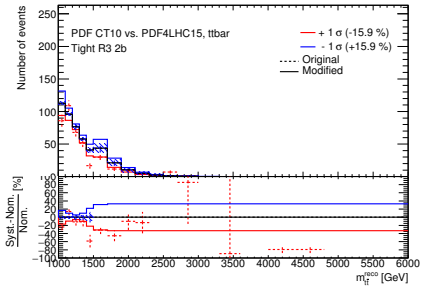

(d) 2 tight b-tag Tight R3

Figure 80: Systematics of PDF for the SM $t\bar{t}$ background

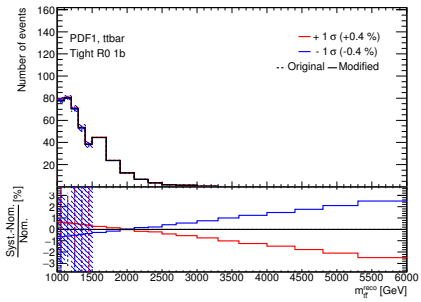

(a) 1 tight b-tag Tight R0

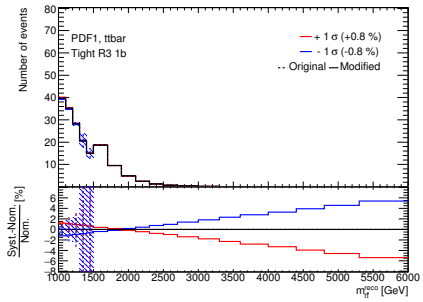

(b) 1 tight b-tag Tight R3

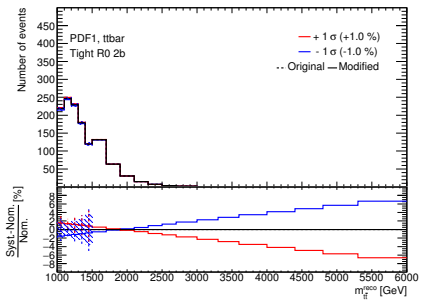

(c) 2 tight b-tag Tight R0

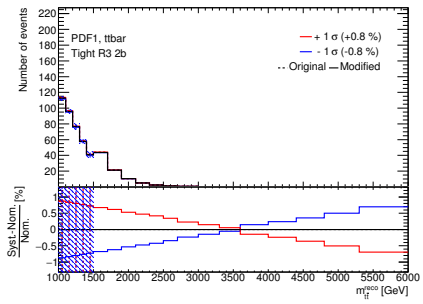

(d) 2 tight b-tag Tight R3

Figure 81: Systematics of PDF for the SM $t\bar{t}$ background

8.6. Systematic uncertainty on multi-jet backgrounds estimation

Two uncertainties are considered for the multi-jet background estimation, one is on the normalization, and the other is on the shape.

As mentioned in earlier (Sec. 7.2), the normalization factor n_{category} is estimated from a simple average of the four control regions (Eq. (40)). This normalization factor has slight difference in the four control regions. We take the maximum deviation $\Delta_{+,-}$ from the averaged value, and assign it as a systematic uncertainty. The deviation $\Delta_{+,-}$ is defined as in Eq. (45) and Eq. (46).

$$\Delta_{+} = \frac{n_{\text{maximum}} - n_{\text{category}}}{n_{\text{category}}} \tag{45}$$

$$\Delta_{-} = \frac{n_{\text{category}} - n_{\text{minimum}}}{n_{\text{category}}} \tag{46}$$

The systematic uncertainty on this QCD multi-jet background estimation is obtained from a possible residual difference after the correction, and the uncertainty on the fitting. The residual shape difference in $m_{t\bar{t}}$ is fitted by a linear function and the difference of the slope from unity is assigned as a shape systematic uncertainty, as shown in Fig. 82.

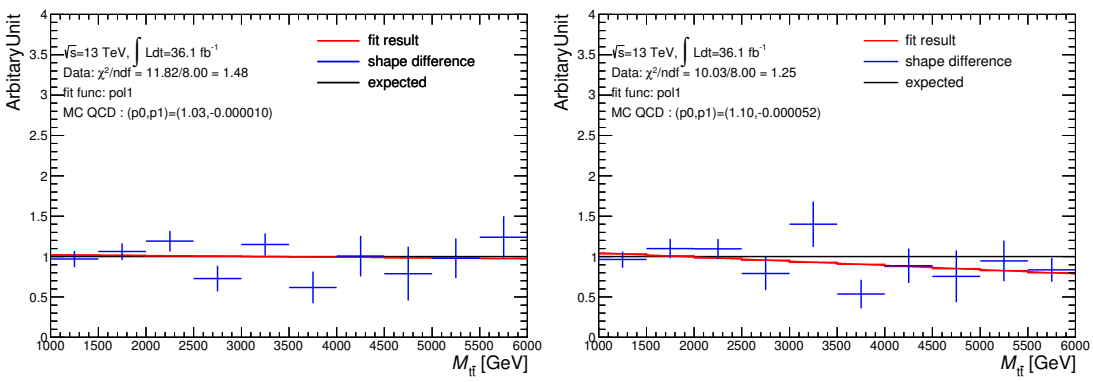

(a) One tight b-tag

(b) Two tight b-tag

Figure 82: Extraction of possible residual difference after the shape correction. Left is for one tight b-tagged events, and right is for two tight b-tagged events.

Systematic uncertainty from the fitting uncertainty is estimated by varying the fit parameter, $p0$ and $p1$, by one sigma while other parameters are floated. Figure 83 shows the variations of this systematics effect, which is used to assign corresponding systematic uncertainty. Variation of the parameter $p2$ is not considered as a systematic uncertainty because the effect is found to be negligible.

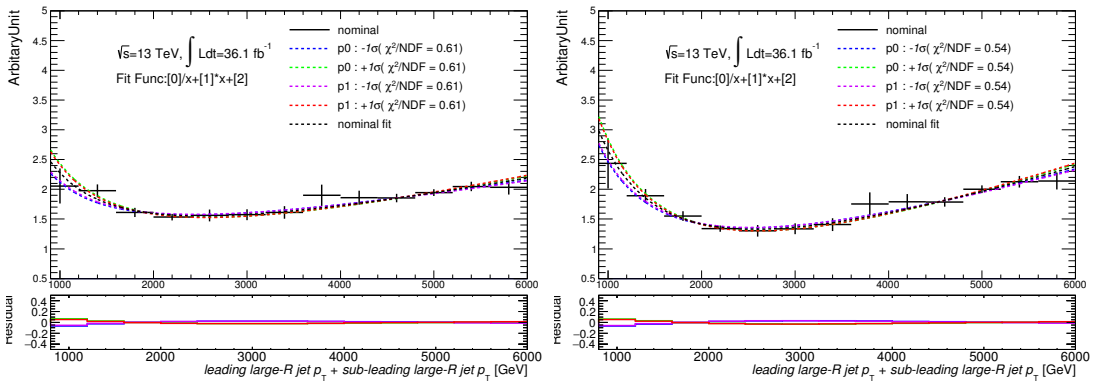

(a) One tight b-tag

(b) Two tight b-tag

Figure 83: Statistical variations of the correction function.

The shapes of the multi-jet background template for the Loose, Medium, and Tight are consistent within statistical uncertainties. However, we took difference between the merged distribution and each distribution as a systematic uncertainty conservatively. To do this we use events in the control regions (CR1,2,3,4) in order to estimate this systematics reasonably with enough statistics, because the statistics in the signal regions is very limited. Estimated systematic uncertainties are showed in Fig. 84. One can see larger systematic uncertainty at lower mass region, this is because the τ_{32}^{wta}-likelihood ratio has a dependence on jet p_T particularly at low p_T region. One tight b-tagged and two tight b-tagged multijet background distributions are estimated from a common template distribution, therefore the systematic uncertainty is treated as fully-correlated uncertainty for one tight b-tag and two tight b-tag.

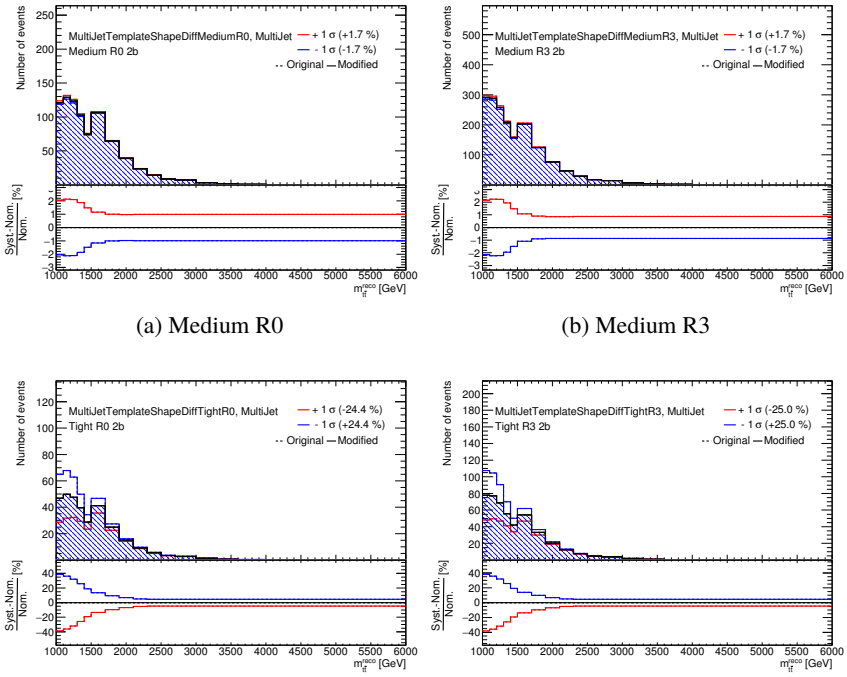

(a) Medium R0

(b) Medium R3

(c) Tight R0

(d) Tight R3

Figure 84: Multijet template shape difference between the merged category and each category.

In addition to them, the multijet background estimation at lower mass region ($m_{t\bar{t}}$< 1.5 TeV) is using histogram instead of the exponential extrapolation. Therefore, the uncertainty at low mass region is simply bin-by-bin statistical uncertainties from the original histogram. As the multijet template for the one tight b-tag and two tight b-tag regions is common (from zero tight b-tag), therefore we treat the bin-by-bin uncertainties 100% correlated between one tight b-tag and two tight b-tag regions.

8.7. Systematic uncertainty on extrapolation

Systematic uncertainty on this extrapolation method (See Sec. 7.3) includes statistical uncertainty of the fit, and stability of the fit range choice. Stability of the fit range choice is evaluated by taking the maximum deviation from the nominal slope parameter when changing the lower edge of the fit range, until the statistical fluctuation becomes large. The nominal fit range is from 1.2 TeVto 4 TeV, and another fit range to estimate systematic uncertainty of this is from 1.7 TeVto 4 TeV. The estimated systematic uncertainties are shown in Fig.85 for the multijet background, and in Fig. 86 for the SM $t\bar{t}$ background.

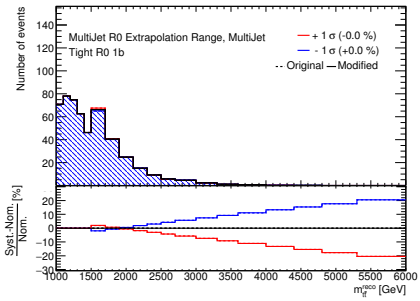

(a) 1 tight b-tag Tight R0

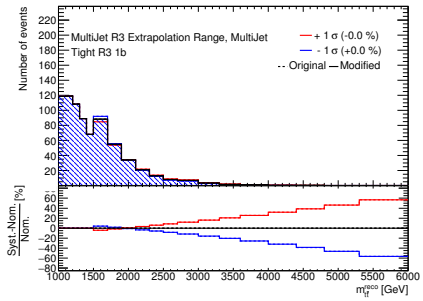

(b) 1 tight b-tag Tight R3

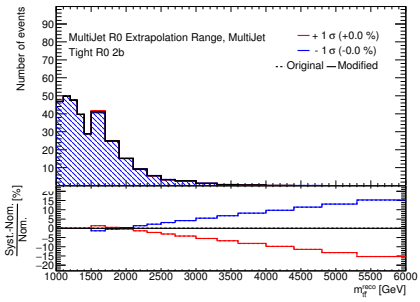

(c) 2 tight b-tag Tight R0

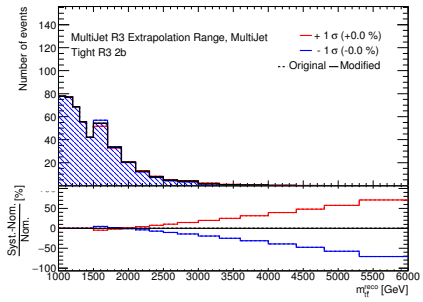

(d) 2 tight b-tag Tight R3

Figure 85: Systematic distributions of $m_{t\bar{t}}$ for fit range variation of extrapolation. Data Driven multijet.

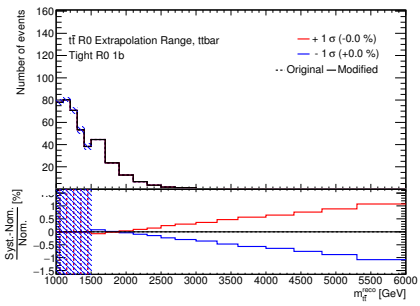

(a) 1 tight b-tag Tight R0

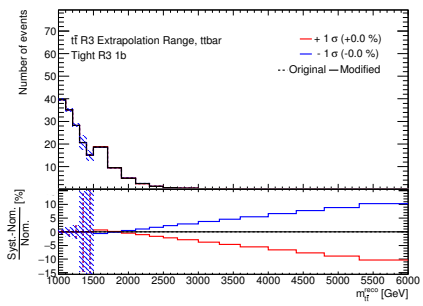

(b) 1 tight b-tag Tight R3

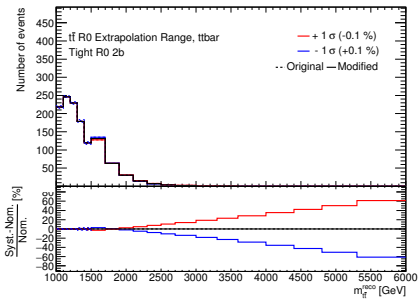

(c) 2 tight b-tag Tight R0

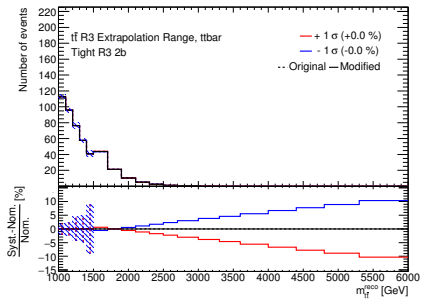

(d) 2 tight b-tag Tight R3

Figure 86: Systematic distributions of $m_{t\bar{t}}$ for fit range variation of extrapolation. Data Driven multijet.

The statistical uncertainty of the fit is evaluated by varying the slope parameter by ±1 sigma, as can be seen in Fig. 87, 88 for QCD multijet background and 89, 90 for the Standard Model $t\bar{t}$ background, respectively. An alternative function, dijet mass function ($p_0 \times (1 - \frac{x}{\sqrt{s}})^{p_1} \times (\frac{x}{\sqrt{s}})^{p_2}$), is also tried, and it is observed that the extrapolation shapes are consistent with the nominal function (exponential) within the statistical uncertainty.

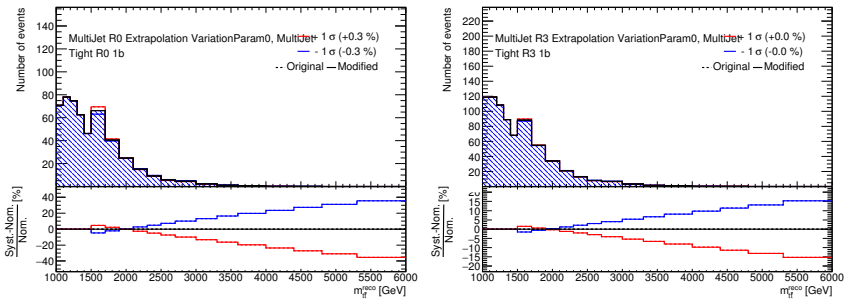

(a) 1 tight b-tag Tight R0

(b) 1 tight b-tag Tight R3

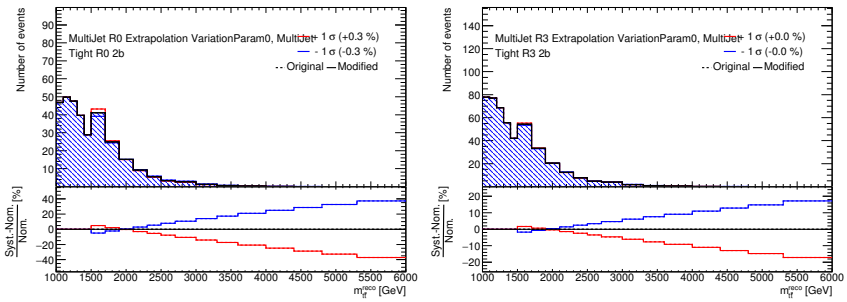

(c) 2 tight b-tag Tight R0

(d) 2 tight b-tag Tight R3

Figure 87: Systematic distributions of $m_{t\bar{t}}$ for p0 parameter. Data Driven multijet.

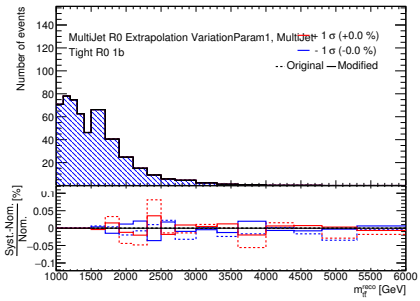

(a) 1 tight b-tag Tight R0

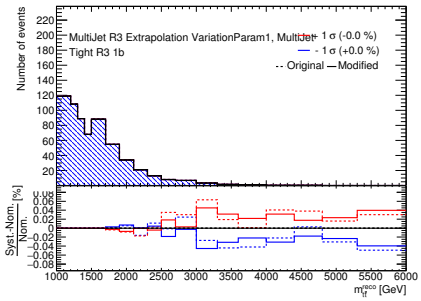

(b) 1 tight b-tag Tight R3

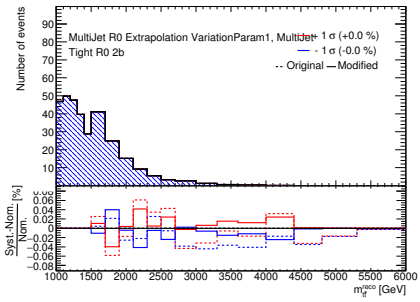

(c) 2 tight b-tag Tight R0

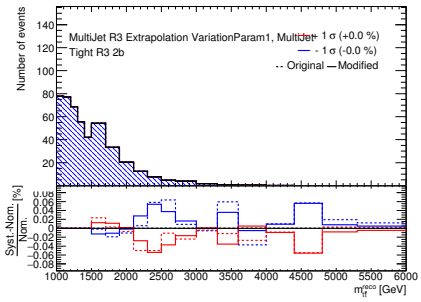

(d) 2 tight b-tag Tight R3

Figure 88: Systematic distributions of $m_{t\bar{t}}$ for p1 parameter. Data Driven multijet.

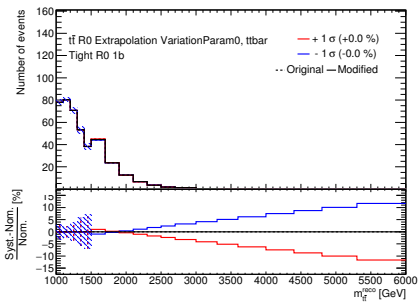

(a) 1 tight b-tag Tight R0

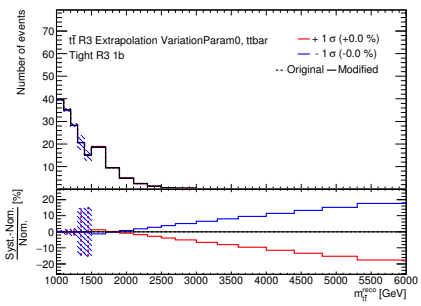

(b) 1 tight b-tag Tight R3

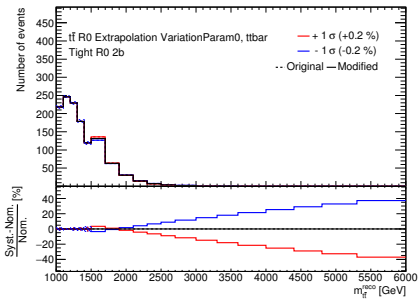

(c) 2 tight b-tag Tight R0

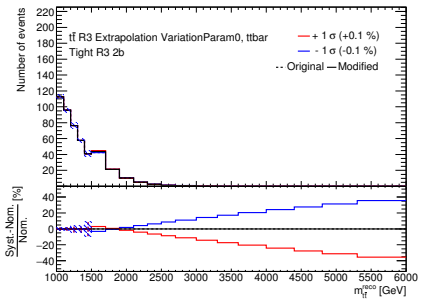

(d) 2 tight b-tag Tight R3

Figure 89: Systematic distributions of $m_{t\bar{t}}$ for p0 parameter. MC $t\bar{t}$.

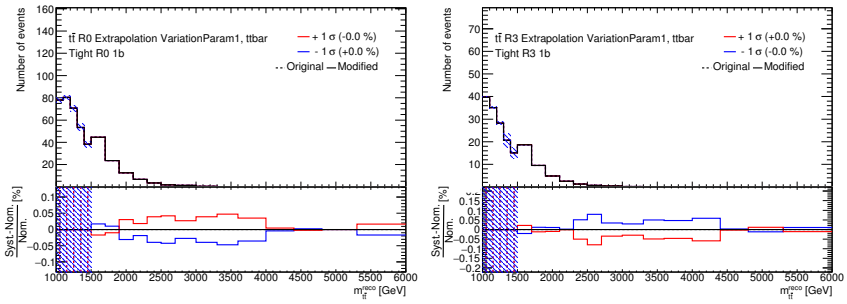

(a) 1 tight b-tag Tight R0

(b) 1 tight b-tag Tight R3

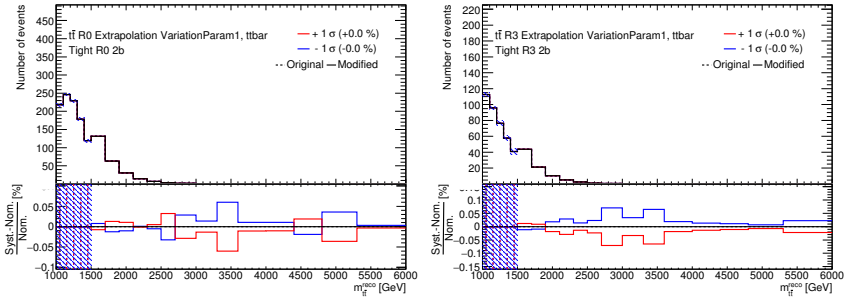

(c) 2 tight b-tag Tight R0

(d) 2 tight b-tag Tight R3

Figure 90: Systematic distributions of $m_{t\bar{t}}$ for p1 parameter. MC $t\bar{t}$.

In addition, the extrapolation is started from 1.5 TeV, and statistical uncertainty above 1.5 TeVis replaced to the systematic uncertainty associated with fit error variation. Therefore $m_{t\bar{t}}$ distribution above 1.5 TeVdon't have statistical uncertainty. Statistical uncertainties below 1.5 TeVare remained, but the statistical uncertainty for multijet have to be fully-correlated between one tight b-tag and two tight b-tag, because one tight b-tagged and two tight b-tagged multijet distributions are estimated by a common no tight b-tagged distribution. Hence, the statistical uncertainties are also replaced to systematic uncertainty in order to treat them as bin-by-bin and fully-correlated uncertainty between one tight b-tag and two tight b-tag. Figure 91 and 92

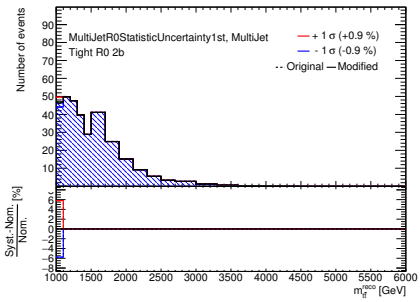

(a) 1st bin

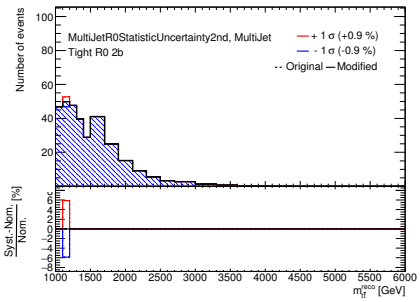

(b) 2nd bin

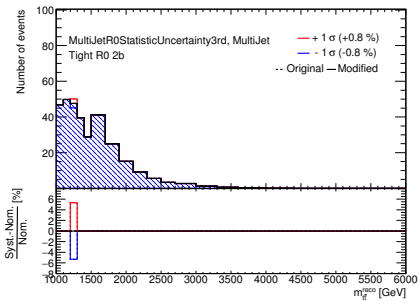

(c) 3rd bin

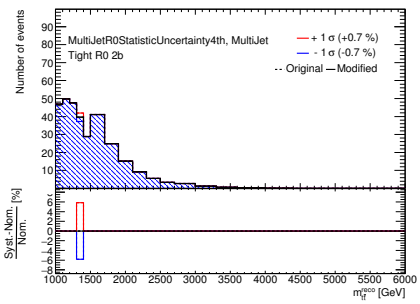

(d) 4th bin

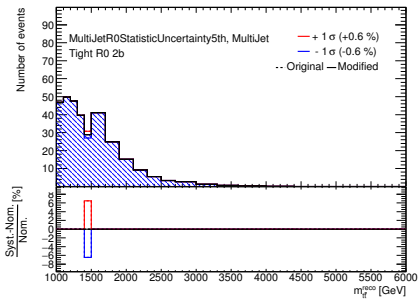

(e) 5th bin

Figure 91: Systematic distributions of $m_{t\bar{t}}$ for statistical uncertainty in R0 Tight 2 tight b-tagged region.

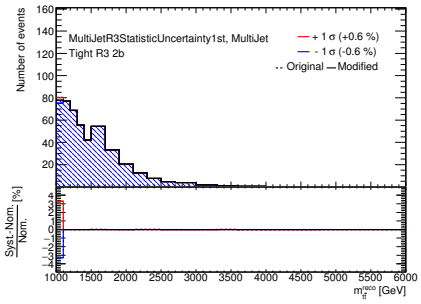

(a) 1st bin

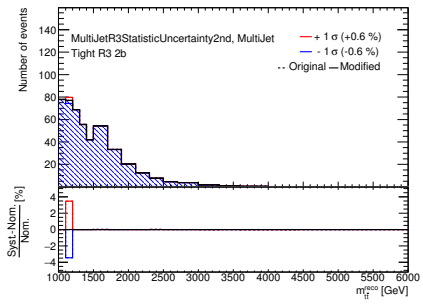

(b) 2nd bin

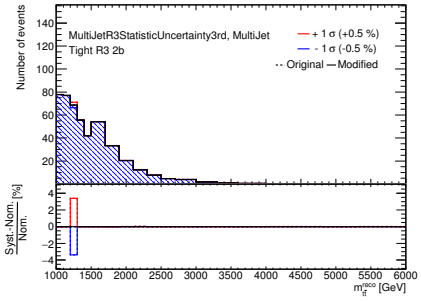

(c) 3rd bin

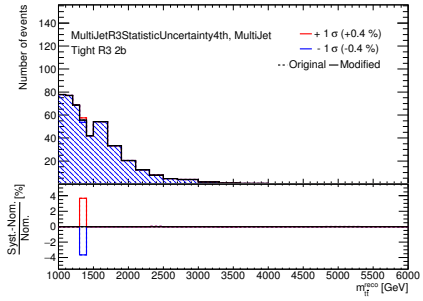

(d) 4th bin

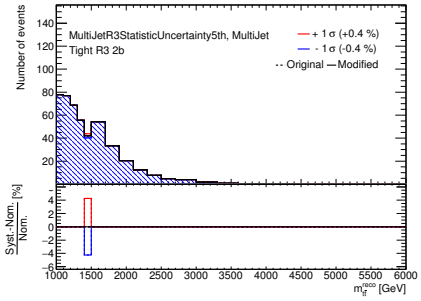

(e) 5th bin

Figure 92: Systematic distributions of $m_{t\bar{t}}$ for statistical uncertainty in R3 Tight 2 tight b-tagged region.

8.8. Summary of systematic uncertainty

Table 15 is showed relative effect of each systematic uncertainty on the yields for 2 tight b-tagged Tight R0, and the summary for other regions can be seen in Appendix. B.

8.9. Validation

In order to validate the estimated background modelings, we checked events in the validation regions. We define the validation region as the events in the Loose regions.

Table 15: Relative effect of each systematic on the yields for two tight b-tagged Tight R0.

	Multijet	$t\bar{t}$	Z' 3 TeV
Luminosity	0 / 0	0.021 / -0.021	0.021 / -0.021
b-tagging	0 / 0	-0.0474 / 0.0474	-0.0538 / 0.0538
Large-R Jet Baseline	0 / 0	0.0148 / -0.0148	-0.028 / 0.028
Large-R Jet Modeling	0 / 0	0.0104 / -0.0104	-0.0306 / 0.0306
Large-R Jet TotalStat	0 / 0	0.00183 / -0.00183	-0.011 / 0.011
Large-R Jet Tracking	0 / 0	0.03 / -0.03	-0.0176 / 0.0176
Large-R Jet p_T resolution	0 / 0	-0.00835 / 0.00835	-0.00138 / 0.00138
Large-R Jet mass resolution	0 / 0	0.00799 / -0.00799	0.00169 / -0.00169
Large-R Jet tau_{32}^{wta} resolution	0 / 0	0.00302 / -0.00302	0.00214 / -0.00214
$t\bar{t}$ Cross-Section	0 / 0	0.056 / -0.061	0 / 0
$t\bar{t}$ generator	0 / 0	-0.165 / 0.165	0 / 0
$t\bar{t}$ parton shower	0 / 0	-0.0631 / 0.0631	0 / 0
$t\bar{t}$ isrfsr	0 / 0	-0.133 / 0.133	0 / 0
$t\bar{t}$ EW	0 / 0	0.0778 / -0.0778	0 / 0
$t\bar{t}$ NNLO reweight	0 / 0	-0.170 / 0.170	0 / 0
PDF CT10 vs. PDF4LHC15	0 / 0	-0.0895 / 0.0895	0 / 0
PDF Eigenvar 30	0 / 0	0.0185 / -0.0185	0 / 0
MultiJet Shape Correction Fit Error Variation of Parameter 0	0.0327 / -0.0327	0 / 0	0 / 0
MultiJet Shape Correction Fit Error Variation of Parameter 1	0.0239 / -0.0239	0 / 0	0 / 0
MultiJet Shape Correction Fit Error Variation of Parameter 2	-0.0281 / 0.0281	0 / 0	0 / 0
Residual Shape Difference of $m_{t\bar{t}}$ Slope from unity	-0.0014 / 0.0014	0 / 0	0 / 0
MultiJet Statistic Uncertainty in no extrapolated region at 1st bin	0.00856 / -0.00856	0 / 0	0 / 0
MultiJet Statistic Uncertainty in no extrapolated region at 2nd bin	0.00924 / -0.00924	0 / 0	0 / 0
MultiJet Statistic Uncertainty in no extrapolated region at 3rd bin	0.00801 / -0.00801	0 / 0	0 / 0
MultiJet Statistic Uncertainty in no extrapolated region at 4th bin	0.00729 / -0.00729	0 / 0	0 / 0
MultiJet Statistic Uncertainty in no extrapolated region at 5th bin	0.0059 / -0.0059	0 / 0	0 / 0
MultiJet Template Shape Difference	-0.244 / 0.244	0 / 0	0 / 0
$n_{MultiJet,SR0rightwotightb-tag}$	0.0997 / -0.0651	0 / 0	0 / 0
Extrapolation Fit Range for $t\bar{t}$	0 / 0	-0.000943 / 0.000943	0 / 0
Extrapolation Fit Error Variation of Parameter 0 for $t\bar{t}$	0 / 0	0.00222 / -0.00222	0 / 0
Extrapolation Fit Error Variation of Parameter 1 for $t\bar{t}$	0 / 0	1.27e-06 / -1.27e-06	0 / 0
Extrapolation Fit Range	2.78e-07 / -2.78e-07	0 / 0	0 / 0
Extrapolation Fit Error Variation of Parameter 0 for MultiJet	0.00318 / -0.00318	0 / 0	0 / 0
Extrapolation Fit Error Variation of Parameter 1 for MultiJet	2.32e-07 / -2.32e-07	0 / 0	0 / 0

Purity of the Standard Model $t\bar{t}$ background events in the validation regions is summarized in Table. 16. The purity in each validation region is a few%, contribution of multijet background is dominant in validation region. Therefore, signal contamination is negligible.

Table 16: Purity of the Standard Model $t\bar{t}$ events in validation regions.

validation region	purity in no tight b-tag	purity in 1 tight b-tag	purity in 2 tight b-tag
VR0-Loose	(1.7 ± 0.25)%	(7.28 ± 0.23)%	(25.6 ± 0.86)%
VR1-Loose	(0.63 ± 0.13)%	(2.74 ± 0.20)%	(9.50 ± 0.45)%
VR2-Loose	(0.64 ± 0.17)%	(2.8 ± 0.19)%	(8.36 ± 0.39)%
VR3-Loose	(0.83 ± 0.08)%	(3.72 ± 0.12)%	(13.13 ± 0.29)%
VR4-Loose	(0.48 ± 0.06)%	(2.21 ± 0.10)%	(6.88 ± 0.20)%

The shape of the multijet background in the Loose region is obtained from the merged regions (Loose+Medium+Tight).

The shape correction for the multijet background modeling for merged region has already validated in Section 7.2.

The estimated background distributions are compared with the data in the validation region as can be seen in Fig.s 93 and 94. The background distributions using the extrapolation method are also shown there. As can be seen, the expected distributions agree well with the data.

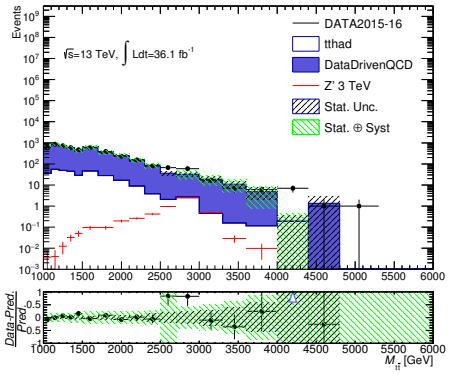

(a) R0 Loose

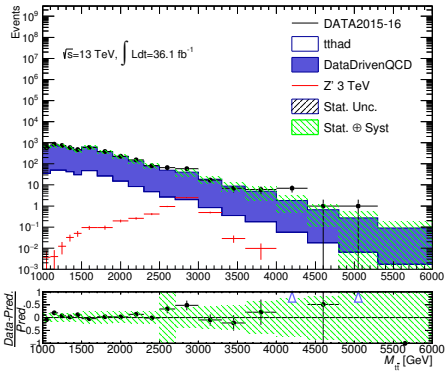

(b) R0 Loose (extrapolation)

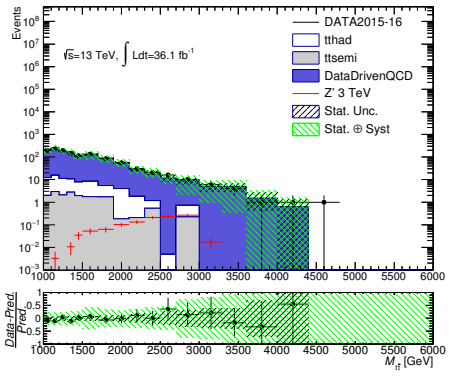

(c) R3 Loose

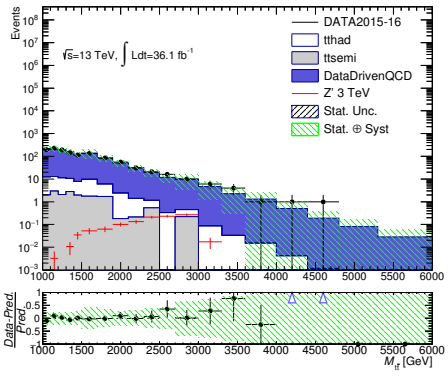

(d) R3 Loose (extrapolation)

Figure 93: Distributions of $m_{t\bar{t}}$ in one tight b-tagged validation region .

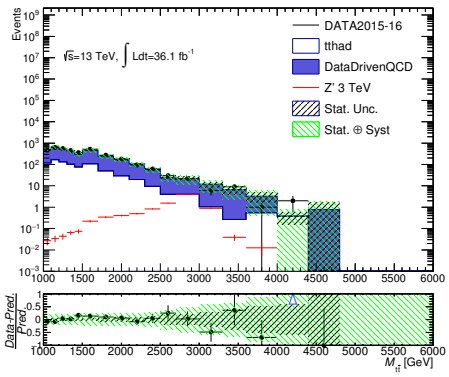

(a) R0 Loose

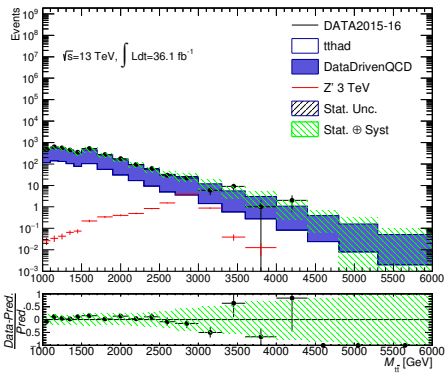

(b) R0 Loose (extrapolation)

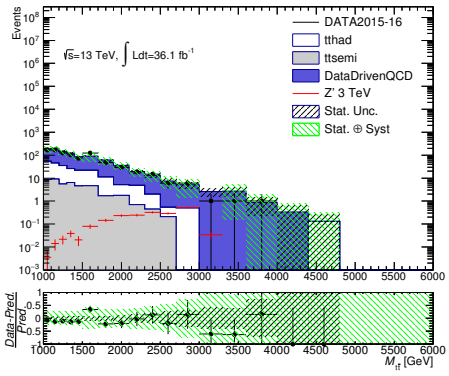

(c) R3 Loose

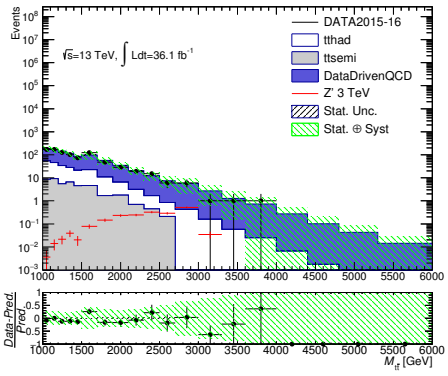

(d) R3 Loose (extrapolation)

Figure 94: Distributions of $m_{t\bar{t}}$ in two tight b-tagged validation region.

8.9.1. Fit results of the Loose R0+R3

In order to check if estimated background and systematic uncertainties are reasonable or not, the $m_{t\bar{t}}$ distributions in the validation regions are fitted, the cross section limits are produced, in the same way as we do for the signal region. Figure 95, 96 show the nuisance parameters and the correlation matrix of each nuisance parameters, the expected size of constraint from the fitting in the Loose R0+R3. Multijet statistic uncertainties for each bin are pulled, but this kind of uncertainties are expected to be widely moved. The other nuisance parameters are stable. For correlation matrix, some multijet normalization factor uncertainties are correlated to multijet shape correction uncertainty. The multijet shape correction uncertainty has a normalization component, therefore it can be understood. In addition, other correlated uncertainties are same kinds of systematic uncertainty between each other, therefore it is reasonable that there is a correlation between same kinds of uncertainty.

Pre-fit and Post-fit $m_{t\bar{t}}$ distributions are showed in Fig. 97 and 98.

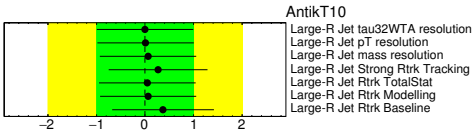

(a) Nuisance parameter of large-R jet

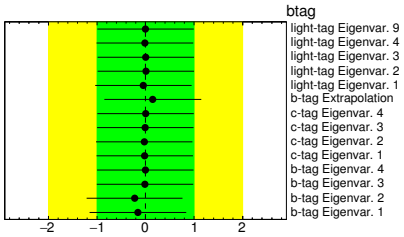

(b) Nuisance parameter of b-tagging

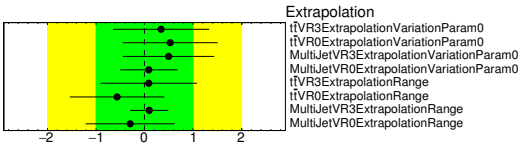

(c) Nuisance parameter of extrapolation

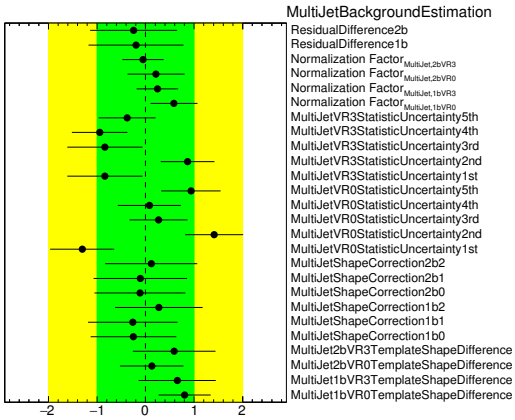

(d) Nuisance parameter of multijet modeling

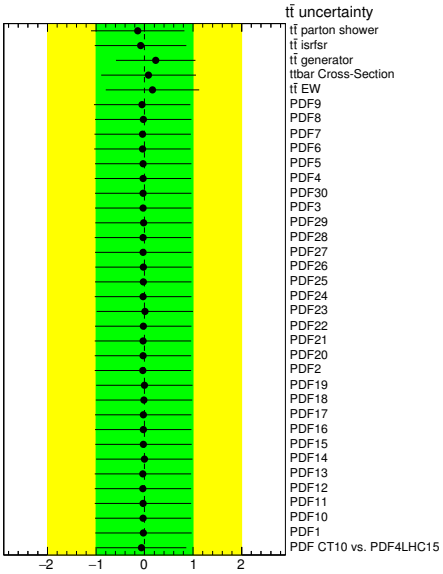

(e) Nuisance parameter of $t\bar{t}$ modeling

Figure 95: Pull plots of each nuisance parameter. The data points denote an impact of each nuisance parameter for the fit. The error bars denote the expected size of constraint from the fitting to each nuisance parameter.

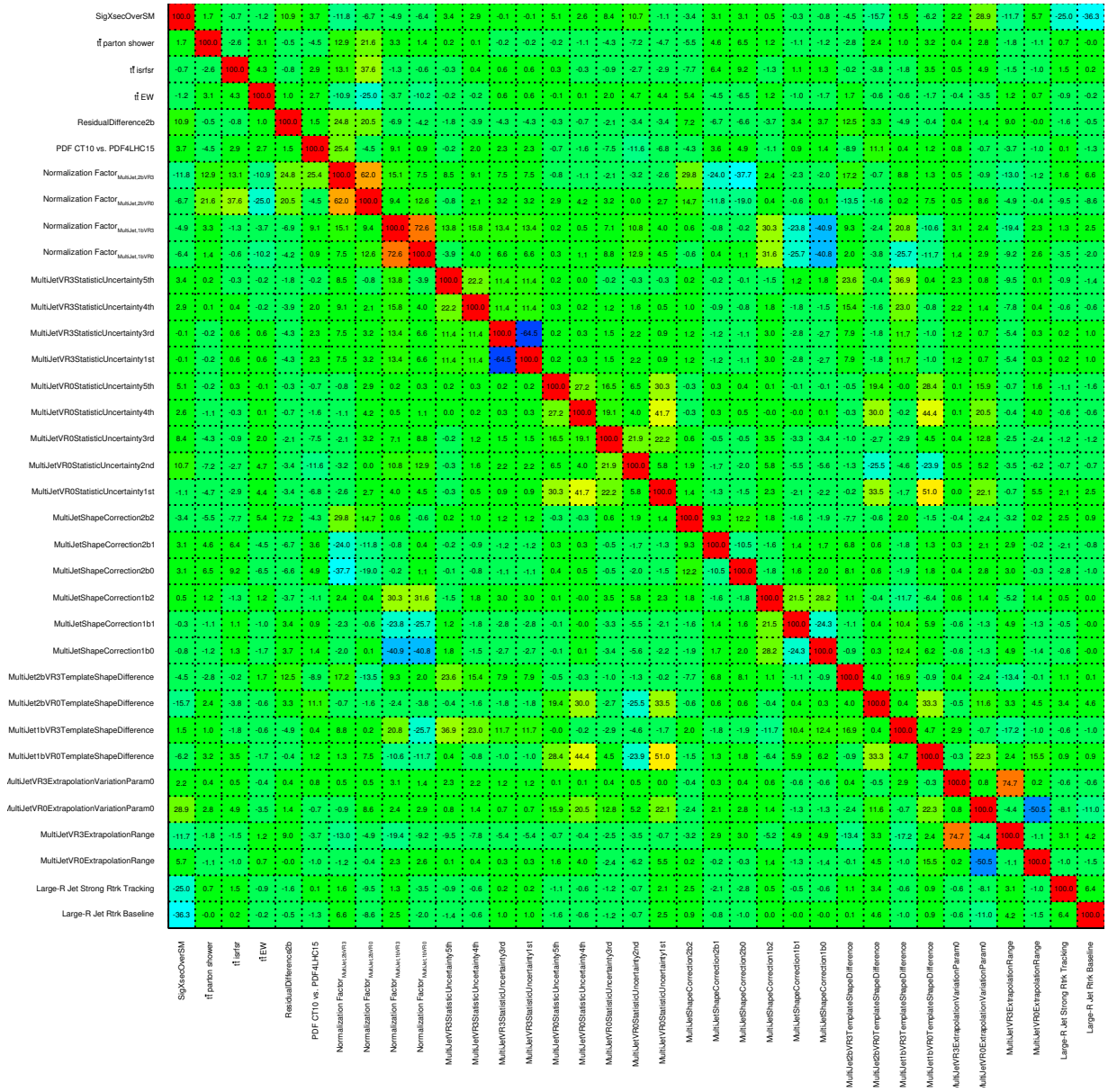

Figure 96: Correlation matrix of the nuisance parameters. Only those with correlation above 20% are shown

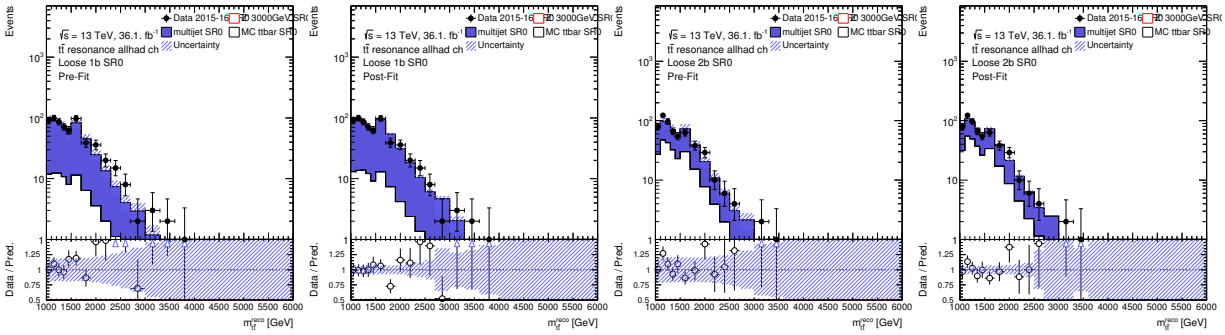

(a) Pre-fit,
one tight b-tagged Loose

(b) Post-fit,
one tight b-tagged Loose

(c) Pre-fit,
two tight b-tagged Loose

(d) Post-fit,
two tight b-tagged Loose

Figure 97: Pre-fit and Post-fit $m_{t\bar{t}}$ distributions for the validation region, R0 Loose and one or two tight b-tagged.

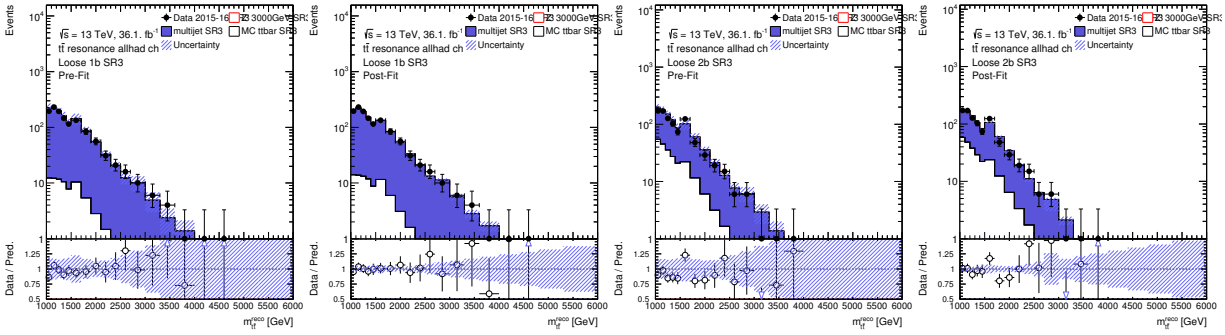

(a) Pre-fit,
one tight b-tagged Loose

(b) Post-fit,
one tight b-tagged Loose

(c) Pre-fit,
two tight b-tagged Loose

(d) Post-fit,
two tight b-tagged Loose

Figure 98: Pre-fit and Post-fit $m_{t\bar{t}}$ distributions for the validation region, R3 Loose and one or two tight b-tagged.

Fit result of Z' without systematic uncertainties is showed in Fig. 99.

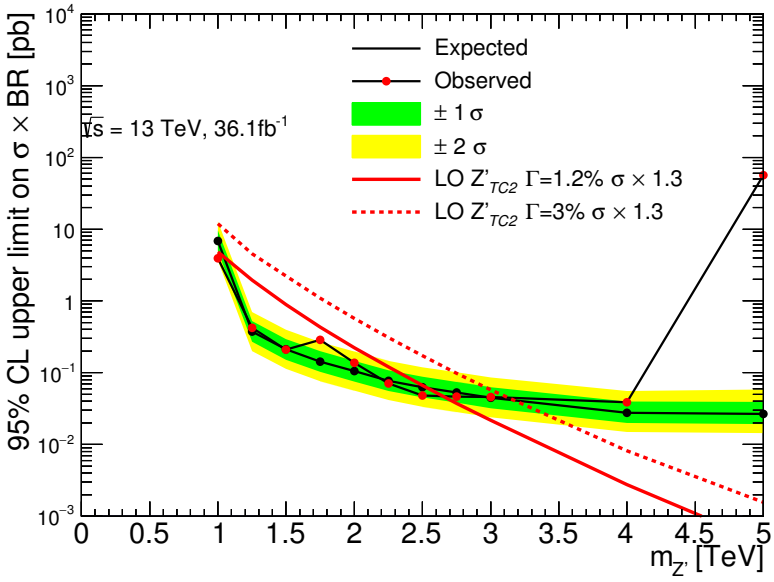

Figure 99: Extracted and observed upper limits on Z' with no systematic uncertainty

Result from a fit with all the systematic uncertainties is shown in Fig. 100. The observed limits well agree with the expected limits.

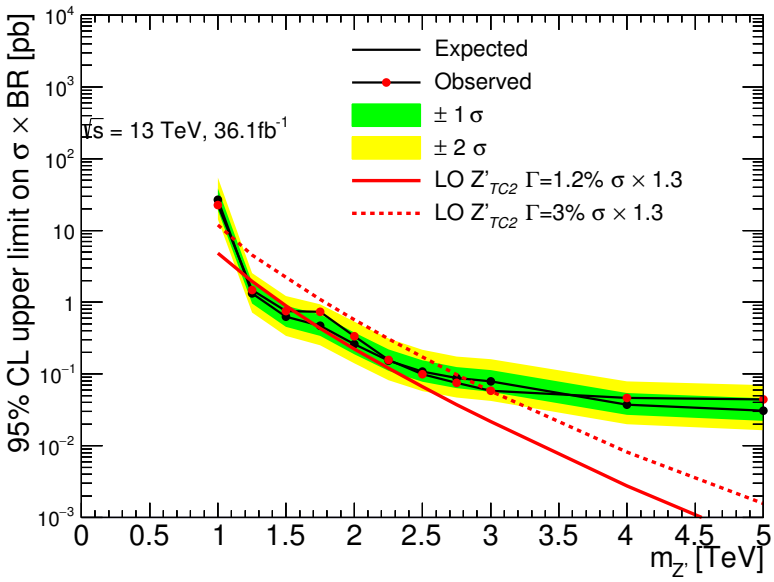

Figure 100: Extracted and observed upper limits on Z' with all systematic uncertainty

9. Results

The $m_{t\bar{t}}$ distributions in one or two tight b-tagged R0 and R3 for Medium and Tight category are used as the final discriminants.

The amount of the Standard Model $t\bar{t}$ background events in the signal regions is summarized in Table. 17. Figure 101, 102, 103 and 104 show the distributions of $m_{t\bar{t}}$ in the R0 and R3 (data points are not shown). Background estimations using the extrapolation are shown separately. Figure 105 and 105 show the number of expected events in each region, and the number of observed events in data.

Table 17: Amount of the Standard Model $t\bar{t}$ events in signal regions.

signal	amount in no tight b-tag	amount in 1 tight b-tag	amount in 2 tight b-tag
R0-Medium	(4.90 ± 0.60)%	(17.92 ± 0.77)%	(51.08 ± 1.61)%
R0-Tight	(14.96 ± 1.84)%	(44.38 ± 1.97)%	(76.08 ± 2.24)%
R3-Medium	(1.80 ± 0.27)%	(8.09 ± 0.36)%	(27.51 +- ± 0.86)%
R3-Tight	(5.31 ± 0.89)%	(17.86 ± 1.03)%	(46.07 ± 1.91)%

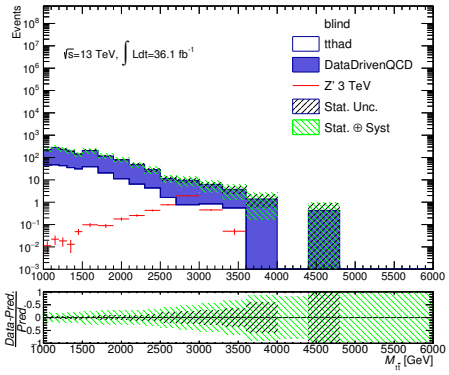

(a) Medium

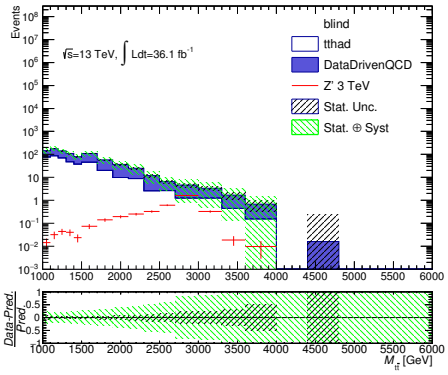

(b) Tight

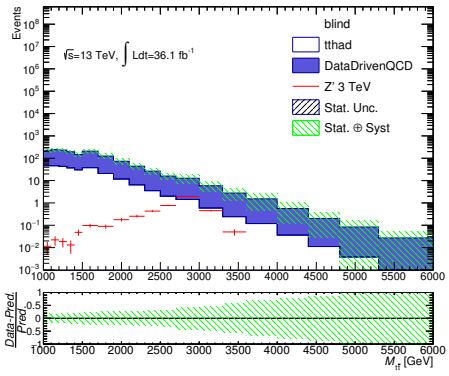

(c) Medium (extrapolation)

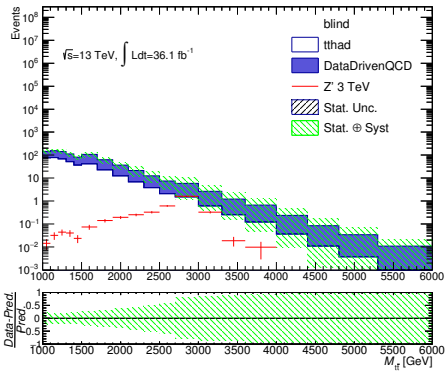

(d) Tight (extrapolation)

Figure 101: Estimated distributions of $m_{t\bar{t}}$ in one tight b-tagged R0.

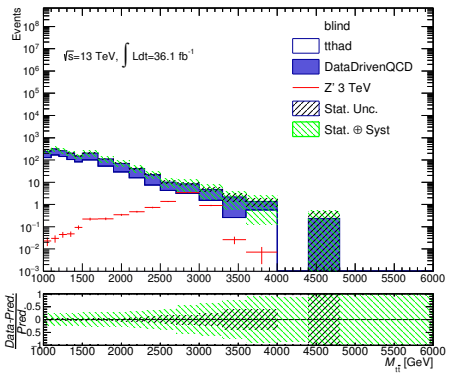

(a) Medium

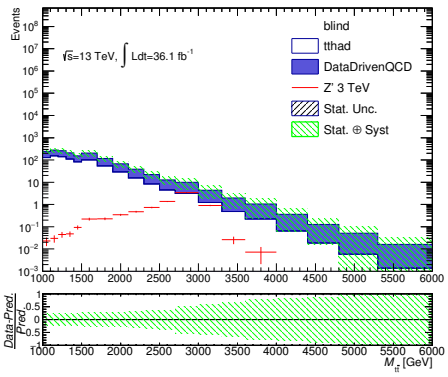

(b) Medium (extrapolation)

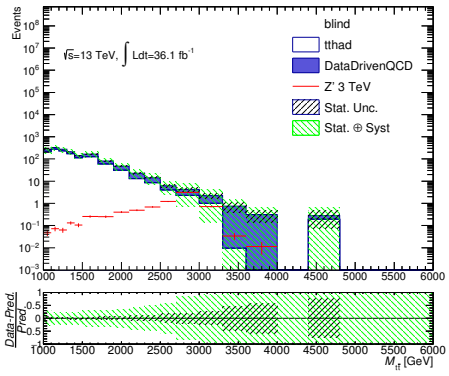

(c) Tight

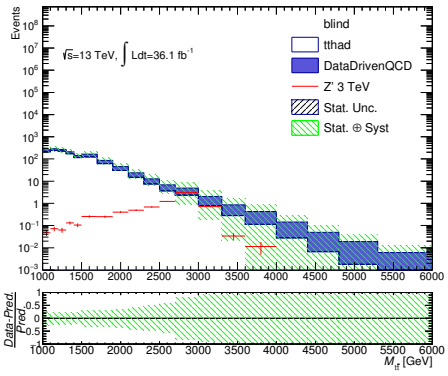

(d) Tight (extrapolation)

Figure 102: Estimated distributions of $m_{t\bar{t}}$ in two tight b-tagged R0.

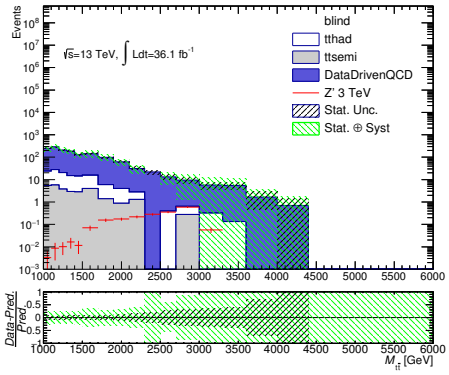

(a) Medium

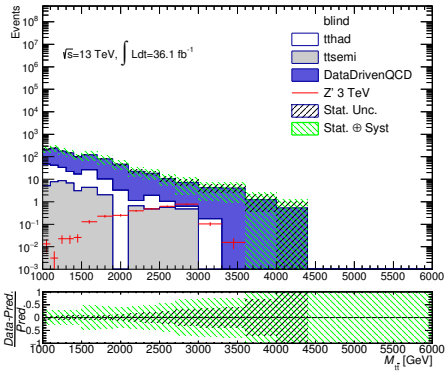

(b) Tight

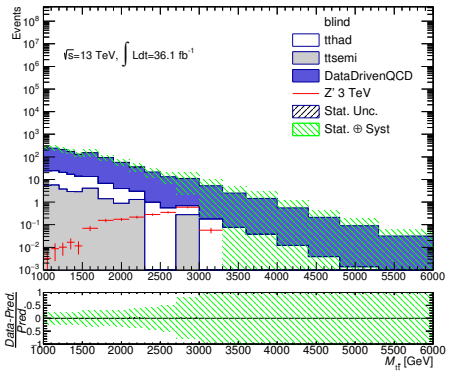

(c) Medium (extrapolation)

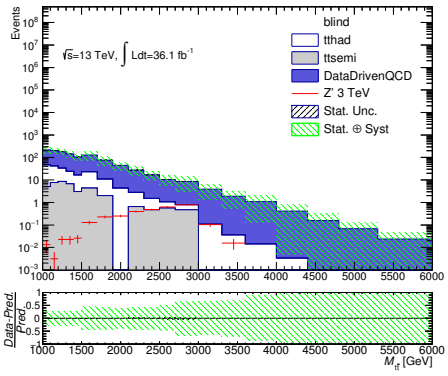

(d) Tight (extrapolation)

Figure 103: Estimated distributions of $m_{t\bar{t}}$ in one tight b-tagged R3.

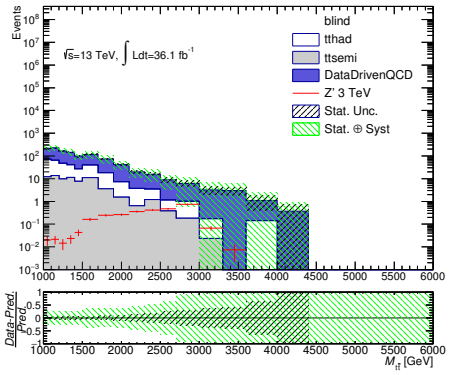

(a) Medium

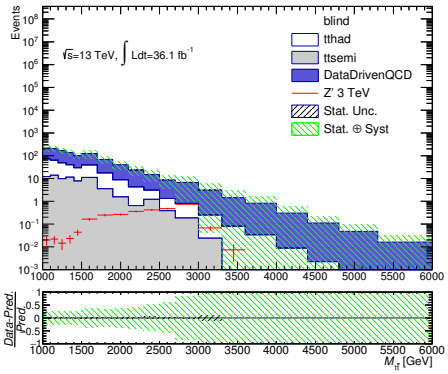

(b) Medium (extrapolation)

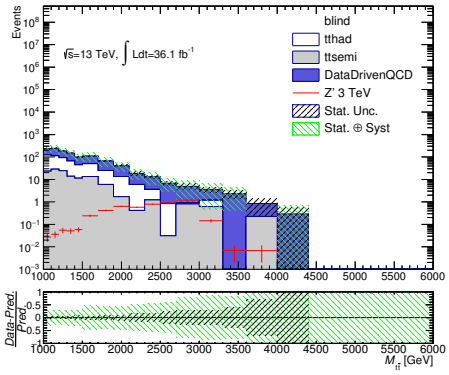

(c) Tight

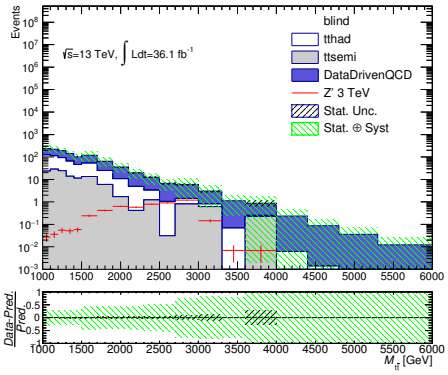

(d) Tight (extrapolation)

Figure 104: Estimated distributions of $m_{t\bar{t}}$ in two tight b-tagged R3.

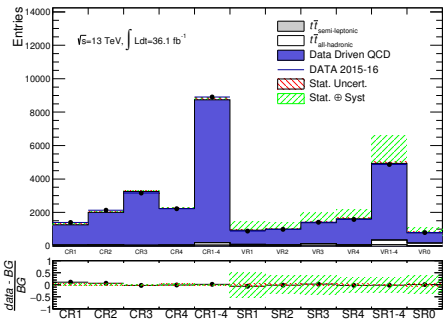

(a) One tight b-tag, Medium

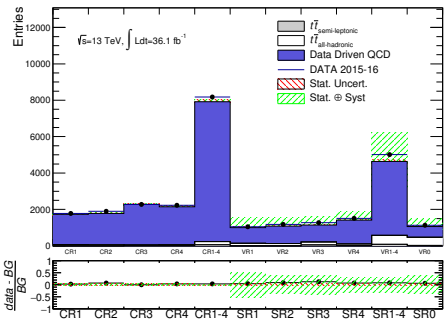

(b) One tight b-tag, Tight

Figure 105: Number of expected events in the control/validation/signal regions, and observed data events for one tight b-tag region.

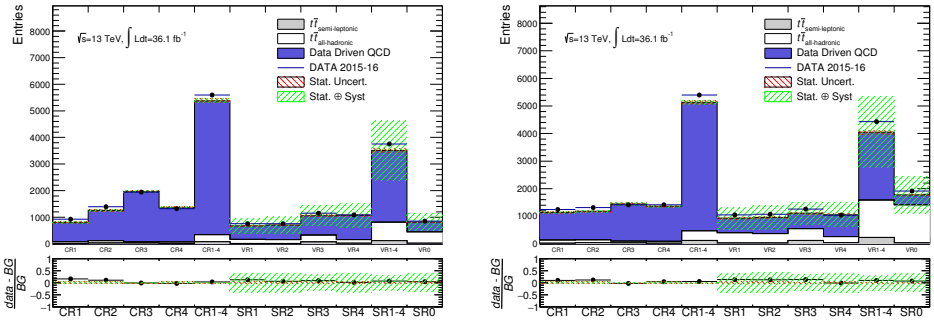

(a) Two tight b-tag, Medium

(b) Two tight b-tag, Tight

Figure 106: Number of expected events in the control/validation/signal regions, and observed data events for the two tight b-tag region.

9.1. Profile likelihood fit

Upper limits are set on the cross-section times signal branching ratio for each new physics model with a profile likelihood fit [94]. A value x is observed for each event, and a histogram $\mathbf{n} = (n_1, ...n_N)$ is constructed by those events. In this analisys, the x is equal to each observed $m_{t\bar{t}}$ value. The expectation value of n_i can be written as

$$E[n_i] = \mu s_i + b_i, \tag{47}$$

where μ denotes the strength of the signal process, s_i and b_i are the mean number of the entries in the ith bin from signal and background. They satisfy

$$s_i = s_{tot} \int_{\text{bin } i} f_s(x; \theta_s) dx, \tag{48}$$

$$b_i = b_{tot} \int_{\text{bin } i} f_b(x; \theta_b) dx, \tag{49}$$

where s_{tot} and b_{tot} denote the total mean numbers of signal and background, the functions $f_s(x; \theta_s)$ and $f_b(x; \theta_b)$ are probability density functions of value of the x for signal and background, and the parameters θ_s and θ_b denote parameters which characterize the shape of probability density function. The value s_{tot} depends on and is determined from the expected signal model. Nuisance parameters of this fit can be written as $\theta = (\theta_s, \theta_b, b_{tot})$. The likelihood function can be written as

$$L(\mu, \theta) = \prod_{j=0}^{N} \frac{(\mu s_j + b_j)^{n_j}}{n_j!} e^{-(\mu s_j + b_j)}. \tag{50}$$

In order to test a hypothesis value of μ, the profile likeihood ratio is considered as

$$\lambda(\mu) = \frac{L(\mu, \hat{\hat{\theta}})}{L(\hat{\mu}, \hat{\theta})}, \tag{51}$$

where $\hat{\hat{\theta}}$ denotes the θ maximize L for μ, and the denominator of Eq. (51) is the maximized likelihood function for $\hat{\mu}$ and $\hat{\theta}$.

9.2. Fitting result for signal region

Figure 107 shows impact of each nuisance parameter for the fit. The error bars show the expected size of constraint from the fitting to each nuisance parameter. Nuisance parameter of extrapolation uncertainty and multijet template shape uncertainty are constrained, because those uncertainties are larger than the other uncertainties. Therefore, those uncertainties are strongly constrained by fitting.

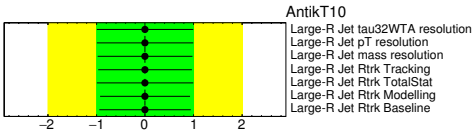

(a) Nuisance parameters of large-R jet

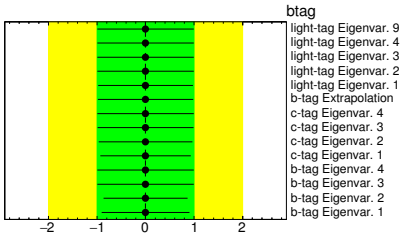

(b) Nuisance parameters of b-tagging

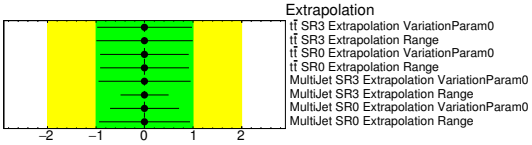

(c) Nuisance parameters of extrapolation

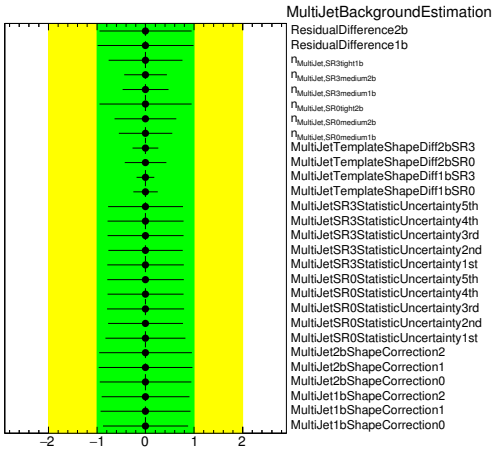

(d) Nuisance parameters of multijet modeling

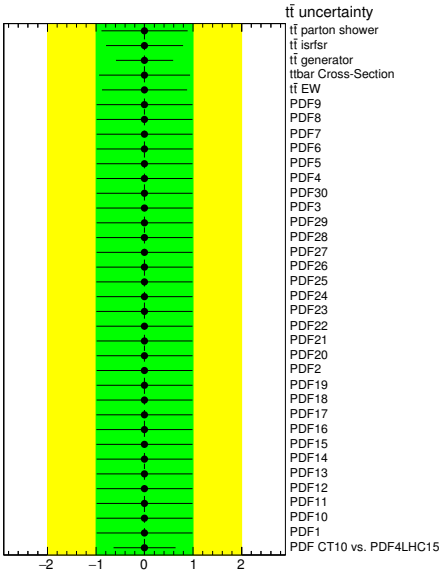

(e) Nuisance parameters of $t\bar{t}$ modeling

Figure 107: Pull plots of each nuisance parameter. The data points denote an impact of each nuisance parameter for the fit. The error bars denote the expected size of constraint from the fitting to each nuisance parameter.

Figure 108 shows the correlation matrix of each nuisance parameter. There are a bit strongly correlated components, but the nuisance parameters in each components are similar type of systematic uncertainty. Therefore, it can be understood that the correlation became a bit strong.

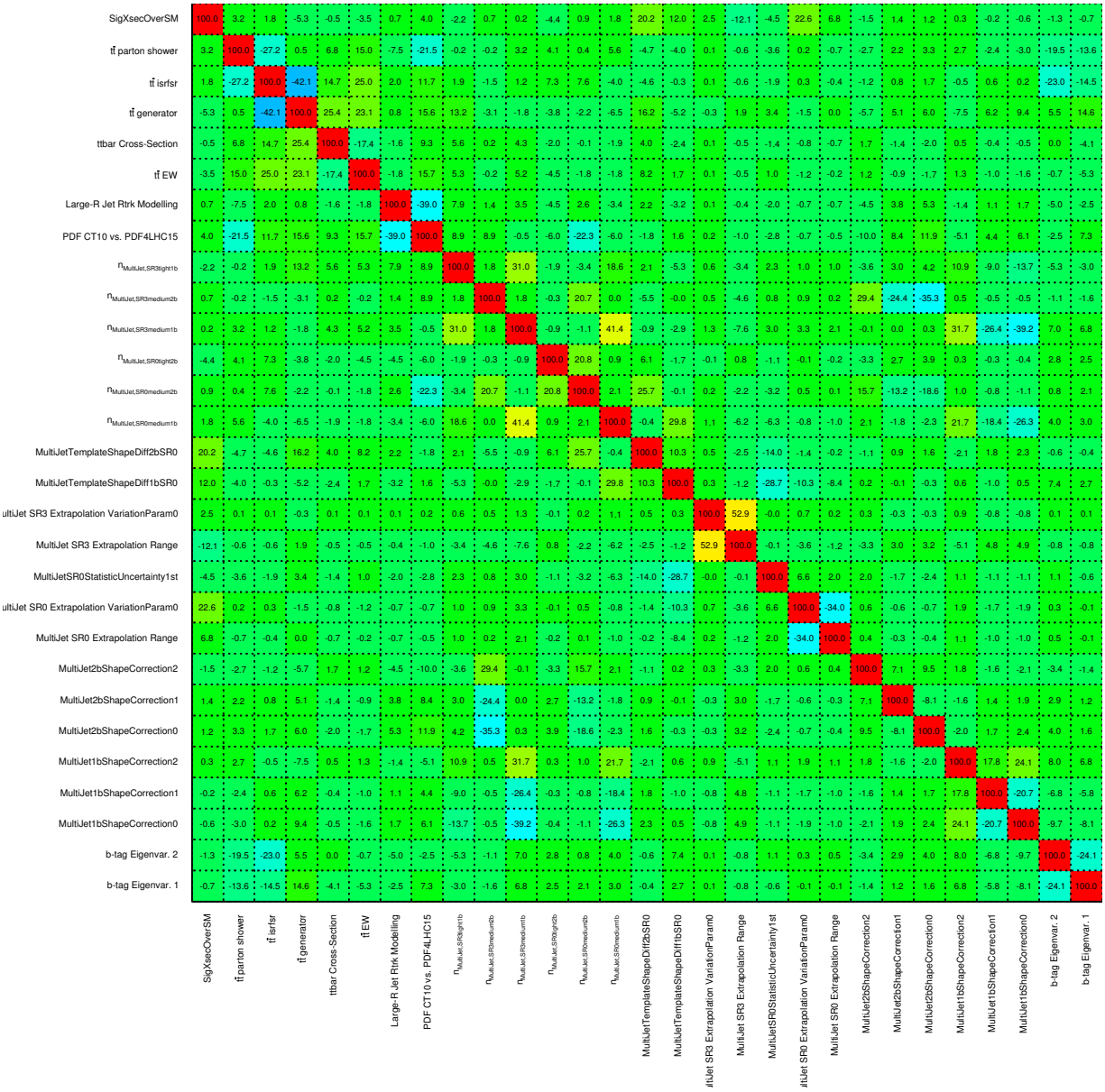

Figure 108: Correlation matrix of the nuisance parameters. Only those with correlation above 20% are shown

Figure 109 show the impact on signal strength for each nuisance parameters for Z' 1, 2 and 3 TeV MC samples. At 1 and 2 TeV, $t\bar{t}$ modeling uncertainties are dominant. Extrapolation uncertainties are dominant at 3 TeV.

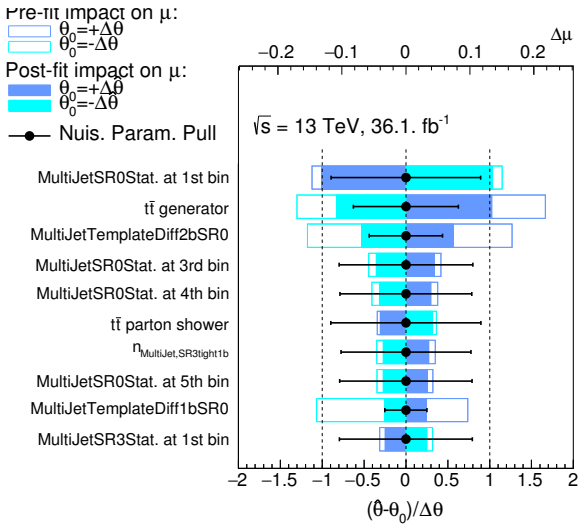

(a) Z' 1 TeV

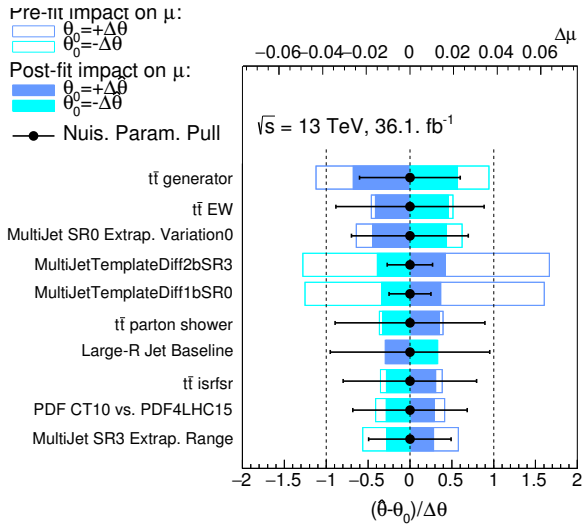

(b) Z' 2 TeV

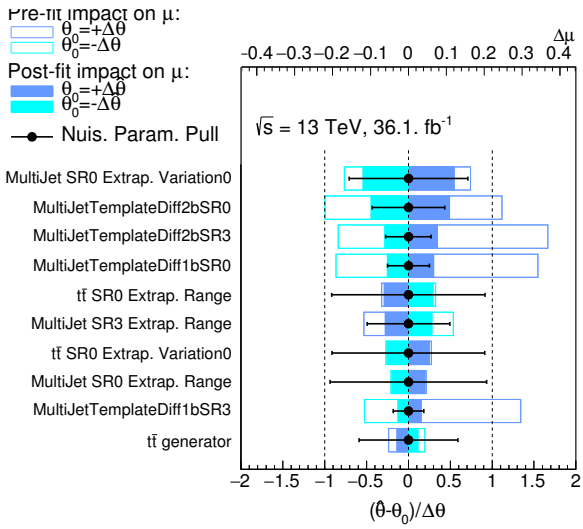

(c) Z' 3 TeV

Figure 109: The impact on signal strength for each nuisance parameters. Top 10 nuisance parameters are shown.

The $m_{t\bar{t}}$ distributions before and after fitting (Called “pre-fit” and “post-fit”,respectively) are shown in Figs. 110 and 111.

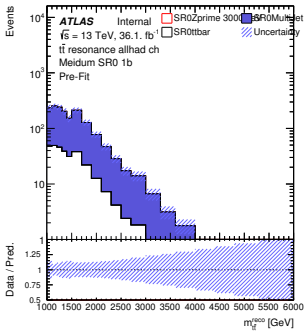

(a) Pre-fit,
one tight b-tagged Medium

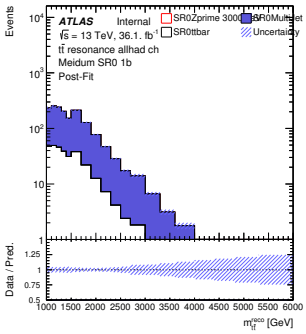

(b) Post-fit,
one tight b-tagged Medium

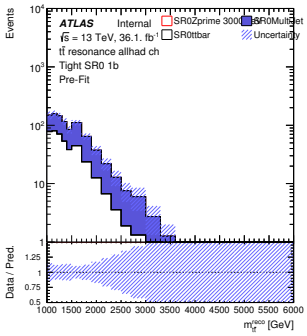

(c) Pre-fit,
one tight b-tagged Tight

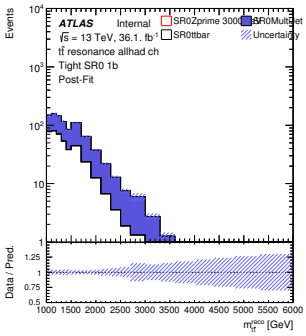

(d) Post-fit,
one tight b-tagged Tight

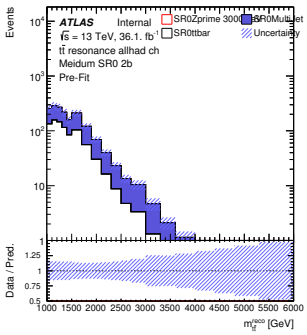

(e) Pre-fit,
two tight b-tagged Medium

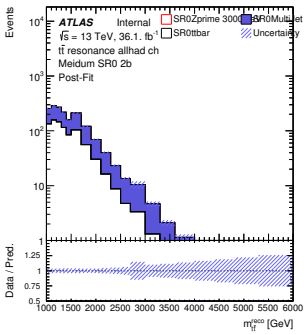

(f) Post-fit,
two tight b-tagged Medium

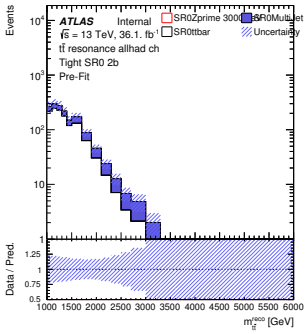

(g) Pre-fit,
two tight b-tagged Tight

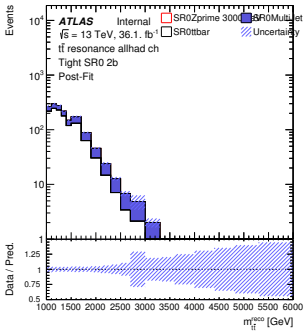

(h) Post-fit,
two tight b-tagged Tight

Figure 110: Pre-fit and Post-fit $m_{t\bar{t}}$ distributions for the signal region, R0 Medium or Tight and one or two tight b-tagged.

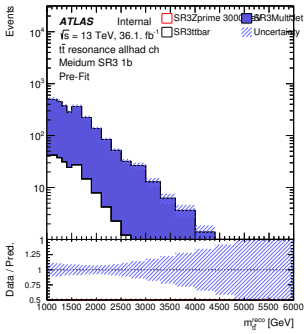

(a) Pre-fit,
one tight b-tagged Medium

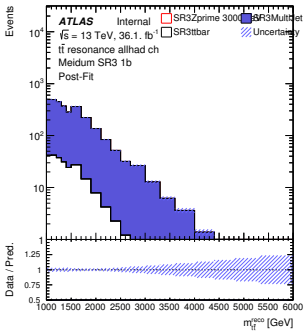

(b) Post-fit,
one tight b-tagged Medium

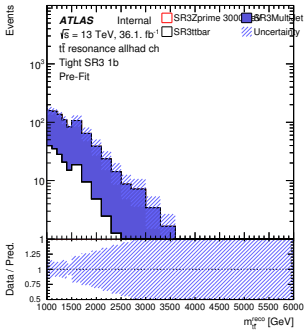

(c) Pre-fit,
one tight b-tagged Tight

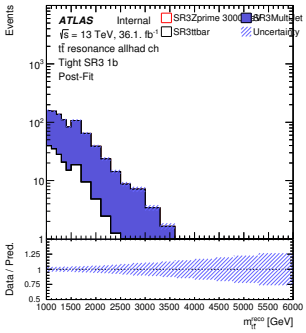

(d) Post-fit,
one tight b-tagged Tight

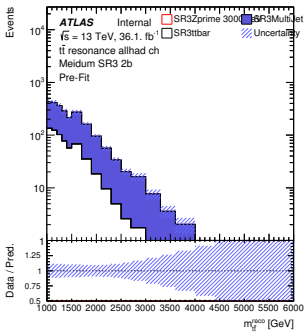

(e) Pre-fit,
two tight b-tagged Medium

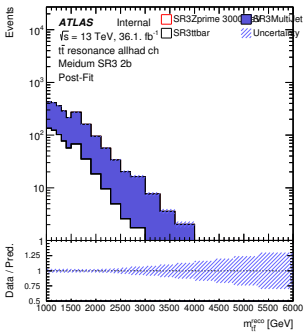

(f) Post-fit,
two tight b-tagged Medium

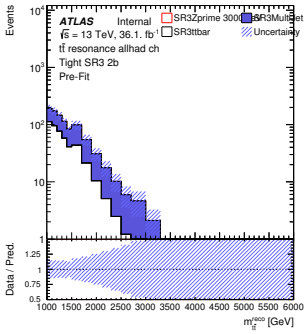

(g) Pre-fit,
two tight b-tagged Tight

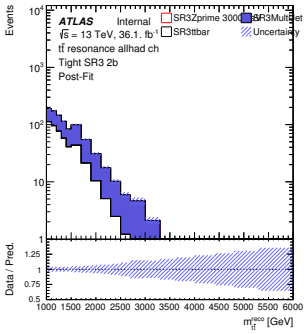

(h) Post-fit,
two tight b-tagged Tight

Figure 111: Pre-fit and Post-fit $m_{t\bar{t}}$ distributions for the signal region, R3 Medium or Tight and one or two tight b-tagged.

The fit result for Z' signal without systematic uncertainties is shown in Fig. 112.

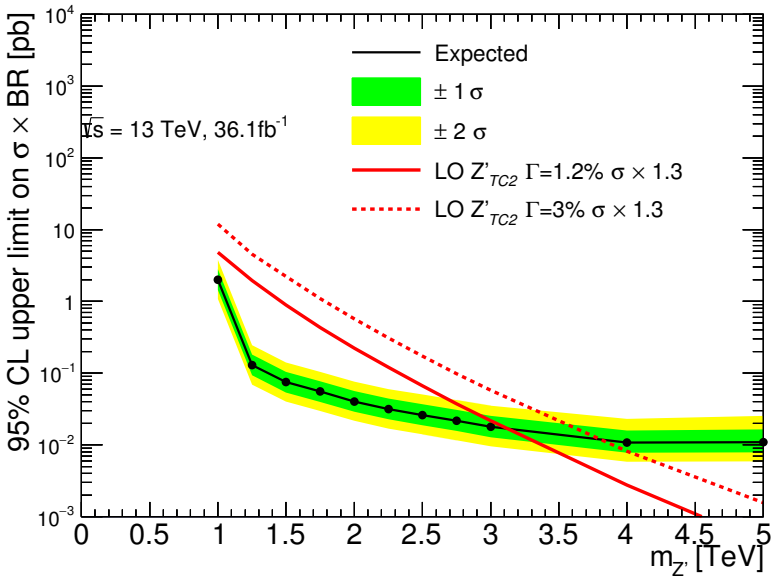

(a) Upper limits on $\sigma_{Z'}$

Figure 112: Extracted upper limits on Z' with no systematic uncertainty

Resulting expected upper limits on production cross section of Z' signal is shown in Fig. 113. Those for the RS graviton signal and KK gluon signal are also shown.

Using a benchmark of BSM signal, Z', we expect upper limits on the production cross section of the Z' to be greater than 3.1 TeV. In addition, we also expect g_{KK} upper limits on the production cross section of the g_{KK} to be greater than 3.2 TeV.

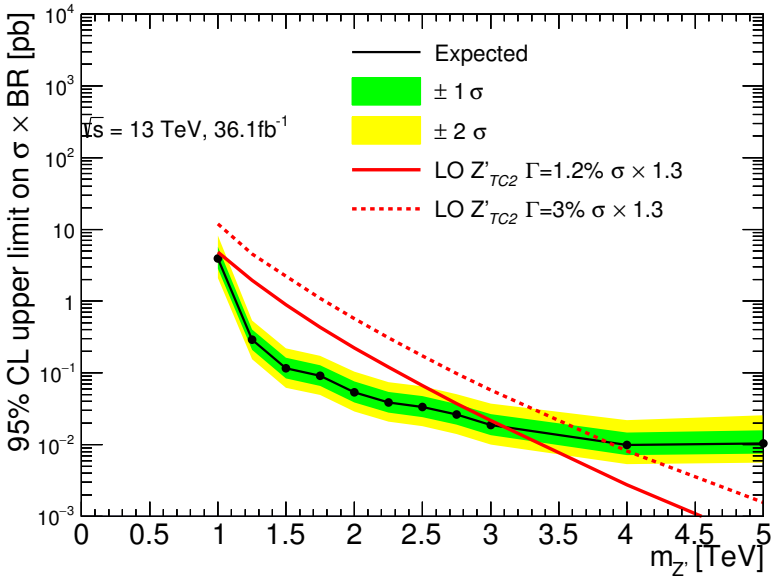

(a) Upper limits on $\sigma_{Z'}$

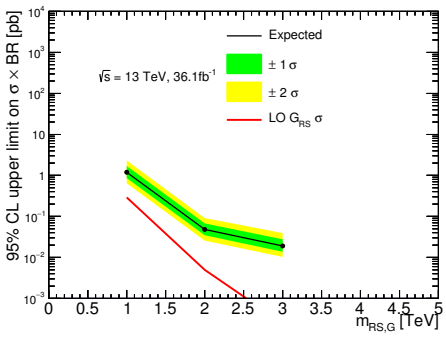

(b) Upper limits on $\sigma_{RS\text{graviton}}$

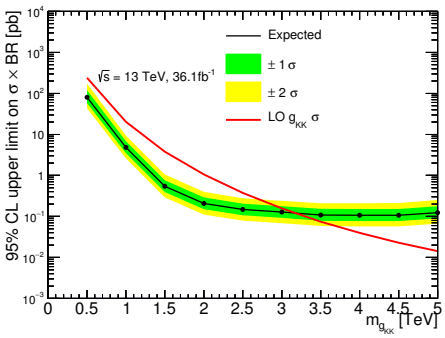

(c) Upper limits on $\sigma_{KK\text{gluon}}$

Figure 113: Extracted upper limits on Z', RS graviton and KK gluon production cross section.

10. Conclusions

In summary, we performed a search for resonances decaying into top and anti-top pair using all hadronic final state from data collected by the ATLAS detector at LHC. This analysis focuses on high mass signal, and the sensitivity is improved by combining several categories. Using a benchmark of BSM signal, Z', we expect upper limits on the production cross section of the Z' to be greater than 3.1 TeV, which significantly improves the past results in ATLAS. In addition, we also expect g_{KK} upper limits on the production cross section of the g_{KK} to be greater than 3.2 TeV.

Appendix

A. Results without liner function fit to estimate some systematic uncertainties

Some systematic uncertainties are estimated to fit a liner function, because those systematics are affected statistical fractuation for low statistics. Each systematic uncertainty is checked in each subsection, and estimated uncertainties are used to estimate the cross section with SR0+SR3 and to compare with the nominal result.

A.1. $t\bar{t}$ B-tagging

The mtt distributions for the systematic samples are compared with the nominal samples as can be found in Fig. 114-118. All the systematic uncertainties before the linear fit are smaller than the statistic uncertainty.

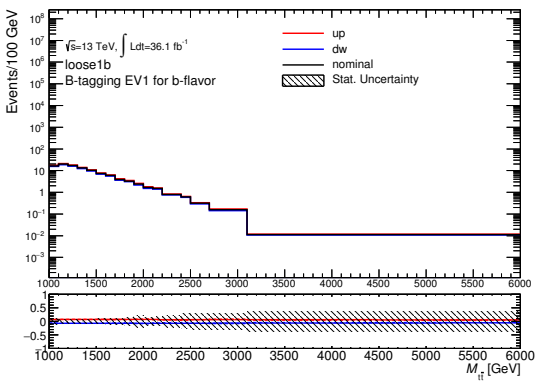

(a) 1 tight b-tagging loose+medium+tight category SR0

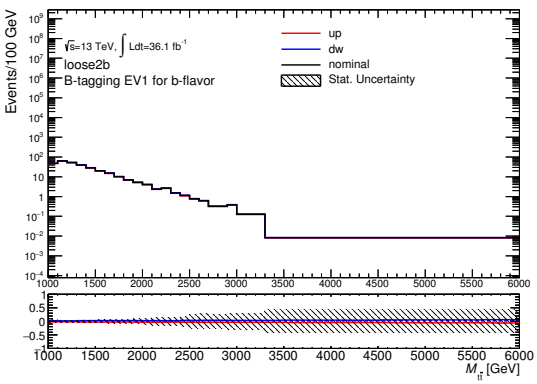

(b) 2 tight b-tagging loose+medium+tight category SR0

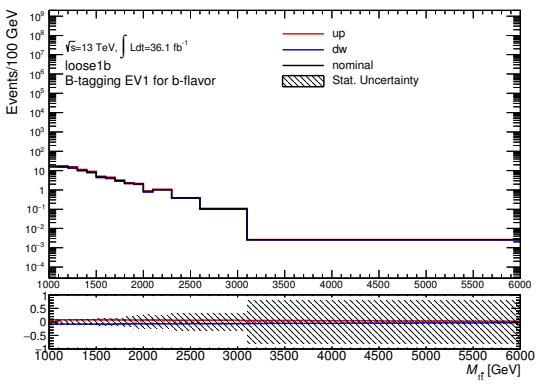

(c) 1 tight b-tagging loose+medium+tight category SR3

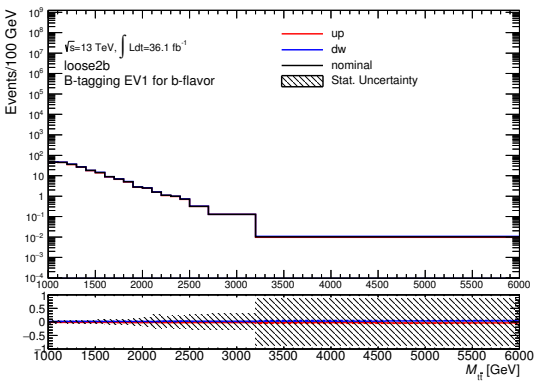

(d) 2 tight b-tagging loose+medium+tight category SR3

Figure 114: Systematics of B-tagging EV 1 of b-flavor for $t\bar{t}$

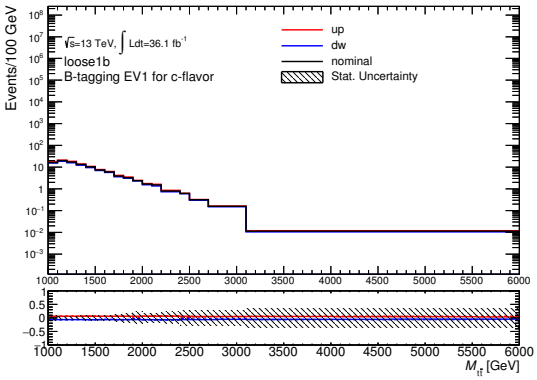

(a) 1 tight b-tagging loose+medium+tight category SR0

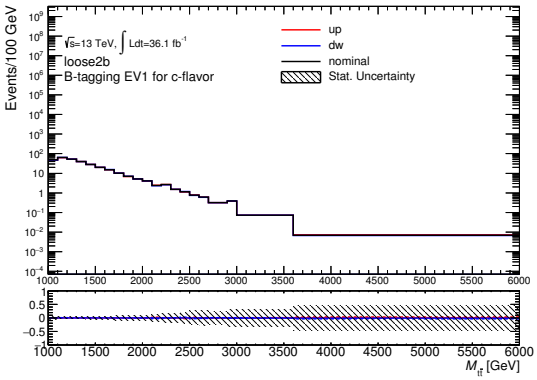

(b) 2 tight b-tagging loose+medium+tight category SR0

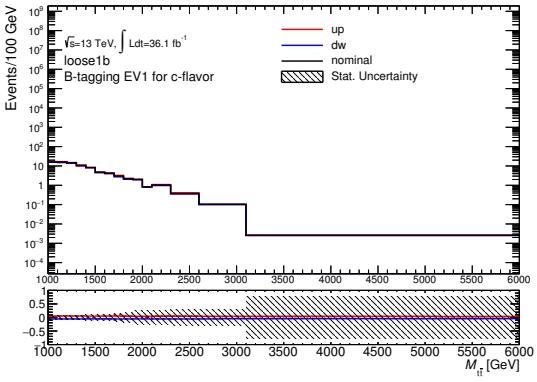

(c) 1 tight b-tagging loose+medium+tight category SR3

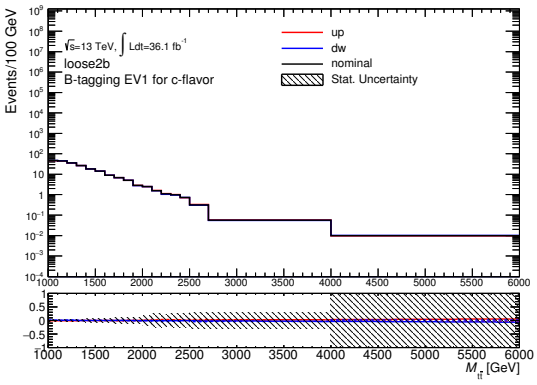

(d) 2 tight b-tagging loose+medium+tight category SR3

Figure 115: Systematics of B-tagging EV 1 of c-flavor for $t\bar{t}$

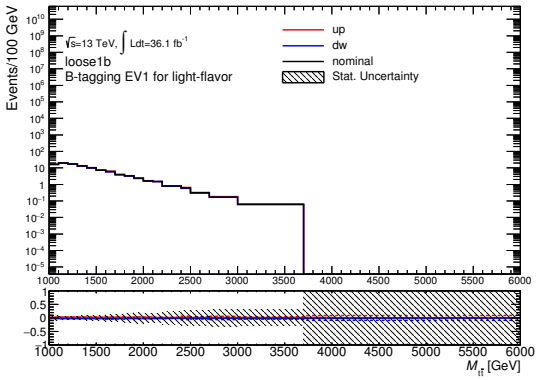

(a) 1 tight b-tagging loose+medium+tight category SR0

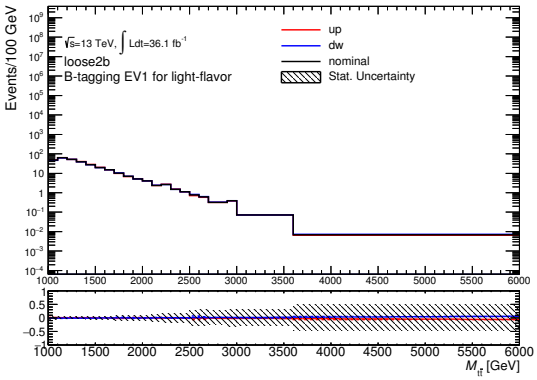

(b) 2 tight b-tagging loose+medium+tight category SR0

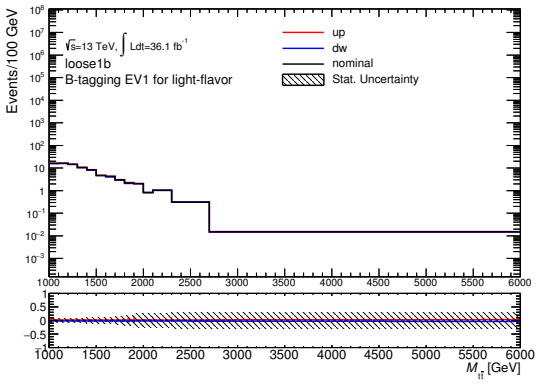

(c) 1 tight b-tagging loose+medium+tight category SR3

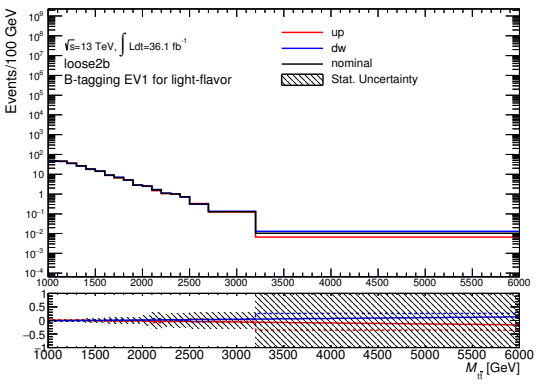

(d) 2 tight b-tagging loose+medium+tight category SR3

Figure 116: Systematics of B-tagging EV 1 of light-flavor for $t\bar{t}$

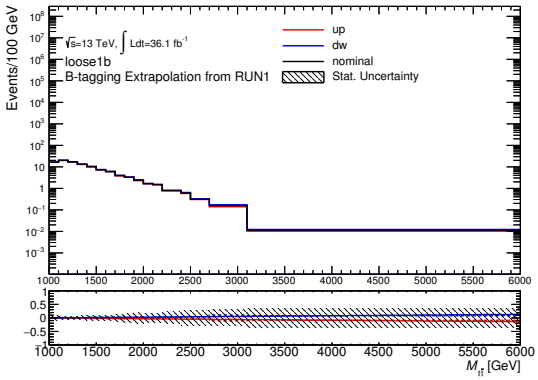

(a) 1 tight b-tagging loose+medium+tight category SR0

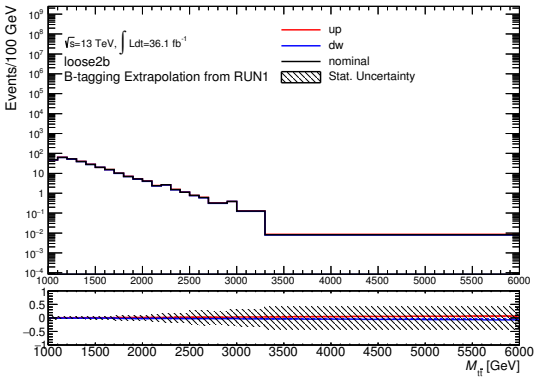

(b) 2 tight b-tagging loose+medium+tight category SR0

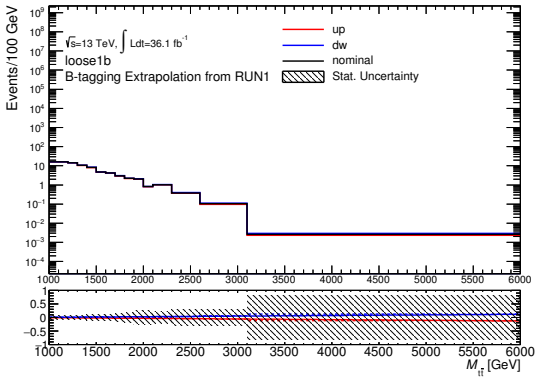

(c) 1 tight b-tagging loose+medium+tight category SR3

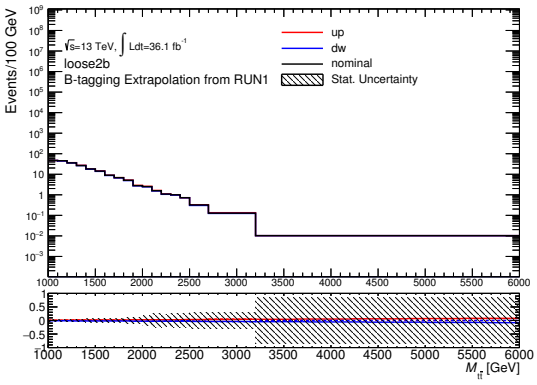

(d) 2 tight b-tagging loose+medium+tight category SR3

Figure 117: Systematics of B-tagging Extrapolation from RUN1 for $t\bar{t}$

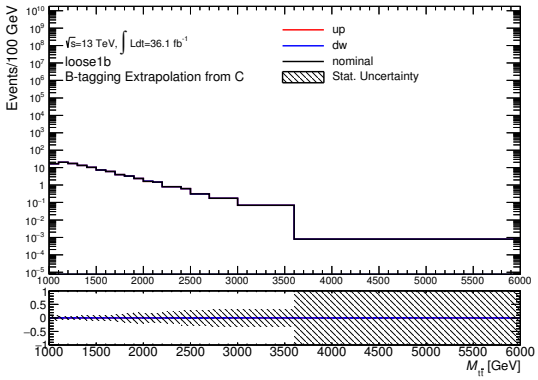

(a) 1 tight b-tagging loose+medium+tight category SR0

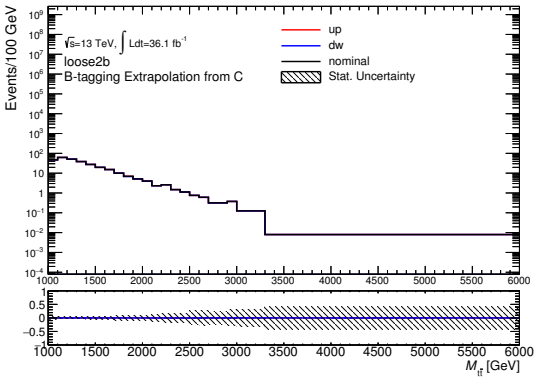

(b) 2 tight b-tagging loose+medium+tight category SR0

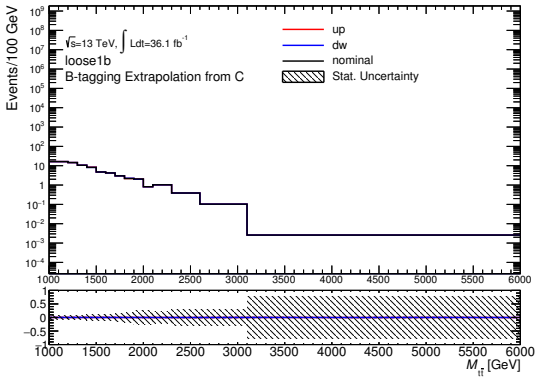

(c) 1 tight b-tagging loose+medium+tight category SR3

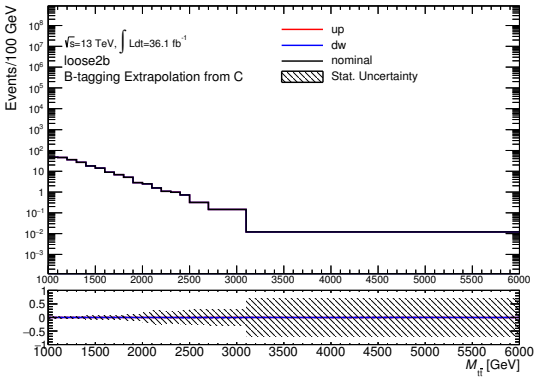

(d) 2 tight b-tagging loose+medium+tight category SR3

Figure 118: Systematics of B-tagging Extrapolation from c-tagging for $t\bar{t}$

A.2. $t\bar{t}$ Large-R jet uncertainty

Systematic varied distributions and nominal distribtuions are compared to in Fig. 119-125. All the systematic uncertainties before the linear fit are smaller than the statistic uncertainty.

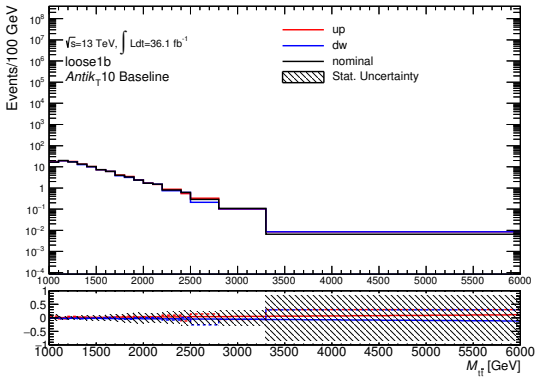

(a) 1 tight b-tagging loose+medium+tight category SR0

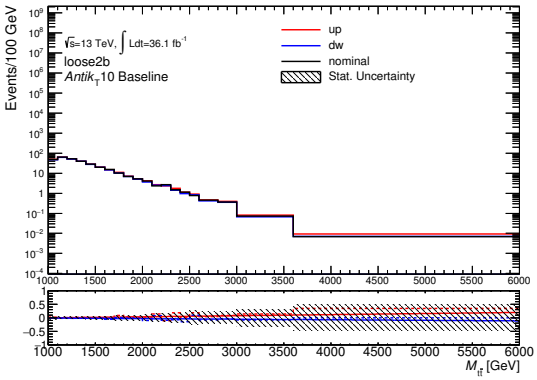

(b) 2 tight b-tagging loose+medium+tight category SR0

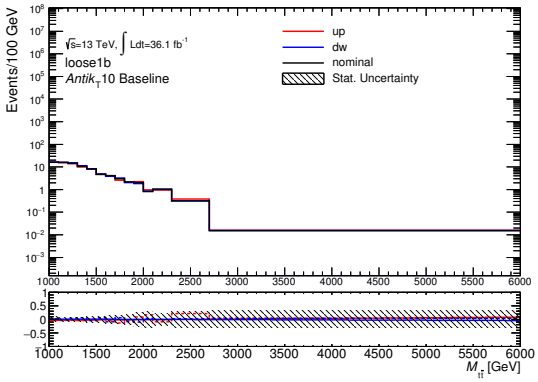

(c) 1 tight b-tagging loose+medium+tight category SR3

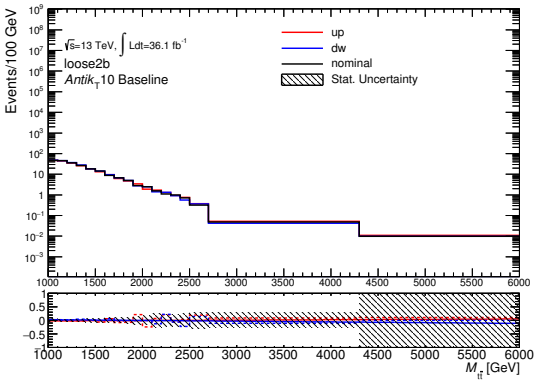

(d) 2 tight b-tagging loose+medium+tight category SR3

Figure 119: Systematics of Large-R jet baseline for $t\bar{t}$

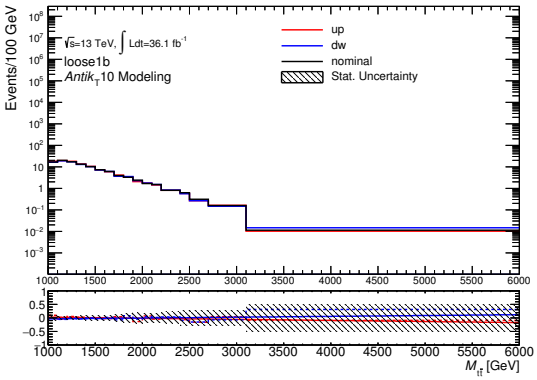

(a) 1 tight b-tagging loose+medium+tight category SR0

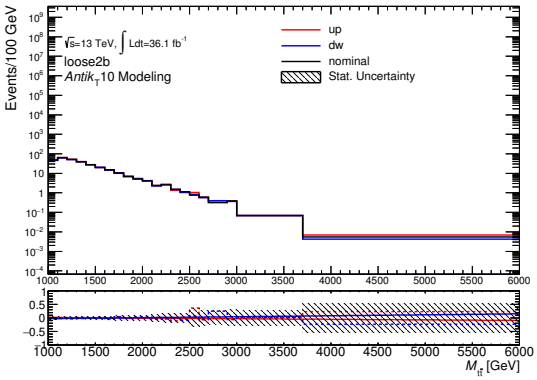

(b) 2 tight b-tagging loose+medium+tight category SR0

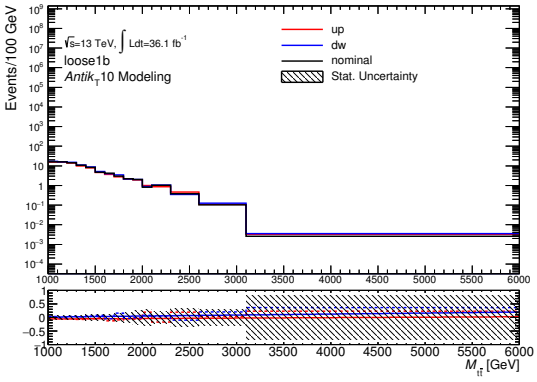

(c) 1 tight b-tagging loose+medium+tight category SR3

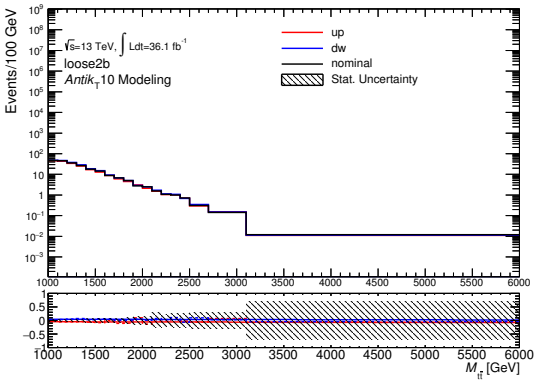

(d) 2 tight b-tagging loose+medium+tight category SR3

Figure 120: Systematics of Large-R jet modeling for $t\bar{t}$

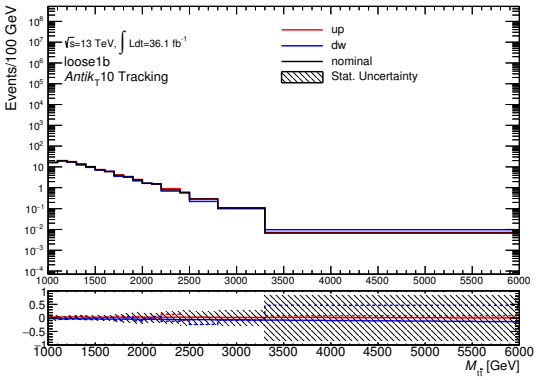

(a) 1 tight b-tagging loose+medium+tight category SR0

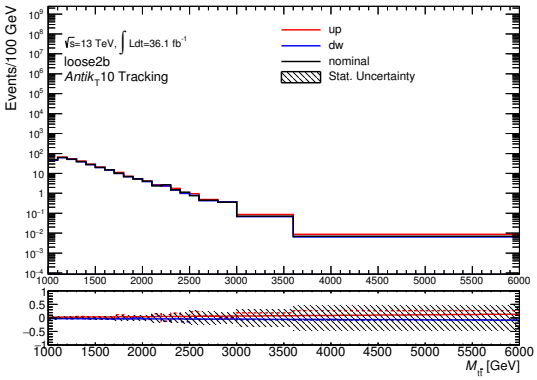

(b) 2 tight b-tagging loose+medium+tight category SR0

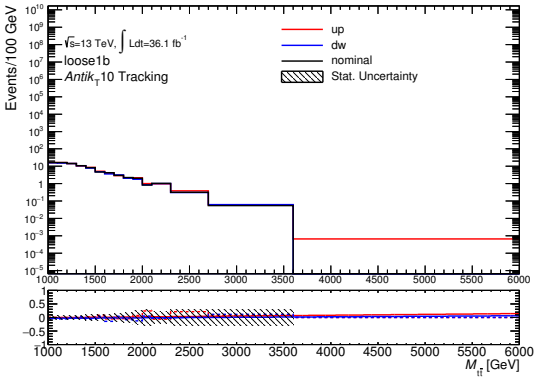

(c) 1 tight b-tagging loose+medium+tight category SR3

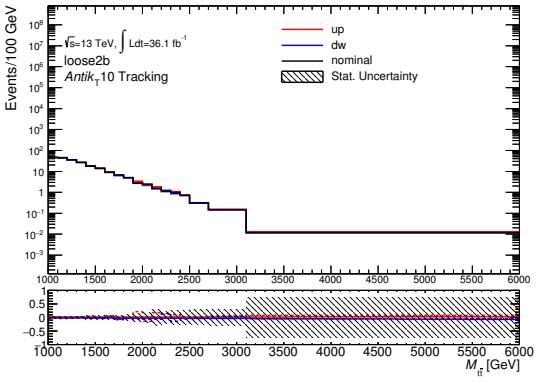

(d) 2 tight b-tagging loose+medium+tight category SR3

Figure 121: Systematics of Large-R jet track uncertainty for $t\bar{t}$

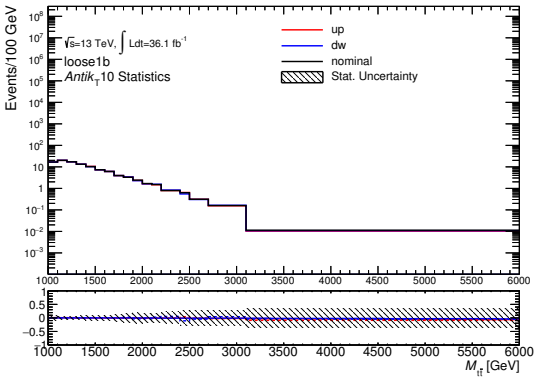

(a) 1 tight b-tagging loose+medium+tight category SR0

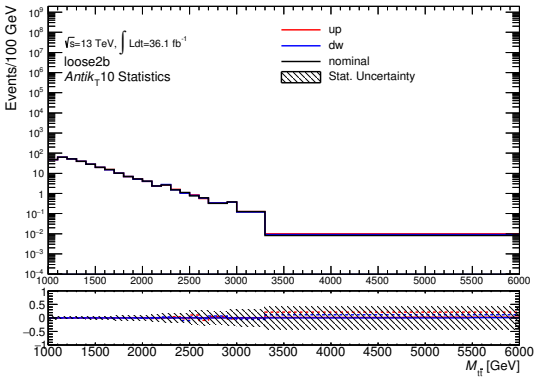

(b) 2 tight b-tagging loose+medium+tight category SR0

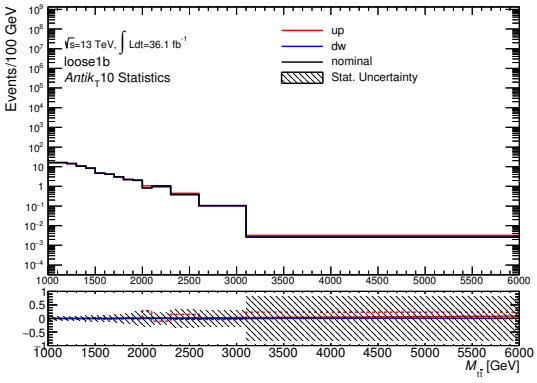

(c) 1 tight b-tagging loose+medium+tight category SR3

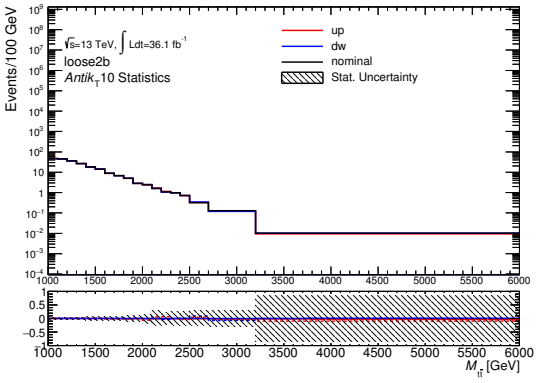

(d) 2 tight b-tagging loose+medium+tight category SR3

Figure 122: Systematics of Large-R jet statistics for $t\bar{t}$

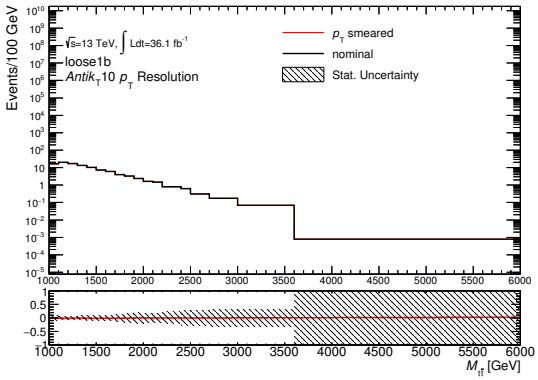

(a) 1 tight b-tagging loose+medium+tight category SR0

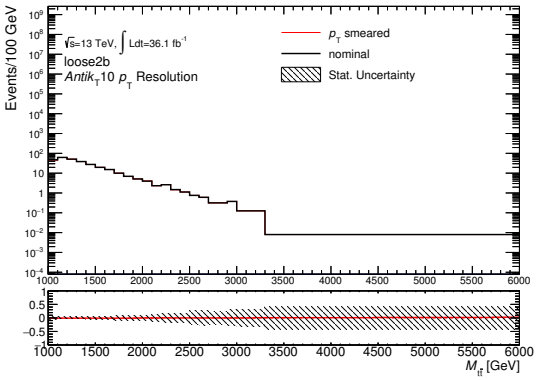

(b) 2 tight b-tagging loose+medium+tight category SR0

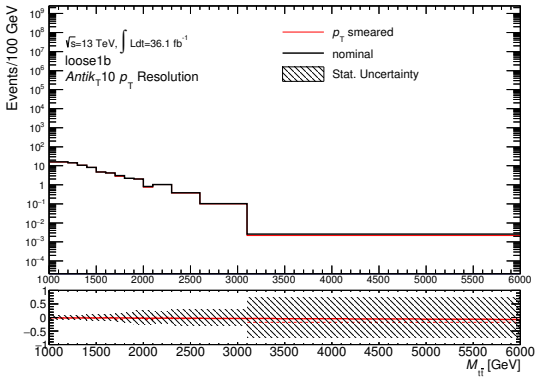

(c) 1 tight b-tagging loose+medium+tight category SR3

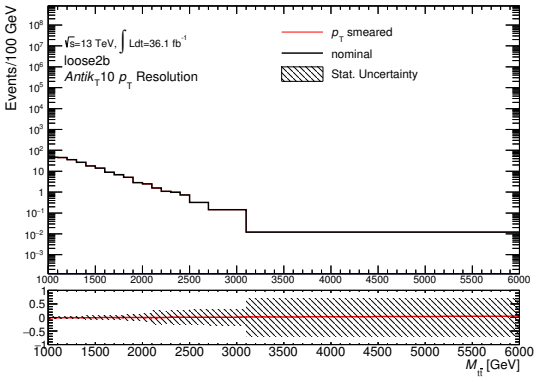

(d) 2 tight b-tagging loose+medium+tight category SR3

Figure 123: Systematics of Large-R jet p_T resolution for $t\bar{t}$

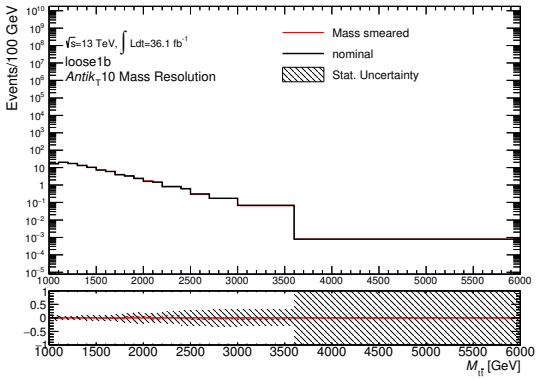

(a) 1 tight b-tagging loose+medium+tight category SR0

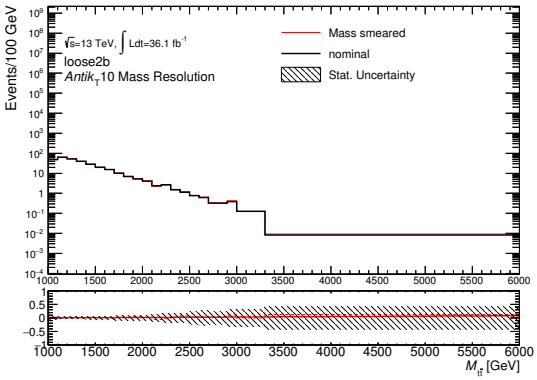

(b) 2 tight b-tagging loose+medium+tight category SR0

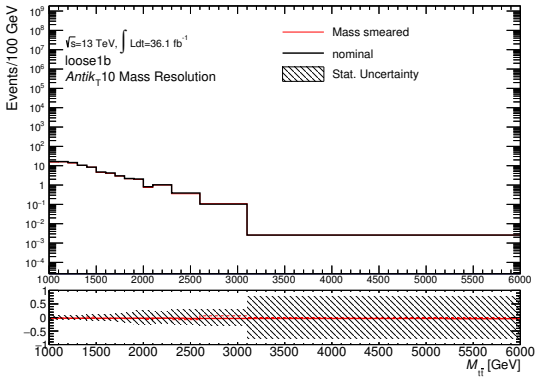

(c) 1 tight b-tagging loose+medium+tight category SR3

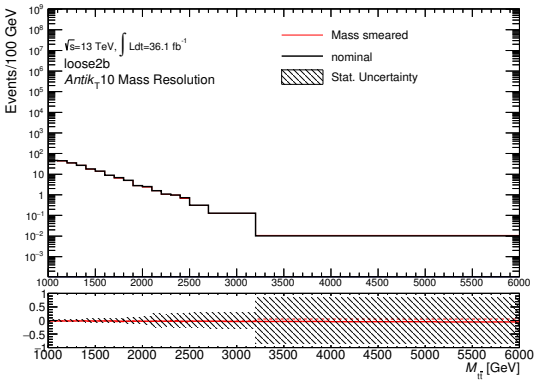

(d) 2 tight b-tagging loose+medium+tight category SR3

Figure 124: Systematics of Large-R jet mass resolution for $t\bar{t}$

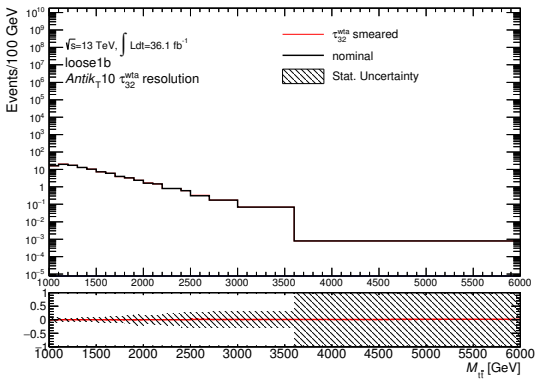

(a) 1 tight b-tagging loose+medium+tight category SR0

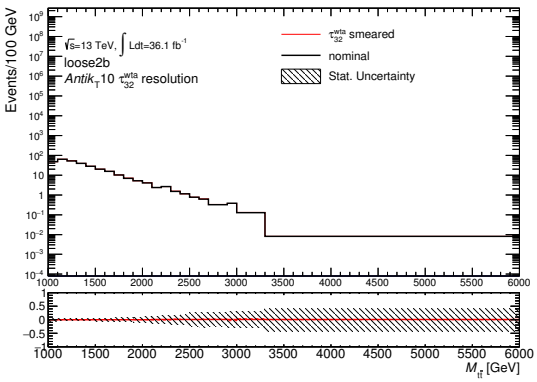

(b) 2 tight b-tagging loose+medium+tight category SR0

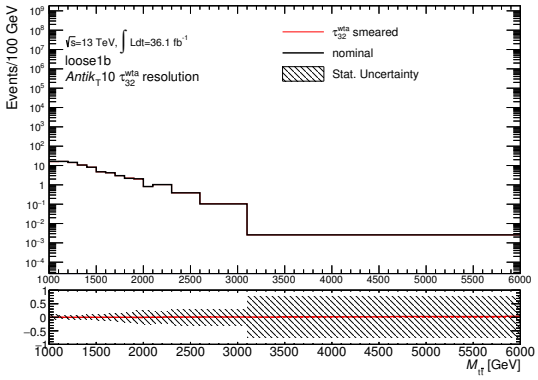

(c) 1 tight b-tagging loose+medium+tight category SR3

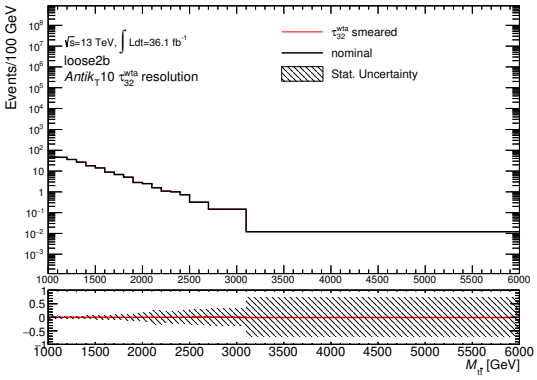

(d) 2 tight b-tagging loose+medium+tight category SR3

Figure 125: Systematics of Large-R jet τ_{32}^{wta} resolution for $t\bar{t}$

A.3. $t\bar{t}$ electroweak correction

Systematic varied distributions and nominal distribtuions are compared to in Fig. 126. All the systematic uncertainties before the linear fit are smaller than the statistic uncertainty.

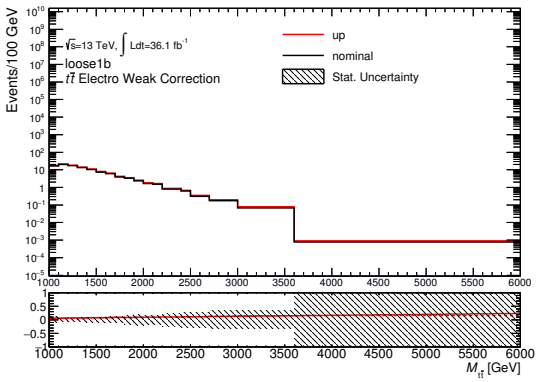

(a) 1 tight b-tagging loose+medium+tight category SR0

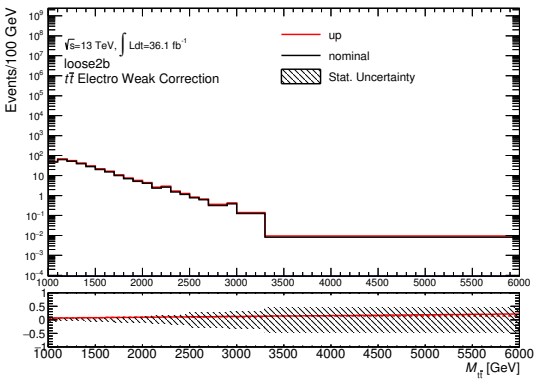

(b) 2 tight b-tagging loose+medium+tight category SR0

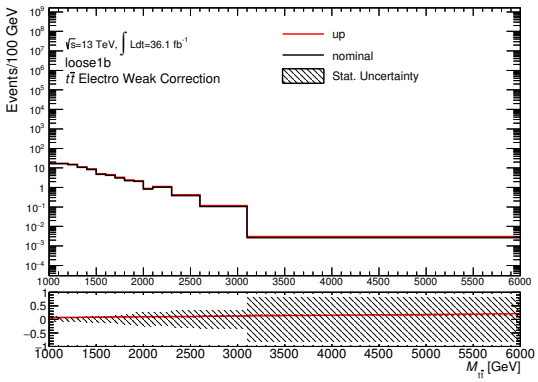

(c) 1 tight b-tagging loose+medium+tight category SR3

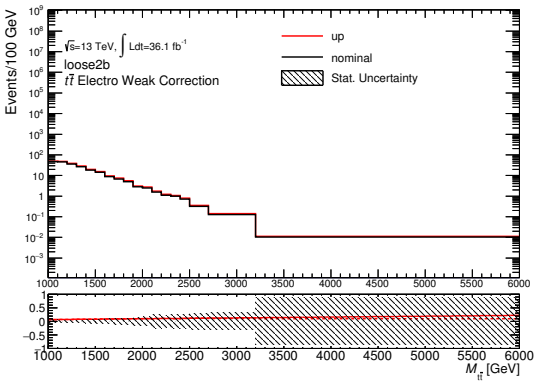

(d) 2 tight b-tagging loose+medium+tight category SR3

Figure 126: Systematics of electroweak correction for $t\bar{t}$

A.4. $t\bar{t}$ generator

Systematic varied distributions and nominal distribtuions are compared to in Fig. 127. All the systematic uncertainties before the linear fit are smaller than the statistic uncertainty.

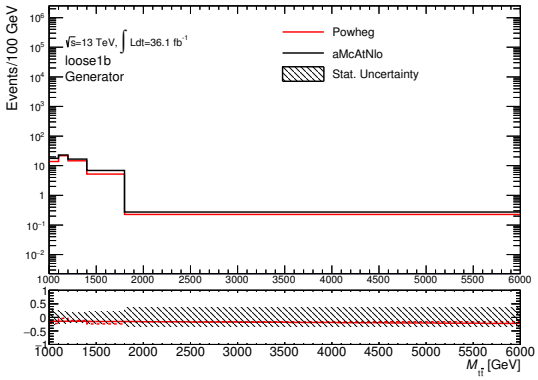

(a) 1 tight b-tagging loose+medium+tight category SR0

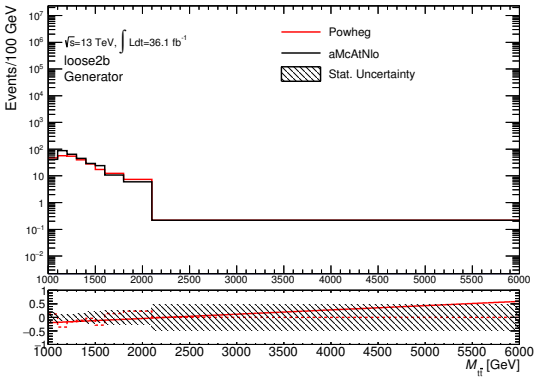

(b) 2 tight b-tagging loose+medium+tight category SR0

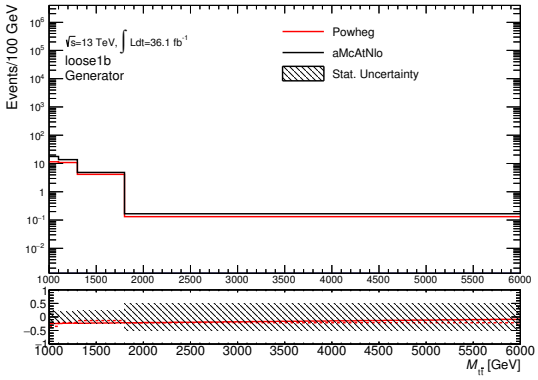

(c) 1 tight b-tagging loose+medium+tight category SR3

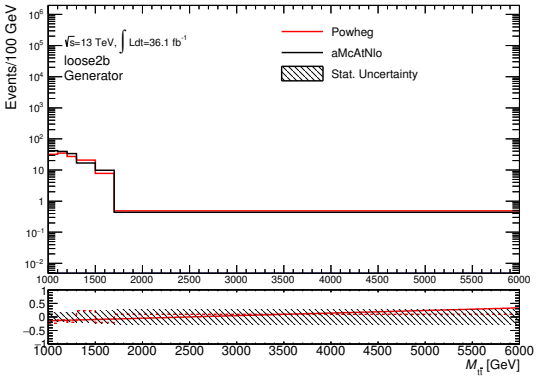

(d) 2 tight b-tagging loose+medium+tight category SR3

Figure 127: Systematics of generator for $t\bar{t}$

A.5. $t\bar{t}$ parton shower model

Systematic varied distributions and nominal distribtuions are compared to in Fig. 128. All the systematic uncertainties before the linear fit are smaller than the statistic uncertainty.

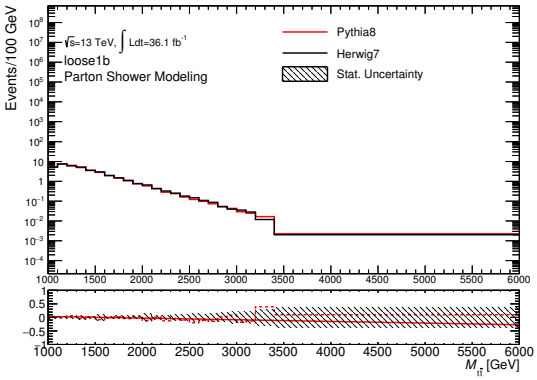

(a) 1 tight b-tagging loose+medium+tight category SR0

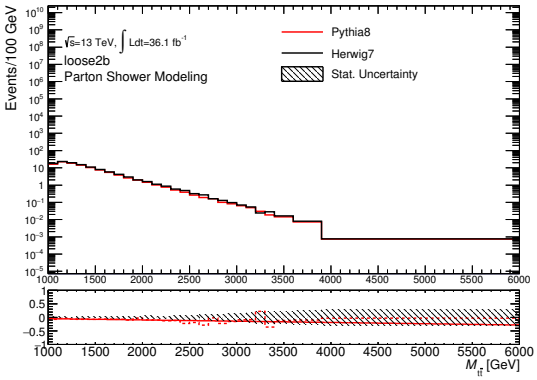

(b) 2 tight b-tagging loose+medium+tight category SR0

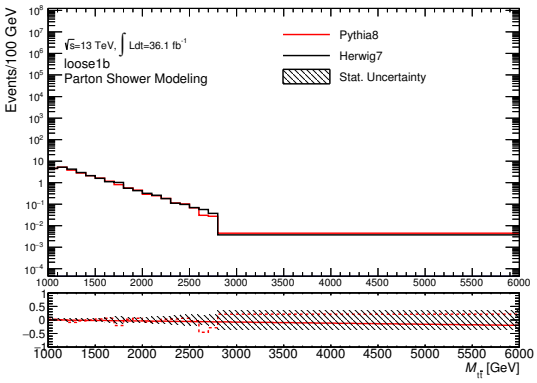

(c) 1 tight b-tagging loose+medium+tight category SR3

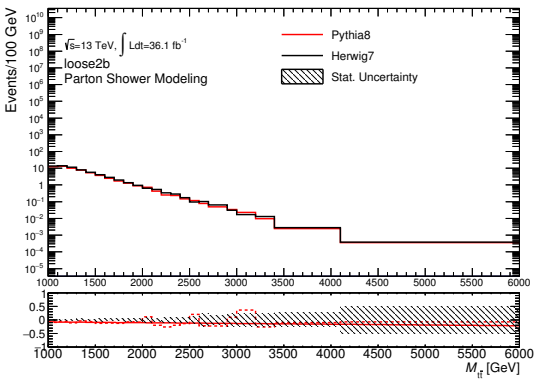

(d) 2 tight b-tagging loose+medium+tight category SR3

Figure 128: Systematics of parton shower for $t\bar{t}$

A.6. $t\bar{t}$ ISR/FSR

Systematic varied distributions and nominal distribtuions are compared to in Fig. 129. All the systematic uncertainties before the linear fit are smaler than the statistic uncertainty.

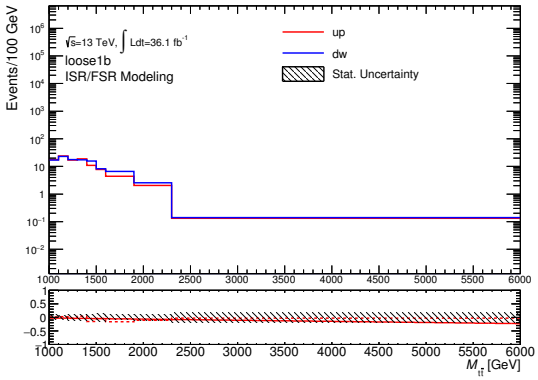

(a) 1 tight b-tagging loose+medium+tight category SR0

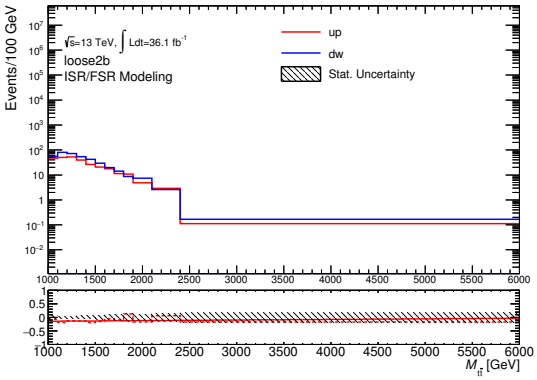

(b) 2 tight b-tagging loose+medium+tight category SR0

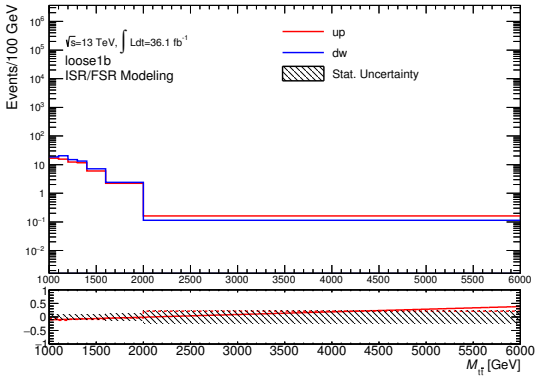

(c) 1 tight b-tagging loose+medium+tight category SR3

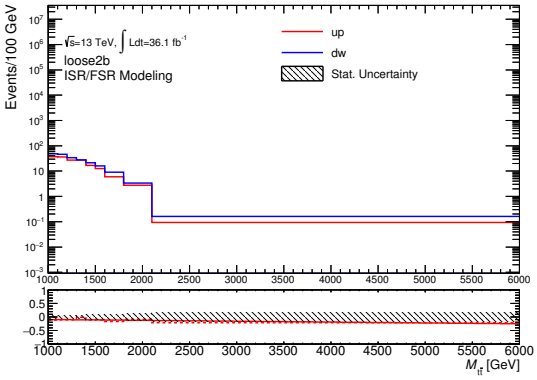

(d) 2 tight b-tagging loose+medium+tight category SR3

Figure 129: Systematics of ISR/FSR for $t\bar{t}$

A.7. $t\bar{t}$ PDF

Systematic varied distributions and nominal distribtuions are compared to in Fig. 130. All the systematic uncertainties before the linear fit are smaler than the statistic uncertainty.

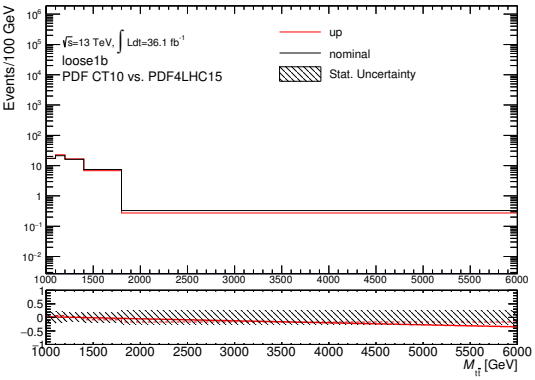

(a) 1 tight b-tagging loose+medium+tight category SR0

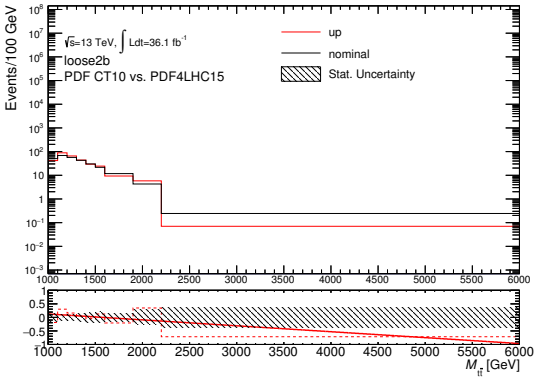

(b) 2 tight b-tagging loose+medium+tight category SR0

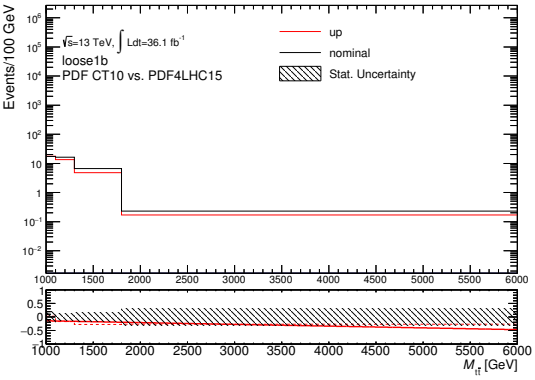

(c) 1 tight b-tagging loose+medium+tight category SR3

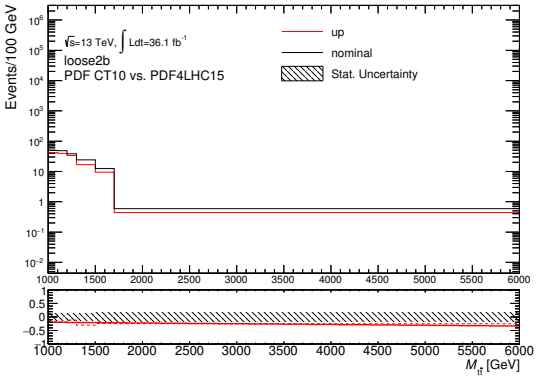

(d) 2 tight b-tagging loose+medium+tight category SR3

Figure 130: Systematics of PDF for $t\bar{t}$

A.8. The result without liner fit to estimate systematic uncertainty

Conditions are same as nominal except for some systematic uncertainties which are estimated without liner fit. Nuisance parameter pulls are showed in Fig. 131.

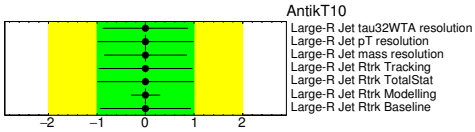

(a) NuisPar AntikT10

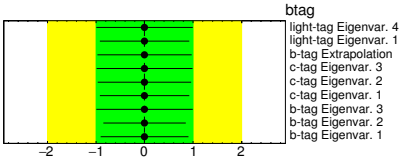

(b) NuisPar btag

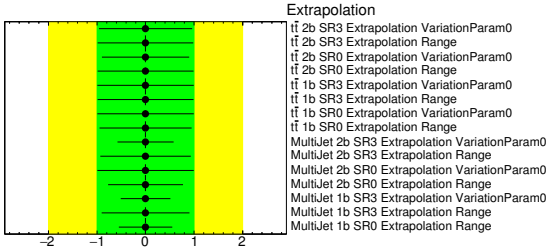

(c) NuisPar Extrapolation

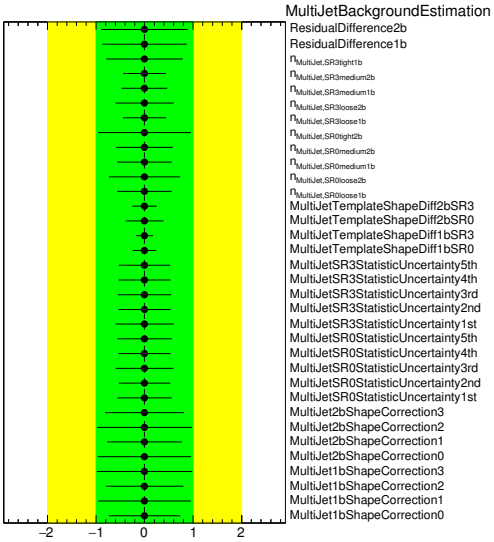

(d) NuisPar multijet

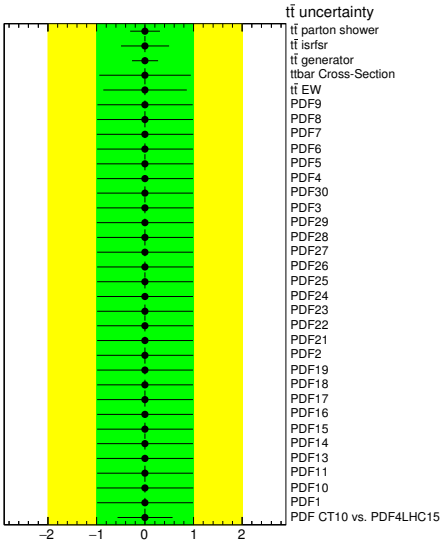

(e) NuisPar ttbar

Figure 131: Nuisance parameters for the fitting.

Correlation matrix are showed in Fig. 132.

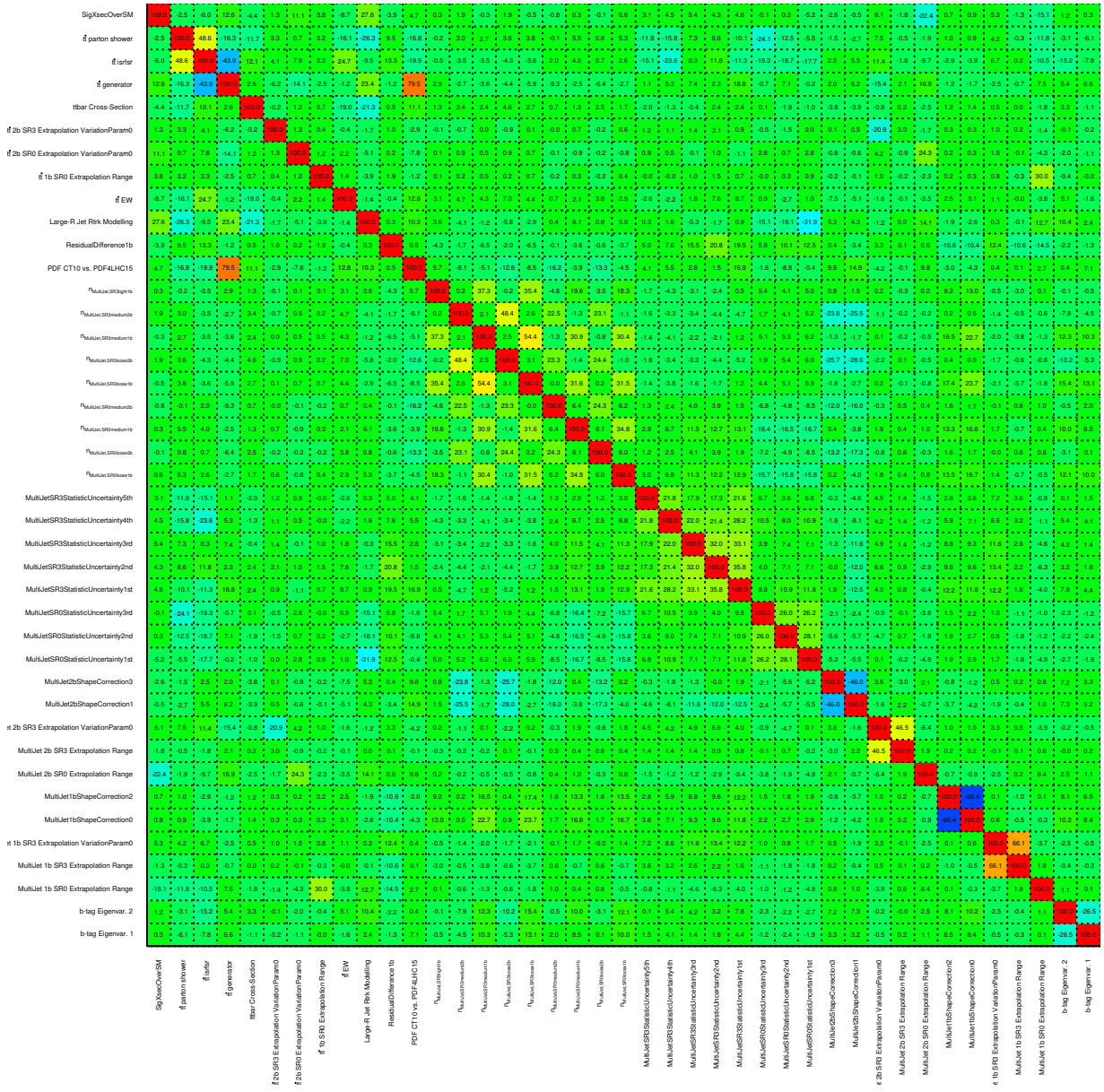

Figure 132: Correlation matrix (Showed nuisance parameters have correlattion value over 20%).

Pre-fit and Post-fit $m_{t\bar{t}}$ distributions are showed in Fig. 133, 134 135 and 136.

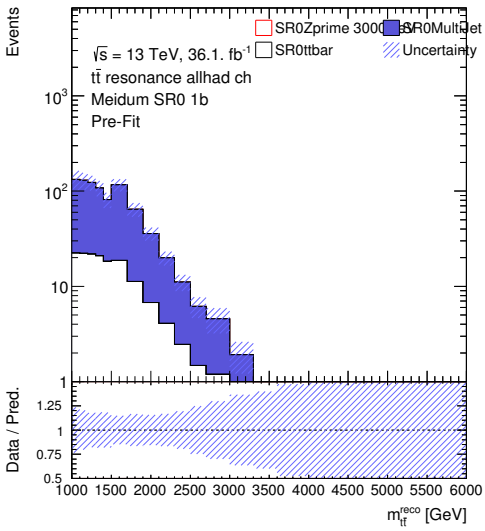

(a) Pre-fit for one tight b-tagged Medium

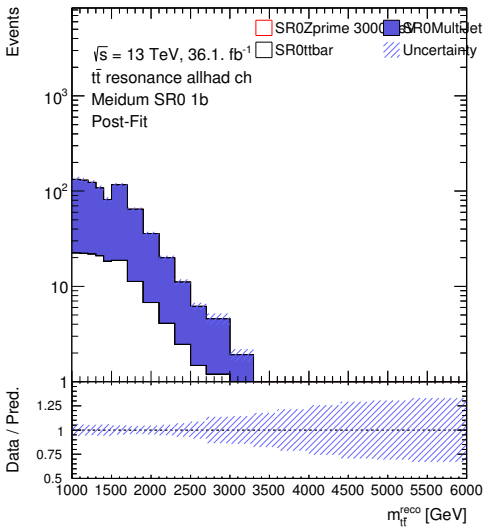

(b) Post-fit for one tight b-tagged Medium

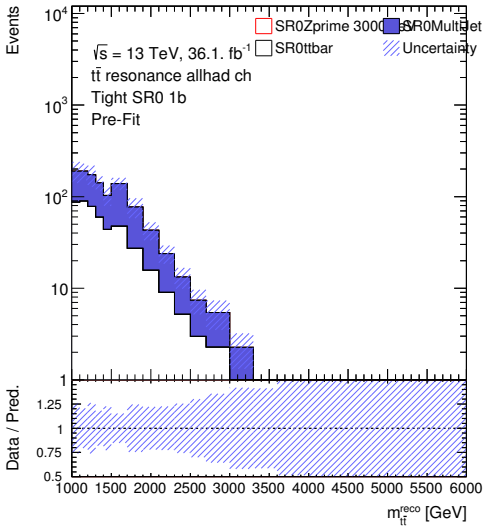

(c) Pre-fit for one tight b-tagged Tight

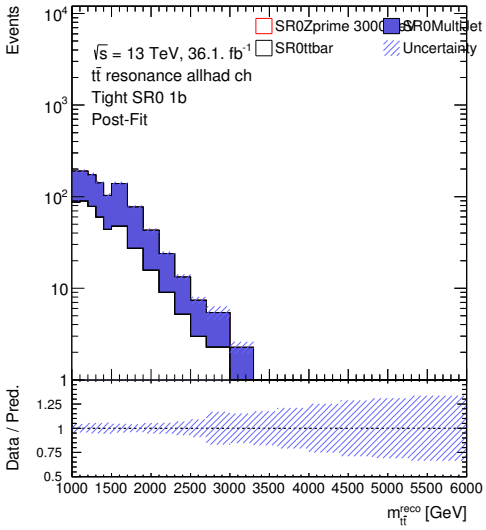

(d) Post-fit for one tight b-tagged Tight

Figure 133: Pre-fit and Post-fit distributions for one tight b-tagged SR0

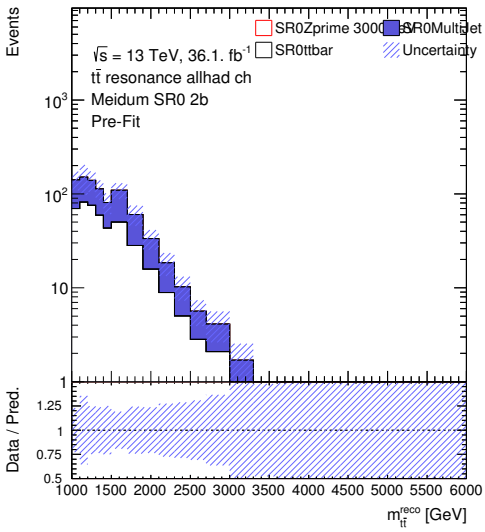

(a) Post-fit for two tight b-tagged Medium

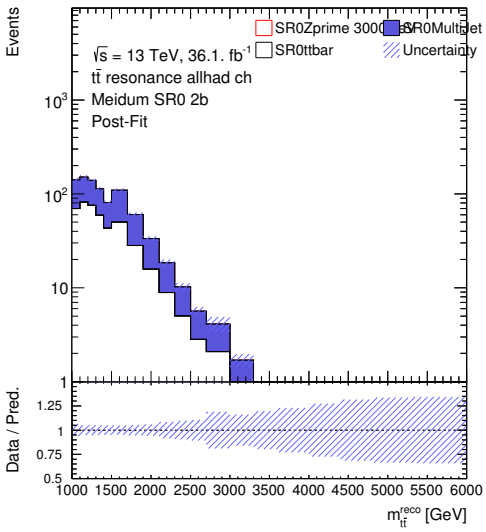

(b) Post-fit for two tight b-tagged Medium

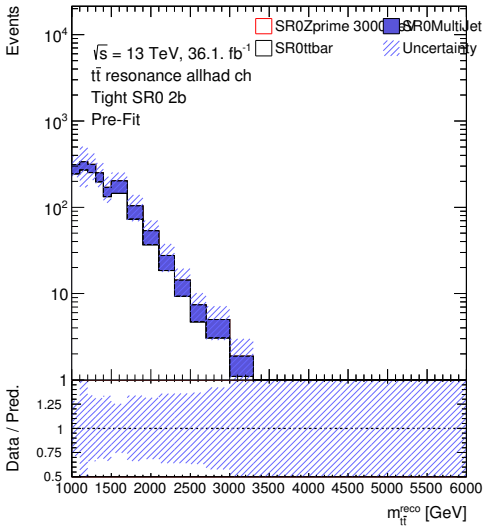

(c) Post-fit for two tight b-tagged Tight

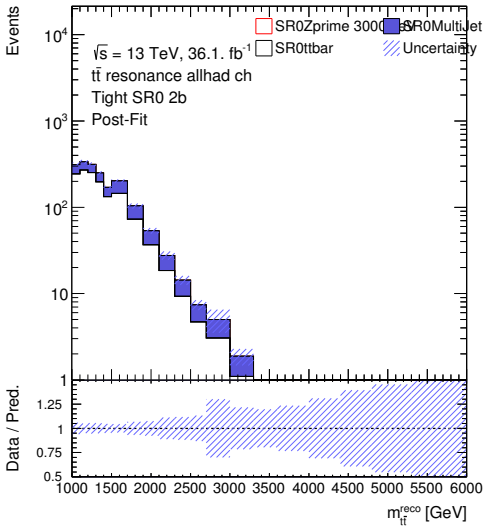

(d) Pre-fit for two tight b-tagged Tight

Figure 134: Pre-fit and Post-fit distributions for two tight b-tagged SR0

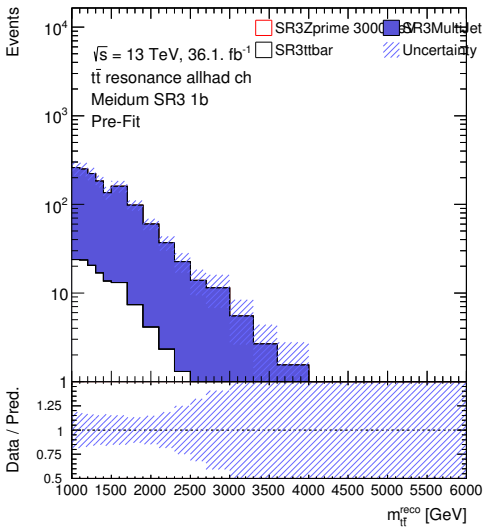

(a) Pre-fit for one tight b-tagged Medium

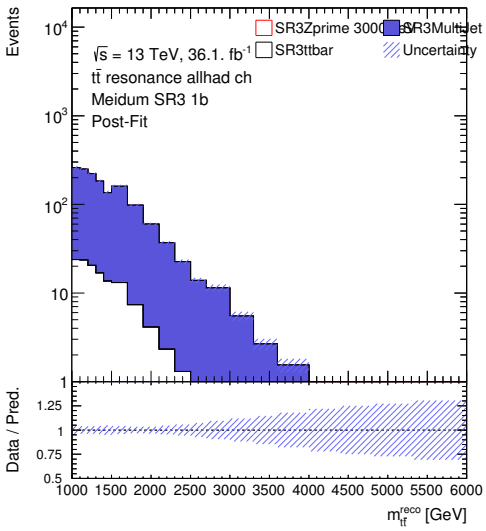

(b) Post-fit for one tight b-tagged Medium

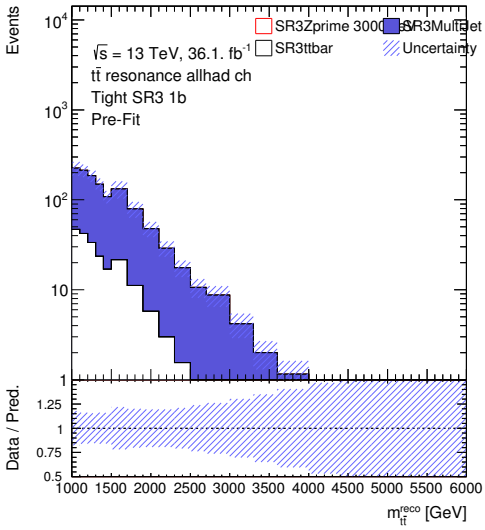

(c) Pre-fit for one tight b-tagged Tight

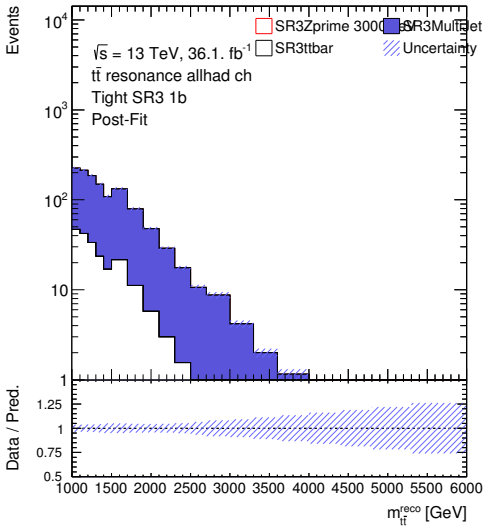

(d) Post-fit for one tight b-tagged Tight

Figure 135: Pre-fit and Post-fit distributions for one tight b-tagged SR3

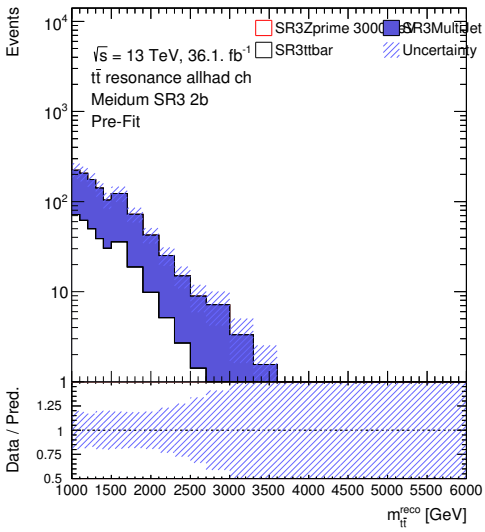

(a) Post-fit for two tight b-tagged Medium

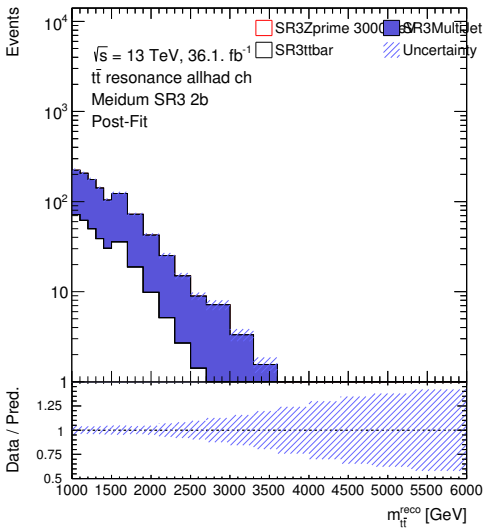

(b) Post-fit for two tight b-tagged Medium

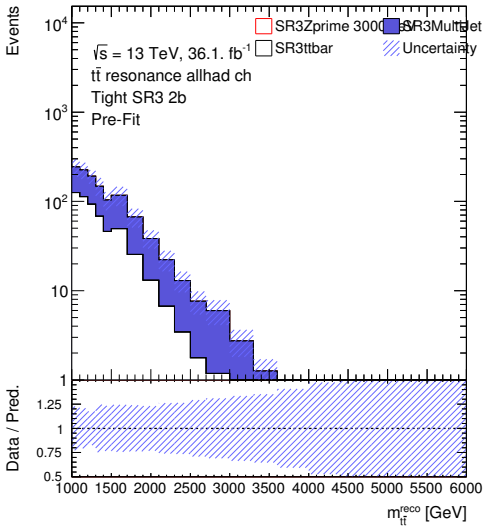

(c) Post-fit for two tight b-tagged Tight

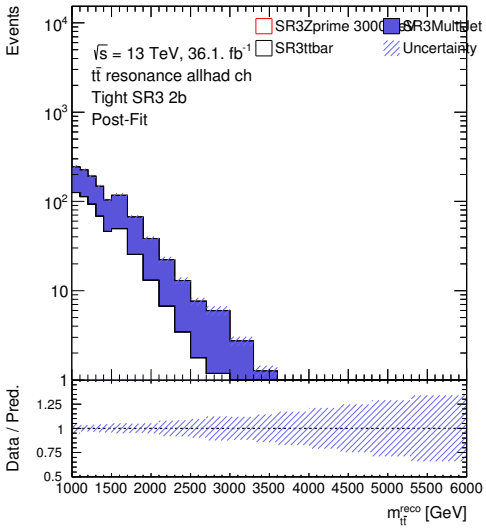

(d) Post-fit for two tight b-tagged Tight

Figure 136: Pre-fit and Post-fit distributions for two tight b-tagged SR3

Fit result is showed in Fig. 137. Comarison of cross section limits between nominal and without liner fit to estimate systematic uncertainties is summarized in Table 18. The higher masss limit are worse if systematic uncertaities are estimated without liner fit, because higher mass bins are low statistics and cover wide $m_{t\bar{t}}$ region. Therefore systematic uncertainties are reasonablly estimated with liner fit to estimate them.

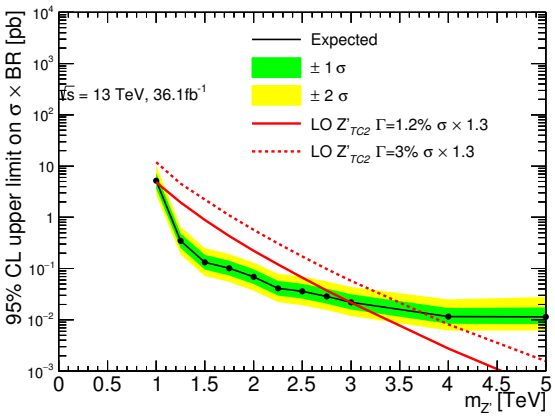

(a) Upper limits on $\sigma_{Z'}$

Figure 137: Extracted upper limits on Z'

Mass Points (TeV)	1	1.25	1.5	1.75	2	2.25	2.5	2.75	3	4	5
SR0+SR3	3.57	0.24	0.11	0.088	0.055	0.041	0.034	0.029	0.024	0.014	0.014
No liner fit	5.16	0.35	0.13	0.10	0.069	0.041	0.036	0.029	0.022	0.012	0.012
Residual(%)	-0.8	12.5	9.1	-2.3	7.3	7.3	11.7	10.3	0	0	0

Table 18: Expected cross-section limits for each Z' mass point. Residual means ((No liner fit)-(Nominal))/(Nominal).

B. Summary of relative systematic effect on each region

Table 19: Relative effect of each systematic on the yields for one tigth b-tagged Tight SR0.

	Multijet	$t\bar{t}$	Z' 3 TeV
MultiJet one tight b-tag ShapeCorrection0	0.0321 / -0.0321	0 / 0	0 / 0
MultiJet one tight b-tag ShapeCorrection1	0.0241 / -0.0241	0 / 0	0 / 0
MultiJet one tight b-tag ShapeCorrection2	-0.0277 / 0.0277	0 / 0	0 / 0
ResidualDifference one tight b-tag	-0.00256 / 0.00256	0 / 0	0 / 0
MultiJetSR0StatisticUncertainty1st	0.00817 / -0.00817	0 / 0	0 / 0
MultiJetSR0StatisticUncertainty2nd	0.009 / -0.009	0 / 0	0 / 0
MultiJetSR0StatisticUncertainty3rd	0.00792 / -0.00792	0 / 0	0 / 0
MultiJetSR0StatisticUncertainty4th	0.00725 / -0.00725	0 / 0	0 / 0
MultiJetSR0StatisticUncertainty5th	0.006 / -0.006	0 / 0	0 / 0
MultiJetTemplateShapeDiff one tight b-tag SR0	-0.0527 / 0.0527	0 / 0	0 / 0
Normalization factor for SR0 Tight one tight b-tag	0.0471 / -0.0432	0 / 0	0 / 0
MultiJet SR0 Extrapolation Range	-7.38e-07 / 7.38e-07	0 / 0	0 / 0
MultiJet SR0 Extrapolation VariationParam0	0.00313 / -0.00313	0 / 0	0 / 0
MultiJet SR0 Extrapolation VariationParam1	5.52e-07 / -5.52e-07	0 / 0	0 / 0
Luminocity	0 / 0	0.021 / -0.021	0.021 / -0.021
b-tag Eigenvar. 1	0 / 0	0.071 / -0.071	0.0727 / -0.0727
b-tag Eigenvar. 2	0 / 0	0.0657 / -0.0657	0.0914 / -0.0914
b-tag Eigenvar. 3	0 / 0	-0.00282 / 0.00282	0.00735 / -0.00735
b-tag Eigenvar. 4	0 / 0	-0.00123 / 0.00123	0.00341 / -0.00341
c-tag Eigenvar. 1	0 / 0	0.0649 / -0.0649	0.0505 / -0.0505
c-tag Eigenvar. 2	0 / 0	0.0377 / -0.0377	0.0342 / -0.0342
c-tag Eigenvar. 3	0 / 0	0.0228 / -0.0228	0.0218 / -0.0218
c-tag Eigenvar. 4	0 / 0	0.009 / -0.009	0.00883 / -0.00883
light-tag Eigenvar. 1	0 / 0	0.026 / -0.026	0.00999 / -0.00999
light-tag Eigenvar. 2	0 / 0	-0.00876 / 0.00876	-0.00642 / 0.00642
light-tag Eigenvar. 3	0 / 0	0.00366 / -0.00366	0.00341 / -0.00341
light-tag Eigenvar. 4	0 / 0	-0.0096 / 0.0096	-0.00889 / 0.00889
light-tag Eigenvar. 5	0 / 0	-0.00332 / 0.00332	-0.00268 / 0.00268
light-tag Eigenvar. 6	0 / 0	-0.000586 / 0.000586	-0.000158 / 0.000158
light-tag Eigenvar. 7	0 / 0	0.00128 / -0.00128	0.00064 / -0.00064
light-tag Eigenvar. 8	0 / 0	-0.000509 / 0.000509	-0.000748 / 0.000748
light-tag Eigenvar. 9	0 / 0	-0.000253 / 0.000253	-0.000316 / 0.000316
light-tag Eigenvar. 10	0 / 0	-0.000671 / 0.000671	-0.00029 / 0.00029
light-tag Eigenvar. 11	0 / 0	-0.000531 / 0.000531	-0.000386 / 0.000386
light-tag Eigenvar. 12	0 / 0	0.000192 / -0.000192	9.7e-05 / -9.7e-05
b-tag Extrapolation from RUN1	0 / 0	-0.0123 / 0.0123	-0.0771 / 0.0771
b-tag Extrapolation from c-tag	0 / 0	-0.000246 / 0.000246	-0.000592 / 0.000592
Large-R Jet Baseline	0 / 0	0.0173 / -0.0173	-0.0268 / 0.0268
Large-R Jet Modelling	0 / 0	0.0186 / -0.0186	-0.0229 / 0.0229
Large-R Jet TotalStat	0 / 0	0.000929 / -0.000929	-0.0121 / 0.0121
Large-R Jet Tracking	0 / 0	0.0338 / -0.0338	-0.0351 / 0.0351
Large-R Jet p_T resolution	0 / 0	-0.00829 / 0.00829	-0.00216 / 0.00216
Large-R Jet mass resolution	0 / 0	-0.00072 / 0.00072	0.00344 / -0.00344
Large-R Jet τ_{32}^{wta} resolution	0 / 0	-0.000255 / 0.000255	0.00202 / -0.00202
$t\bar{t}$ Cross-Section	0 / 0	0.056 / -0.061	0 / 0
$t\bar{t}$ generator	0 / 0	-0.146 / 0.146	0 / 0
$t\bar{t}$ parton shower	0 / 0	0.0136 / -0.0136	0 / 0
$t\bar{t}$ isrfsr	0 / 0	-0.0372 / 0.0372	0 / 0
$t\bar{t}$ EW	0 / 0	0.0744 / -0.0744	0 / 0
PDF CT10 vs. PDF4LHC15	0 / 0	-0.00215 / 0.00215	0 / 0
PDF1	0 / 0	0.00436 / -0.00436	0 / 0
PDF2	0 / 0	0.00672 / -0.00672	0 / 0
PDF3	0 / 0	-0.00338 / 0.00338	0 / 0
PDF4	0 / 0	0.00293 / -0.00293	0 / 0
PDF5	0 / 0	-0.0021 / 0.0021	0 / 0
PDF6	0 / 0	-0.00674 / 0.00674	0 / 0
PDF7	0 / 0	-0.000296 / 0.000296	0 / 0
PDF8	0 / 0	0.00428 / -0.00428	0 / 0
PDF9	0 / 0	0.00161 / -0.00161	0 / 0
PDF10	0 / 0	0.00115 / -0.00115	0 / 0
PDF11	0 / 0	0.00433 / -0.00433	0 / 0
PDF12	0 / 0	-0.000666 / 0.000666	0 / 0
PDF13	0 / 0	0.00193 / -0.00193	0 / 0
PDF14	0 / 0	0.00536 / -0.00536	0 / 0
PDF15	0 / 0	0.00327 / -0.00327	0 / 0
PDF16	0 / 0	0.00315 / -0.00315	0 / 0
PDF17	0 / 0	0.00278 / -0.00278	0 / 0
PDF18	0 / 0	0.00927 / -0.00927	0 / 0
PDF19	0 / 0	0.00607 / -0.00607	0 / 0
PDF20	0 / 0	-0.0021 / 0.0021	0 / 0
PDF21	0 / 0	0.00542 / -0.00542	0 / 0
PDF22	0 / 0	0.00332 / -0.00332	0 / 0
PDF23	0 / 0	0.0136 / -0.0136	0 / 0
PDF24	0 / 0	0.0048 / -0.0048	0 / 0
PDF25	0 / 0	0.00381 / -0.00381	0 / 0
PDF26	0 / 0	0.00405 / -0.00405	0 / 0
PDF27	0 / 0	0.00513 / -0.00513	0 / 0
PDF28	0 / 0	0.00283 / -0.00283	0 / 0
PDF29	0 / 0	0.00693 / -0.00693	0 / 0
PDF30	0 / 0	0.00463 / -0.00463	0 / 0
$t\bar{t}$ SR0 Extrapolation Range	0 / 0	-2.21e-05 / 2.21e-05	0 / 0
$t\bar{t}$ SR0 Extrapolation VariationParam0	0 / 0	0.000414 / -0.000414	0 / 0
$t\bar{t}$ SR0 Extrapolation VariationParam1	0 / 0	-4.83e-06 / 4.83e-06	0 / 0

Table 20: Relative effect of each systematic on the yields for two tigth b-tagged Medium SR0.

	Multijet	$t\bar{t}$	Z' 3 TeV
MultiJet two tight b-tag ShapeCorrection0	0.0327 / -0.0327	0 / 0	0 / 0
MultiJet two tight b-tag ShapeCorrection1	0.0239 / -0.0239	0 / 0	0 / 0
MultiJet two tight b-tag ShapeCorrection2	-0.0281 / 0.0281	0 / 0	0 / 0
ResidualDifference two tight b-tag	-0.0014 / 0.0014	0 / 0	0 / 0
MultiJetSR0StatisticUncertainty1st	0.00856 / -0.00856	0 / 0	0 / 0
MultiJetSR0StatisticUncertainty2nd	0.00924 / -0.00924	0 / 0	0 / 0
MultiJetSR0StatisticUncertainty3rd	0.00801 / -0.00801	0 / 0	0 / 0
MultiJetSR0StatisticUncertainty4th	0.00729 / -0.00729	0 / 0	0 / 0
MultiJetSR0StatisticUncertainty5th	0.0059 / -0.0059	0 / 0	0 / 0
MultiJetTemplateShapeDiff two tight b-tag SR0	-0.0634 / 0.0634	0 / 0	0 / 0
Normalization factor for SR0 Medium two tight b-tag	0.0748 / -0.108	0 / 0	0 / 0
MultiJet SR0 Extrapolation Range	1.26e-07 / -1.26e-07	0 / 0	0 / 0
MultiJet SR0 Extrapolation VariationParam0	0.00317 / -0.00317	0 / 0	0 / 0
MultiJet SR0 Extrapolation VariationParam1	-1.61e-06 / 1.61e-06	0 / 0	0 / 0
Luminocity	0 / 0	0.021 / -0.021	0.021 / -0.021
b-tag Eigenvar. 1	0 / 0	-0.023 / 0.023	-0.0277 / 0.0277
b-tag Eigenvar. 2	0 / 0	-0.0478 / 0.0478	-0.0543 / 0.0543
b-tag Eigenvar. 3	0 / 0	3.77e-05 / -3.77e-05	-0.00467 / 0.00467
b-tag Eigenvar. 4	0 / 0	0.000891 / -0.000891	-0.00161 / 0.00161
c-tag Eigenvar. 1	0 / 0	0.00011 / -0.00011	0.00586 / -0.00586
c-tag Eigenvar. 2	0 / 0	-0.0135 / 0.0135	-0.00311 / 0.00311
c-tag Eigenvar. 3	0 / 0	-0.0081 / 0.0081	-0.0007 / 0.0007
c-tag Eigenvar. 4	0 / 0	-0.00162 / 0.00162	0.000997 / -0.000997
light-tag Eigenvar. 1	0 / 0	0.00577 / -0.00577	-0.00978 / 0.00978
light-tag Eigenvar. 2	0 / 0	-0.00465 / 0.00465	-0.00704 / 0.00704
light-tag Eigenvar. 3	0 / 0	0.00533 / -0.00533	0.00416 / -0.00416
light-tag Eigenvar. 4	0 / 0	-0.0104 / 0.0104	-0.00984 / 0.00984
light-tag Eigenvar. 5	0 / 0	-0.00221 / 0.00221	-0.00178 / 0.00178
light-tag Eigenvar. 6	0 / 0	-0.000633 / 0.000633	0.000624 / -0.000624
light-tag Eigenvar. 7	0 / 0	0.00072 / -0.00072	0.000152 / -0.000152
light-tag Eigenvar. 8	0 / 0	-0.000587 / 0.000587	-0.00169 / 0.00169
light-tag Eigenvar. 9	0 / 0	-0.000667 / 0.000667	-1.54e-05 / 1.54e-05
light-tag Eigenvar. 10	0 / 0	-0.000249 / 0.000249	-0.000271 / 0.000271
light-tag Eigenvar. 11	0 / 0	-0.000307 / 0.000307	-0.000459 / 0.000459
light-tag Eigenvar. 12	0 / 0	6.26e-05 / -6.26e-05	0.000335 / -0.000335
b-tag Extrapolation from RUN1	0 / 0	0.00921 / -0.00921	0.0355 / -0.0355
b-tag Extrapolation from c-tag	0 / 0	-4.57e-05 / 4.57e-05	-0.000251 / 0.000251
Large-R Jet Baseline	0 / 0	0.0163 / -0.0163	-0.025 / 0.025
Large-R Jet Modelling	0 / 0	0.00903 / -0.00903	-0.0329 / 0.0329
Large-R Jet TotalStat	0 / 0	0.00194 / -0.00194	-0.0111 / 0.0111
Large-R Jet Tracking	0 / 0	0.0308 / -0.0308	-0.0178 / 0.0178
Large-R Jet p_T resolution	0 / 0	-0.00801 / 0.00801	-0.000961 / 0.000961
Large-R Jet mass resolution	0 / 0	0.00875 / -0.00875	0.00121 / -0.00121
Large-R Jet τ_{32}^{wta} resolution	0 / 0	0.00312 / -0.00312	0.00235 / -0.00235
$t\bar{t}$ Cross-Section	0 / 0	0.056 / -0.061	0 / 0
$t\bar{t}$ generator	0 / 0	-0.13 / 0.13	0 / 0
$t\bar{t}$ parton shower	0 / 0	-0.0654 / 0.0654	0 / 0
$t\bar{t}$ isrfsr	0 / 0	-0.132 / 0.132	0 / 0
$t\bar{t}$ EW	0 / 0	0.0792 / -0.0792	0 / 0
PDF CT10 vs. PDF4LHC15	0 / 0	0.0166 / -0.0166	0 / 0
PDF1	0 / 0	0.00927 / -0.00927	0 / 0
PDF2	0 / 0	0.0101 / -0.0101	0 / 0
PDF3	0 / 0	0.00201 / -0.00201	0 / 0
PDF4	0 / 0	0.008 / -0.008	0 / 0
PDF5	0 / 0	0.00189 / -0.00189	0 / 0
PDF6	0 / 0	-0.00295 / 0.00295	0 / 0
PDF7	0 / 0	0.00357 / -0.00357	0 / 0
PDF8	0 / 0	0.00937 / -0.00937	0 / 0
PDF9	0 / 0	0.00706 / -0.00706	0 / 0
PDF10	0 / 0	0.00556 / -0.00556	0 / 0
PDF11	0 / 0	0.00939 / -0.00939	0 / 0
PDF12	0 / 0	0.00394 / -0.00394	0 / 0
PDF13	0 / 0	0.00659 / -0.00659	0 / 0
PDF14	0 / 0	0.0104 / -0.0104	0 / 0
PDF15	0 / 0	0.00835 / -0.00835	0 / 0
PDF16	0 / 0	0.00833 / -0.00833	0 / 0
PDF17	0 / 0	0.0082 / -0.0082	0 / 0
PDF18	0 / 0	0.0148 / -0.0148	0 / 0
PDF19	0 / 0	0.0113 / -0.0113	0 / 0
PDF20	0 / 0	0.00175 / -0.00175	0 / 0
PDF21	0 / 0	0.00995 / -0.00995	0 / 0
PDF22	0 / 0	0.00867 / -0.00867	0 / 0
PDF23	0 / 0	0.018 / -0.018	0 / 0
PDF24	0 / 0	0.00976 / -0.00976	0 / 0
PDF25	0 / 0	0.00894 / -0.00894	0 / 0
PDF26	0 / 0	0.00897 / -0.00897	0 / 0
PDF27	0 / 0	0.0103 / -0.0103	0 / 0
PDF28	0 / 0	0.00829 / -0.00829	0 / 0
PDF29	0 / 0	0.012 / -0.012	0 / 0
PDF30	0 / 0	0.00993 / -0.00993	0 / 0
$t\bar{t}$ SR0 Extrapolation Range	0 / 0	0.000498 / -0.000498	0 / 0
$t\bar{t}$ SR0 Extrapolation VariationParam0	0 / 0	0.00127 / -0.00127	0 / 0
$t\bar{t}$ SR0 Extrapolation VariationParam1	0 / 0	2.41e-06 / -2.41e-06	0 / 0

Table 21: Relative effect of each systematic on the yields for one tigth b-tagged Medium SR0.

	Multijet	$t\bar{t}$	Z' 3 TeV
MultiJet one tight b-tag ShapeCorrection0	0.0321 / -0.0321	0 / 0	0 / 0
MultiJet one tight b-tag ShapeCorrection1	0.0241 / -0.0241	0 / 0	0 / 0
MultiJet one tight b-tag ShapeCorrection2	-0.0277 / 0.0277	0 / 0	0 / 0
ResidualDifference one tight b-tag	-0.00256 / 0.00256	0 / 0	0 / 0
MultiJetSR0StatisticUncertainty1st	0.00817 / -0.00817	0 / 0	0 / 0
MultiJetSR0StatisticUncertainty2nd	0.009 / -0.009	0 / 0	0 / 0
MultiJetSR0StatisticUncertainty3rd	0.00792 / -0.00792	0 / 0	0 / 0
MultiJetSR0StatisticUncertainty4th	0.00725 / -0.00725	0 / 0	0 / 0
MultiJetSR0StatisticUncertainty5th	0.006 / -0.006	0 / 0	0 / 0
MultiJetTemplateShapeDiff one tight b-tag SR0	-0.0645 / 0.0645	0 / 0	0 / 0
Normalization factor for SR0Medium one tight b-tag	0.0518 / -0.083	0 / 0	0 / 0
MultiJet SR0 Extrapolation Range	-8.05e-07 / 8.05e-07	0 / 0	0 / 0
MultiJet SR0 Extrapolation VariationParam0	0.00314 / -0.00314	0 / 0	0 / 0
MultiJet SR0 Extrapolation VariationParam1	2.86e-06 / -2.86e-06	0 / 0	0 / 0
Luminocity	0 / 0	0.021 / -0.021	0.021 / -0.021
b-tag Eigenvar. 1	0 / 0	0.0708 / -0.0708	0.0728 / -0.0728
b-tag Eigenvar. 2	0 / 0	0.0663 / -0.0663	0.0922 / -0.0922
b-tag Eigenvar. 3	0 / 0	-0.00235 / 0.00235	0.00789 / -0.00789
b-tag Eigenvar. 4	0 / 0	-0.000996 / 0.000996	0.00368 / -0.00368
c-tag Eigenvar. 1	0 / 0	0.0646 / -0.0646	0.0484 / -0.0484
c-tag Eigenvar. 2	0 / 0	0.0373 / -0.0373	0.033 / -0.033
c-tag Eigenvar. 3	0 / 0	0.0225 / -0.0225	0.0211 / -0.0211
c-tag Eigenvar. 4	0 / 0	0.00886 / -0.00886	0.00856 / -0.00856
light-tag Eigenvar. 1	0 / 0	0.0257 / -0.0257	0.0108 / -0.0108
light-tag Eigenvar. 2	0 / 0	-0.00873 / 0.00873	-0.00663 / 0.00663
light-tag Eigenvar. 3	0 / 0	0.00349 / -0.00349	0.00357 / -0.00357
light-tag Eigenvar. 4	0 / 0	-0.00937 / 0.00937	-0.0087 / 0.0087
light-tag Eigenvar. 5	0 / 0	-0.00326 / 0.00326	-0.00255 / 0.00255
light-tag Eigenvar. 6	0 / 0	-0.000561 / 0.000561	-0.000149 / 0.000149
light-tag Eigenvar. 7	0 / 0	0.00129 / -0.00129	0.00061 / -0.00061
light-tag Eigenvar. 8	0 / 0	-0.000464 / 0.000464	-0.000718 / 0.000718
light-tag Eigenvar. 9	0 / 0	-0.000217 / 0.000217	-0.000327 / 0.000327
light-tag Eigenvar. 10	0 / 0	-0.000643 / 0.000643	-0.000346 / 0.000346
light-tag Eigenvar. 11	0 / 0	-0.000531 / 0.000531	-0.00037 / 0.00037
light-tag Eigenvar. 12	0 / 0	0.000161 / -0.000161	0.000108 / -0.000108
b-tag Extrapolation from RUN1	0 / 0	-0.014 / 0.014	-0.0804 / 0.0804
b-tag Extrapolation from c-tag	0 / 0	-0.000223 / 0.000223	-0.000466 / 0.000466
Large-R Jet Baseline	0 / 0	0.0186 / -0.0186	-0.0207 / 0.0207
Large-R Jet Modelling	0 / 0	0.0164 / -0.0164	-0.0228 / 0.0228
Large-R Jet TotalStat	0 / 0	0.000701 / -0.000701	-0.0126 / 0.0126
Large-R Jet Tracking	0 / 0	0.0343 / -0.0343	-0.0338 / 0.0338
Large-R Jet p_T resolution	0 / 0	-0.00777 / 0.00777	-0.00202 / 0.00202
Large-R Jet mass resolution	0 / 0	-0.000744 / 0.000744	0.00257 / -0.00257
Large-R Jet τ_{32}^{wta} resolution	0 / 0	8.78e-06 / -8.78e-06	0.00196 / -0.00196
$t\bar{t}$ Cross-Section	0 / 0	0.056 / -0.061	0 / 0
$t\bar{t}$ generator	0 / 0	-0.147 / 0.147	0 / 0
$t\bar{t}$ parton shower	0 / 0	0.00975 / -0.00975	0 / 0
$t\bar{t}$ isrfsr	0 / 0	-0.0399 / 0.0399	0 / 0
$t\bar{t}$ EW	0 / 0	0.0766 / -0.0766	0 / 0
PDF CT10 vs. PDF4LHC15	0 / 0	-0.00447 / 0.00447	0 / 0
PDF1	0 / 0	0.00393 / -0.00393	0 / 0
PDF2	0 / 0	0.00646 / -0.00646	0 / 0
PDF3	0 / 0	-0.0039 / 0.0039	0 / 0
PDF4	0 / 0	0.00243 / -0.00243	0 / 0
PDF5	0 / 0	-0.00257 / 0.00257	0 / 0
PDF6	0 / 0	-0.00727 / 0.00727	0 / 0
PDF7	0 / 0	-0.000797 / 0.000797	0 / 0
PDF8	0 / 0	0.00382 / -0.00382	0 / 0
PDF9	0 / 0	0.00113 / -0.00113	0 / 0
PDF10	0 / 0	0.00069 / -0.00069	0 / 0
PDF11	0 / 0	0.0039 / -0.0039	0 / 0
PDF12	0 / 0	-0.00111 / 0.00111	0 / 0
PDF13	0 / 0	0.00145 / -0.00145	0 / 0
PDF14	0 / 0	0.00493 / -0.00493	0 / 0
PDF15	0 / 0	0.00283 / -0.00283	0 / 0
PDF16	0 / 0	0.00265 / -0.00265	0 / 0
PDF17	0 / 0	0.00234 / -0.00234	0 / 0
PDF18	0 / 0	0.00884 / -0.00884	0 / 0
PDF19	0 / 0	0.00561 / -0.00561	0 / 0
PDF20	0 / 0	-0.00248 / 0.00248	0 / 0
PDF21	0 / 0	0.00501 / -0.00501	0 / 0
PDF22	0 / 0	0.00286 / -0.00286	0 / 0
PDF23	0 / 0	0.0134 / -0.0134	0 / 0
PDF24	0 / 0	0.00436 / -0.00436	0 / 0
PDF25	0 / 0	0.00333 / -0.00333	0 / 0
PDF26	0 / 0	0.00362 / -0.00362	0 / 0
PDF27	0 / 0	0.00468 / -0.00468	0 / 0
PDF28	0 / 0	0.00238 / -0.00238	0 / 0
PDF29	0 / 0	0.00643 / -0.00643	0 / 0
PDF30	0 / 0	0.00419 / -0.00419	0 / 0
$t\bar{t}$ SR0 Extrapolation Range	0 / 0	9.34e-06 / -9.34e-06	0 / 0
$t\bar{t}$ SR0 Extrapolation VariationParam0	0 / 0	0.000103 / -0.000103	0 / 0
$t\bar{t}$ SR0 Extrapolation VariationParam1	0 / 0	9.25e-08 / -9.25e-08	0 / 0

Table 22: Relative effect of each systematic on the yields for two tigth b-tagged Tight SR3.

	Multijet	$t\bar{t}$	Z' 3 TeV
MultiJet two tight b-tag ShapeCorrection0	0.0311 / -0.0311	0 / 0	0 / 0
MultiJet two tight b-tag ShapeCorrection1	0.0225 / -0.0225	0 / 0	0 / 0
MultiJet two tight b-tag ShapeCorrection2	-0.0266 / 0.0266	0 / 0	0 / 0
ResidualDifference two tight b-tag	-0.000964 / 0.000964	0 / 0	0 / 0
MultiJetSR3StatisticUncertainty1st	0.00557 / -0.00557	0 / 0	0 / 0
MultiJetSR3StatisticUncertainty2nd	0.00578 / -0.00578	0 / 0	0 / 0
MultiJetSR3StatisticUncertainty3rd	0.00505 / -0.00505	0 / 0	0 / 0
MultiJetSR3StatisticUncertainty4th	0.00441 / -0.00441	0 / 0	0 / 0
MultiJetSR3StatisticUncertainty5th	0.00388 / -0.00388	0 / 0	0 / 0
MultiJetTemplateShapeDiff two tight b-tag SR3	-0.0168 / 0.0168	0 / 0	0 / 0
Normalization factor for SR3Tight two tight b-tag	0.0997 / -0.0651	0 / 0	0 / 0
MultiJet SR3 Extrapolation Range	1.71e-07 / -1.71e-07	0 / 0	0 / 0
MultiJet SR3 Extrapolation VariationParam0	0.000184 / -0.000184	0 / 0	0 / 0
MultiJet SR3 Extrapolation VariationParam1	1.35e-06 / -1.35e-06	0 / 0	0 / 0
Luminocity	0 / 0	0.021 / -0.021	0.021 / -0.021
b-tag Eigenvar. 1	0 / 0	-0.0193 / 0.0193	-0.0272 / 0.0272
b-tag Eigenvar. 2	0 / 0	-0.0548 / 0.0548	-0.0619 / 0.0619
b-tag Eigenvar. 3	0 / 0	-0.00267 / 0.00267	-0.00664 / 0.00664
b-tag Eigenvar. 4	0 / 0	-0.000298 / 0.000298	-0.0025 / 0.0025
c-tag Eigenvar. 1	0 / 0	-0.00431 / 0.00431	0.00658 / -0.00658
c-tag Eigenvar. 2	0 / 0	-0.0173 / 0.0173	-0.00404 / 0.00404
c-tag Eigenvar. 3	0 / 0	-0.00907 / 0.00907	-0.00119 / 0.00119
c-tag Eigenvar. 4	0 / 0	-0.00173 / 0.00173	0.000804 / -0.000804
light-tag Eigenvar. 1	0 / 0	0.00194 / -0.00194	0.00163 / -0.00163
light-tag Eigenvar. 2	0 / 0	-0.00437 / 0.00437	-0.00735 / 0.00735
light-tag Eigenvar. 3	0 / 0	0.00541 / -0.00541	0.00283 / -0.00283
light-tag Eigenvar. 4	0 / 0	-0.0113 / 0.0113	-0.0101 / 0.0101
light-tag Eigenvar. 5	0 / 0	-0.00253 / 0.00253	-0.002 / 0.002
light-tag Eigenvar. 6	0 / 0	-0.000669 / 0.000669	0.000169 / -0.000169
light-tag Eigenvar. 7	0 / 0	0.000606 / -0.000606	0.000359 / -0.000359
light-tag Eigenvar. 8	0 / 0	-0.000985 / 0.000985	-0.00113 / 0.00113
light-tag Eigenvar. 9	0 / 0	-0.000968 / 0.000968	0.000258 / -0.000258
light-tag Eigenvar. 10	0 / 0	-0.000129 / 0.000129	-0.000271 / 0.000271
light-tag Eigenvar. 11	0 / 0	-0.00039 / 0.00039	-0.000149 / 0.000149
light-tag Eigenvar. 12	0 / 0	4.75e-05 / -4.75e-05	0.000277 / -0.000277
b-tag Extrapolation from RUN1	0 / 0	0.0146 / -0.0146	0.0441 / -0.0441
b-tag Extrapolation from c-tag	0 / 0	-0.000167 / 0.000167	-0.000507 / 0.000507
Large-R Jet Baseline	0 / 0	-0.0156 / 0.0156	-0.0692 / 0.0692
Large-R Jet Modelling	0 / 0	-0.0462 / 0.0462	-0.0563 / 0.0563
Large-R Jet TotalStat	0 / 0	-0.000781 / 0.000781	-0.00928 / 0.00928
Large-R Jet Tracking	0 / 0	0.0167 / -0.0167	-0.0481 / 0.0481
Large-R Jet p_T resolution	0 / 0	-0.00694 / 0.00694	-0.00409 / 0.00409
Large-R Jet mass resolution	0 / 0	-0.019 / 0.019	-0.0112 / 0.0112
Large-R Jet τ_{32}^{wta} resolution	0 / 0	-0.00143 / 0.00143	-0.000259 / 0.000259
$t\bar{t}$ Cross-Section	0 / 0	0.056 / -0.061	0 / 0
$t\bar{t}$ generator	0 / 0	-0.11 / 0.11	0 / 0
$t\bar{t}$ parton shower	0 / 0	-0.0825 / 0.0825	0 / 0
$t\bar{t}$ isrfsr	0 / 0	-0.105 / 0.105	0 / 0
$t\bar{t}$ EW	0 / 0	0.0784 / -0.0784	0 / 0
PDF CT10 vs. PDF4LHC15	0 / 0	-0.102 / 0.102	0 / 0
PDF1	0 / 0	0.00779 / -0.00779	0 / 0
PDF2	0 / 0	0.00961 / -0.00961	0 / 0
PDF3	0 / 0	0.00133 / -0.00133	0 / 0
PDF4	0 / 0	0.00578 / -0.00578	0 / 0
PDF5	0 / 0	0.00621 / -0.00621	0 / 0
PDF6	0 / 0	-0.00266 / 0.00266	0 / 0
PDF7	0 / 0	0.00424 / -0.00424	0 / 0
PDF8	0 / 0	0.00623 / -0.00623	0 / 0
PDF9	0 / 0	0.00418 / -0.00418	0 / 0
PDF10	0 / 0	0.00485 / -0.00485	0 / 0
PDF11	0 / 0	0.00695 / -0.00695	0 / 0
PDF12	0 / 0	0.00241 / -0.00241	0 / 0
PDF13	0 / 0	0.00488 / -0.00488	0 / 0
PDF14	0 / 0	0.00847 / -0.00847	0 / 0
PDF15	0 / 0	0.00776 / -0.00776	0 / 0
PDF16	0 / 0	0.0067 / -0.0067	0 / 0
PDF17	0 / 0	0.0084 / -0.0084	0 / 0
PDF18	0 / 0	0.0123 / -0.0123	0 / 0
PDF19	0 / 0	0.00684 / -0.00684	0 / 0
PDF20	0 / 0	-0.00101 / 0.00101	0 / 0
PDF21	0 / 0	0.00824 / -0.00824	0 / 0
PDF22	0 / 0	0.00707 / -0.00707	0 / 0
PDF23	0 / 0	0.016 / -0.016	0 / 0
PDF24	0 / 0	0.00795 / -0.00795	0 / 0
PDF25	0 / 0	0.00762 / -0.00762	0 / 0
PDF26	0 / 0	0.00696 / -0.00696	0 / 0
PDF27	0 / 0	0.008 / -0.008	0 / 0
PDF28	0 / 0	0.00624 / -0.00624	0 / 0
PDF29	0 / 0	0.0108 / -0.0108	0 / 0
PDF30	0 / 0	0.00741 / -0.00741	0 / 0
$t\bar{t}$ SR3 Extrapolation Range	0 / 0	7.35e-05 / -7.35e-05	0 / 0
$t\bar{t}$ SR3 Extrapolation VariationParam0	0 / 0	0.00139 / -0.00139	0 / 0
$t\bar{t}$ SR3 Extrapolation VariationParam1	0 / 0	4.94e-06 / -4.94e-06	0 / 0

Table 23: Relative effect of each systematic on the yields for one tigth b-tagged Tight SR3.

	Multijet	$t\bar{t}$	Z' 3 TeV
MultiJet one tight b-tag ShapeCorrection0	0.0304 / -0.0304	0 / 0	0 / 0
MultiJet one tight b-tag ShapeCorrection1	0.0226 / -0.0226	0 / 0	0 / 0
MultiJet one tight b-tag ShapeCorrection2	-0.0261 / 0.0261	0 / 0	0 / 0
ResidualDifference one tight b-tag	-0.00247 / 0.00247	0 / 0	0 / 0
MultiJetSR3StatisticUncertainty1st	0.00533 / -0.00533	0 / 0	0 / 0
MultiJetSR3StatisticUncertainty2nd	0.00564 / -0.00564	0 / 0	0 / 0
MultiJetSR3StatisticUncertainty3rd	0.005 / -0.005	0 / 0	0 / 0
MultiJetSR3StatisticUncertainty4th	0.00442 / -0.00442	0 / 0	0 / 0
MultiJetSR3StatisticUncertainty5th	0.00392 / -0.00392	0 / 0	0 / 0
MultiJetTemplateShapeDiff one tight b-tag SR3	-0.0208 / 0.0208	0 / 0	0 / 0
Normalization factor for SR3Tight one tight b-tag	0.0471 / -0.0432	0 / 0	0 / 0
MultiJet SR3 Extrapolation Range	-1.37e-06 / 1.37e-06	0 / 0	0 / 0
MultiJet SR3 Extrapolation VariationParam0	0.000171 / -0.000171	0 / 0	0 / 0
MultiJet SR3 Extrapolation VariationParam1	-7.96e-07 / 7.96e-07	0 / 0	0 / 0
Luminocity	0 / 0	0.021 / -0.021	0.021 / -0.021
b-tag Eigenvar. 1	0 / 0	0.0789 / -0.0789	0.0798 / -0.0798
b-tag Eigenvar. 2	0 / 0	0.0642 / -0.0642	0.0937 / -0.0937
b-tag Eigenvar. 3	0 / 0	-4.14e-05 / 4.14e-05	0.0093 / -0.0093
b-tag Eigenvar. 4	0 / 0	0.000863 / -0.000863	0.0049 / -0.0049
c-tag Eigenvar. 1	0 / 0	0.05 / -0.05	0.0434 / -0.0434
c-tag Eigenvar. 2	0 / 0	0.0235 / -0.0235	0.0296 / -0.0296
c-tag Eigenvar. 3	0 / 0	0.0153 / -0.0153	0.0206 / -0.0206
c-tag Eigenvar. 4	0 / 0	0.00684 / -0.00684	0.00891 / -0.00891
light-tag Eigenvar. 1	0 / 0	0.0172 / -0.0172	0.0181 / -0.0181
light-tag Eigenvar. 2	0 / 0	-0.00786 / 0.00786	-0.00796 / 0.00796
light-tag Eigenvar. 3	0 / 0	0.00447 / -0.00447	0.00215 / -0.00215
light-tag Eigenvar. 4	0 / 0	-0.0105 / 0.0105	-0.00832 / 0.00832
light-tag Eigenvar. 5	0 / 0	-0.00248 / 0.00248	-0.00239 / 0.00239
light-tag Eigenvar. 6	0 / 0	-0.000411 / 0.000411	-0.000223 / 0.000223
light-tag Eigenvar. 7	0 / 0	0.000637 / -0.000637	0.000735 / -0.000735
light-tag Eigenvar. 8	0 / 0	-0.000268 / 0.000268	-0.00058 / 0.00058
light-tag Eigenvar. 9	0 / 0	-0.000563 / 0.000563	-0.000188 / 0.000188
light-tag Eigenvar. 10	0 / 0	-3.95e-05 / 3.95e-05	-0.000187 / 0.000187
light-tag Eigenvar. 11	0 / 0	-0.000221 / 0.000221	-0.000302 / 0.000302
light-tag Eigenvar. 12	0 / 0	-0.000116 / 0.000116	0.000105 / -0.000105
b-tag Extrapolation from RUN1	0 / 0	-0.0142 / 0.0142	-0.086 / 0.086
b-tag Extrapolation from c-tag	0 / 0	-0.00137 / 0.00137	-0.00246 / 0.00246
Large-R Jet Baseline	0 / 0	-0.0176 / 0.0176	-0.0588 / 0.0588
Large-R Jet Modelling	0 / 0	-0.039 / 0.039	-0.0457 / 0.0457
Large-R Jet TotalStat	0 / 0	0.00177 / -0.00177	-0.00237 / 0.00237
Large-R Jet Tracking	0 / 0	0.014 / -0.014	-0.0142 / 0.0142
Large-R Jet p_T resolution	0 / 0	-0.0161 / 0.0161	-0.000437 / 0.000437
Large-R Jet mass resolution	0 / 0	-0.0275 / 0.0275	-0.012 / 0.012
Large-R Jet τ_{32}^{wta} resolution	0 / 0	-0.00188 / 0.00188	-0.000635 / 0.000635
$t\bar{t}$ Cross-Section	0 / 0	0.056 / -0.061	0 / 0
$t\bar{t}$ generator	0 / 0	-0.23 / 0.23	0 / 0
$t\bar{t}$ parton shower	0 / 0	-0.0105 / 0.0105	0 / 0
$t\bar{t}$ isrfsr	0 / 0	-0.0728 / 0.0728	0 / 0
$t\bar{t}$ EW	0 / 0	0.0762 / -0.0762	0 / 0
PDF CT10 vs. PDF4LHC15	0 / 0	-0.0827 / 0.0827	0 / 0
PDF1	0 / 0	0.00807 / -0.00807	0 / 0
PDF2	0 / 0	0.00919 / -0.00919	0 / 0
PDF3	0 / 0	0.00507 / -0.00507	0 / 0
PDF4	0 / 0	0.00657 / -0.00657	0 / 0
PDF5	0 / 0	0.00251 / -0.00251	0 / 0
PDF6	0 / 0	-0.00256 / 0.00256	0 / 0
PDF7	0 / 0	0.00362 / -0.00362	0 / 0
PDF8	0 / 0	0.00775 / -0.00775	0 / 0
PDF9	0 / 0	0.00243 / -0.00243	0 / 0
PDF10	0 / 0	0.00441 / -0.00441	0 / 0
PDF11	0 / 0	0.00801 / -0.00801	0 / 0
PDF12	0 / 0	0.00294 / -0.00294	0 / 0
PDF13	0 / 0	0.00573 / -0.00573	0 / 0
PDF14	0 / 0	0.00928 / -0.00928	0 / 0
PDF15	0 / 0	0.00769 / -0.00769	0 / 0
PDF16	0 / 0	0.00746 / -0.00746	0 / 0
PDF17	0 / 0	0.00674 / -0.00674	0 / 0
PDF18	0 / 0	0.0135 / -0.0135	0 / 0
PDF19	0 / 0	0.00888 / -0.00888	0 / 0
PDF20	0 / 0	0.000464 / -0.000464	0 / 0
PDF21	0 / 0	0.00803 / -0.00803	0 / 0
PDF22	0 / 0	0.00795 / -0.00795	0 / 0
PDF23	0 / 0	0.0156 / -0.0156	0 / 0
PDF24	0 / 0	0.00806 / -0.00806	0 / 0
PDF25	0 / 0	0.00849 / -0.00849	0 / 0
PDF26	0 / 0	0.00804 / -0.00804	0 / 0
PDF27	0 / 0	0.00921 / -0.00921	0 / 0
PDF28	0 / 0	0.00768 / -0.00768	0 / 0
PDF29	0 / 0	0.0113 / -0.0113	0 / 0
PDF30	0 / 0	0.00853 / -0.00853	0 / 0
$t\bar{t}$ SR3 Extrapolation Range	0 / 0	0.000176 / -0.000176	0 / 0
$t\bar{t}$ SR3 Extrapolation VariationParam0	0 / 0	0.000455 / -0.000455	0 / 0
$t\bar{t}$ SR3 Extrapolation VariationParam1	0 / 0	5.1e-06 / -5.1e-06	0 / 0

Table 24: Relative effect of each systematic on the yields for two tigth b-tagged Medium SR3.

	Multijet	$t\bar{t}$	Z' 3 TeV
MultiJet two tight b-tag ShapeCorrection0	0.0311 / -0.0311	0 / 0	0 / 0
MultiJet two tight b-tag ShapeCorrection1	0.0225 / -0.0225	0 / 0	0 / 0
MultiJet two tight b-tag ShapeCorrection2	-0.0266 / 0.0266	0 / 0	0 / 0
ResidualDifference two tight b-tag	-0.000964 / 0.000964	0 / 0	0 / 0
MultiJetSR3StatisticUncertainty1st	0.00557 / -0.00557	0 / 0	0 / 0
MultiJetSR3StatisticUncertainty2nd	0.00578 / -0.00578	0 / 0	0 / 0
MultiJetSR3StatisticUncertainty3rd	0.00505 / -0.00505	0 / 0	0 / 0
MultiJetSR3StatisticUncertainty4th	0.00441 / -0.00441	0 / 0	0 / 0
MultiJetSR3StatisticUncertainty5th	0.00388 / -0.00388	0 / 0	0 / 0
MultiJetTemplateShapeDiff two tight b-tag SR3	-0.0347 / 0.0347	0 / 0	0 / 0
Normalization factor for SR3Medium two tight b-tag	0.0748 / -0.108	0 / 0	0 / 0
MultiJet SR3 Extrapolation Range	-1.01e-06 / 1.01e-06	0 / 0	0 / 0
MultiJet SR3 Extrapolation VariationParam0	0.000184 / -0.000184	0 / 0	0 / 0
MultiJet SR3 Extrapolation VariationParam1	4.71e-07 / -4.71e-07	0 / 0	0 / 0
Luminocity	0 / 0	0.021 / -0.021	0.021 / -0.021
b-tag Eigenvar. 1	0 / 0	-0.0195 / 0.0195	-0.0269 / 0.0269
b-tag Eigenvar. 2	0 / 0	-0.0549 / 0.0549	-0.0616 / 0.0616
b-tag Eigenvar. 3	0 / 0	-0.00277 / 0.00277	-0.00657 / 0.00657
b-tag Eigenvar. 4	0 / 0	-0.000366 / 0.000366	-0.00249 / 0.00249
c-tag Eigenvar. 1	0 / 0	-0.00383 / 0.00383	0.00609 / -0.00609
c-tag Eigenvar. 2	0 / 0	-0.0168 / 0.0168	-0.00438 / 0.00438
c-tag Eigenvar. 3	0 / 0	-0.00876 / 0.00876	-0.0014 / 0.0014
c-tag Eigenvar. 4	0 / 0	-0.00165 / 0.00165	0.000664 / -0.000664
light-tag Eigenvar. 1	0 / 0	0.000836 / -0.000836	0.00128 / -0.00128
light-tag Eigenvar. 2	0 / 0	-0.00426 / 0.00426	-0.00743 / 0.00743
light-tag Eigenvar. 3	0 / 0	0.00555 / -0.00555	0.00308 / -0.00308
light-tag Eigenvar. 4	0 / 0	-0.0113 / 0.0113	-0.00984 / 0.00984
light-tag Eigenvar. 5	0 / 0	-0.00247 / 0.00247	-0.00199 / 0.00199
light-tag Eigenvar. 6	0 / 0	-0.000641 / 0.000641	0.000225 / -0.000225
light-tag Eigenvar. 7	0 / 0	0.000585 / -0.000585	0.000345 / -0.000345
light-tag Eigenvar. 8	0 / 0	-0.00103 / 0.00103	-0.00118 / 0.00118
light-tag Eigenvar. 9	0 / 0	-0.00097 / 0.00097	0.000255 / -0.000255
light-tag Eigenvar. 10	0 / 0	-0.000106 / 0.000106	-0.000285 / 0.000285
light-tag Eigenvar. 11	0 / 0	-0.000419 / 0.000419	-0.000152 / 0.000152
light-tag Eigenvar. 12	0 / 0	6.49e-05 / -6.49e-05	0.000279 / -0.000279
b-tag Extrapolation from RUN1	0 / 0	0.0151 / -0.0151	0.0447 / -0.0447
b-tag Extrapolation from c-tag	0 / 0	-0.000174 / 0.000174	-0.00057 / 0.00057
Large-R Jet Baseline	0 / 0	-0.0148 / 0.0148	-0.064 / 0.064
Large-R Jet Modelling	0 / 0	-0.0462 / 0.0462	-0.0553 / 0.0553
Large-R Jet TotalStat	0 / 0	-0.000959 / 0.000959	-0.0101 / 0.0101
Large-R Jet Tracking	0 / 0	0.017 / -0.017	-0.0452 / 0.0452
Large-R Jet p_T resolution	0 / 0	-0.00652 / 0.00652	-0.00456 / 0.00456
Large-R Jet mass resolution	0 / 0	-0.0193 / 0.0193	-0.0123 / 0.0123
Large-R Jet τ_{32}^{wta} resolution	0 / 0	-0.00149 / 0.00149	0.000203 / -0.000203
$t\bar{t}$ Cross-Section	0 / 0	0.056 / -0.061	0 / 0
$t\bar{t}$ generator	0 / 0	-0.107 / 0.107	0 / 0
$t\bar{t}$ parton shower	0 / 0	-0.0835 / 0.0835	0 / 0
$t\bar{t}$ isrfsr	0 / 0	-0.106 / 0.106	0 / 0
$t\bar{t}$ EW	0 / 0	0.0795 / -0.0795	0 / 0
PDF CT10 vs. PDF4LHC15	0 / 0	-0.103 / 0.103	0 / 0
PDF1	0 / 0	0.00766 / -0.00766	0 / 0
PDF2	0 / 0	0.00948 / -0.00948	0 / 0
PDF3	0 / 0	0.00116 / -0.00116	0 / 0
PDF4	0 / 0	0.00562 / -0.00562	0 / 0
PDF5	0 / 0	0.006 / -0.006	0 / 0
PDF6	0 / 0	-0.00287 / 0.00287	0 / 0
PDF7	0 / 0	0.00407 / -0.00407	0 / 0
PDF8	0 / 0	0.00612 / -0.00612	0 / 0
PDF9	0 / 0	0.00407 / -0.00407	0 / 0
PDF10	0 / 0	0.00471 / -0.00471	0 / 0
PDF11	0 / 0	0.00685 / -0.00685	0 / 0
PDF12	0 / 0	0.00228 / -0.00228	0 / 0
PDF13	0 / 0	0.00475 / -0.00475	0 / 0
PDF14	0 / 0	0.00835 / -0.00835	0 / 0
PDF15	0 / 0	0.00763 / -0.00763	0 / 0
PDF16	0 / 0	0.00657 / -0.00657	0 / 0
PDF17	0 / 0	0.00827 / -0.00827	0 / 0
PDF18	0 / 0	0.0122 / -0.0122	0 / 0
PDF19	0 / 0	0.00677 / -0.00677	0 / 0
PDF20	0 / 0	-0.00114 / 0.00114	0 / 0
PDF21	0 / 0	0.00813 / -0.00813	0 / 0
PDF22	0 / 0	0.00695 / -0.00695	0 / 0
PDF23	0 / 0	0.0159 / -0.0159	0 / 0
PDF24	0 / 0	0.00784 / -0.00784	0 / 0
PDF25	0 / 0	0.00749 / -0.00749	0 / 0
PDF26	0 / 0	0.00687 / -0.00687	0 / 0
PDF27	0 / 0	0.00789 / -0.00789	0 / 0
PDF28	0 / 0	0.00612 / -0.00612	0 / 0
PDF29	0 / 0	0.0107 / -0.0107	0 / 0
PDF30	0 / 0	0.0073 / -0.0073	0 / 0
$t\bar{t}$ SR3 Extrapolation Range	0 / 0	-8.26e-05 / 8.26e-05	0 / 0
$t\bar{t}$ SR3 Extrapolation VariationParam0	0 / 0	0.001 / -0.001	0 / 0
$t\bar{t}$ SR3 Extrapolation VariationParam1	0 / 0	-8.34e-07 / 8.34e-07	0 / 0

Table 25: Relative effect of each systematic on the yields for one tigth b-tagged Medium SR3.

	Multijet	$t\bar{t}$	Z' 3 TeV
MultiJet one tight b-tag ShapeCorrection0	0.0304 / -0.0304	0 / 0	0 / 0
MultiJet one tight b-tag ShapeCorrection1	0.0226 / -0.0226	0 / 0	0 / 0
MultiJet one tight b-tag ShapeCorrection2	-0.0261 / 0.0261	0 / 0	0 / 0
ResidualDifference one tight b-tag	-0.00247 / 0.00247	0 / 0	0 / 0
MultiJetSR3StatisticUncertainty1st	0.00533 / -0.00533	0 / 0	0 / 0
MultiJetSR3StatisticUncertainty2nd	0.00564 / -0.00564	0 / 0	0 / 0
MultiJetSR3StatisticUncertainty3rd	0.005 / -0.005	0 / 0	0 / 0
MultiJetSR3StatisticUncertainty4th	0.00442 / -0.00442	0 / 0	0 / 0
MultiJetSR3StatisticUncertainty5th	0.00392 / -0.00392	0 / 0	0 / 0
MultiJetTemplateShapeDiff one tight b-tag SR3	-0.0369 / 0.0369	0 / 0	0 / 0
Normalization factor for SR3Medium one tight b-tag	0.0518 / -0.083	0 / 0	0 / 0
MultiJet SR3 Extrapolation Range	4.36e-07 / -4.36e-07	0 / 0	0 / 0
MultiJet SR3 Extrapolation VariationParam0	0.000172 / -0.000172	0 / 0	0 / 0
MultiJet SR3 Extrapolation VariationParam1	1.44e-07 / -1.44e-07	0 / 0	0 / 0
Luminocity	0 / 0	0.021 / -0.021	0.021 / -0.021
b-tag Eigenvar. 1	0 / 0	0.0784 / -0.0784	0.0796 / -0.0796
b-tag Eigenvar. 2	0 / 0	0.064 / -0.064	0.0933 / -0.0933
b-tag Eigenvar. 3	0 / 0	0.000157 / -0.000157	0.00946 / -0.00946
b-tag Eigenvar. 4	0 / 0	0.000911 / -0.000911	0.00493 / -0.00493
c-tag Eigenvar. 1	0 / 0	0.0499 / -0.0499	0.0451 / -0.0451
c-tag Eigenvar. 2	0 / 0	0.0235 / -0.0235	0.0306 / -0.0306
c-tag Eigenvar. 3	0 / 0	0.0152 / -0.0152	0.0212 / -0.0212
c-tag Eigenvar. 4	0 / 0	0.0069 / -0.0069	0.0093 / -0.0093
light-tag Eigenvar. 1	0 / 0	0.0173 / -0.0173	0.0179 / -0.0179
light-tag Eigenvar. 2	0 / 0	-0.00794 / 0.00794	-0.00795 / 0.00795
light-tag Eigenvar. 3	0 / 0	0.00451 / -0.00451	0.00218 / -0.00218
light-tag Eigenvar. 4	0 / 0	-0.0103 / 0.0103	-0.0084 / 0.0084
light-tag Eigenvar. 5	0 / 0	-0.00241 / 0.00241	-0.00254 / 0.00254
light-tag Eigenvar. 6	0 / 0	-0.000391 / 0.000391	-0.000212 / 0.000212
light-tag Eigenvar. 7	0 / 0	0.000612 / -0.000612	0.000757 / -0.000757
light-tag Eigenvar. 8	0 / 0	-0.000304 / 0.000304	-0.000637 / 0.000637
light-tag Eigenvar. 9	0 / 0	-0.000552 / 0.000552	-0.000216 / 0.000216
light-tag Eigenvar. 10	0 / 0	-3.09e-05 / 3.09e-05	-0.000163 / 0.000163
light-tag Eigenvar. 11	0 / 0	-0.000216 / 0.000216	-0.000332 / 0.000332
light-tag Eigenvar. 12	0 / 0	-0.000105 / 0.000105	8.24e-05 / -8.24e-05
b-tag Extrapolation from RUN1	0 / 0	-0.0152 / 0.0152	-0.0857 / 0.0857
b-tag Extrapolation from c-tag	0 / 0	-0.00138 / 0.00138	-0.00248 / 0.00248
Large-R Jet Baseline	0 / 0	-0.0168 / 0.0168	-0.0765 / 0.0765
Large-R Jet Modelling	0 / 0	-0.0394 / 0.0394	-0.0517 / 0.0517
Large-R Jet TotalStat	0 / 0	0.0021 / -0.0021	-0.00288 / 0.00288
Large-R Jet Tracking	0 / 0	0.0142 / -0.0142	-0.0291 / 0.0291
Large-R Jet p_T resolution	0 / 0	-0.0165 / 0.0165	-0.00244 / 0.00244
Large-R Jet mass resolution	0 / 0	-0.0276 / 0.0276	-0.0149 / 0.0149
Large-R Jet τ_{32}^{wta} resolution	0 / 0	-0.00157 / 0.00157	5.24e-05 / -5.24e-05
$t\bar{t}$ Cross-Section	0 / 0	0.056 / -0.061	0 / 0
$t\bar{t}$ generator	0 / 0	-0.229 / 0.229	0 / 0
$t\bar{t}$ parton shower	0 / 0	-0.0122 / 0.0122	0 / 0
$t\bar{t}$ isrfsr	0 / 0	-0.0686 / 0.0686	0 / 0
$t\bar{t}$ EW	0 / 0	0.0774 / -0.0774	0 / 0
PDF CT10 vs. PDF4LHC15	0 / 0	-0.0841 / 0.0841	0 / 0
PDF1	0 / 0	0.00746 / -0.00746	0 / 0
PDF2	0 / 0	0.00866 / -0.00866	0 / 0
PDF3	0 / 0	0.00455 / -0.00455	0 / 0
PDF4	0 / 0	0.00577 / -0.00577	0 / 0
PDF5	0 / 0	0.00218 / -0.00218	0 / 0
PDF6	0 / 0	-0.00318 / 0.00318	0 / 0
PDF7	0 / 0	0.00305 / -0.00305	0 / 0
PDF8	0 / 0	0.00705 / -0.00705	0 / 0
PDF9	0 / 0	0.000397 / -0.000397	0 / 0
PDF10	0 / 0	0.0038 / -0.0038	0 / 0
PDF11	0 / 0	0.00734 / -0.00734	0 / 0
PDF12	0 / 0	0.00234 / -0.00234	0 / 0
PDF13	0 / 0	0.00513 / -0.00513	0 / 0
PDF14	0 / 0	0.00868 / -0.00868	0 / 0
PDF15	0 / 0	0.00708 / -0.00708	0 / 0
PDF16	0 / 0	0.00686 / -0.00686	0 / 0
PDF17	0 / 0	0.00614 / -0.00614	0 / 0
PDF18	0 / 0	0.0129 / -0.0129	0 / 0
PDF19	0 / 0	0.0082 / -0.0082	0 / 0
PDF20	0 / 0	-0.000185 / 0.000185	0 / 0
PDF21	0 / 0	0.00743 / -0.00743	0 / 0
PDF22	0 / 0	0.00732 / -0.00732	0 / 0
PDF23	0 / 0	0.015 / -0.015	0 / 0
PDF24	0 / 0	0.00737 / -0.00737	0 / 0
PDF25	0 / 0	0.00789 / -0.00789	0 / 0
PDF26	0 / 0	0.00751 / -0.00751	0 / 0
PDF27	0 / 0	0.00857 / -0.00857	0 / 0
PDF28	0 / 0	0.00706 / -0.00706	0 / 0
PDF29	0 / 0	0.0106 / -0.0106	0 / 0
PDF30	0 / 0	0.00792 / -0.00792	0 / 0
$t\bar{t}$ SR3 Extrapolation Range	0 / 0	3.45e-05 / -3.45e-05	0 / 0
$t\bar{t}$ SR3 Extrapolation VariationParam0	0 / 0	0.000216 / -0.000216	0 / 0
$t\bar{t}$ SR3 Extrapolation VariationParam1	0 / 0	-9.8e-07 / 9.8e-07	0 / 0

C. signal injection test with psedo data

The pseudo-asimov data sets are created with the estimated background and the Z' signal with mass $m_{Z'} = 1\ \text{TeV}, 2\ \text{TeV}, 3\ \text{TeV}$. In addition the pseudo-asimov data is smeared with a Poisson distribution. Background only and signal+background fits are performed with the pseudo-asimov data, $\mu = 2$ and SR0+SR3 regions.

Figures 138, 139 and 140 show the each nuisance parameter pull.

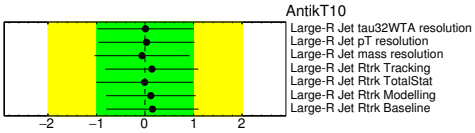

(a) NuisPar AntikT10

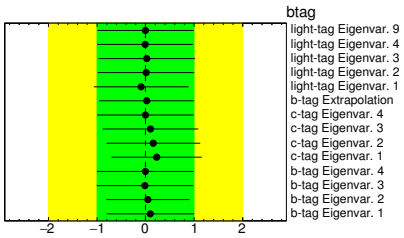

(b) NuisPar btag

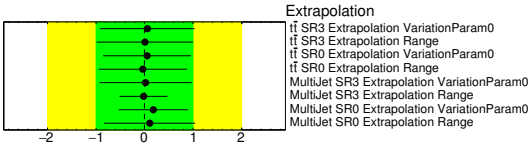

(c) NuisPar Extrapolation

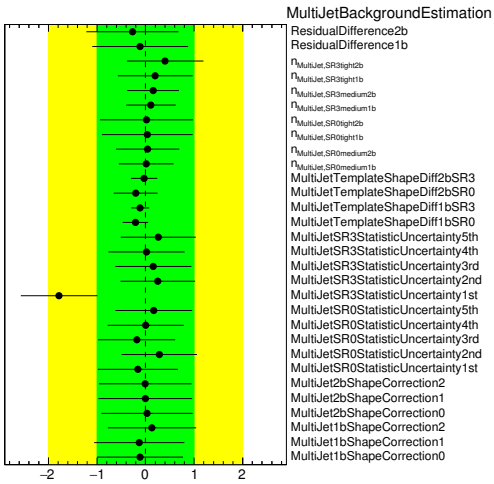

(d) NuisPar multijet

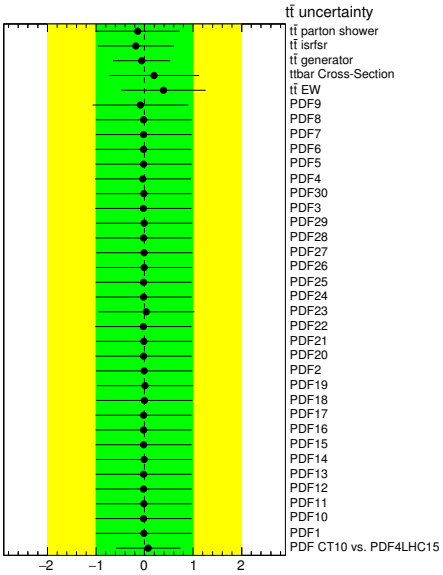

(e) NuisPar ttbar

Figure 138: Nuisance parameter pulls for fitting with the pseudo date injected Z' 1 TeV

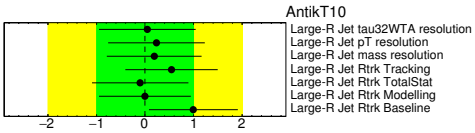

(a) NuisPar AntikT10

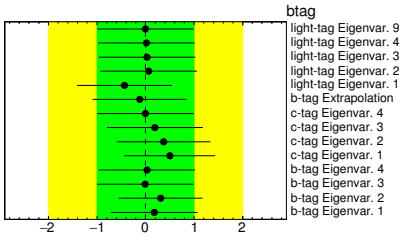

(b) NuisPar btag

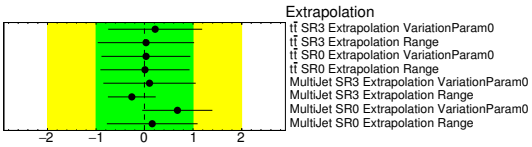

(c) NuisPar Extrapolation

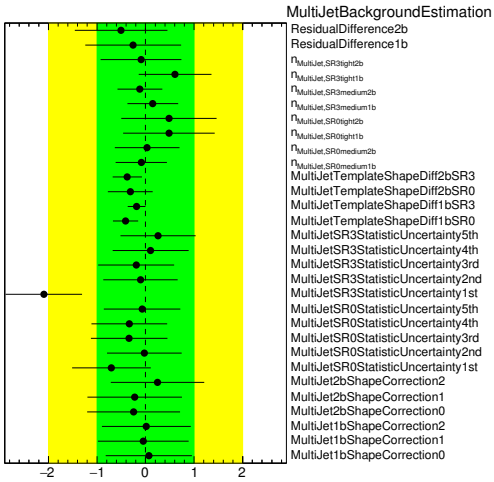

(d) NuisPar multijet

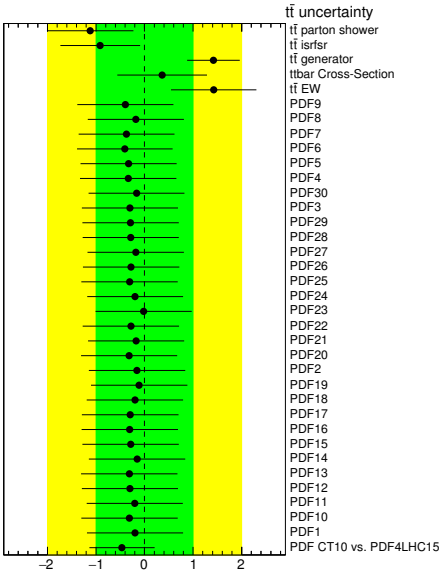

(e) NuisPar ttbar

Figure 139: Nuisance parameter pulls for fitting with the pseudo date injected Z' 2 TeV

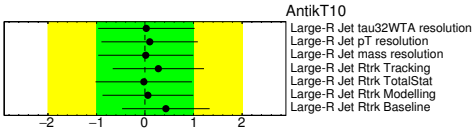

(a) NuisPar AntikT10

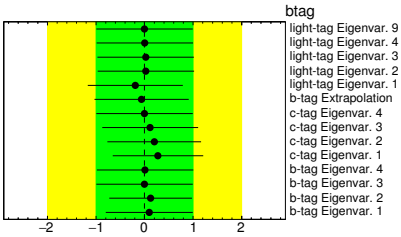

(b) NuisPar btag

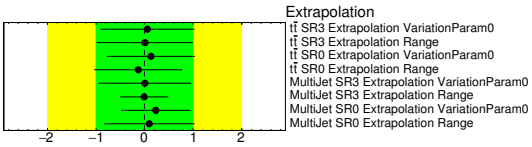

(c) NuisPar Extrapolation

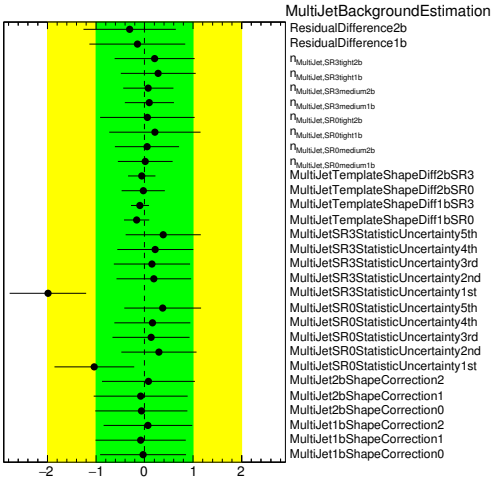

(d) NuisPar multijet

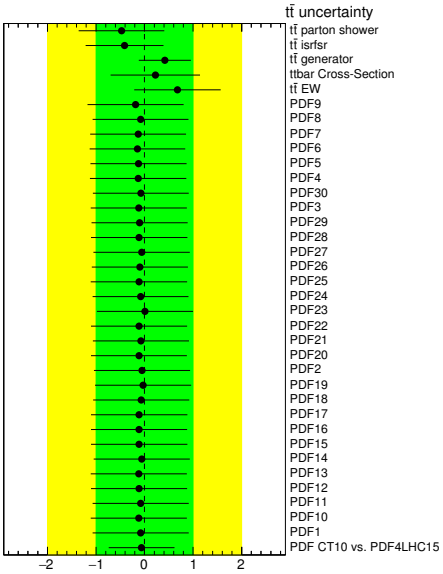

(e) NuisPar ttbar

Figure 140: Nuisance parameter pulls for fitting with the pseudo date injected Z' 3 TeV

Pre-fit and Post-fit $m_{t\bar{t}}$ distributions are showed in Figure 141 and 142 for the pseudo-asimov data injected Z' 1 TeV.

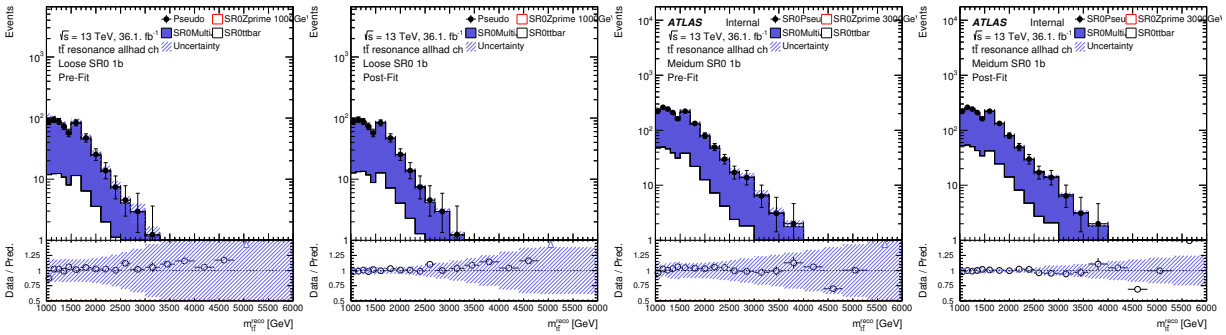

(a) Pre-fit,
one tight b-tagged Loose

(b) Post-fit,
one tight b-tagged Loose

(c) Pre-fit,
one tight b-tagged Medium

(d) Post-fit,
one tight b-tagged Medium

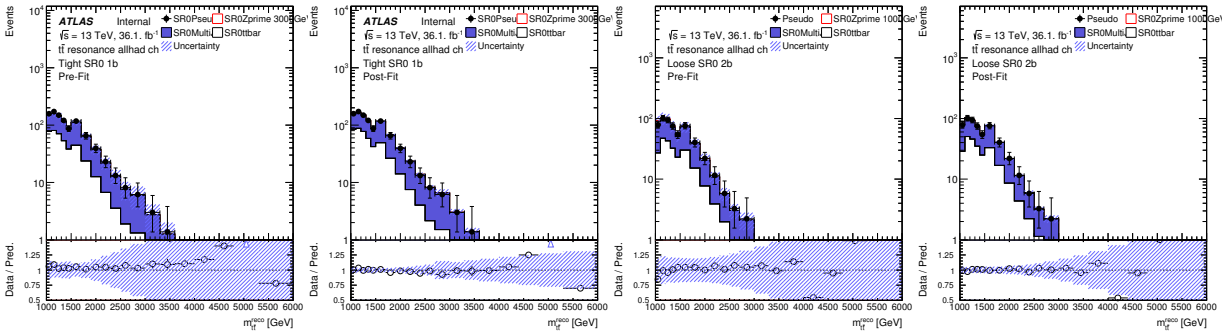

(e) Pre-fit,
one tight b-tagged Tight

(f) Post-fit,
one tight b-tagged Tight

(g) Pre-fit,
two tight b-tagged Loose

(h) Post-fit,
two tight b-tagged Loose

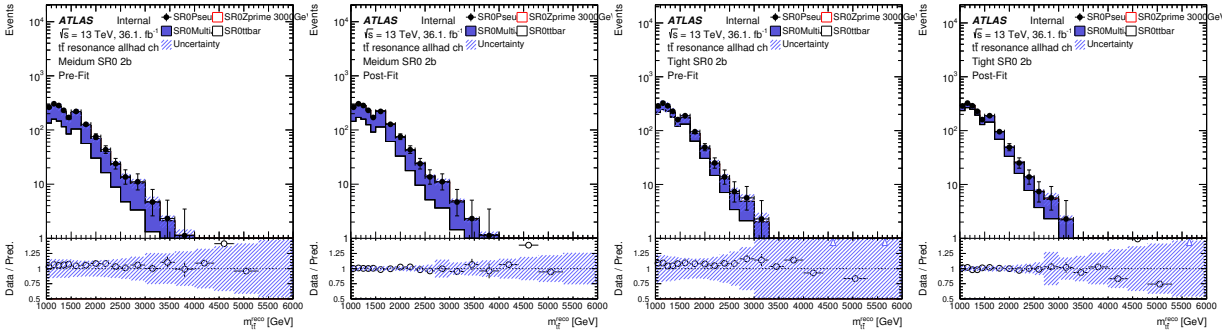

(i) Pre-fit,
two tight b-tagged Medium

(j) Post-fit,
two tight b-tagged Medium

(k) Pre-fit,
two tight b-tagged Tight

(l) Post-fit,
two tight b-tagged Tight

Figure 141: Pre-fit and Post-fit distributions for SR0 and the pseudo date injected Z' 1 TeV

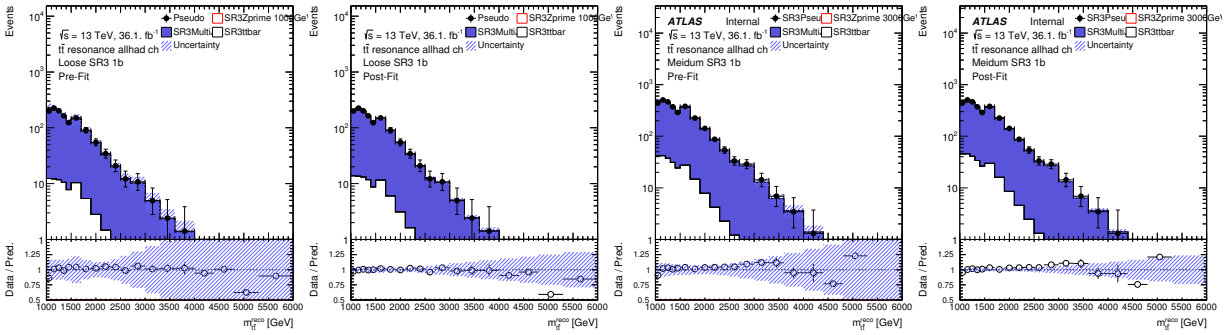

(a) Pre-fit,
one tight b-tagged Loose

(b) Post-fit,
one tight b-tagged Loose

(c) Pre-fit,
one tight b-tagged Medium

(d) Post-fit,
one tight b-tagged Medium

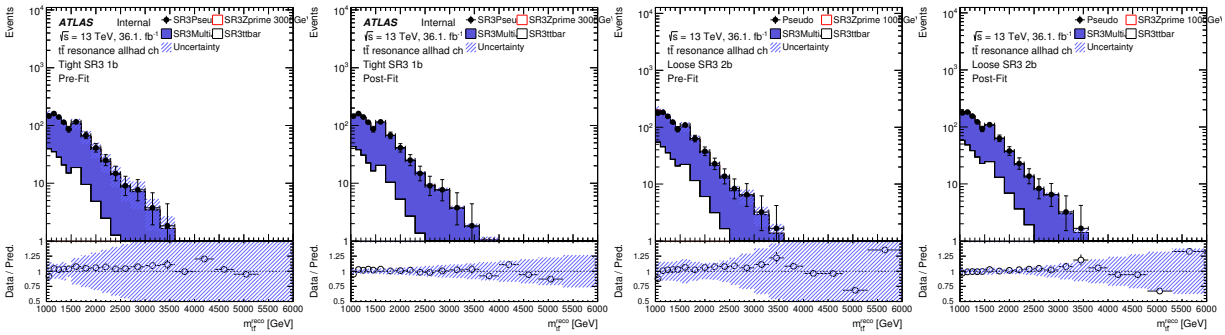

(e) Pre-fit,
one tight b-tagged Tight

(f) Post-fit,
one tight b-tagged Tight

(g) Pre-fit,
two tight b-tagged Loose

(h) Post-fit,
two tight b-tagged Loose

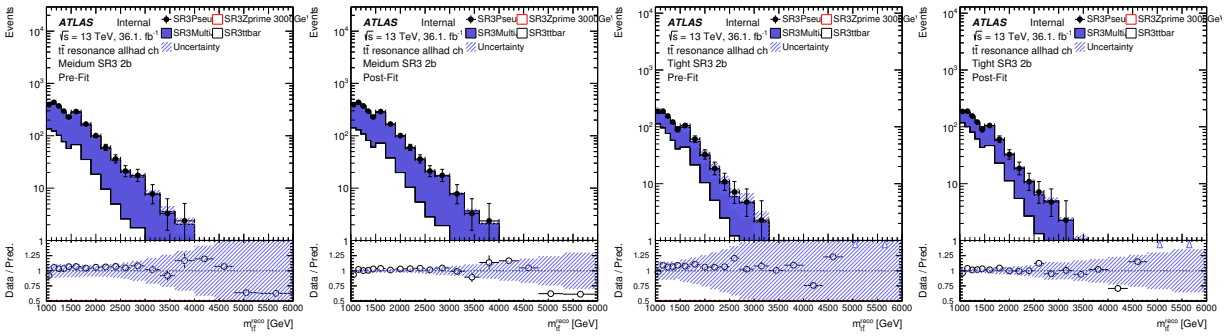

(i) Pre-fit,
two tight b-tagged Medium

(j) Post-fit,
two tight b-tagged Medium

(k) Pre-fit,
two tight b-tagged Tight

(l) Post-fit,
two tight b-tagged Tight

Figure 142: Pre-fit and Post-fit distributions for SR3 and the pseudo date injected Z' 1 TeV

For the pseudo-asimov data injected Z' 2 TeV, Pre-fit and Post-fit $m_{t\bar{t}}$ distributions are showed in Figure 143 and 144.

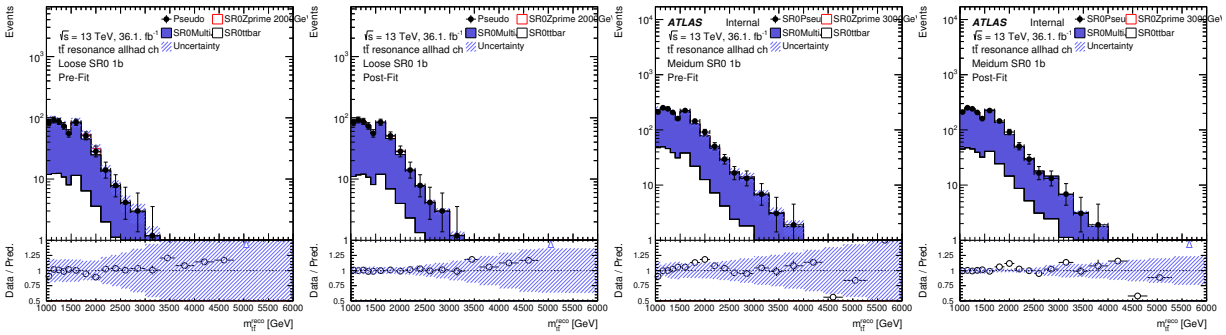

(a) Pre-fit,
one tight b-tagged Loose

(b) Post-fit,
one tight b-tagged Loose

(c) Pre-fit,
one tight b-tagged Medium

(d) Post-fit,
one tight b-tagged Medium

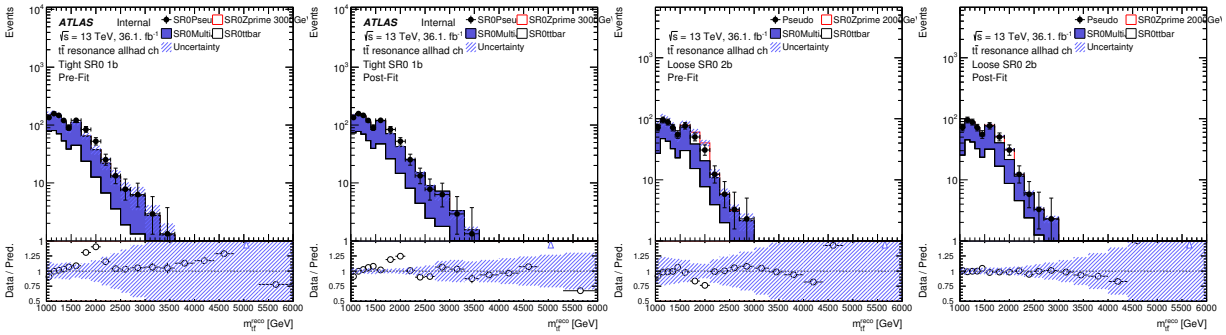

(e) Pre-fit,
one tight b-tagged Tight

(f) Post-fit,
one tight b-tagged Tight

(g) Pre-fit,
two tight b-tagged Loose

(h) Post-fit,
two tight b-tagged Loose

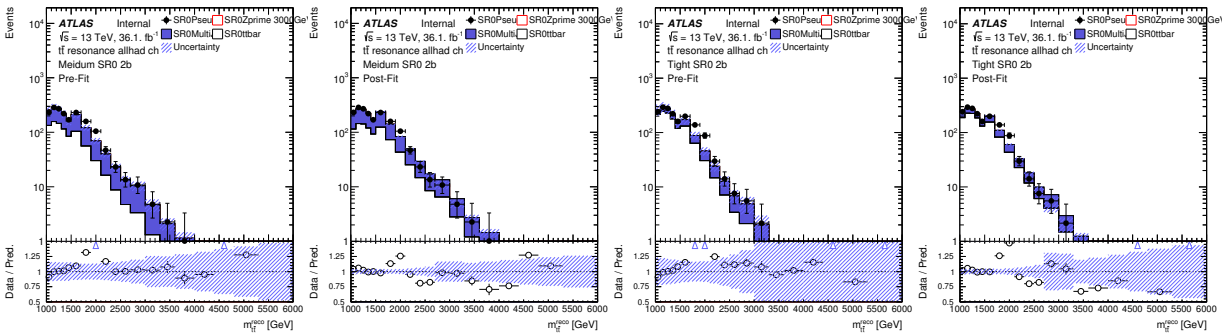

(i) Pre-fit,
two tight b-tagged Medium

(j) Post-fit,
two tight b-tagged Medium

(k) Pre-fit,
two tight b-tagged Tight

(l) Post-fit,
two tight b-tagged Tight

Figure 143: Pre-fit and Post-fit distributions for SR0 and the pseudo date injected Z' 2 TeV

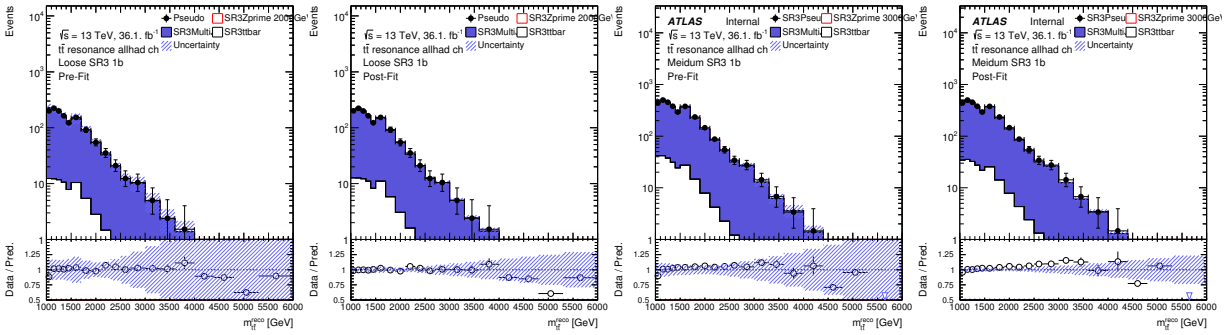

(a) Pre-fit, one tight b-tagged Loose

(b) Post-fit, one tight b-tagged Loose

(c) Pre-fit, one tight b-tagged Medium

(d) Post-fit, one tight b-tagged Medium

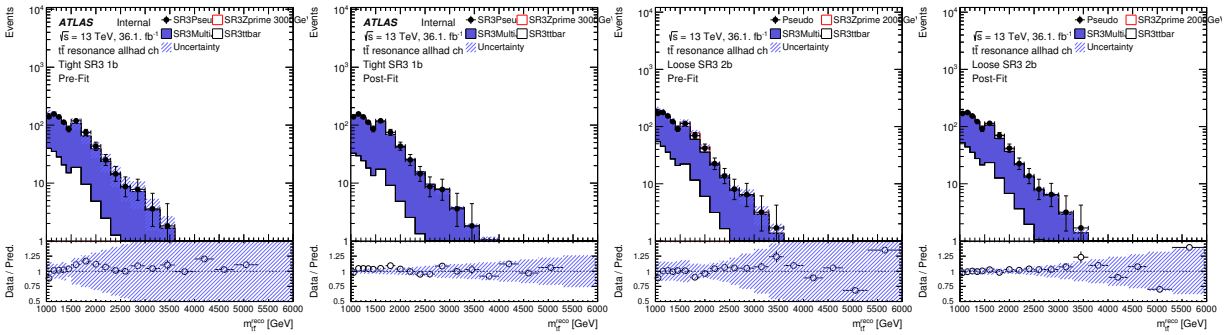

(e) Pre-fit, one tight b-tagged Tight

(f) Post-fit, one tight b-tagged Tight

(g) Pre-fit, two tight b-tagged Loose

(h) Post-fit, two tight b-tagged Loose

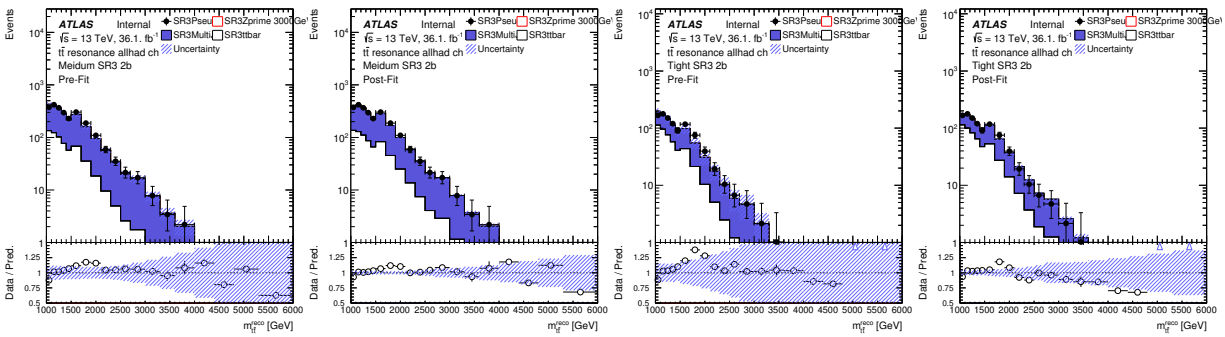

(i) Pre-fit, two tight b-tagged Medium

(j) Post-fit, two tight b-tagged Medium

(k) Pre-fit, two tight b-tagged Tight

(l) Post-fit, two tight b-tagged Tight

Figure 144: Pre-fit and Post-fit distributions for SR3 and the pseudo date injected Z' 2 TeV

For the pseudo-asimov data injected Z' 3 TeV, Pre-fit and Post-fit $m_{t\bar{t}}$ distributions are showed in Figure 145 and 146.

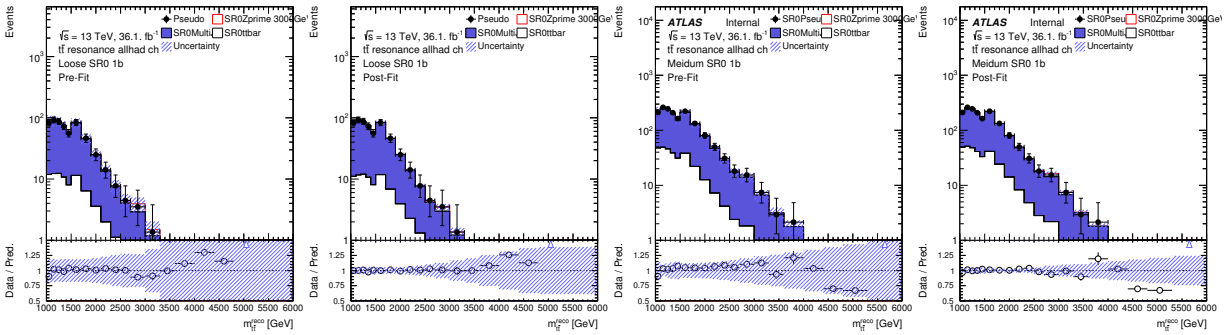

(a) Pre-fit,
one tight b-tagged Loose

(b) Post-fit,
one tight b-tagged Loose

(c) Pre-fit,
one tight b-tagged Medium

(d) Post-fit,
one tight b-tagged Medium

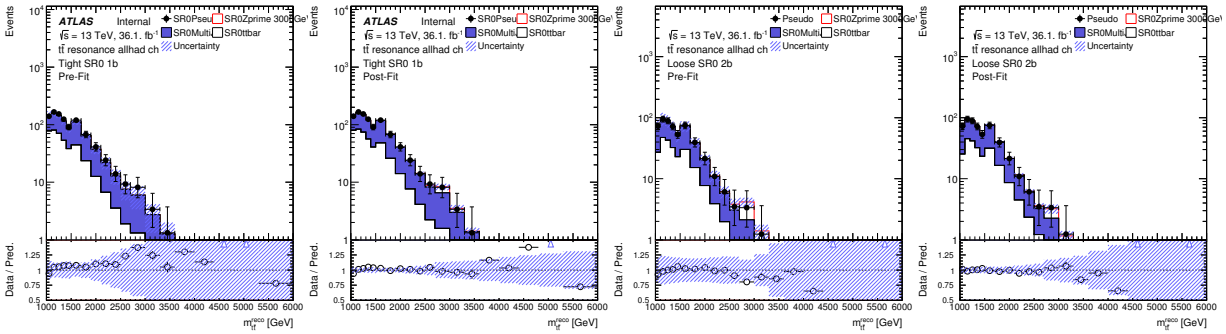

(e) Pre-fit,
one tight b-tagged Tight

(f) Post-fit,
one tight b-tagged Tight

(g) Pre-fit,
two tight b-tagged Loose

(h) Post-fit,
two tight b-tagged Loose

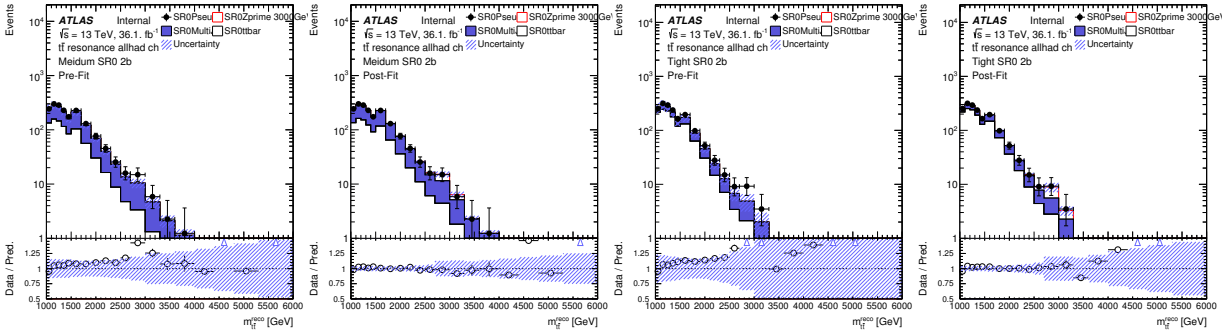

(i) Pre-fit,
two tight b-tagged Medium

(j) Post-fit,
two tight b-tagged Medium

(k) Pre-fit,
two tight b-tagged Tight

(l) Post-fit,
two tight b-tagged Tight

Figure 145: Pre-fit and Post-fit distributions for SR0 and the pseudo date injected Z' 3 TeV

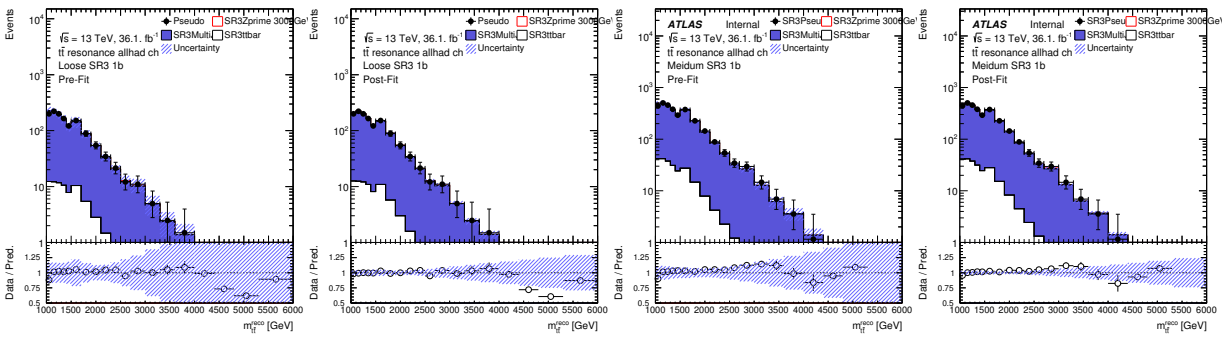

(a) Pre-fit,
one tight b-tagged Loose

(b) Post-fit,
one tight b-tagged Loose

(c) Pre-fit,
one tight b-tagged Medium

(d) Post-fit,
one tight b-tagged Medium

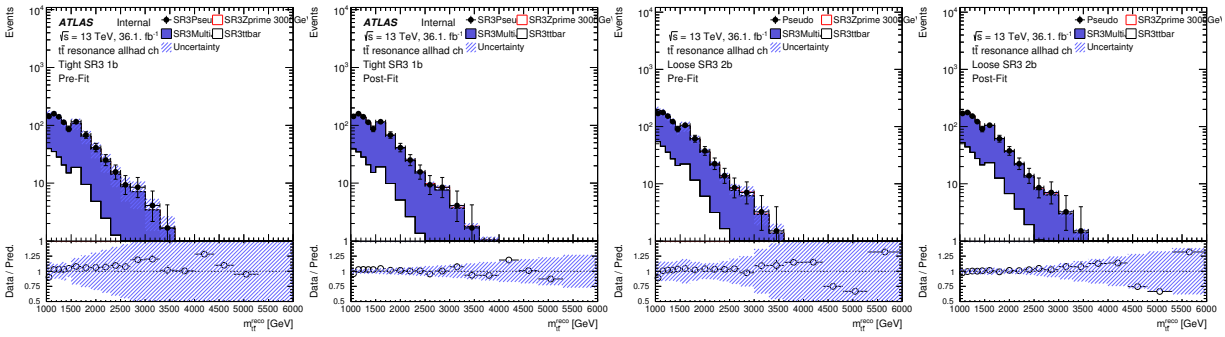

(e) Pre-fit,
one tight b-tagged Tight

(f) Post-fit,
one tight b-tagged Tight

(g) Pre-fit,
two tight b-tagged Loose

(h) Post-fit,
two tight b-tagged Loose

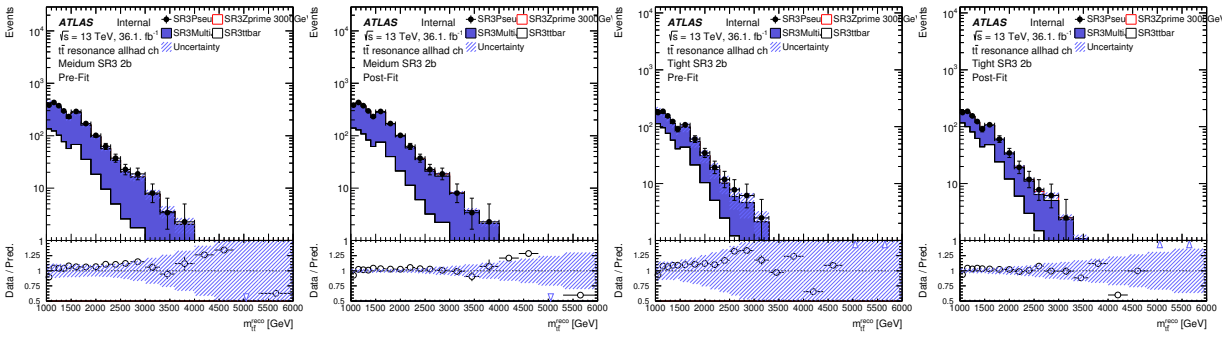

(i) Pre-fit,
two tight b-tagged Medium

(j) Post-fit,
two tight b-tagged Medium

(k) Pre-fit,
two tight b-tagged Tight

(l) Post-fit,
two tight b-tagged Tight

Figure 146: Pre-fit and Post-fit distributions for SR3 and the pseudo date injected Z' 3 TeV

Resulting expected upper limits on production cross section of Z' for the each pseudo-asimov data are shown in Figure 147. The exsitence of signal can be found if Z' signal is included in data as can be seen except for 1 TeVin Figure 147. In low $m_{t\bar{t}}$ region, the buckets analisys has better sensitivity, and the buckets analysis can find such the lower mass signal.

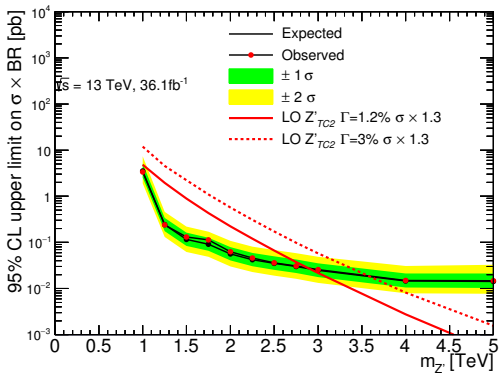

(a) Upper limits on $\sigma_{Z'}$ for the pseudo-asimov data injected 1 TeVZ'

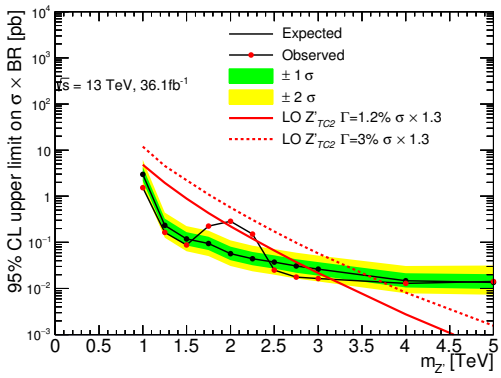

(b) Upper limits on $\sigma_{Z'}$ for the pseudo-asimov data injected 2 TeVZ'

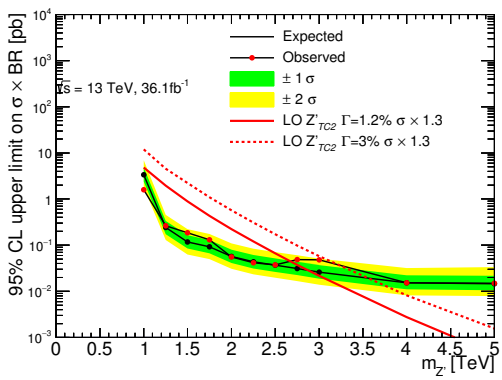

(c) Upper limits on $\sigma_{Z'}$ for the pseudo-asimov data injected 3 TeVZ'

Figure 147: Extracted upper limits on Z' production cross section for the each pseudo-asimov data

D. Other kinematic distributions for each region in τ_{32}-analysis

VR3

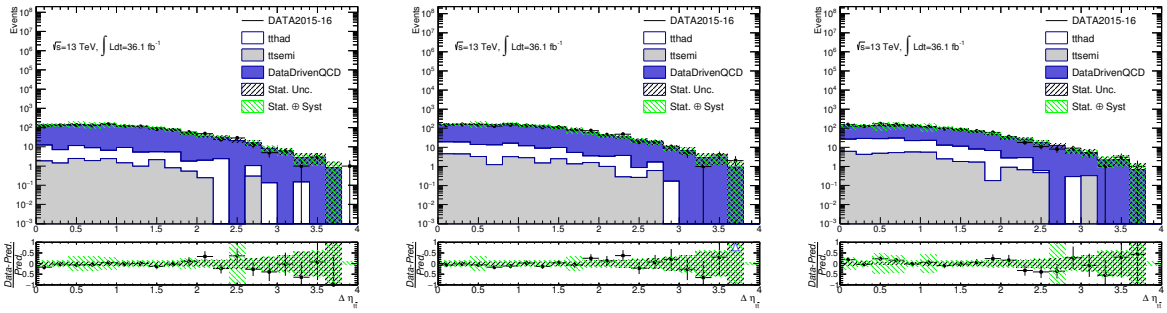

(a) Loose (b) Medium (c) Tight

Figure 148: Distributions of angular differnece between the two large-R jets in η in the validation region for one tight b-tag category.

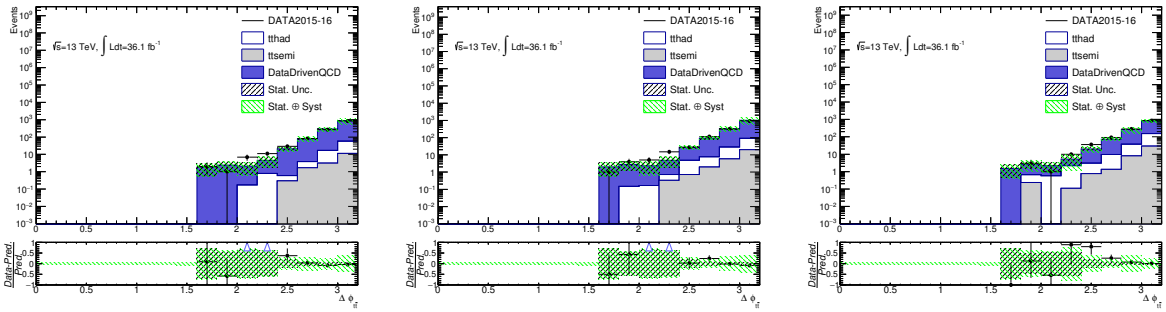

(a) Loose (b) Medium (c) Tight

Figure 149: Distributions of angular differnece between the two large-R jets in ϕ in the validation region for one tight b-tag category.

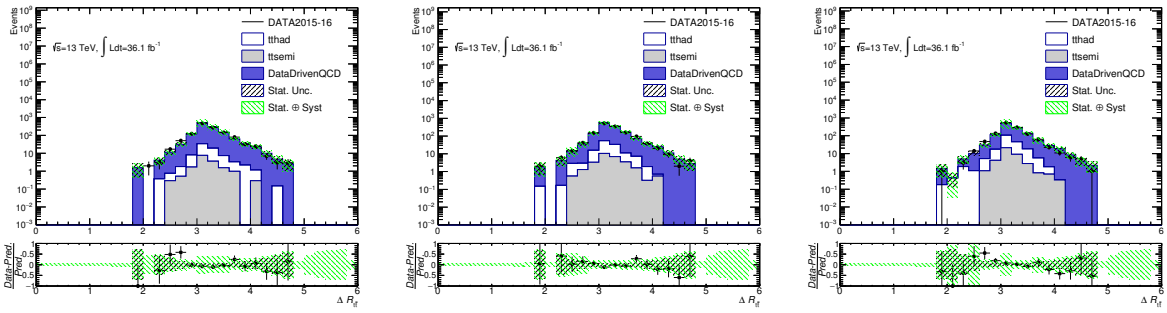

(a) Loose (b) Medium (c) Tight

Figure 150: Distributions of angular differnece between the two large-R jets in R in the validation region for one tight b-tag category.

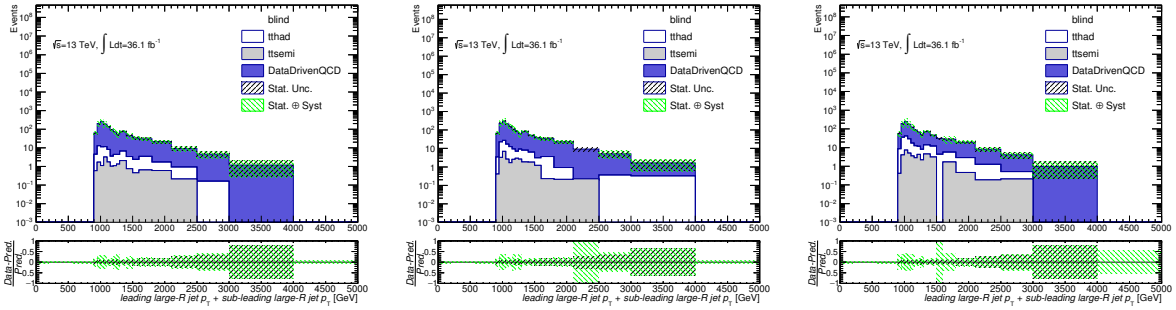

(a) Loose (b) Medium (c) Tight

Figure 151: Distributions of scalar sum of p_T of the two large-R jets in the validation region for one tight b-tag category.

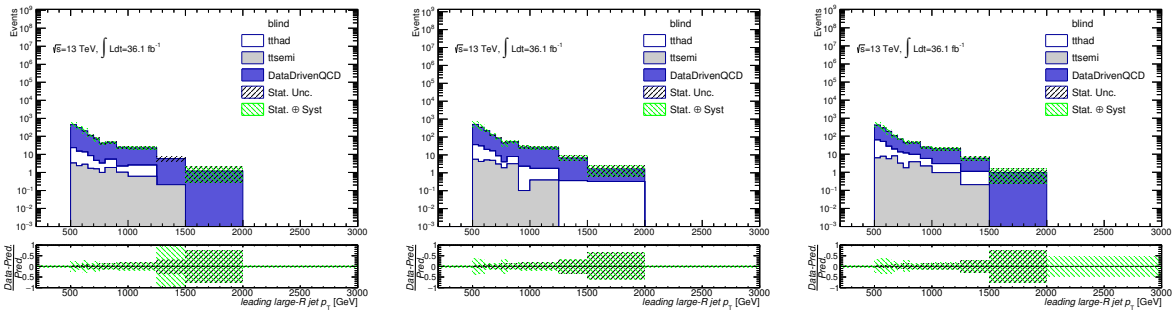

(a) Leading large-R jet, Loose (b) Leading large-R jet, Medium (c) Leading large-R jet, Tight

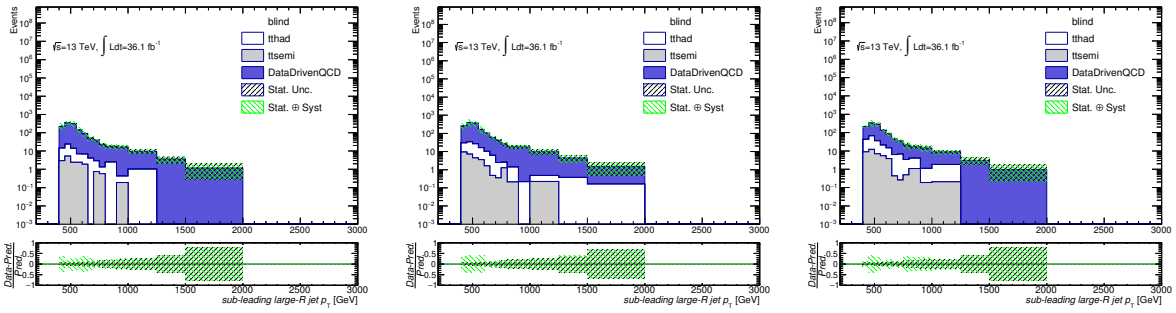

(d) Subleading large-R jet, Loose (e) Subleading large-R jet, Medium (f) Subleading large-R jet, Tight

Figure 152: Distributions of p_T of the large-R jets in the validation region for one tight b-tag category.

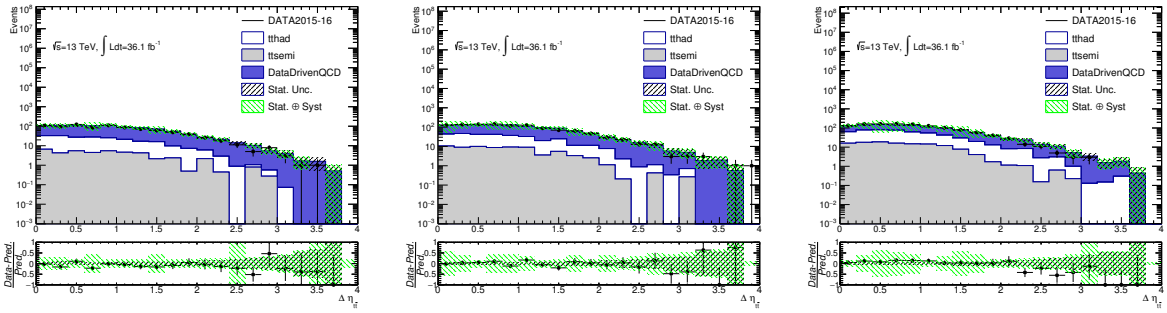

(a) Loose (b) Medium (c) Tight

Figure 153: Distributions of angular differnece between the two large-R jets in η in the validation region for two tight b-tag category.

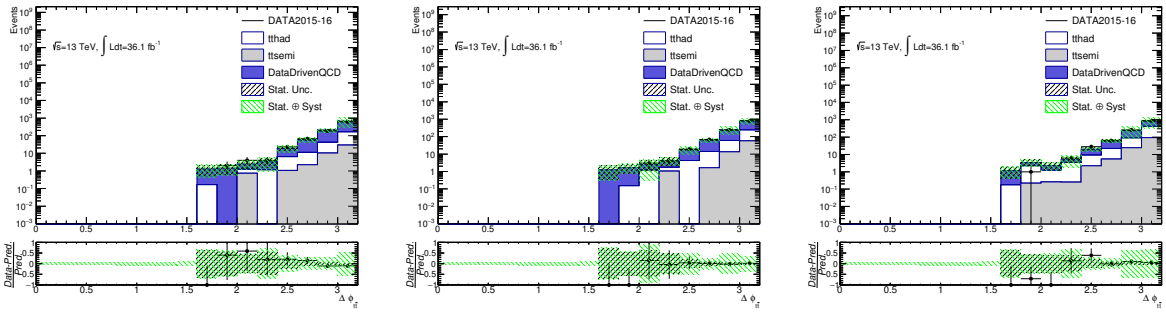

(a) Loose (b) Medium (c) Tight

Figure 154: Distributions of angular differnece between the two large-R jets in ϕ in the validation region for two tight b-tag category.

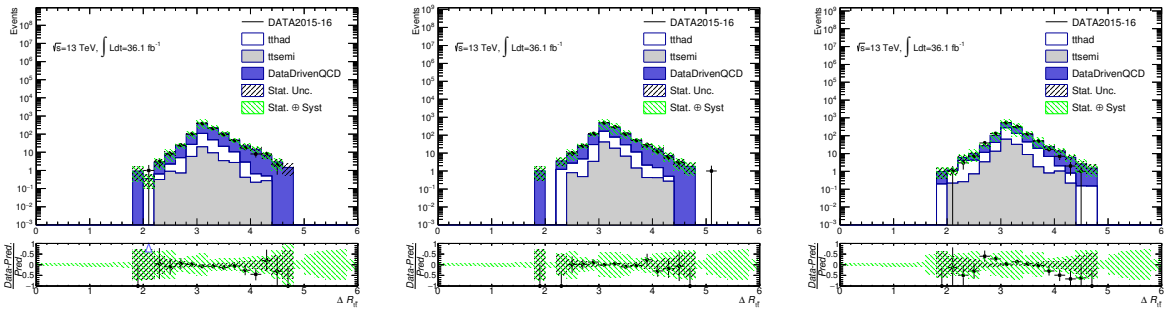

(a) Loose (b) Medium (c) Tight

Figure 155: Distributions of angular differnece between the two large-R jets in R in the validation region for two tight b-tag category.

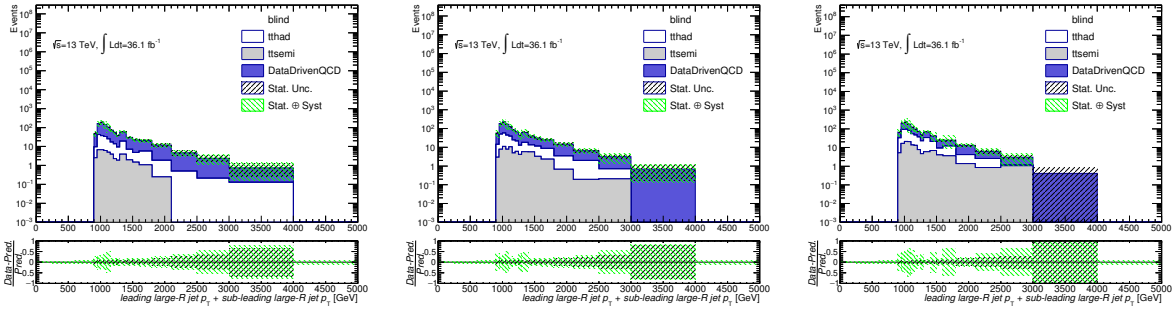

(a) Loose (b) Medium (c) Tight

Figure 156: Distributions of scalar sum of p_T of the two large-R jets in the validation region for two tight b-tag category.

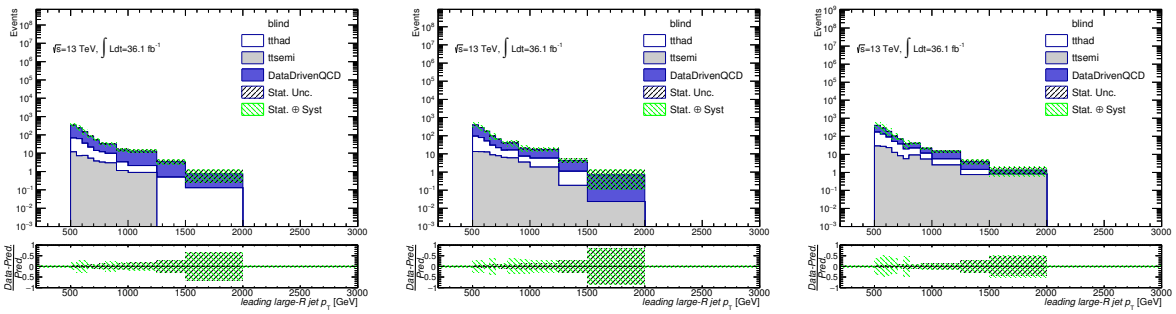

(a) Leading p_T jet, Loose (b) Leading p_T jet, Medium (c) Leading p_T jet, Tight

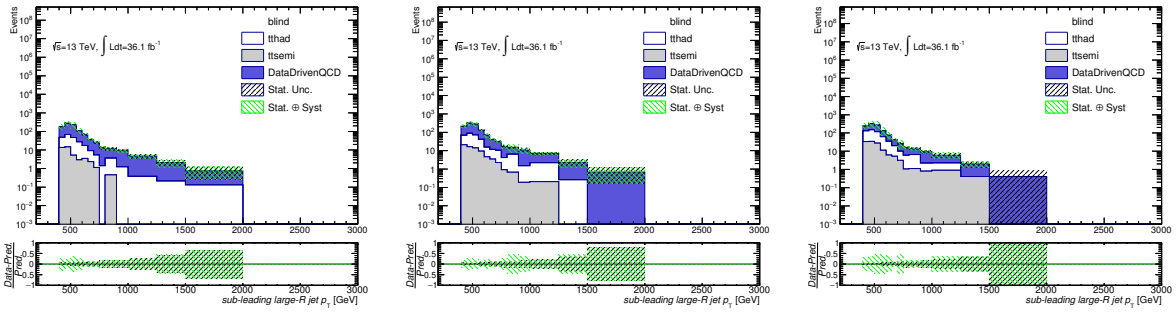

(d) Subeading p_T jet, Loose (e) Subleading p_T jet, Medium (f) Subleading p_T jet, Tight

Figure 157: Distributions of p_T of the large-R jets in the validation region for two tight b-tag category.

SR

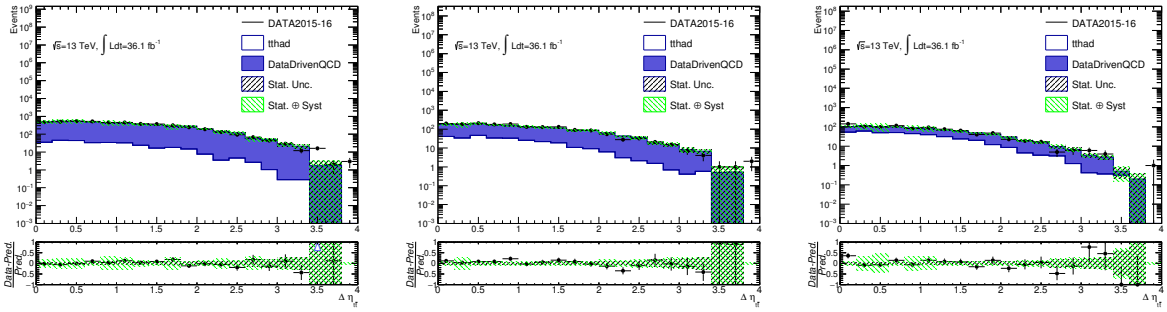

(a) Loose (b) Medium (c) Tight

Figure 158: Distributions of angular differnece between the two large-R jets in η in the signal region for one tight b-tag category.

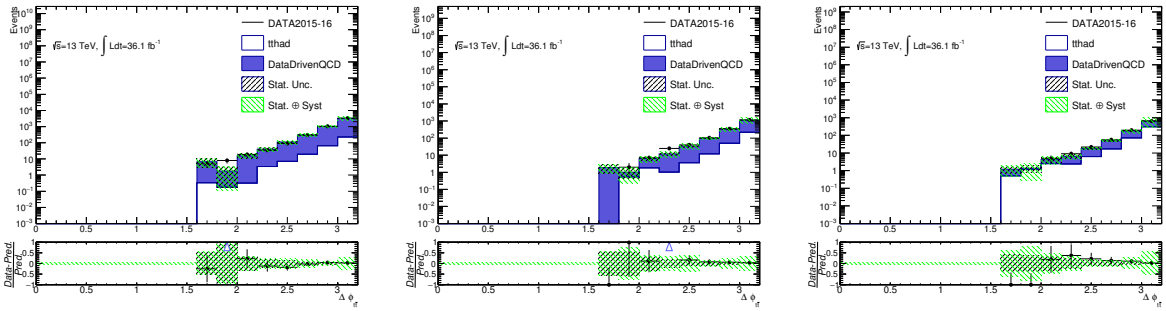

(a) Loose (b) Medium (c) Tight

Figure 159: Distributions of angular differnece between the two large-R jets in ϕ in the signal region for one tight b-tag category.

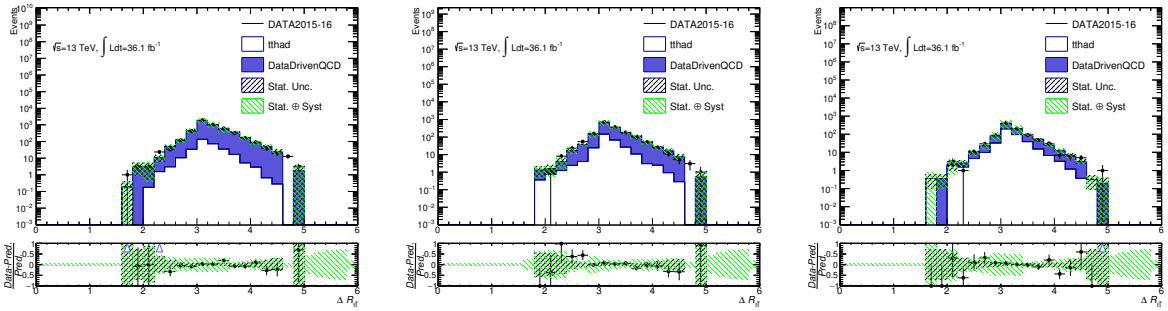

(a) Loose (b) Medium (c) Tight

Figure 160: Distributions of angular differnece between the two large-R jets in R in the signal region for one tight b-tag category.

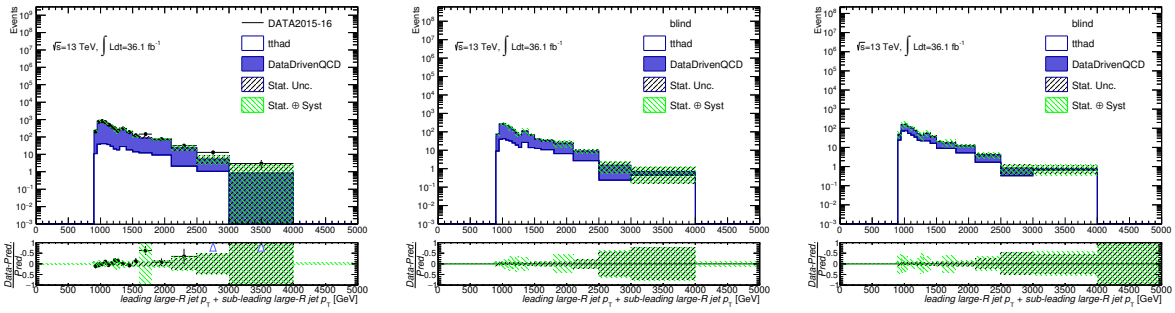

(a) Loose (b) Medium (c) Tight

Figure 161: Distributions of scalar sum of p_T of the two large-R jets in the signal region for one tight b-tag category.

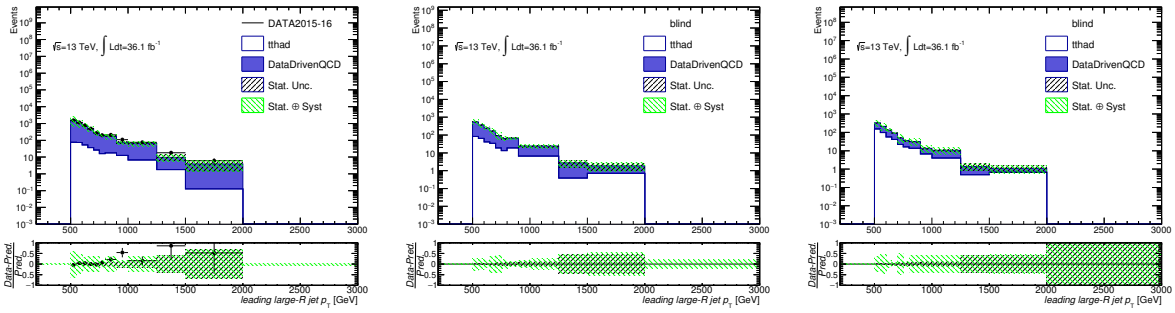

(a) Leading p_T jet, Loose (b) Leading p_T jet, Medium (c) Leading p_T jet, Tight

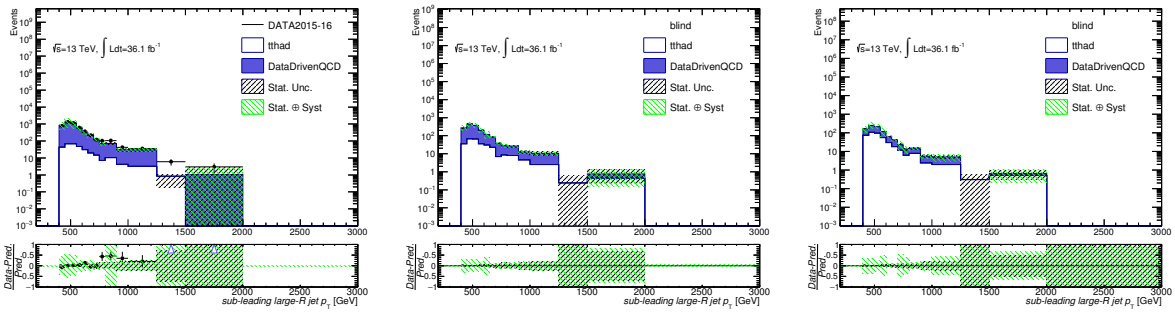

(d) Subleading p_T jet, Loose (e) Subleading p_T jet, Medium (f) Subleading p_T jet, Tight

Figure 162: Distributions of p_T of the large-R jets in the signal region for one tight b-tag category.

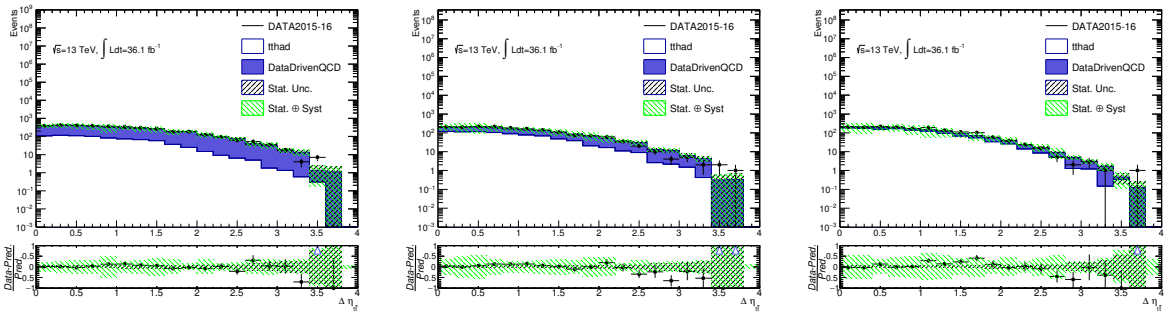

(a) Loose (b) Medium (c) Tight

Figure 163: Distributions of angular differnece between the two large-R jets in η in the signal region for two tight b-tag category.

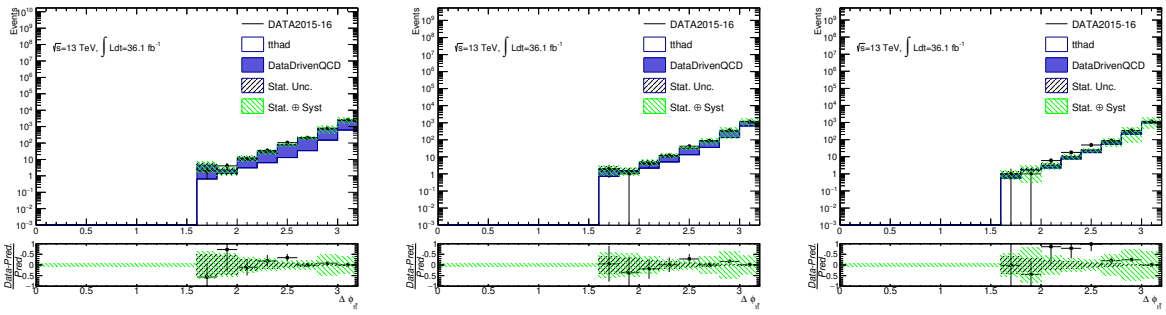

(a) Loose (b) Medium (c) Tight

Figure 164: Distributions of angular differnece between the two large-R jets in ϕ in the signal region for two tight b-tag category.

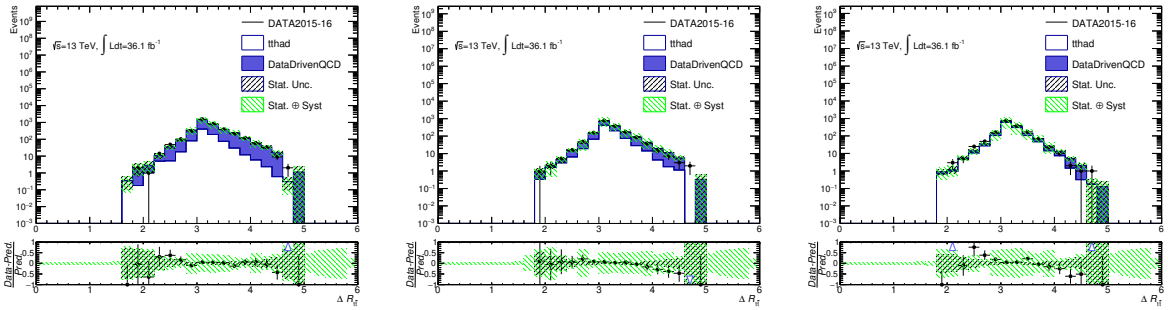

(a) Loose (b) Medium (c) Tight

Figure 165: Distributions of angular differnece between the two large-R jets in R in the signal region for two tight b-tag category.

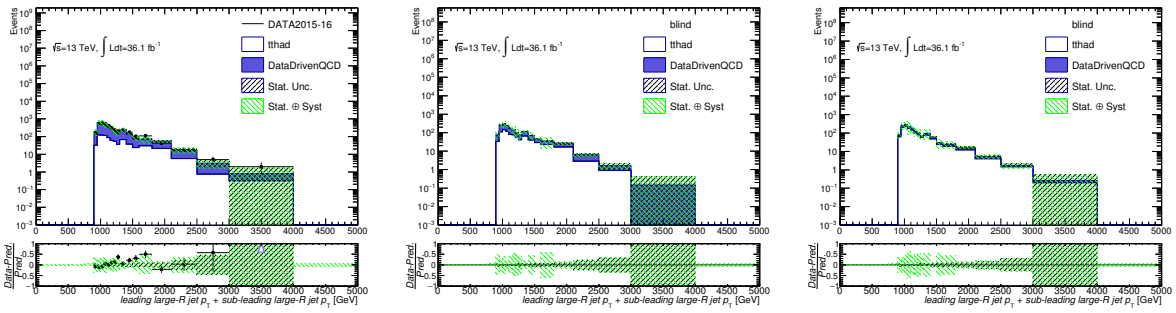

(a) Loose (b) Medium (c) Tight

Figure 166: Distributions of scalar sum of p_T of the two large-R jets in the signal region for two tight b-tag category.

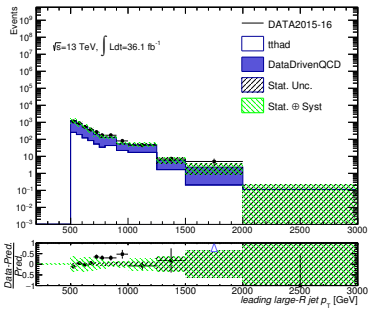

(a) Leading p_T jet, Loose

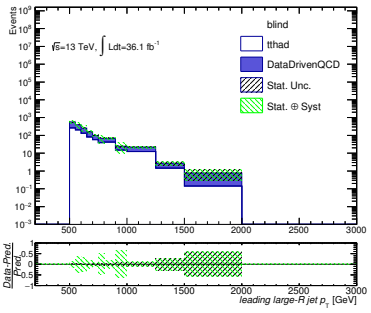

(b) Leading p_T jet, Medium

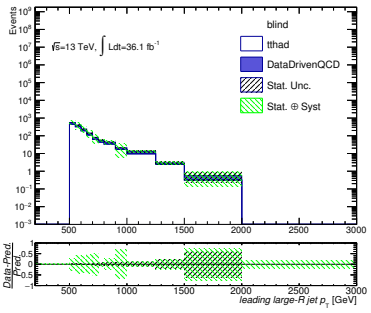

(c) Leading p_T jet, Tight

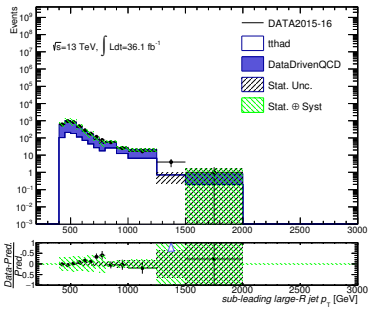

(d) Subleading p_T jet, Loose

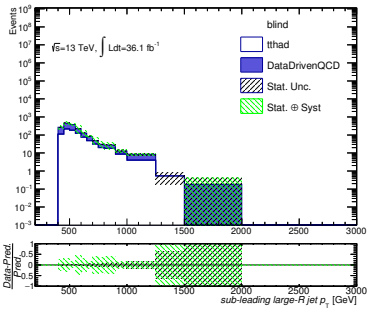

(e) Subleading p_T jet, Medium

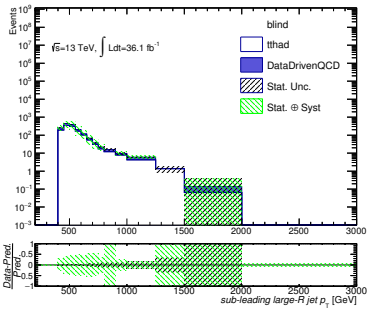

(f) Subleading p_T jet, Tight

Figure 167: Distributions of p_T of the large-R jets in the signal region for two tight b-tag category.

E. Shape difference of each kinematic distribution for $\tau_{32,wta}$-likelihood ratio

In order to reduce the effect of statistical uncertainty, $\tau_{32,wta}$-likelihood categories (loose, medium, tight) are merged. The shape differences of kinematic distribution between each $\tau_{32,wta}$-likelihood category are small. Those results of shape difference are showed in this appendix.

E.1. MC $t\bar{t}$ shape difference

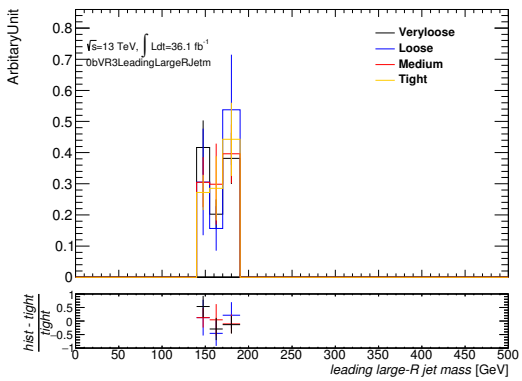

(a) Leading Large-R Jet in one tight b-tag

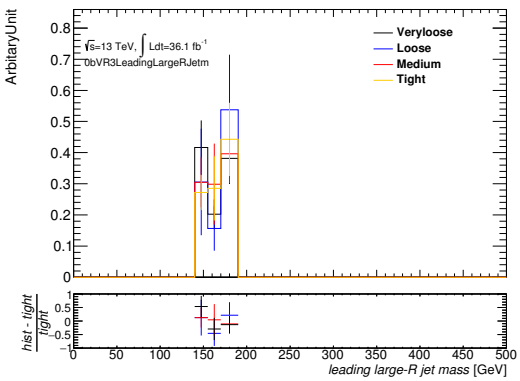

(b) Leading Large-R Jet in two tight b-tag

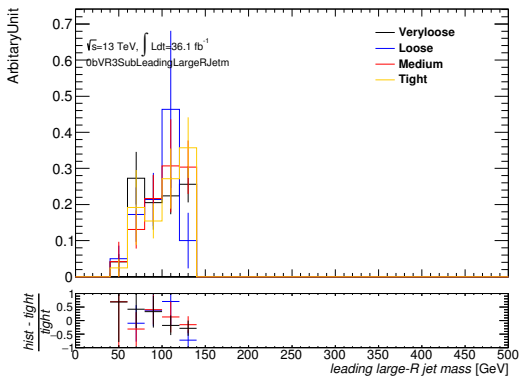

(c) Sub-leading Large-R Jet in one tight b-tag

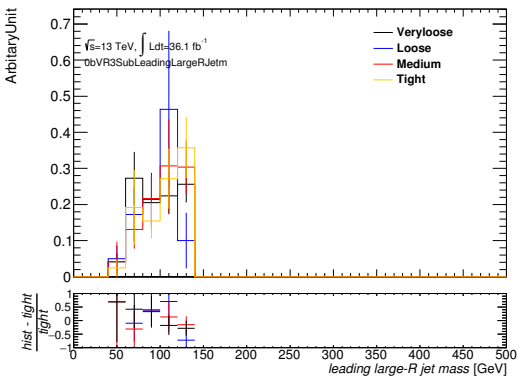

(d) Sub-leading Large-R Jet in two tight b-tag

Figure 168: Shape differences of Large-R Jet for MC $t\bar{t}$

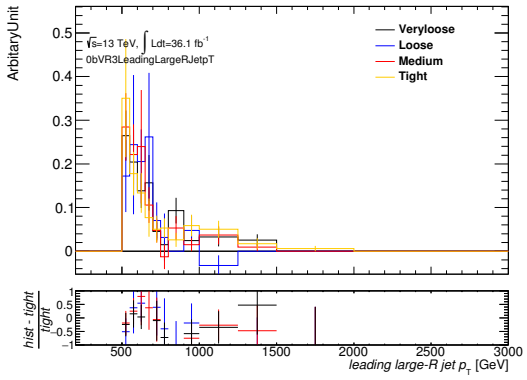

(a) Leading Large-R Jet in one tight b-tag

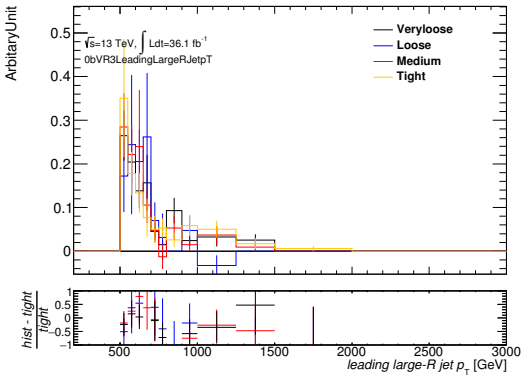

(b) Leading Large-R Jet in two tight b-tag

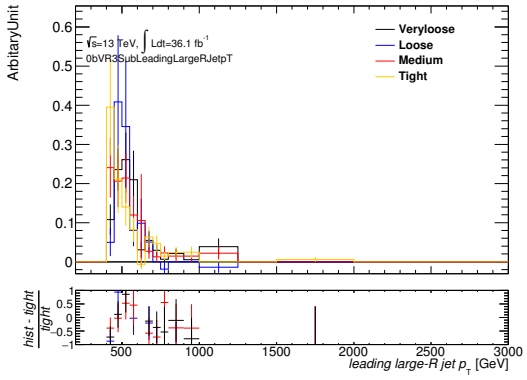

(c) Sub-leading Large-R Jet in one tight b-tag

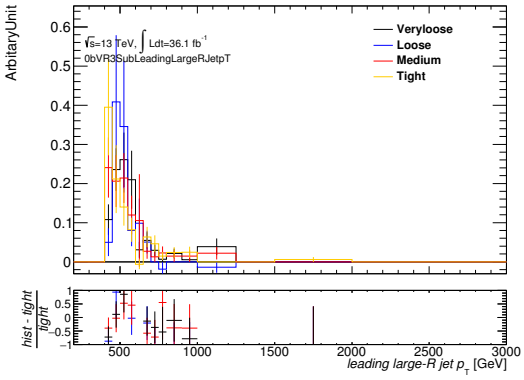

(d) Sub-leading Large-R Jet in two tight b-tag

Figure 169: Shape differences of Large-R Jet for MC $t\bar{t}$

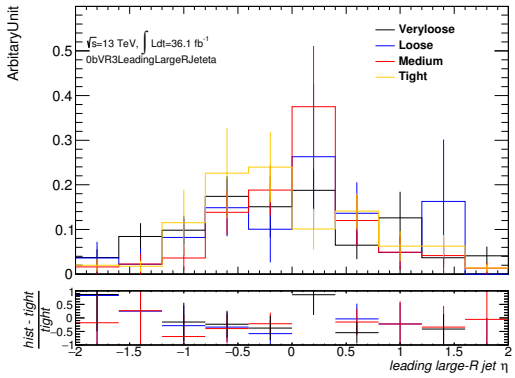

(a) Leading Large-R Jet in one tight b-tag

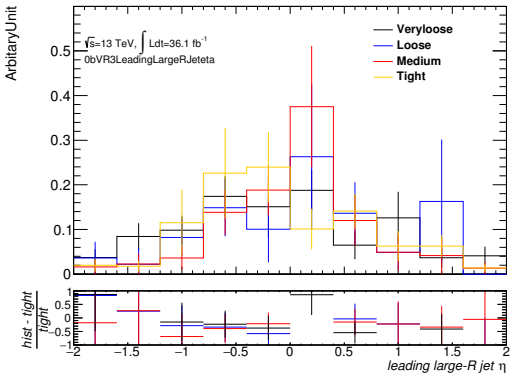

(b) Leading Large-R Jet in two tight b-tag

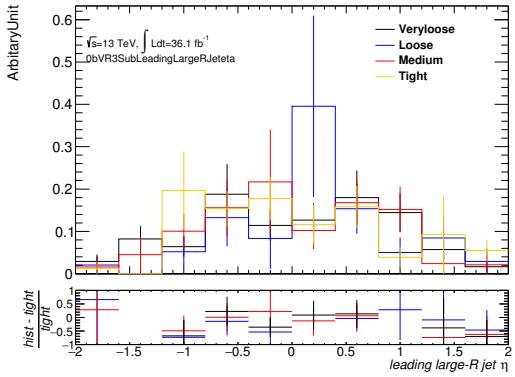

(c) Sub-leading Large-R Jet in one tight b-tag

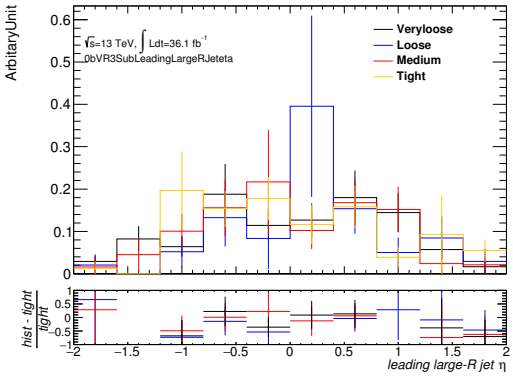

(d) Sub-leading Large-R Jet in two tight b-tag

Figure 170: Shape differences of Large-R Jet for MC $t\bar{t}$

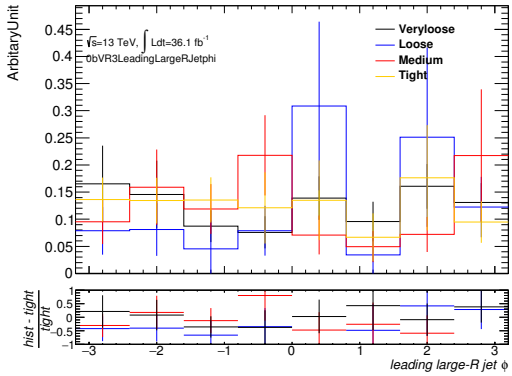

(a) Leading Large-R Jet in one tight b-tag

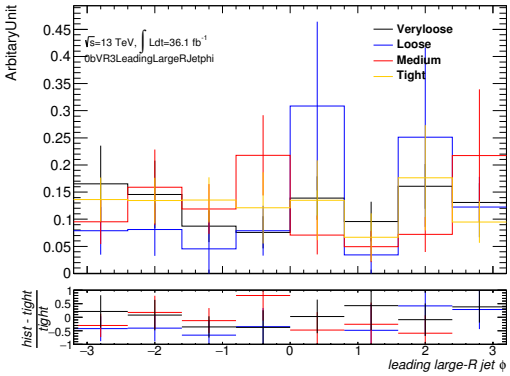

(b) Leading Large-R Jet in two tight b-tag

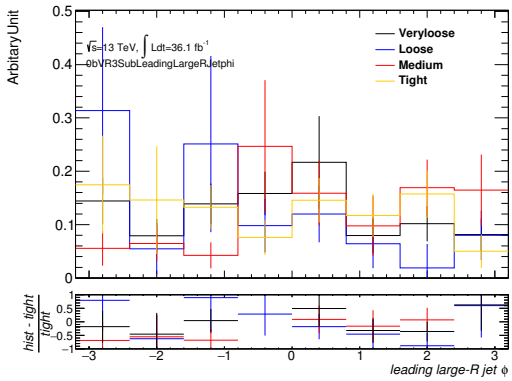

(c) Sub-leading Large-R Jet in one tight b-tag

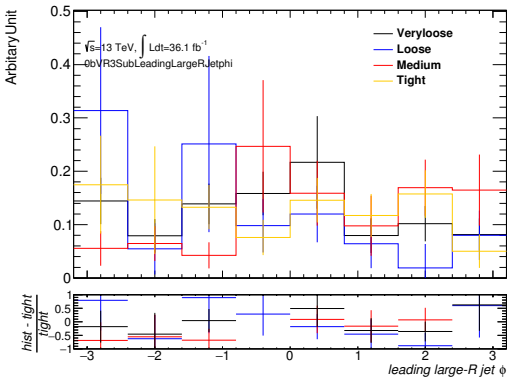

(d) Sub-leading Large-R Jet in two tight b-tag

Figure 171: Shape differences of Large-R Jet for MC $t\bar{t}$

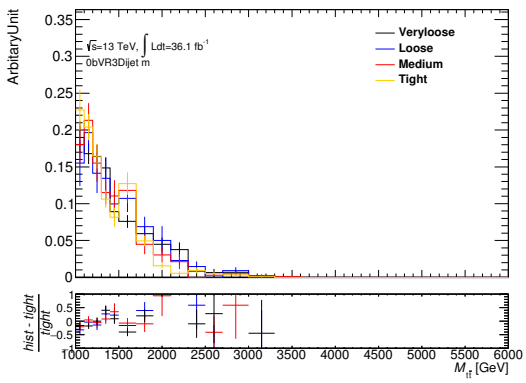

(a) Large-R Jet in one tight b-tag

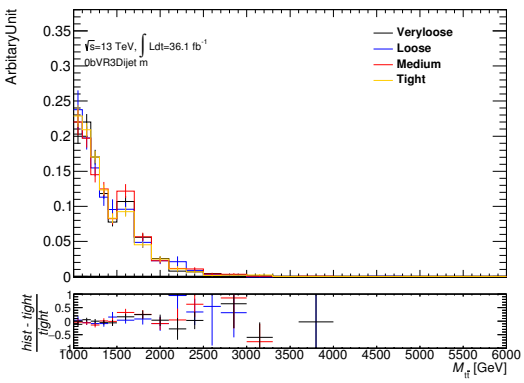

(b) Large-R Jet in two tight b-tag

Figure 172: Shape differences of Di-large R Jet for MC $t\bar{t}$

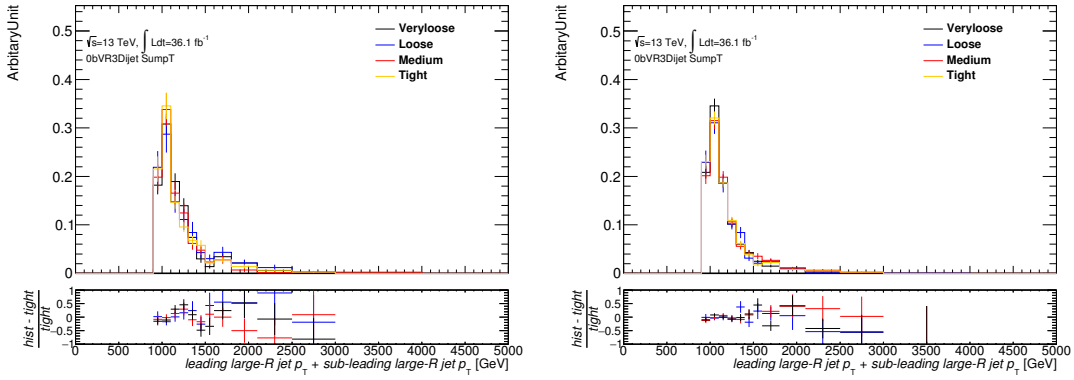

(a) Large-R Jet in one tight b-tag

(b) Large-R Jet in two tight b-tag

Figure 173: Shape differences of Di-large R Jet for MC $t\bar{t}$

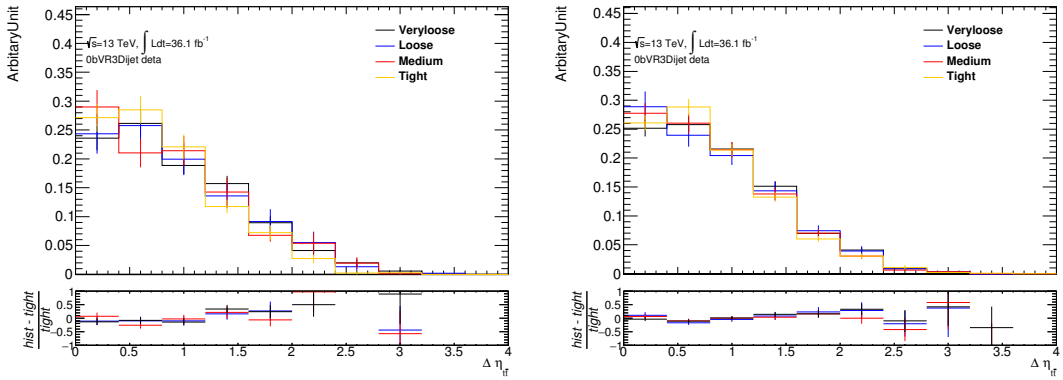

(a) Large-R Jet in one tight b-tag

(b) Large-R Jet in two tight b-tag

Figure 174: Shape differences of Di-large R Jet for MC $t\bar{t}$

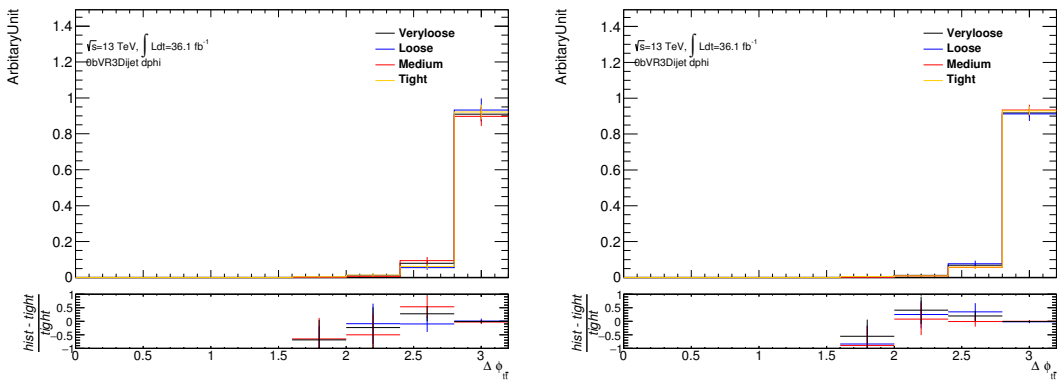

(a) Large-R Jet in one tight b-tag

(b) Large-R Jet in two tight b-tag

Figure 175: Shape differences of Di-large R Jet for MC $t\bar{t}$

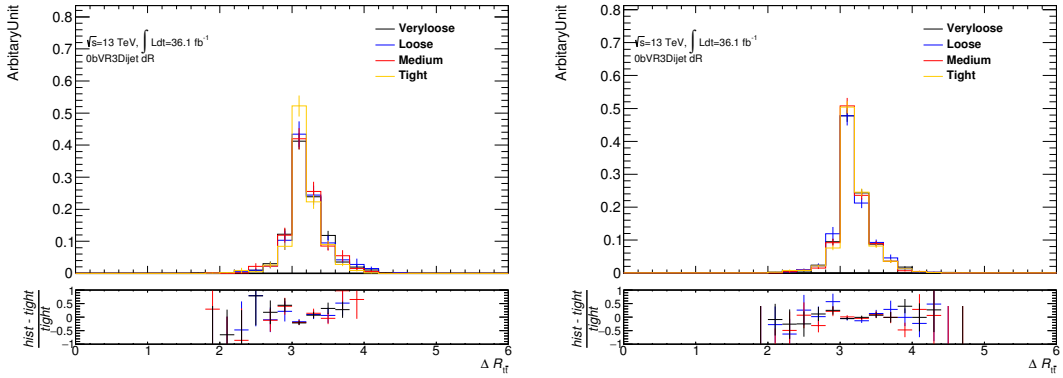

(a) Large-R Jet in one tight b-tag

(b) Large-R Jet in two tight b-tag

Figure 176: Shape differences of Di-large R Jet for MC $t\bar{t}$

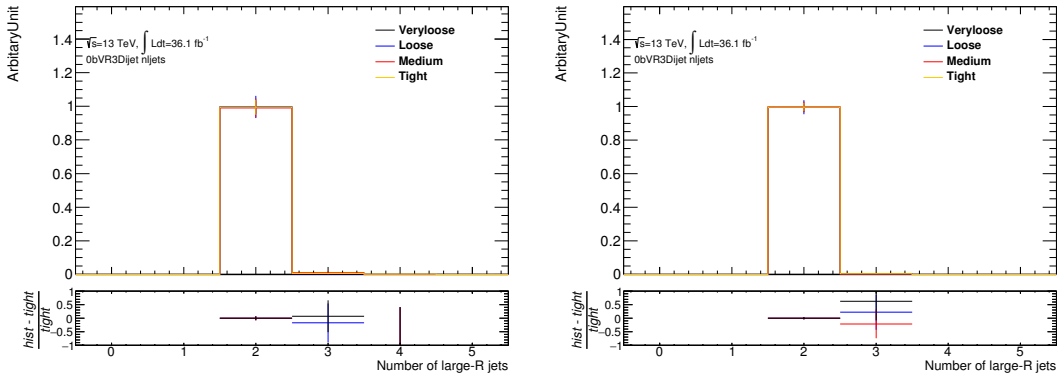

(a) Large-R Jet in one tight b-tag

(b) Large-R Jet in two tight b-tag

Figure 177: Shape differences of Di-large R Jet for MC $t\bar{t}$

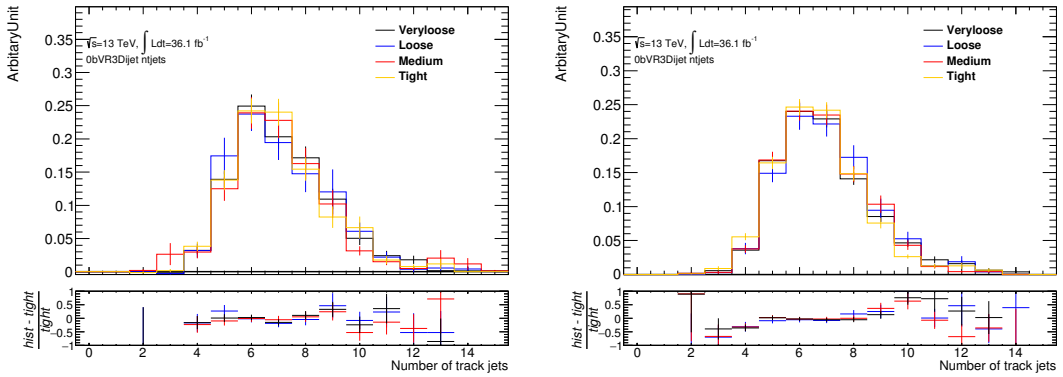

(a) Large-R Jet in one tight b-tag

(b) Large-R Jet in two tight b-tag

Figure 178: Shape differences of Di-large R Jet for MC $t\bar{t}$

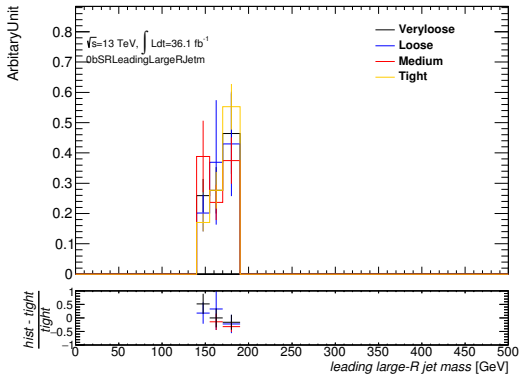

(a) Leading Large-R Jet in one tight b-tag

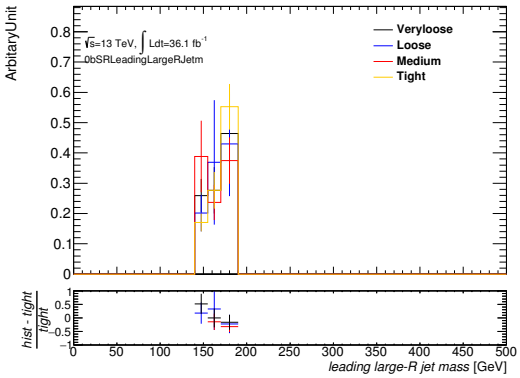

(b) Leading Large-R Jet in two tight b-tag

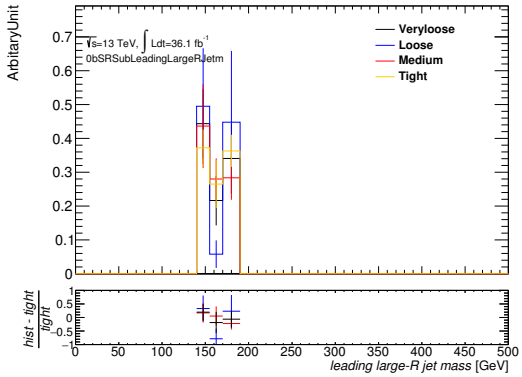

(c) Sub-leading Large-R Jet in one tight b-tag

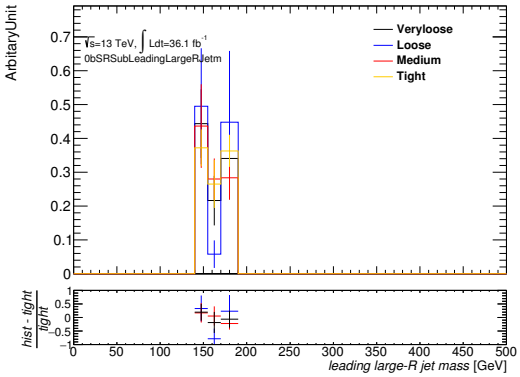

(d) Sub-leading Large-R Jet in two tight b-tag

Figure 179: Shape differences of Large-R Jet for MC $t\bar{t}$

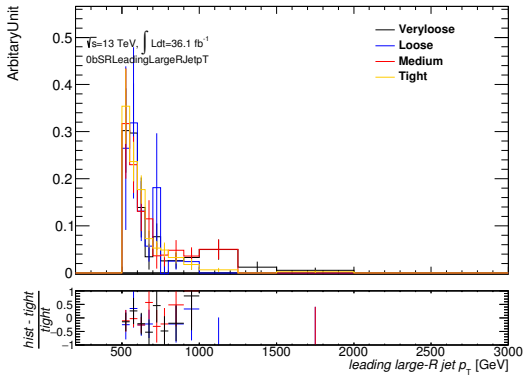

(a) Leading Large-R Jet in one tight b-tag

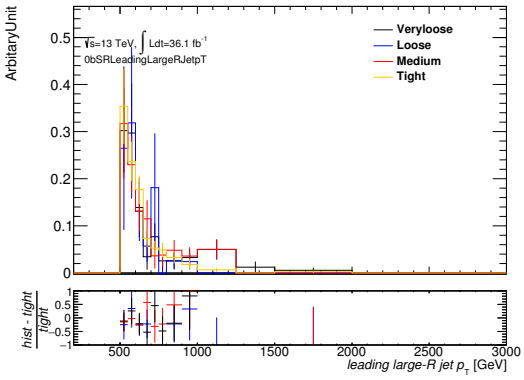

(b) Leading Large-R Jet in two tight b-tag

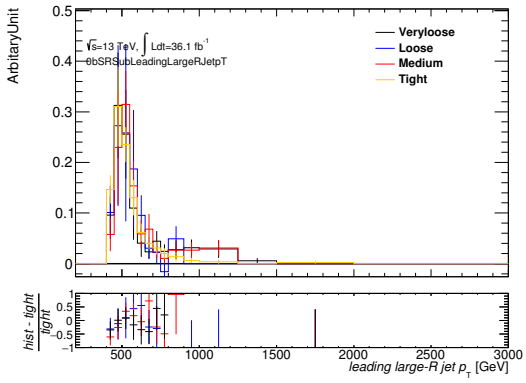

(c) Sub-leading Large-R Jet in one tight b-tag

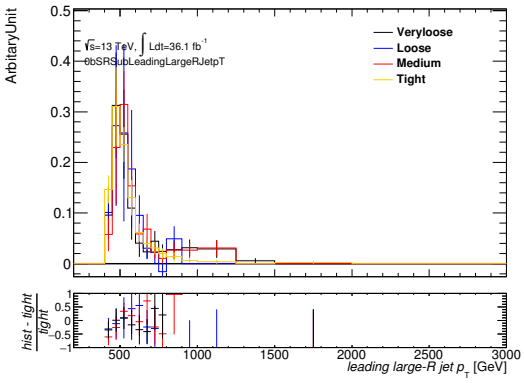

(d) Sub-leading Large-R Jet in two tight b-tag

Figure 180: Shape differences of Large-R Jet for MC $t\bar{t}$

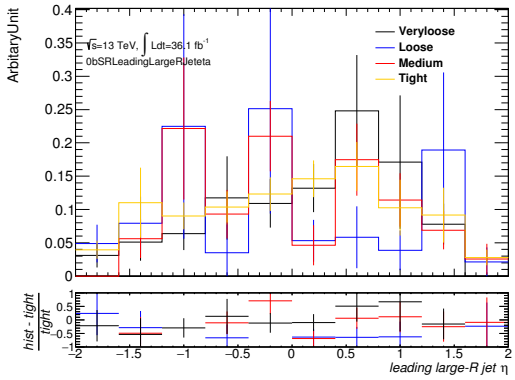

(a) Leading Large-R Jet in one tight b-tag

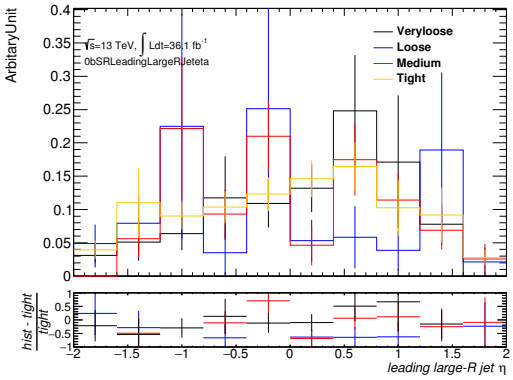

(b) Leading Large-R Jet in two tight b-tag

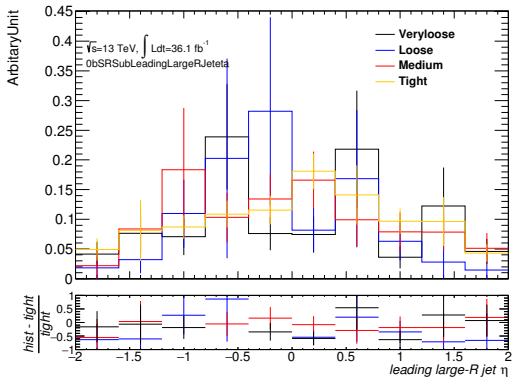

(c) Sub-leading Large-R Jet in one tight b-tag

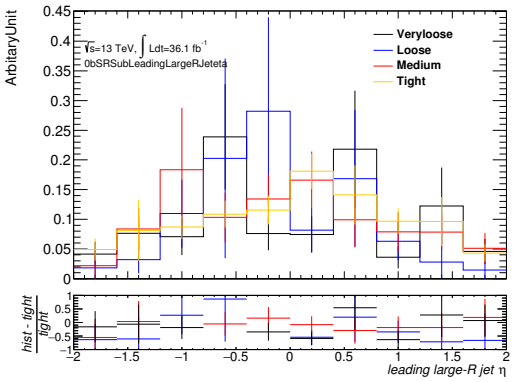

(d) Sub-leading Large-R Jet in two tight b-tag

Figure 181: Shape differences of Large-R Jet for MC $t\bar{t}$

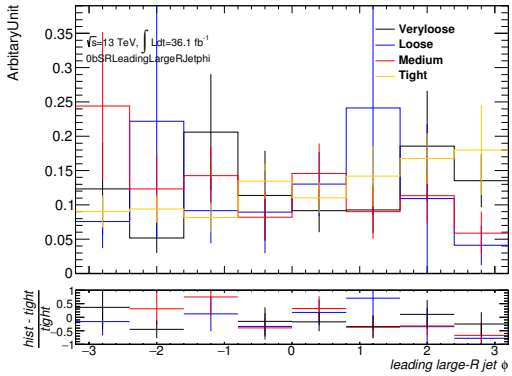

(a) Leading Large-R Jet in one tight b-tag

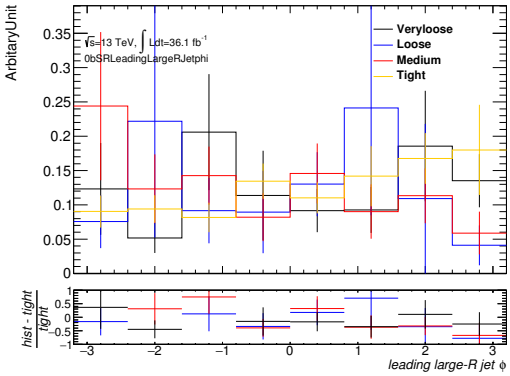

(b) Leading Large-R Jet in two tight b-tag

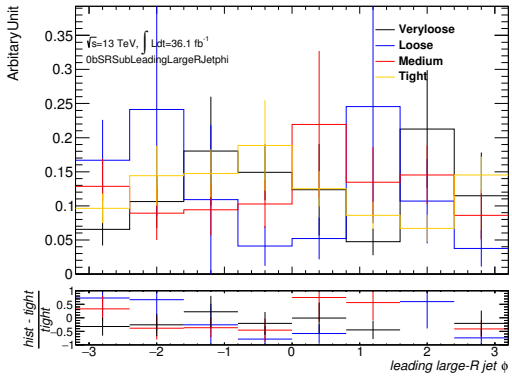

(c) Sub-leading Large-R Jet in one tight b-tag

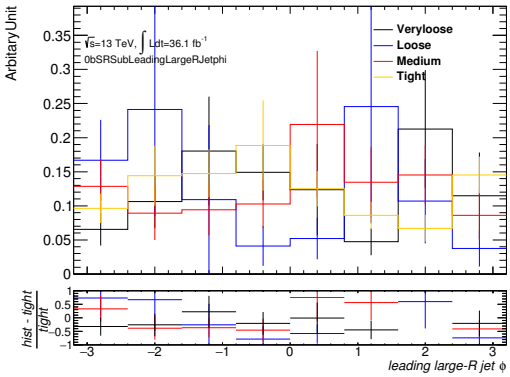

(d) Sub-leading Large-R Jet in two tight b-tag

Figure 182: Shape differences of Large-R Jet for MC $t\bar{t}$

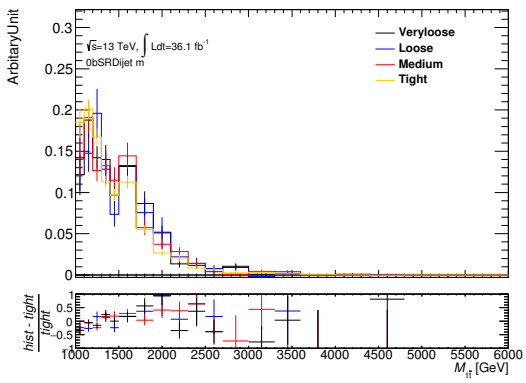

(a) Large-R Jet in one tight b-tag

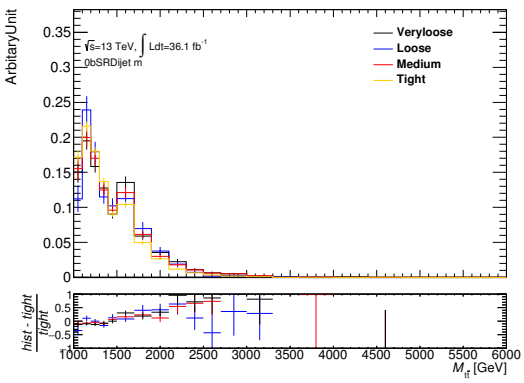

(b) Large-R Jet in two tight b-tag

Figure 183: Shape differences of Di-large R Jet for MC $t\bar{t}$

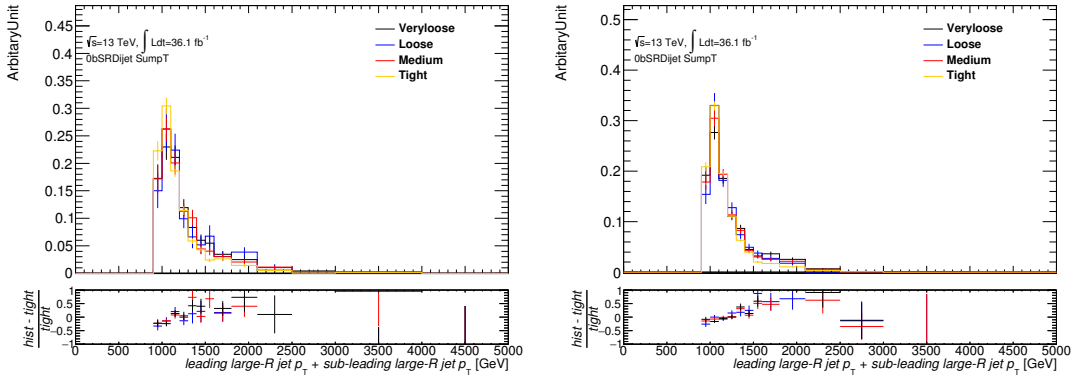

(a) Large-R Jet in one tight b-tag

(b) Large-R Jet in two tight b-tag

Figure 184: Shape differences of Di-large R Jet for MC $t\bar{t}$

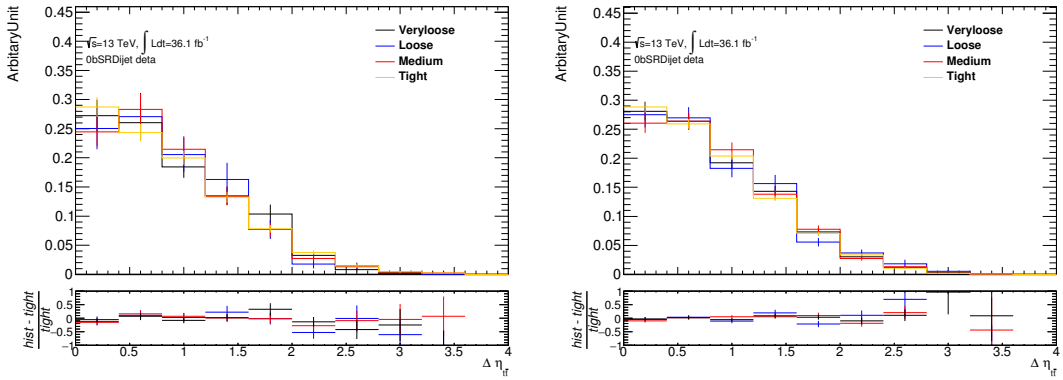

(a) Large-R Jet in one tight b-tag

(b) Large-R Jet in two tight b-tag

Figure 185: Shape differences of Di-large R Jet for MC $t\bar{t}$

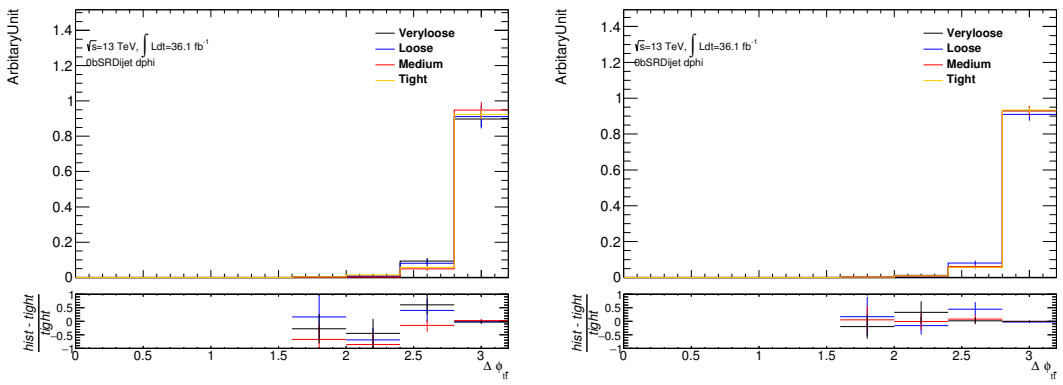

(a) Large-R Jet in one tight b-tag

(b) Large-R Jet in two tight b-tag

Figure 186: Shape differences of Di-large R Jet for MC $t\bar{t}$

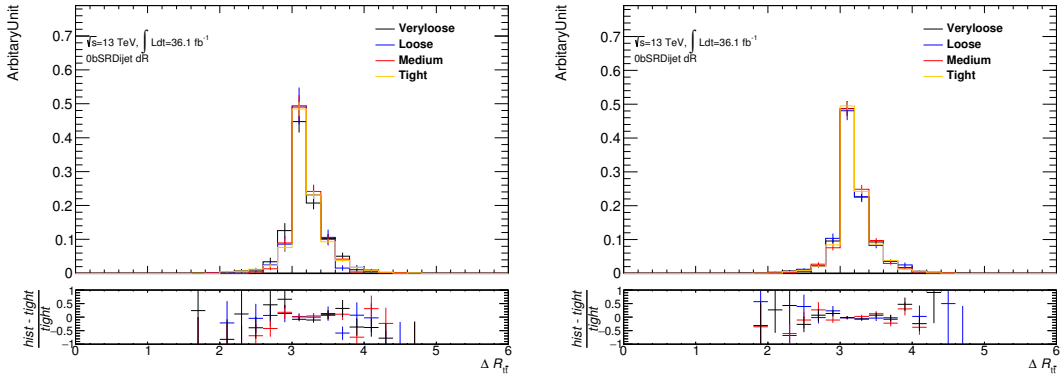

(a) Large-R Jet in one tight b-tag

(b) Large-R Jet in two tight b-tag

Figure 187: Shape differences of Di-large R Jet for MC $t\bar{t}$

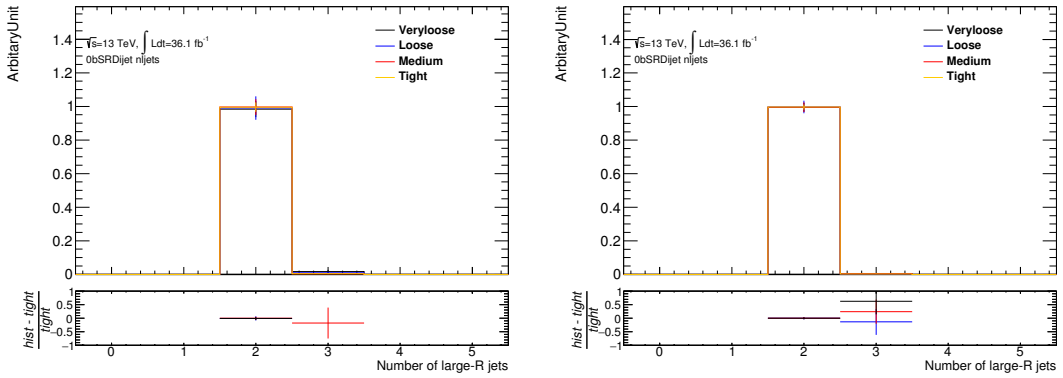

(a) Large-R Jet in one tight b-tag

(b) Large-R Jet in two tight b-tag

Figure 188: Shape differences of Di-large R Jet for MC $t\bar{t}$

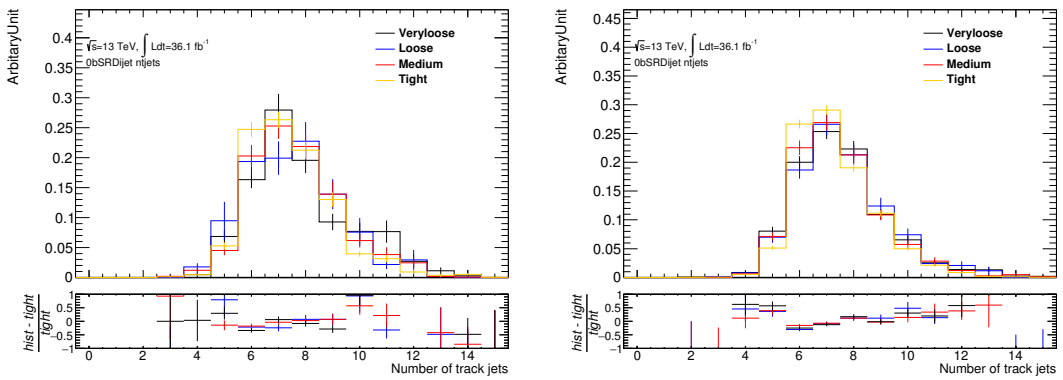

(a) Large-R Jet in one tight b-tag

(b) Large-R Jet in two tight b-tag

Figure 189: Shape differences of Di-large R Jet for MC $t\bar{t}$

E.2. Data subtracted MC $t\bar{t}$ shape difference for Data Driven multijet

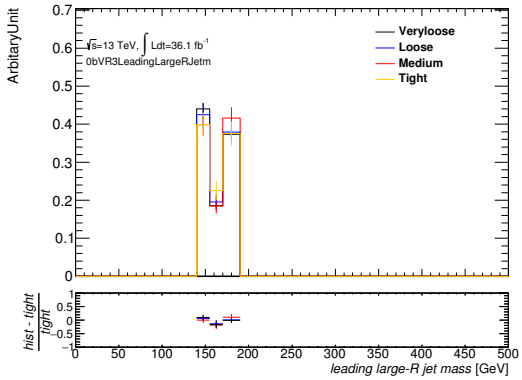

(a) Leading Large-R Jet in no tight b-tag

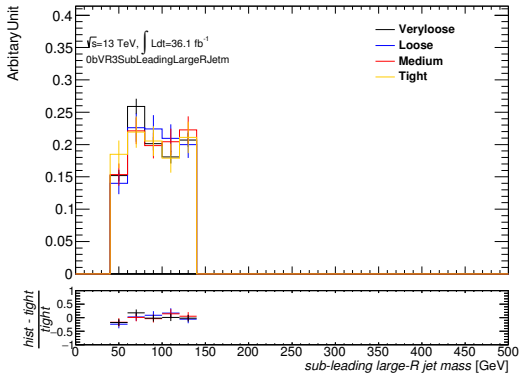

(b) Sub-leading Large-R Jet in no tight b-tag

Figure 190: Shape differences of Large-R Jet for Data - ttbar

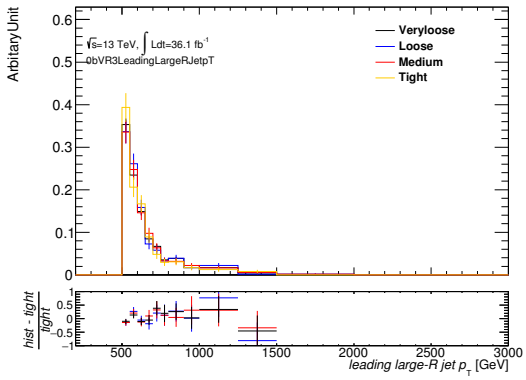

(a) Leading Large-R Jet in no tight b-tag

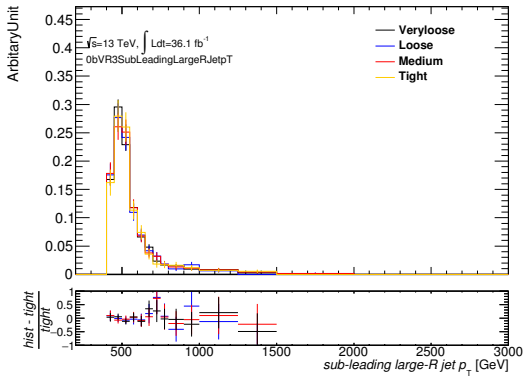

(b) Sub-leading Large-R Jet in no tight b-tag

Figure 191: Shape differences of Large-R Jet for Data - ttbar

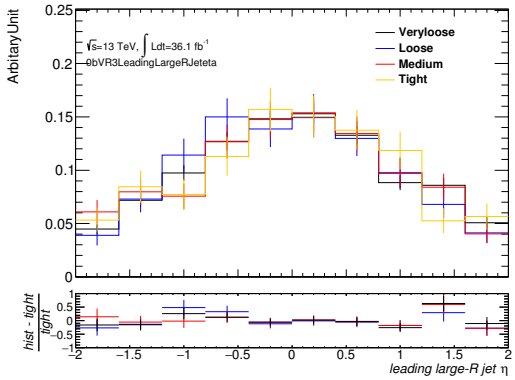

(a) Leading Large-R Jet in no tight b-tag

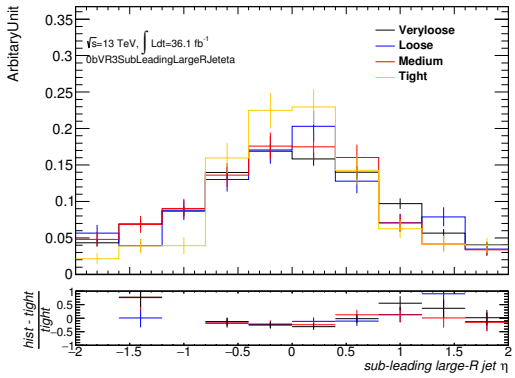

(b) Sub-leading Large-R Jet in no tight b-tag

Figure 192: Shape differences of Large-R Jet for Data - ttbar

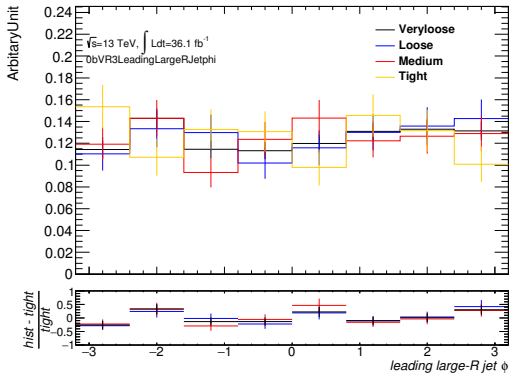

(a) Leading Large-R Jet in no tight b-tag

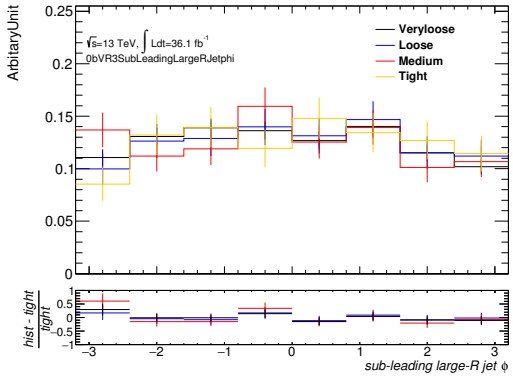

(b) Sub-leading Large-R Jet in no tight b-tag

Figure 193: Shape differences of Large-R Jet for Data - ttbar

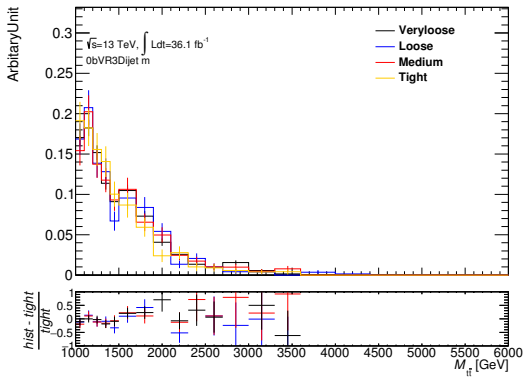

(a) Di-Large R Jet in no tight b-tag

Figure 194: Shape differences of Di-large R Jet for Data - ttbar

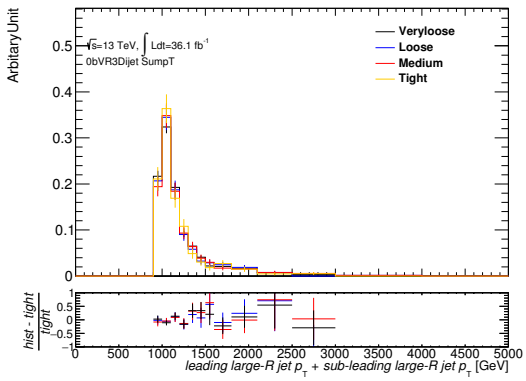

(a) Di-Large R Jet in no tight b-tag

Figure 195: Shape differences of Di-large R Jet for Data - ttbar

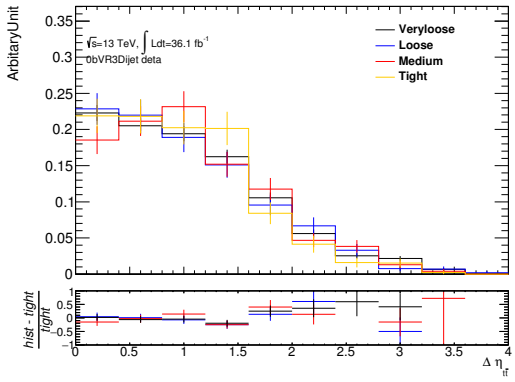

(a) Di-Large R Jet in no tight b-tag

Figure 196: Shape differences of Di-large R Jet for Data - ttbar

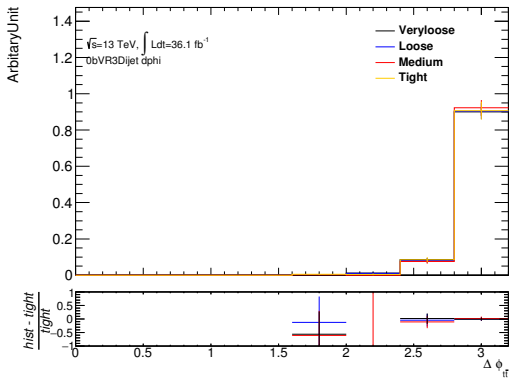

(a) Di-Large R Jet in no tight b-tag

Figure 197: Shape differences of Di-large R Jet for Data - ttbar

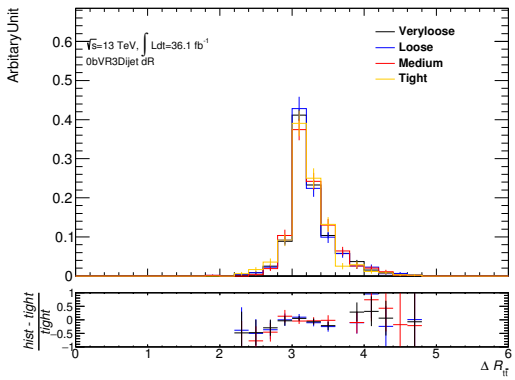

(a) Di-Large R Jet in no tight b-tag

Figure 198: Shape differences of Di-large R Jet for Data - ttbar

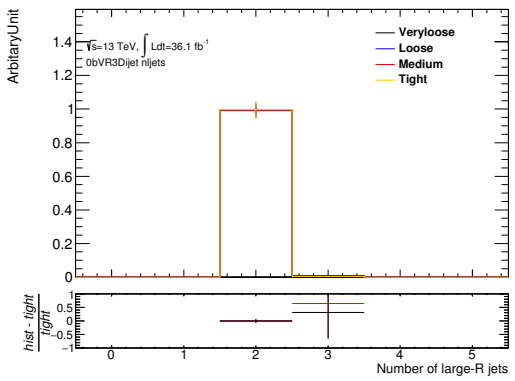

(a) Di-Large R Jet in no tight b-tag

Figure 199: Shape differences of Di-large R Jet for Data - ttbar

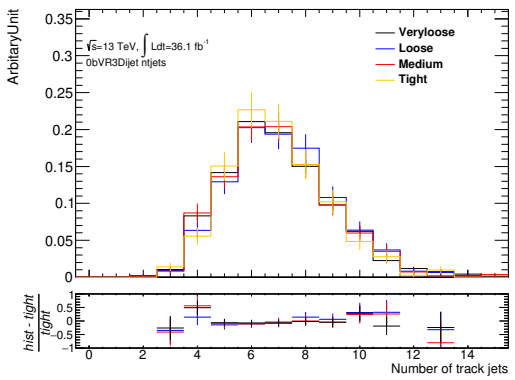

(a) Di-Large R Jet in no tight b-tag

Figure 200: Shape differences of Di-large R Jet for Data - ttbar

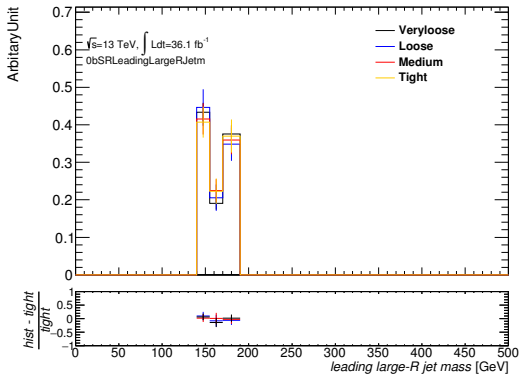

(a) Leading Large-R Jet in no tight b-tag

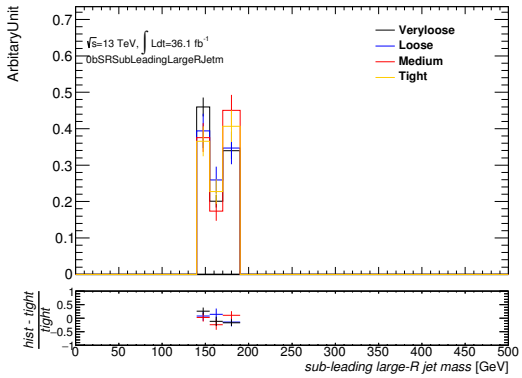

(b) Sub-leading Large-R Jet in no tight b-tag

Figure 201: Shape differences of Large-R Jet for Data - ttbar

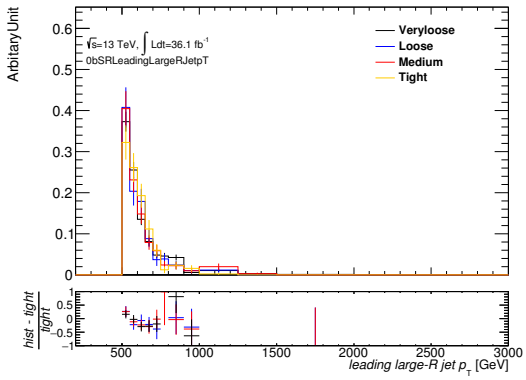

(a) Leading Large-R Jet in no tight b-tag

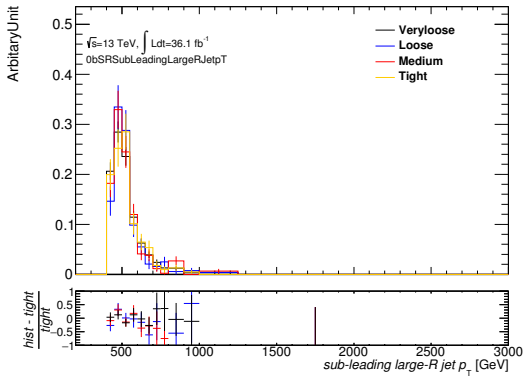

(b) Sub-leading Large-R Jet in no tight b-tag

Figure 202: Shape differences of Large-R Jet for Data - ttbar

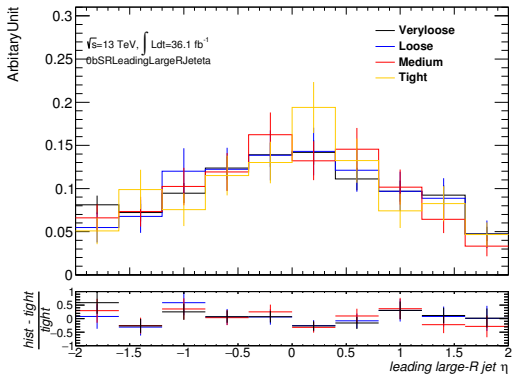

(a) Leading Large-R Jet in no tight b-tag

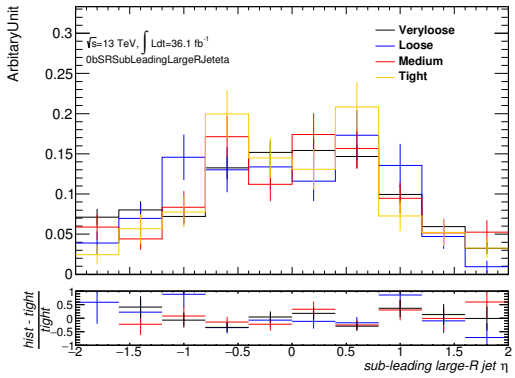

(b) Sub-leading Large-R Jet in no tight b-tag

Figure 203: Shape differences of Large-R Jet for Data - ttbar

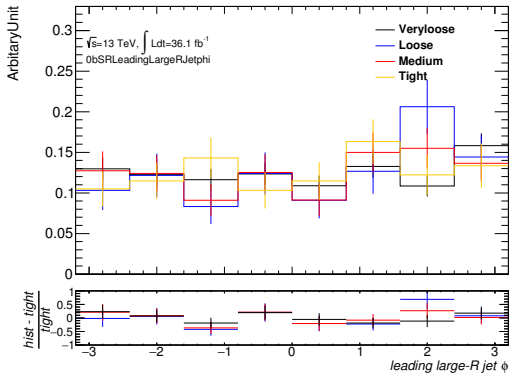

(a) Leading Large-R Jet in no tight b-tag

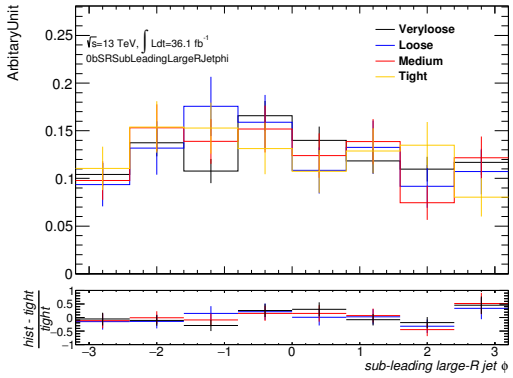

(b) Sub-leading Large-R Jet in no tight b-tag

Figure 204: Shape differences of Large-R Jet for Data - ttbar

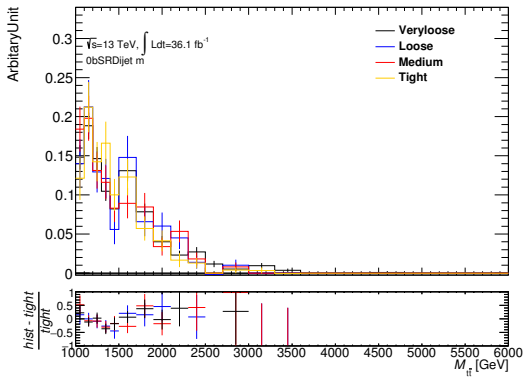

(a) Di-Large R Jet in no tight b-tag

Figure 205: Shape differences of Di-large R Jet for Data - ttbar

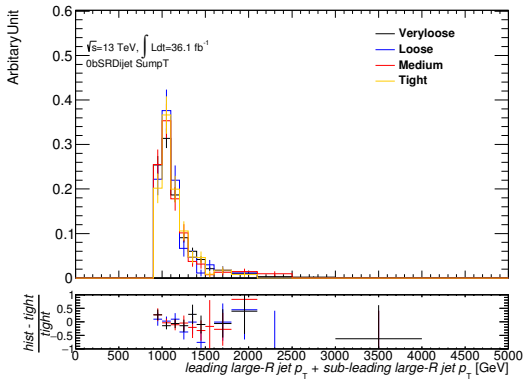

(a) Di-Large R Jet in no tight b-tag

Figure 206: Shape differences of Di-large R Jet for Data - ttbar

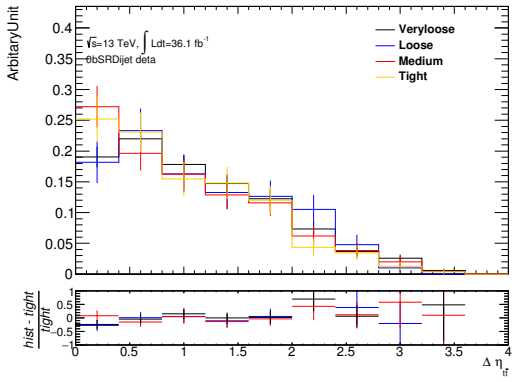

(a) Di-Large R Jet in no tight b-tag

Figure 207: Shape differences of Di-large R Jet for Data - ttbar

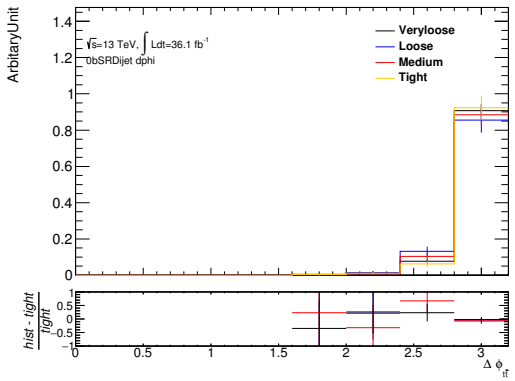

(a) Di-Large R Jet in no tight b-tag

Figure 208: Shape differences of Di-large R Jet for Data - ttbar

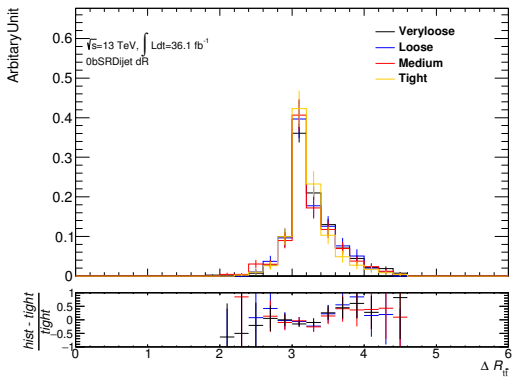

(a) Di-Large R Jet in no tight b-tag

Figure 209: Shape differences of Di-large R Jet for Data - ttbar

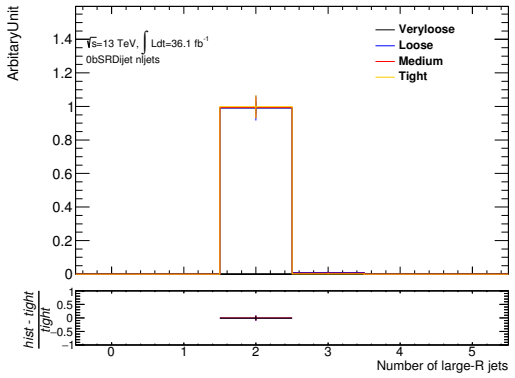

(a) Di-Large R Jet in no tight b-tag

Figure 210: Shape differences of Di-large R Jet for Data - ttbar

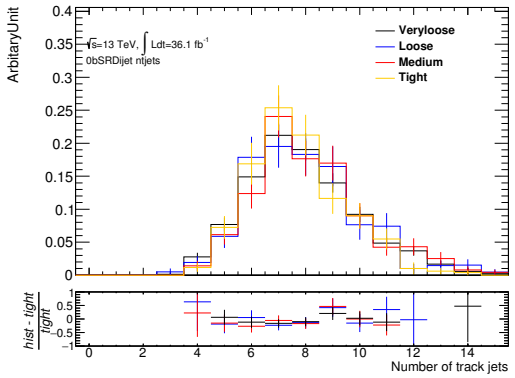

(a) Di-Large R Jet in no tight b-tag

Figure 211: Shape differences of Di-large R Jet for Data - ttbar

References

[1] G. Aad et al., *A search for $t\bar{t}$ resonances using lepton-plus-jets events in proton-proton collisions at $\sqrt{s}$ = 8 TeV with the ATLAS detector*, JHEP **08** (2015) 148, arXiv: 1505.07018 [hep-ex].

[2] V. Khachatryan et al., *Search for Resonant $t\bar{t}$ Production in Proton-Proton Collisions at $\sqrt{s}$ = 8 TeV*, (2015), arXiv: 1506.03062 [hep-ex].

[3] T. Aaltonen et al., *Search for Resonant Top-Antitop Production in the Lepton Plus Jets Decay Mode Using the Full CDF Data Set*, Phys. Rev. Lett. **110** (2013) 121802, arXiv: 1211.5363 [hep-ex].

[4] V. Abazov et al., *Search for $t\bar{t}$ resonances in the lepton plus jets final state in $p\bar{p}$ collisions at $\sqrt{s}$ = 1.96 TeV*, Phys. Lett. **B668** (2008) 98, arXiv: 0804.3664 [hep-ex].

[5] S. Chatrchyan et al., *Searches for new physics using the $t\bar{t}$ invariant mass distribution in pp collisions at $\sqrt{s}$ = 8 TeV*, Phys. Rev. Lett. **111** (2013) 211804, [Erratum: Phys. Rev. Lett.112,no.11,119903(2014)], arXiv: 1309.2030 [hep-ex].

[6] S. Chatrchyan et al., *Search for Anomalous $t\bar{t}$ Production in the Highly-Boosted All-Hadronic Final State*, JHEP **09** (2012) 029, [Erratum: JHEP03,132(2014)], arXiv: 1204.2488 [hep-ex].

[7] S. Chatrchyan et al., *Search for resonant $t\bar{t}$ production in lepton+jets events in pp collisions at $\sqrt{s}$ = 7 TeV*, JHEP **12** (2012) 015, arXiv: 1209.4397 [hep-ex].

[8] S. Chatrchyan et al., *Search for Z ' resonances decaying to $t\bar{t}$ in dilepton+jets final states in pp collisions at $\sqrt{s}$ = 7 TeV*, Phys. Rev. **D87** (2013) 072002, arXiv: 1211.3338 [hep-ex].

[9] G. Aad et al., *Search for $t\bar{t}$ resonances in the lepton plus jets final state with ATLAS using 4.7 fb^{-1} of pp collisions at $\sqrt{s}$ = 7 TeV*, Phys. Rev. **D88** (2013) 012004, arXiv: 1305.2756 [hep-ex].

[10] G. Aad et al., *Search for resonances decaying into top-quark pairs using fully hadronic decays in pp collisions with ATLAS at $\sqrt{s}$ = 7 TeV*, JHEP **01** (2013) 116, arXiv: 1211.2202 [hep-ex].

[11] V. M. Abazov et al., *Search for a Narrow $t\bar{t}$ Resonance in $p\bar{p}$ Collisions at $\sqrt{s}$ = 1.96 TeV*, Phys. Rev. **D85** (2012) 051101, arXiv: 1111.1271 [hep-ex].

[12] T. Aaltonen et al., *Search for resonant production of $t\bar{t}$ decaying to jets in $p\bar{p}$ collisions at $\sqrt{s}$ = 1.96 TeV*, Phys. Rev. **D84** (2011) 072003, arXiv: 1108.4755 [hep-ex].

[13] 'Search for heavy particles decaying to pairs of highly-boosted top quarks using lepton-plus-jets events in proton–proton collisions at $\sqrt{s}$ = 13 TeV with the ATLAS detector', tech. rep. ATLAS-CONF-2016-014, CERN, 2016, URL: http://cds.cern.ch/record/2141001.

[14] 'Search for $t\bar{t}$ resonances in boosted semileptonic final states in pp collisions at $\sqrt{s}$ = 13 TeV', tech. rep. CMS-PAS-B2G-15-002, CERN, 2016, URL: https://cds.cern.ch/record/2138345.

[15] ATLAS Collaboration, *Observation of a new particle in the search for the Standard Model Higgs boson with the ATLAS detector at the LHC*, Phys. Lett. B **716** (2012) 1, arXiv: 1207.7214 [hep-ex].

[16] C. Patrignani and et al, *Review of Particle Physics*, Chin. Phys. C **40** (2016) 100001.

[17] P. W. Higgs, *Broken symmetries, massless particles and gauge fields*, Phys. Rev. Lett. **12** (1964) 132.

[18] S.Tomonaga, *On a Relativistically Invariant Formulation of the Quantum Theory of Wave Fields*, Prog. Theor. Phys. **1** (1946) 27.

[19] J.Schwinger, *On Gauge Invariance and Vacuum Polarization*, Phys. Rev. **82** (1951) 664.

[20] R.P.Feynman, *Mathematical Formulation of the Quantum Theory of Electromagnetic Interaction*, Phys. Rev. **80** (1950) 440.

[21] R.P.Feynman, *An Operator calculus having applications in quantum electrodynamics*, Phys. Rev. **84** (1951) 108.

[22] W.A. et al., *Light cone current algebra, π_0 decay, and e^+e^- annihilation*, R. Gato (ed.), Scale and Conformal Symmetry in Hadron Physics (1973) 139.

[23] D. J. Gross and F. Wilczek, *Ultraviolet Behavior of Non-Abelian Gauge Theories*, Phys. Rev. Lett. **30** (1973) 1343.

[24] D. J. Gross and F. Wilczek, *Asymptotically Free Gauge Theories. I*, Phys. Rev. D **8** (1973) 3633.

[25] D. J. Gross and F. Wilczek, *Asymptotically Free Gauge Theories. II*, Phys. Rev. D **9** (1974) 980.

[26] H. D. Politzer, *Reliable Perturbative Results for Strong Interactions?*, Phys. Rev. Lett. **30** (1973) 1346.

[27] H. D. Politzer, *Asymptotic freedom: An approach to strong interactions*, Physics Reports **14** (1974) 129.

[28] S. Glashow, *Partial Symmetries of Weak Interactions*, Nucl.Phys. **22** (1961) 579.

[29] S. A. and W. J. C., *Electromagnetic and weak interactions*, Phys. Lett. **13** (1964) 168.

[30] S. Weinberg, *A Model of Leptons*, Phys. Rev. Lett. **19** (1967) 1264.

[31] V. C. Rubin and J. Ford W. Kent, *Rotation of the Andromeda Nebula from a Spectroscopic Survey of Emission Regions*, Astrophysical Journal **159** (1970) 471.

[32] W. K. J. T. N. Rubin Vera C. Ford, *Rotational properties of 21 SC galaxies with a large range of luminosities and radii, from NGC 4605 /R = 4kpc/ to UGC 2885 /R = 122 kpc/*, Astrophysical Journal **238** (1980) 471.

[33] R. Massey, J. E. Rhodes and S. Richard, *Dark matter maps reveal cosmic scaffolding*, Nature **445** (2007) 286.

[34] C. T. Hill, *Topcolor assisted technicolor*, Phys. Lett. **B345** (1995) 483, arXiv: hep-ph/9411426 [hep-ph].

[35] R. M. Harris, C. T. Hill and S. J. Parke, *Cross-section for topcolor Z-prime(t) decaying to t anti-t: Version 2.6*, (1999), arXiv: hep-ph/9911288 [hep-ph].

[36] R. M. Harris and S. Jain, *Cross Sections for Leptophobic Topcolor Z' Decaying to Top-Antitop*, Eur. Phys. J. **C72** (2012) 2072, arXiv: 1112.4928 [hep-ph].

[37] K. Agashe et al., *Warped Gravitons at the LHC and Beyond*, Phys.Rev. **D76** (2007) 036006, arXiv: hep-ph/0701186 [hep-ph].

[38] T. Kaluza, *Zum Unitätsproblem in der Physik*, Sitzungsber. Preuss. Akad. Wiss. Berlin (1921) 966.

[39] O. Klein, *Quantentheorie und fünfdimensionale Relativitätstheorie*, Zeitschrift für Physik **37** (1926) 895, ISSN: 0044-3328, URL: https://doi.org/10.1007/BF01397481.

[40] L. Randall and R. Sundrum, *A Large mass hierarchy from a small extra dimension*, Phys. Rev. Lett. **83** (1999) 3370, arXiv: hep-ph/9905221 [hep-ph].

[41] B. Lillie, L. Randall and L.-T. Wang, *The Bulk RS KK-gluon at the LHC*, JHEP **09** (2007) 074, arXiv: hep-ph/0701166 [hep-ph].

[42] B. C. Allanach et al., *Gluon-initiated production of a Kaluza-Klein gluon in a Bulk Randall-Sundrum model*, JHEP **03** (2010) 014, arXiv: 0910.1350 [hep-ph].

[43] G. Roland, *Plans for Upgrading the CERN Proton Accelerator Complex*, J. Phys.: Conf. Ser. **110** (2008) 112003.

[44] ATLAS Collaboration, *The ATLAS Experiment at the CERN Large Hadron Collider*, JINST **3** (2008) S08003.

[45] ATLAS Collaboration, *Studies of the performance of the ATLAS detector using cosmic-ray muons*, Eur.Phys.J. C **71** (2011) 1593, arXiv: 1011.6665 [physics.ins-det].

[46] G. Aad et al., *The ATLAS Experiment at the CERN Large Hadron Collider*, JINST **3** (2008) S08003.

[47] ATLAS Collaboration, *Performance of the ATLAS Trigger System in 2010*, Eur. Phys. J. C **72** (2012) 1849, arXiv: 1110.1530 [hep-ex].

[48] D. J. Lange, *The EvtGen particle decay simulation package*, Nucl. Instrum. Meth. A **462** (2001) 152.

[49] ATLAS Collaboration, *The ATLAS Simulation Infrastructure*, Eur. Phys. J. C **70** (2010) 823, arXiv: 1005.4568 [physics.ins-det].

[50] S. Agostinelli et al., *GEANT4: A simulation toolkit*, Nucl. Instrum. Meth. A **506** (2003) 250.

[51] T. Sjöstrand, S. Mrenna and P. Z. Skands, *A Brief Introduction to PYTHIA 8.1*, Comput. Phys. Commun. **178** (2008) 852, arXiv: 0710.3820 [hep-ph].

[52] A. Martin et al., *Parton distributions for the LHC*, Eur. Phys. J. C **63** (2009) 189, arXiv: 0901.0002 [hep-ph].

[53] ATLAS Collaboration, *Summary of ATLAS Pythia 8 tunes*, ATL-PHYS-PUB-2012-003, 2012, URL: http://cds.cern.ch/record/1474107.

[54] J. Butterworth et al., *PDF4LHC recommendations for LHC Run II*, J. Phys. G **43** (2016) 023001, arXiv: 1510.03865 [hep-ph].

[55] ATLAS Collaboration, *ATLAS Run 1 Pythia 8 tunes*, ATL-PHYS-PUB-2014-021, 2014, URL: http://cds.cern.ch/record/1966419.

[56] R. Bonciani et al., *Electroweak top-quark pair production at the LHC with Z' bosons to NLO QCD in POWHEG*, JHEP **1602** (2016) 141, arXiv: 1511.08185 [hep-ph].

[57] J. Gao et al., *Next-to-leading order QCD corrections to the heavy resonance production and decay into top quark pair at the LHC*, Phys. Rev. **D82** (2010) 014020, arXiv: 1004.0876 [hep-ph].

[58] F. Caola, K. Melnikov and M. Schulze, *Complete next-to-leading order QCD description of resonant Z' production and decay into $t\bar{t}$ final states*, Phys. Rev. **D87** (2013) 034015, arXiv: 1211.6387 [hep-ph].

[59] J. Alwall et al., *The automated computation of tree-level and next-to-leading order differential cross sections, and their matching to parton shower simulations*, JHEP **1407** (2014) 079, arXiv: 1405.0301 [hep-ph].

[60] R. D. Ball et al., *Parton distributions with LHC data*, Nucl. Phys. B **867** (2013) 244, arXiv: 1207.1303 [hep-ph].

[61] P. Nason, *A New method for combining NLO QCD with shower Monte Carlo algorithms*, JHEP **0411** (2004) 040, arXiv: hep-ph/0409146 [hep-ph].

[62] S. Frixione, P. Nason and C. Oleari, *Matching NLO QCD computations with Parton Shower simulations: the POWHEG method*, JHEP **0711** (2007) 070, arXiv: 0709.2092 [hep-ph].

[63] S. Alioli et al., *A general framework for implementing NLO calculations in shower Monte Carlo programs: the POWHEG BOX*, JHEP **1006** (2010) 043, arXiv: 1002.2581 [hep-ph].

[64] H.-L. Lai et al., *New parton distributions for collider physics*, Phys. Rev. D **82** (2010) 074024, arXiv: 1007.2241 [hep-ph].

[65] J. Gao et al., *CT10 next-to-next-to-leading order global analysis of QCD*, Phys. Rev. D **89** (2014) 033009, arXiv: 1302.6246 [hep-ph].

[66] M. Cacciari et al., *Top-pair production at hadron colliders with next-to-next-to-leading logarithmic soft-gluon resummation*, Phys. Lett. B **710** (2012) 612, arXiv: 1111.5869 [hep-ph].

[67] M. Beneke et al., *Hadronic top-quark pair production with NNLL threshold resummation*, Nucl. Phys. B **855** (2012) 695, arXiv: 1109.1536 [hep-ph].

[68] P. Baernreuther, M. Czakon and A. Mitov, *Percent Level Precision Physics at the Tevatron: First Genuine NNLO QCD Corrections to $q\bar{q} \to t\bar{t} + X$*, Phys. Rev. Lett. **109** (2012) 132001, arXiv: 1204.5201 [hep-ph].

[69] M. Czakon and A. Mitov, *NNLO corrections to top-pair production at hadron colliders: the all-fermionic scattering channels*, JHEP **1212** (2012) 054, arXiv: 1207.0236 [hep-ph].

[70] M. Czakon and A. Mitov, *NNLO corrections to top pair production at hadron colliders: the quark-gluon reaction*, JHEP **1301** (2013) 080, arXiv: 1210.6832 [hep-ph].

[71] M. Czakon, P. Fiedler and A. Mitov, *The total top quark pair production cross-section at hadron colliders through $O(\alpha_S^4)$*, Phys. Rev. Lett. **110** (2013) 252004, arXiv: 1303.6254 [hep-ph].

[72] M. Czakon and A. Mitov,
Top++: A Program for the Calculation of the Top-Pair Cross-Section at Hadron Colliders,
Comput. Phys. Commun. **185** (2014) 2930, arXiv: 1112.5675 [hep-ph].

[73] T. Sjöstrand, S. Mrenna and P. Z. Skands, *PYTHIA 6.4 Physics and Manual*,
JHEP **0605** (2006) 026, arXiv: hep-ph/0603175 [hep-ph].

[74] J. Pumplin et al.,
New generation of parton distributions with uncertainties from global QCD analysis,
JHEP **0207** (2002) 012, arXiv: hep-ph/0201195 [hep-ph].

[75] P. Z. Skands, *Tuning Monte Carlo Generators: The Perugia Tunes*,
Phys. Rev. D **82** (2010) 074018, arXiv: 1005.3457 [hep-ph].

[76] ATLAS Collaboration,
Topological cell clustering in the ATLAS calorimeters and its performance in LHC Run 1,
Eur. Phys. J C **77** (2017) 490, arXiv: 1603.02934 [hep-ex].

[77] M. Cacciari, G. P. Salam and G. Soyez, *The Anti-k_t jet clustering algorithm*,
JHEP **0804** (2008) 063, arXiv: 0802.1189 [hep-ph].

[78] 'Jet Calibration and Systematic Uncertainties for Jets Reconstructed in the ATLAS Detector at $\sqrt{s}$ = 13 TeV', tech. rep. ATL-PHYS-PUB-2015-015, CERN, 2015,
URL: http://cds.cern.ch/record/2037613.

[79] ATLAS Collaboration, *Tagging and suppression of pileup jets with the ATLAS detector*,
ATLAS-CONF-2014-018, 2014, URL: http://cdsweb.cern.ch/record/1700870.

[80] 'Selection of jets produced in 13TeV proton-proton collisions with the ATLAS detector',
tech. rep. ATLAS-CONF-2015-029, CERN, 2015,
URL: http://cds.cern.ch/record/2037702.

[81] D. Krohn, J. Thaler and L.-T. Wang, *Jet Trimming*, JHEP **1002** (2010) 084,
arXiv: 0912.1342 [hep-ph].

[82] S. Catani et al., *New clustering algorithm for multi - jet cross-sections in e^+e^- annihilation*,
Phys. Lett. B **269** (1991) 432.

[83] S. D. Ellis and D. E. Soper, *Successive combination jet algorithm for hadron collisions*,
Phys. Rev. D **48** (1993) 3160, arXiv: hep-ph/9305266 [hep-ph].

[84] S. Catani et al., *Longitudinally invariant K_t clustering algorithms for hadron hadron collisions*,
Nucl. Phys. B **406** (1993) 187.

[85] ATLAS Collaboration, *Performance of jet substructure techniques in early $\sqrt{s}$ = 13 TeV pp collisions with the ATLAS detector*, ATLAS-CONF-2015-035, 2015,
URL: http://cdsweb.cern.ch/record/2041462.

[86] ATLAS Collaboration, *Jet mass reconstruction with the ATLAS Detector in early Run 2 data*,
ATLAS-CONF-2016-035, 2016, URL: https://cds.cern.ch/record/2200211.

[87] ATLAS Collaboration,
Flavor Tagging with Track-Jets in Boosted Topologies with the ATLAS Detector,
ATL-PHYS-PUB-2014-013, 2014, URL: https://atlas.web.cern.ch/Atlas/GROUPS/PHYSICS/PUBNOTES/ATL-PHYS-PUB-2014-013.

[88] ATLAS Collaboration, *Electron efficiency measurements with the ATLAS detector using the 2012 LHC proton–proton collision data*, ATLAS-CONF-2014-032, 2014, URL: http://cdsweb.cern.ch/record/1706245.

[89] ATLAS Collaboration, *Muon reconstruction performance of the ATLAS detector in proton–proton collision data at $\sqrt{s}$ =13 TeV*, Eur. Phys. J. C **76** (2016) 292, arXiv: 1603.05598 [hep-ex].

[90] J. Thaler and K. Van Tilburg, *Identifying Boosted Objects with N-subjettiness*, JHEP **1103** (2011) 015, arXiv: 1011.2268 [hep-ph].

[91] J. Thaler and K. Van Tilburg, *Maximizing Boosted Top Identification by Minimizing N-subjettiness*, JHEP **1202** (2012) 093, arXiv: 1108.2701 [hep-ph].

[92] D. N. A. J. Larkoski and J. Thaler, *Jet Shapes with the Broadening Axis*, JHEP **1404** (2014) 017, arXiv: 1401.2158 [hep-ph].

[93] J. Kühn, A. Scharf and P. Uwer, *Weak Interactions in Top-Quark Pair Production at Hadron Colliders: An Update*, (2013), arXiv: 1305.5773 [hep-ph].

[94] C. K. G. E. e. a. Cowan G., *Asymptotic formulae for likelihood-based tests of new physics*, Eur. Phys. J. C **71** (2011) 1264.